



This is to certify that the  
dissertation entitled

**HYPERSPECTRAL DATA MODELING FOR WATER  
QUALITY STUDIES IN MICHIGAN'S INLAND LAKES**

presented by

**Narumon Wiangwang**

has been accepted towards fulfillment  
of the requirements for the

Ph.D. degree in Geography

  
Major Professor's Signature

6/30/06

Date

*MSU is an Affirmative Action/Equal Opportunity Institution*

**LIBRARY  
Michigan State  
University**

**PLACE IN RETURN BOX** to remove this checkout from your record.  
**TO AVOID FINES** return on or before date due.  
**MAY BE RECALLED** with earlier due date if requested.

DATE DUE	DATE DUE	DATE DUE
JUL 24 2009		
APR 1 2010		
SEP 29 2010		
093010		

**HYPERSPECTRAL DATA MODELING FOR WATER QUALITY STUDIES  
IN MICHIGAN'S INLAND LAKES**

**By**

**Narumon Wiangwang**

**A DISSERTATION**

**Submitted to  
Michigan State University  
in partial fulfillment of the requirements  
for the degree of**

**DOCTOR OF PHILOSOPHY**

**Department of Geography**

**2006**

## **ABSTRACT**

### **HYPERSPECTRAL DATA MODELING FOR WATER QUALITY STUDIES IN MICHIGAN'S INLAND LAKES**

By

Narumon Wiangwang

Hyperspectral remote sensing imagery has been used to estimate spatial and temporal variation of water quality, such as chlorophyll *a*, transparency, and suspended solids, primarily for marine and coastal waters. Although physicochemical properties of marine and inland waters differ, hyperspectral data and modeling may provide an alternative tool for inland lake assessment. However, little has been done to identify the most suitable spectral bands for water quality estimation and there is a lack of quantitative relationship between water quality and hyperspectral data. The primary objectives of this study are to identify optimal spectral bands most sensitive to water quality indicators and to develop improved hyperspectral water quality indicators of inland lakes. The secondary objective is to determine the most effective filters for noise removal in hyperspectral data.

To address these objectives, a field campaign was conducted on 42 inland lakes in Michigan in 2004. Radiometric spectra, Secchi disk depth, dissolved oxygen, temperature, and light extinction profile data were collected. Water samples were analyzed for chlorophyll *a*, suspended solid, total nitrogen, total phosphorus, non-purgable organic carbon, and phytoplankton species composition. Spectral radiances were measured with a hand-held spectrometer

(LabSpec® Pro) and with an airborne Imaging Spectrometer for Applications (AISA) sensor, to correlate the water quality and hyperspectral data.

Principal Component Analysis was used to identify the narrow-wavebands, and derivative analysis used to determine the region-wavebands. Statistical spectral water quality indicators were developed to correlate with Secchi depth, chlorophyll *a*, total suspended solid, non-purgable organic carbon, diatom biomass, green algal biomass, and bluegreen algal biomass. These relations were validated to suggest that high accuracies were achieved for Secchi depth ( $R^2$  0.76 – 0.84), chlorophyll *a* ( $R^2$  0.70 – 0.76), and bluegreen algae ( $R^2$  0.56 – 0.72). The quantitative relationship between remotely sensed variables and water quality indicators can be used to extrapolate point-based water quality measurements to large spatial extents for an improved water quality assessment. Additionally, the Savitsky Golay filter was found the best to remove spectral noises. The innovation of this study is that it developed a quantitative relationship between hyperspectral data and water quality variables of inland lakes in Michigan.

Copyright by

NARUMON WIANGWANG

2006

**To my parents, whose love and faith has been unconditional.**

## **ACKNOWLEDGMENTS**

Getting to this point has been a long, eventful journey. Although I have a great feeling of accomplishment upon finishing my dissertation, there is a stronger feeling of gratitude for all the people who helped me reach this point and who helped to make the experience such an intellectually fulfilling and enjoyable one. Mentioning all the people who have helped along the way would fill a substantial volume. For this and for the miracle of life and all that it brings with it, I am eternally indebted, first of all, to my parents. Beyond that, there are too many debts to adequately acknowledge, but a few deserve special mention.

I am grateful that I have two wonderful parents who have raised me to be strong and to have confidence in myself to try anything and to be confident in their unending love. I thank my husband for believing in me. His commitment, emotional support, dedication, and love made this achievement possible.

While my parents are the reasons I was able to begin this research, Professor Jiaguo Qi, my advisor, is the reason I was able to complete it. I first met Dr. Qi when I had just begun my Master's program. Although he was not my major advisor at the time, I had been working closely with him as he was one of the research committee members. Since he became my major advisor at the beginning of my Doctoral program, Dr. Qi has been a constant, buoyant source of encouragement and inspiration. As a fine academic example, he artfully

combines rigorous standards with gentle support and caring. He always listens generously to students and respects their ideas, never forcing his own agenda, but instead working hard to clarify and help them flourish. Dr. Qi has been my teacher, my director, my employer, my discussant, and always my mentor. I thank him for the long hours and thoughtful responses. He went beyond the call of duty, and he did so with complete respect for the ways in which the personal, political, and professional interact. I wish all doctoral students could have directors who worked as hard and who made them feel as successful as Dr. Jiaguo Qi has me.

I wish to express my sincerest appreciation to each member of my committee, Dr. Joseph Messina, Dr. Robert Jan Stevenson, and Dr. David Lusch. They have been a pleasure to work with and have always offered advice, encouragement and support. I would like to express my deepest gratefulness to Dr. Messina not only for his professional guidance on research but also his understanding, encouragement and support throughout my time at Michigan State University. Several times, I wonder how someone, let alone a university professor, could be incredibly patient with my writing. I am amazed with how Dr. Messina spent time and effort on revising my thesis, dissertation, and publication writing through all these years. He too is someone I will always look up to. I am obliged to Dr. Stevenson for his expertise and his kindness. He alone brought the entire ecological perspective to the research. I am thankful for Dr. Lusch's comments on the research. His detailed insight has completed this work. Together, these four members of my guidance committee have tried their best to form pieces of this work into a complete research effort.

Committee members who care about their students and understand their development as a scholar are invaluable. Superb mentors, they have remained constant and patient throughout a very long process. The flaws that remain in this work are mine alone.

My friends and officemates at Michigan State University made the cold winters enjoyable and continue to push my thinking further. Thanks especially to Cuizhen Wang, Yasuyo Makido, Jianjun Ge, Nate Torbick, Meleia Egger, Meghan Burns, and Eraldo Matricardi and many others for their continuing understanding and support. They have made my six years away from home and family so pleasurable. With them, Michigan State University is a 'home' away from home. A special thanks goes out to my dearest friends Meghan and Eraldo for being such warm-hearted individuals. They have always been there for me. I am blessed to get to know and be their friend. They will forever be in my thoughts.

I wish to thank The Royal Thai Government, my scholarship sponsor for both Master's and Ph.D degrees, for belief in me and for their financial support which helped make all of this possible. The Great Lakes Fisheries Trust receives my sincere gratitude for supporting the Muskegon River Watershed Ecological Assessment Project and making it possible for me to conduct fieldwork, make academic presentations, and work to complete this dissertation. The funding from this research project, through considerations of Dr. Qi and Dr. Stevenson, provided a boat for a safe field data collection, valuable hyperspectral data to use in the research, and many more resources

needed in order to complete this research. I am deeply thankful for Dr. Richard Hauer, University of Montana, for his help providing the airborne hyperspectral data. He flew his personal aircraft all the way from Montana to acquire the imagery over the study lakes in Michigan. My gratitude extends to The Department of Geography for the wonderful academic facility, and The Graduate School for The Dissertation Completion Fellowship. A million thanks go to Sharon Ruggles, Graduate Secretary of Department of Geography, Michigan State University, who always help with regulations and paperwork. She made my life a lot easier and my experience at Michigan State University truly delightful.

This research would have been far different without the help of my field crews, Praveen Ummadi, Brian Napoletano, Nathan Torbic, Meghan and Perry. I am deeply indebted to Meghan and Perry for their dedicated assistance, and always being there when needed. They have gone beyond duty to help. Dr. Stevenson's lab staff and former staff: Vanessa, Lara, Kalina and others, have provided tremendous help with the field and laboratory equipment. Intensive MATLAB learning could not have gone smoothly without help from Roma – Rahmatullia Igamberdiev.

Of all people who have parts in my accomplishment, the person who contributed the most to this research and makes it ever possible is my advisor. To Dr. Qi, I will forever be thankful.

## TABLE OF CONTENTS

<b>LIST OF TABLES</b> .....	<b>XIV</b>
<b>LIST OF FIGURES</b> .....	<b>XVIII</b>
<b>CHAPTER 1</b> .....	<b>1</b>
<b>INTRODUCTION</b> .....	<b>1</b>
1.1 EUTROPHICATION CONSEQUENCES ON WATER QUALITY .....	3
1.2 REMOTE SENSING ALTERNATIVE .....	5
1.3 CURRENT PROBLEMS WITH REMOTE SENSING WATER QUALITY .....	7
1.4 HYPERSPECTRAL REMOTE SENSING.....	8
1.4.1 Spectral Data Characteristics.....	10
1.4.2 Hyperspectral Data Volume and Redundancy .....	12
1.5 RESEARCH OBJECTIVES .....	12
<b>CHAPTER 2</b> .....	<b>14</b>
<b>LITERATURE REVIEW</b> .....	<b>14</b>
2.1 SPECTRAL RESPONSE OF WATER BODIES.....	15
2.2 SPECTRAL CHARACTERISTICS OF CHLOROPHYLL <i>a</i> .....	18
2.3 SPECTRAL CHARACTERISTICS OF COMPLICATING FACTORS (TSS AND DOC).....	24
2.3.1 Spectral Characteristics of Suspended Sediments.....	28
2.3.2 Spectral Characteristics of Dissolved Organic Carbon .....	33
2.4 SPECTRAL CHARACTERISTICS OF ALGAE.....	35
2.4.1 Spectral Characteristics of Algal Pigments .....	37
2.4.2 Cyanobacteria (Bluegreen Algae) Detection (Potential Toxic Algal Detection).....	41
2.5 MOST SENSITIVE SPECTRAL BANDS.....	44
2.6 SPECTRAL BAND SELECTION METHODS .....	46
2.6.1 Principle Component Analysis (PCA) .....	46
2.6.2 Spectral Derivative Analysis .....	49
2.7 SPECTRAL INDICATORS .....	51
2.7.1 Spectral Band Ratio Method.....	51
2.7.2 Statistical Method .....	53
<b>CHAPTER 3</b> .....	<b>57</b>
<b>EXPERIMENTAL DESIGN</b> .....	<b>57</b>
3.1 DESCRIPTION OF THE STUDY AREA.....	58
3.1.1 Climate .....	58
3.1.2 Bedrock Geology .....	59

3.1.3	Physiography .....	60
3.1.4	History of Land use/ Land cover in Michigan .....	60
3.1.5	Selected Lakes in this Study .....	63
3.2	REMOTE SENSING DATA ACQUISITION .....	65
3.2.1	Hand-held Analytical Spectral Devices (ASD) .....	65
3.2.2	Airborne Imaging Spectrometer for Applications (AISA) .....	68
3.3	WATER QUALITY PARAMETER DATA .....	71
3.3.1	Lab Analytical Methods for Chlorophyll <i>a</i> .....	72
3.3.2	Lab Analytical Methods for Total Suspended Sediment .....	74
3.3.3	Lab Analytical Methods for Non – Purgable Organic Carbon .....	74
3.3.4	Lab Analytical Methods for Algal Community Counting .....	77
3.4	SPECTRAL ANALYTICAL METHODS .....	80
3.4.1	ASD Data Preprocessing .....	81
3.4.2	AISA Image Preprocessing .....	84
3.4.3	Air-Water Interface Correction .....	89
3.4.4	Noise Reduction .....	95
3.4.5	Narrow-Waveband (1 nm) Indicator: Principal Component Analysis .....	98
3.4.6	Spectral Derivative Analysis .....	102
3.4.7	Region-Waveband .....	108
3.4.8	Area Under Spectral Curve Indicator .....	111
3.4.9	Spectral Curve Height/Width Ratio Indicator .....	113
3.4.10	Spectral Band Ratio Technique .....	114
3.4.11	Development of New Spectral Indicators for Water Quality .....	115
<b>CHAPTER 4</b>	.....	<b>117</b>
<b>RESULTS AND DISCUSSION</b>	.....	<b>117</b>
4.1	MICHIGAN LAKE WATER QUALITY FROM FIELD OBSERVATION .....	117
4.2	OPTIMAL SPECTRAL BANDS .....	123
4.3	SPECTRAL INDICATORS .....	124
4.3.1	Spectral Indicators for Chlorophyll <i>a</i> .....	124
4.3.2	Spectral Indicators for Secchi Depth .....	128
4.3.3	Spectral Indicators for TSS .....	133
4.3.4	Spectral Indicators for NPOC .....	135
4.3.5	Spectral Indicators for Diatom .....	137
4.3.6	Spectral Indicators for Green Algae .....	140
4.3.7	Spectral Indicators for Bluegreen Algae .....	144
4.4	MODEL VALIDATION .....	148
4.4.1	Chlorophyll <i>a</i> Model Validation .....	148
4.4.1.1	Chlorophyll <i>a</i> ASD Validation .....	149
4.4.1.2	Chlorophyll <i>a</i> AISA Validation .....	151
4.4.2	Secchi Depth Model Validation .....	153
4.4.2.1	Secchi Depth ASD Validation .....	154
4.4.2.2	Secchi Depth AISA Validation .....	156

4.4.3 TSS Model Validation .....	158
4.4.3.1 TSS ASD Validation .....	158
4.4.3.2 TSS AISA Validation .....	159
4.4.4 NPOC Model Validation .....	162
4.4.4.1 NPOC ASD Validation .....	162
4.4.4.2 NPOC AISA Validation .....	163
4.4.5 Algal Model Validation.....	165
4.4.5.1 Diatom ASD Validation .....	166
4.4.5.2 Diatom AISA Validation .....	168
4.4.5.3 Green Algae ASD Validation.....	170
4.4.5.4 Green Algae AISA Validation.....	172
4.4.5.5 Bluegreen Algae ASD Validation .....	173
4.4.5.6 Bluereen Algae AISA Validation .....	175
4.5 DISCUSSION ON SPECTRAL INDICATORS FOR WATER QUALITY ASSESSMENT.....	177
4.5.1 Chlorophyll <i>a</i> .....	177
4.5.2 Secchi Depth.....	179
4.5.3 TSS and NPOC.....	181
4.5.4 Algae.....	182
<b>CHAPTER 5.....</b>	<b>186</b>
<b>CONCLUSIONS AND FUTURE RESEARCH .....</b>	<b>186</b>
5.1 OPTIMAL SPECTRAL BANDS .....	187
5.2 SPECTRAL INDICATORS FOR WATER QUALITY ASSESSMENT.....	189
5.3 EFFECTIVE FILTERS FOR NOISE REMOVAL.....	190
5.4 MAJOR FINDINGS.....	191
5.5 FUTURE RESEARCH.....	193
<b>APPENDIX A .....</b>	<b>196</b>
<b>WATER QUALITY FIELD WORK PROTOCOL.....</b>	<b>196</b>
<b>APPENDIX B .....</b>	<b>202</b>
<b>AISA IMAGERY .....</b>	<b>202</b>
<b>APPENDIX C .....</b>	<b>207</b>
<b>NOISE REMOVAL FILTERS COMPARISON .....</b>	<b>207</b>
<b>APPENDIX D .....</b>	<b>213</b>
<b>AREA UNDER THE SPECTRAL CURVE.....</b>	<b>213</b>
<b>APPENDIX E .....</b>	<b>219</b>
<b>MAXIMUM SPECTRAL CURVE HEIGHT .....</b>	<b>219</b>

**APPENDIX F..... 225**  
**NARROW-WAVEBAND VOLUME REFLECTANCE..... 225**

**APPENDIX G ..... 231**  
**PRACTICAL PROBLEM WITH AISA IMAGE..... 231**

## LIST OF TABLES

Table 2-1 Optical properties of pure water (derived from various sources by Bukata et al., 1995).....	16
Table 2-2 Characteristics of common major associations of the phytoplankton in relation to increasing lake fertility (after Hutchinson, 1967 as cited in Wetzel, 2001).....	36
Table 2-3 Summary of wavebands from literature review .....	45
Table 3-1 Spectral configurations of the 20 band AISA data.....	69
Table 3-2 Spectral configurations of the 30 band AISA data.....	70
Table 3-3 Pearson correlation between 20 band AISA and ASD spectra .....	85
Table 3-4 Pearson correlation between 30 band AISA and ASD spectra .....	87
Table 3-5 Selected waveband regions for water quality assessment.....	109
Table 4-1 Pearson correlation matrix of water quality indicators.....	122
Table 4-2 Identified region-wavebands.....	123
Table 4-3 Identified narrow-wavebands.....	124
Table 4-4 Chlorophyll <i>a</i> area models using the optimal wavebands.....	125
Table 4-5 Chlorophyll <i>a</i> height/width models using the optimal wavebands.	125
Table 4-6 Chlorophyll <i>a</i> narrow-waveband models using the optimal wavebands .....	127
Table 4-7 Secchi depth area models using the optimal wavebands.....	128
Table 4-8 Secchi depth a height/width models using the optimal wavebands	129
Table 4-9 SD narrow-waveband models using the optimal wavebands .....	132

Table 4-10 TSS area models using the optimal wavebands .....	133
Table 4-11 TSS height/width models using the optimal wavebands.....	133
Table 4-12 TSS narrow-waveband models using the optimal wavebands .....	134
Table 4-13 NPOC area models using the optimal wavebands .....	135
Table 4-14 NPOC height/width models using the optimal wavebands.....	135
Table 4-15 NPOC narrow-waveband models using the optimal wavebands ...	136
Table 4-16 Diatom area models using the optimal wavebands .....	138
Table 4-17 Diatom height/width models using the optimal wavebands.....	138
Table 4-18 Diatom narrow-waveband models using the optimal wavebands .	139
Table 4-19 Green algae area models using the optimal wavebands .....	141
Table 4-20 Green algae height/width models using the optimal wavebands..	142
Table 4-21 Green algae narrow-waveband models using the optimal wavebands .....	142
Table 4-22 Bluegreen algae area models using the optimal wavebands.....	145
Table 4-23 Bluegreen algae height/width models using the optimal wavebands .....	146
Table 4-24 Bluegreen algae narrow-waveband models using the optimal wavebands .....	146
Table 4-25 Chlorophyll ASD validation.....	150
Table 4-26 Pearson correlation matrix of actual and predicted chlorophyll from ASD.....	150
Table 4-27 Chlorophyll AISA validation.....	152
Table 4-28 Pearson correlation matrix of actual and predicted chlorophyll from AISA.....	152

Table 4-29 Pearson correlation matrix of actual and predicted chlorophyll from AISA without Mitchell and Muskegon Lakes .....	153
Table 4-30 Secchi depth ASD validation.....	155
Table 4-31 Pearson correlation matrix of actual and predicted Secchi depth from ASD .....	155
Table 4-32 Secchi depth AISA validation.....	156
Table 4-33 Pearson correlation matrix of actual and predicted Secchi depth from AISA.....	157
Table 4-34 Pearson correlation matrix of actual and predicted Secchi depth from AISA without Mitchell and Muskegon Lakes.....	157
Table 4-35 TSS ASD validation .....	158
Table 4-36 Pearson correlation matrix of actual and predicted TSS from ASD .....	159
Table 4-37 TSS AISA validation.....	160
Table 4-38 Pearson correlation matrix of actual and predicted TSS from AISA .....	160
Table 4-39 Pearson correlation matrix of actual and predicted TSS from AISA without Mitchell and Muskegon Lakes .....	161
Table 4-40 NPOC algae ASD validation .....	162
Table 4-41 Pearson correlation matrix of actual and predicted NPOC from ASD .....	163
Table 4-42 NPOC AISA validation.....	164
Table 4-43 Pearson correlation matrix of actual and predicted NPOC from AISA .....	164
Table 4-44 Statistical comparison of modeling and validating data set.....	165
Table 4-45 Diatom ASD validation .....	167

Table 4-46 Pearson correlation matrix of actual and predicted diatom from ASD .....	167
Table 4-47 Diatom AISA validation .....	168
Table 4-48 Pearson correlation matrix of actual and predicted diatom from AISA .....	169
Table 4-49 Pearson correlation matrix of actual and predicted diatom from AISA without Mitchell and Muskegon Lakes .....	170
Table 4-50 Green algae ASD validation .....	171
Table 4-51 Pearson correlation matrix of actual and predicted green algae from ASD.....	171
Table 4-52 Green algae AISA validation .....	172
Table 4-53 Pearson correlation matrix of actual and predicted green algae from AISA.....	173
Table 4-54 Bluegreen algae ASD validation .....	174
Table 4-55 Pearson correlation matrix of actual and predicted bluegreen algae from ASD .....	174
Table 4-56 Bluegreen algae AISA validation .....	175
Table 4-57 Pearson correlation matrix of actual and predicted bluegreen algae from AISA.....	176
Table 4-58 Pearson correlation matrix of actual and predicted bluegreen algae from AISA without Mitchell, Muskegon, and Higgins Lakes .....	177
Table 4-59 Chlorophyll model performances .....	178
Table 4-60 Secchi depth model performances .....	179
Table 4-61 TSS model performances .....	181
Table 4-62 NPOC model performances .....	181
Table 4-63 Diatom models performances .....	182

Table 4-64 Green algae models performances .....	182
Table 4-65 Bluegreen algae models performances .....	183
Table A-1 List of selected sample lakes .....	197

## LIST OF FIGURES

Figure 1-1 Hyperspectral “cube” of image data such as recorded by an imaging spectrometer (after Richard and Jia, 1999).....	11
Figure 2-1 Absorption and scattering of light in pure water (after Jensen, 2000) .....	17
Figure 2-2 Percent reflectance of clear and algae-laden water based on <i>in situ</i> spectroradiometer measurements (after Han, 1997) .....	19
Figure 2-3 Spectra reflectance of Frisian waters, measured <i>in situ</i> in August 1995, with Landsat TM bands 1-4 superimposed (after Dekker et al., 2001).....	21
Figure 2-4 The lower three curves represent the absorption of water and its constituents: the dashed curve the absorption of water, the (---) absorption of 60 mg/l of chlorophyll, the dotted curve is the DOM absorption (0.14 /m @440 nm) and the solid represents the sum of the water, chlorophyll and DOM absorption. The upper hatched curve is an observed reflectance spectrum over the lake (after Green 1998).....	22
Figure 2-5 Example reflectance from a high chlorophyll content lake (85 mg/l – dash line) and one from a low chlorophyll content lake (3 mg/l; TSM 3.5 mg/l – solid line) (after Green, 1998) .....	23
Figure 2-6 Reflectance spectra of the water bodies studied in Dall’Olmo and Gitelson (2005). Some examples are highlighted: curve “Low” (Chl-a = 11 mg/l; TSS = 5 mg/l), curve “High” (Chl-a = 89 mg/l; TSS = 21 mg/l), and curve “Moderate” (Chl-a = 24 mg/l; TSS = 55 mg/l) .....	24
Figure 2-7 Absorption spectral properties of optically active constituents in water (after Dall’Olmo, 2005) .....	27
Figure 2-8 Percent reflectance of algae-laden water with various concentrations of suspended sediment ranging from 0 – 500 mg/l (after Han, 1997) .....	30

Figure 2-9 (a) <i>In situ</i> spectral reflectance measurements of clear water and clear water with various levels of clayey soil suspended sediment concentrations from 0 – 1,000 mg/l. (b) <i>In situ</i> spectral reflectance measurements of clear water and clear water with various levels of silty soil suspended sediment concentrations (after Lodhi et al., 1997) .....	32
Figure 2-10 Examples of water reflectance for different chlorophyll <i>a</i> concentrations in natural waters (after Dall’Olmo, 2005).....	35
Figure 2-11 Maximum and minimum absorption values in the reflectance spectra of pure algal culture (after Shafique et al., 2001).....	39
Figure 2-12 Two reflectance curves from lakes with similar high levels of chlorophyll – but one contains phycocyanin, indicating a cyanobacteria (the phycocyanin absorption peak at 630 nm is expressed as a trough in reflectance), while the other exhibits the properties of green algae (after Green, 1998) .....	40
Figure 2-13 Reflectance model for chlorophyll = 10 mg/m <sup>3</sup> (after Subramaniam et al., 1999) .....	43
Figure 2-14 Standard deviation of the data at different wavelengths for Lake Erken (after Flink et al., 2001).....	47
Figure 3-1 Geographic location of the lakes sampled in the study.....	64
Figure 3-2 The variation of up- and down-welling radiance as measured from ASD. The 10x of mean of upwelling radiance are plotted to scale the reflectance values up for visual comparison with the downwelling radiance .....	67
Figure 3-3 Spectral analytical procedure flow diagrams .....	80
Figure 3-4 ASD spectral signatures (350 nm – 2,500 nm) of 48 representative water samples .....	82
Figure 3-5 ASD spectral signatures (400 nm – 900 nm) of 48 representative water samples .....	82
Figure 3-6 ASD spectral characteristics of different biophysical dominate in waters .....	83

Figure 3-7 Comparison between ASD and 20 band AISA spectral signatures of Higgins Lake. AISA stripe image overlay on Landsat image. Red point represents the corresponding sample site.....	86
Figure 3-8 Comparison between ASD and 30 band AISA spectral signatures of Hess Lake. AISA stripe image overlay on Landsat image. Red point represents the corresponding sample site.....	88
Figure 3-9 Down- and up-welling radiances from water bodies (after Jensen, 2000).....	90
Figure 3-10 Remote sensing reflectance $R_{rs}$ .....	94
Figure 3-11 Subsurface volume reflectance $R(O-)$ .....	94
Figure 3-12 Examples of Mean and Savitsky Golay (Sgolay) filter transformation on Pickerel Lake .....	97
Figure 3-13 Examples of Daubechies (db1) and Symlet (s8) wavelet de-noising transformation on Pickerel Lake .....	97
Figure 3-14 Example of PCA result .....	102
Figure 3-15 First derivatives approximation from 4 different filtrations of the volume reflectance spectra .....	105
Figure 3-16 Second derivatives approximation from 4 different filtrations of the volume reflectance spectra .....	107
Figure 3-17 Example of region-waveband selection on Sgolay method .....	110
Figure 3-18 Examples of curve fitting on 1 <sup>st</sup> derivative data. Graph (a) and (b) represent absorption curves, and (c) and (d) represent reflectance curves .....	112
Figure 3-19 Examples of height and width measurements .....	113
Figure 4-1 Bar graphs of SD, CHL, NPOC and TSS .....	118
Figure 4-2 Bar graphs of diatom, green and bluegreen algae.....	119
Figure 4-3 Histogram distributions of the raw water quality parameters.....	120

Figure 4-4 Histogram distributions of LN transformed water quality parameters ..... 121

Figure 4-5 Pearson correlation graphs and histogram plots of water quality indicators ..... 122

Figure 4-6 Volume reflectance curves ..... 130

Figure 4-7 Examples of volume reflectance curves on different SD in B and C waveband regions..... 131

Figure 4-8 Examples of fitting curves on different SD in B and C waveband regions ..... 131

Figure 4-9 Comparison between high NPOC lake (Croton dam pond) and other lakes with similar water condition but lower NPOC ..... 137

Figure 4-10 Examples of volume reflectance of green algal dominated waters 141

Figure 4-11 Examples of spectra that produce the same height but different under curve area ..... 143

Figure 4-12 Examples of volume reflectance of bluegreen algal dominated waters ..... 144

Figure 4-13 Correlation graphs between actual and predicted CHL from ASD150

Figure 4-14 Correlation graphs between actual and predicted CHL from AISA ..... 152

Figure 4-15 Correlation graphs between actual and predicted CHL from AISA without Mitchell and Muskegon Lakes ..... 153

Figure 4-16 Correlation graphs between actual and predicted SD from ASD. 155

Figure 4-17 Correlation graphs between actual and predicted SD from AISA 157

Figure 4-18 Correlation graphs between actual and predicted SD from AISA without Mitchell and Muskegon Lakes ..... 157

Figure 4-19 Correlation graphs between actual and predicted TSS biomass from ASD..... 159

Figure 4-20 Correlation graphs between actual and predicted TSS from AISA ..... 160

Figure 4-21 Correlation graphs between actual and predicted TSS from AISA without Mitchell and Muskegon Lakes ..... 161

Figure 4-22 Correlation graphs between actual and predicted NPOC from ASD ..... 163

Figure 4-23 Correlation graphs between actual and predicted NPOC from AISA ..... 164

Figure 4-24 Distribution of modeling and validating data set..... 166

Figure 4-25 Correlation graphs between actual and predicted diatom biomass from ASD ..... 167

Figure 4-26 Correlation graphs between actual and predicted diatom from AISA ..... 169

Figure 4-27 Correlation graphs between actual and predicted diatom from AISA without Mitchell and Muskegon Lakes ..... 170

Figure 4-28 Correlation graphs between actual and predicted green algal biomass from ASD..... 171

Figure 4-29 Correlation graphs between actual and predicted green algae from AISA..... 173

Figure 4-30 Correlation graphs between actual and predicted bluegreen algal biomass from ASD..... 174

Figure 4-31 Correlation graphs between actual and predicted green algae from AISA..... 176

Figure 4-32 Correlation graphs between actual and predicted bluegreen algae from AISA without Mitchell, Muskegon, and Higgins Lakes ..... 177

Figure A-1 Trophic conditions of the selected sample lakes..... 196

Images in this dissertation are presented in color.

# **CHAPTER 1**

## **INTRODUCTION**

Lakes are valuable water resources. Tens of thousands of inland lakes have served as crucial resources for drinking water, irrigation, industry, transportation, recreation, fishing, support of biodiversity, and sheer aesthetic enjoyment for the 516,000 km<sup>2</sup> area of the Upper Midwest region (Carpenter et al., 1998). These lakes are of immense importance to the region (Lillesand, 2002). Fresh water is a limited resource. Although over 70 percent of the Earth's surface is water-covered, only 2.6 percent of it is freshwater. It can be increased only slightly with tremendous cost, for example, desalinization of ocean water requires enormous energy, and once the product is obtained distribution is energetically prohibitive. For many reasons, the usable freshwater supply is in reality much smaller than the absolute total. Of all the freshwater, 77 percent is tied up in the polar ice caps and 11 percent is stored in deep groundwater aquifers leaving 12 percent in an active circulation (Brooks et al., 2003). Water consumption has increased exponentially with demotechnic growth. And potentially the most serious factor from the growth is the severe degradation by contaminants to water quality (Wetzel, 2001).

Fresh waters around the world are experiencing accelerating rates of qualitative and quantitative degradation (Wetzel, 1992). Throughout human history, water has been used to wash away and dilute pollutants. Pollutant inputs have increased in recent decades and have degraded water quality of many rivers,

lakes, and coastal oceans. Degradation of these vital water resources can be measured as the loss of natural ecosystems, their component species, and the amenities they provide (Postel and Carpenter, 1997; U.S. EPA, 1996). Water shortages are increasingly common and likely to become more severe in the future (Postel, 1997; Postel et al., 1996). In 2001, the United Nations commemorated a World Day for Water in which it concluded that the demands for freshwater exceeded supplies by 17 percent and over the next 25 years, two-thirds of the world population will experience a severe water shortage (Brooks et al., 2003).

A well documented effect of human activities upon aquatic ecosystems is *eutrophication*, a process whereby water bodies, such as lakes, estuaries, or slow-moving streams receive excess nutrients that stimulate excessive productivity, simplification of biotic communities, and a reduction in the ability of the metabolism of the organisms to adapt to the nutrient loading. When eutrophication occurs, excessive inputs often exceed the capacity of the ecosystems to be balanced, thus the conditions lead to reduced stability of the ecosystem. In order to effectively maintain the quality of inland waters, it is necessary to monitor humans' utilization of these resources independently in terms of residential, industrial, and agricultural activities (Wetzel, 2001). Although the fundamental laws of resource utilization may be recognized by most agencies and industries, they are not being seriously implemented. Therefore, an effective water quality assessment and monitoring techniques are needed to maintain a sustainable natural ecosystems.

### **1.1 Eutrophication Consequences on Water Quality**

Eutrophication caused by excessive inputs of phosphorus and nitrogen is the most common impairment of surface waters in the United States (U.S. EPA, 1990), with impairment measured as the area of surface water not suitable for designated uses such as drinking, irrigation, industry, recreation, or fishing. Eutrophication accounts for approximately 50 percent of impaired lake areas and 60 percent of the impaired river reaches in the United States (U.S. EPA, 1996), and is the most widespread pollution problem of U.S. estuaries (NRC, 1993).

Eutrophication has many negative effects on aquatic ecosystems. Perhaps the most obvious consequence is the increased growth of algae and aquatic weeds that interfere with use of the water for fisheries, recreation, industry, agriculture, and drinking water. As the mass of algae in the water grows, the water may become murkier and less aesthetically pleasing. Particularly, when the algae die and decompose, periods of oxygen depletion (hypoxia and anoxia) occur more frequently (Carpenter et al., 1998). Even living algae create conditions favorable for some species over others and may cause shifts in the structure of phytoplankton, zooplankton, and bottom-dwelling (benthic) communities (Howarth et al., 2000). Eutrophication brings on ecological changes that decrease the biological diversity – the variety of living organisms – in the ecosystem (Seehausen et al., 1997).

Explosive growth of nuisance algae are among the most damaging effects of eutrophication (Anderson and Garrison, 1997). Blooms of harmful algae such as red and brown tide organisms may become more frequent and extensive. These algae are harmful to humans and other organisms, sometimes resulting in human illness via shellfish poisonings (Carpenter et al., 1998). Just as important, subtle changes in the plankton community and other ecological factors may trigger reduced growth and recruitment of fish species and a lowered fishery production (Howarth et al., 2000). For example, in marine systems, blooms of *Lyngbya majuscula* in Moreton Bay, southeast Queensland, Australia have significantly impacted the environment (Relfsema et al., 2001). In freshwater, blooms of cyanobacteria (bluegreen algae) are a prominent symptom of eutrophication (Smith, 1998; Kotak et al., 1993; McComb and Davis, 1993). These blooms contribute to a wide range of water-related problems including summer fishkills, foul odors, and unpalatable drinking water (Kotak et al., 1994; Palmstrom et al., 1988). Water-soluble neuro- and hepatotoxins, released when cyanobacterial blooms die or are ingested, can kill livestock and may pose a serious health hazard to humans (Carpenter et al., 1998).

Various mathematical models have been developed and applied to rivers, lakes, and estuaries in an effort to monitor, simulate and control eutrophication (e.g., Kloiber et al., 2002; Dekker et al., 2001; Flink et al., 2001; Giardino et al., 2001; Koponen et al., 2001; Pulliainen et al., 2001; Shafique et al., 2001; Subramaniam et al., 1999). Most water quality models demand comprehensive

water quality sampling programs. In an ideal circumstance, monitoring of water bodies includes the determination of concentrations of water quality variables and the processes that generate their spatial distribution and temporal variation of those variables (Fisher, 1994; Van Stokkom et al., 1993). However, the conventional measurement of water quality requires *in situ* sampling, and expensive and time-consuming laboratory work (Giardino et al., 2001). Therefore, it is usually based on the determination of concentrations at one or only a few fixed stations that are assumed to represent the overall distribution of phytoplankton in a lake, or the spatial interpolation of the concentration from the stations to obtain continuous field maps of the various water quality parameters (Kallio et al., 2003). Algal blooms are extremely patchy, both temporally and spatially. Consequently, they often remain unobserved using the traditional sampling methods based on temporally sparse sampling at fixed monitoring stations (Harma et al., 2001). Traditional *in situ* sampling methods also do not provide the spatial overview that is necessary for the regional assessment and monitoring of lake water quality (Shafique et al., 2001). On the other hand, optical indications of water quality have the potential of enhancing the abilities of resource managers to monitor water bodies in a timely and cost-effective manner.

## **1.2 Remote Sensing Alternative**

*Remote sensing* is defined as acquisition of information about the properties of electromagnetic waves emitted, reflected or diffracted by the sensed objects without being in direct physical contact. Broad scope remote sensing based

water quality research has been developed to detect environmental indicators that are useful in assessing, quantifying and monitoring inland water quality. More fundamentally, the absorption and scattering of light by components of the lacustrine water column provide basic information about the substances suspended in the water (Jupp et al., 1994). Although a fairly new method, the development of spectral indices can be a useful and effective tool for the diagnosis of water conditions by water resource managers (Shafique et al., 2001).

Remote sensing offers a significant source of information, and methods have been developed for operational large-scale monitoring of water quality (Harma et al., 2001). For example, remote sensing enables the monitoring of a wide spatial extent of phytoplankton distribution in the surface water layer more effectively (Shafique et al., 2001). Reliable spatial coverage and cost-efficient remote monitoring techniques of lakes and coastal waters are generally growing in importance as a consequence of increasing symptoms of eutrophication processes (Giardino et al., 2001; Harma et al., 2001). A number of studies have shown that applications of remote sensing can meet the demand for the large sample sizes required of water quality studies conducted on the watershed scale. Algal blooms have been mapped successfully from remotely sensed data in a number of different riverine (Lathrop and Lillesand, 1989; Lillesand et al., 1983), estuarine (Harding et al., 1995; Verdin, 1985), and oceanic (Ruiz-Azuara, 1995) environments around the world. Imagery from satellite and aircraft remote sensing systems have been used in the assessment of water quality

parameters such as temperature, chlorophyll *a*, turbidity, and total suspended solids (Relfsema et al., 2001; Jupp et al., 1994). Estimation of chlorophyll *a* distribution in lakes by remote sensing techniques has included the use of airborne photography (Wrigley and Horne, 1974), airborne spectrometry (George and Malthus, 2001; Ostlund et al., 2001; Heege and Fischer, 2000; Jupp et al., 1994; Dekker et al., 1992) and satellite sensors (Giardino et al., 2001; Ostlund et al., 2001; Vos and Rijkeboer, 2000; Dekker and Peters, 1993). Results were usually reported in the form of concentration maps (Kallio et al., 2003).

### **1.3 Current Problems with Remote Sensing Water Quality**

Data acquisition by remote sensing is fast (e.g., tens of lakes may be acquired within a day by an airborne sensor or hundreds of lakes by a spaceborne sensor), and large areas can be surveyed over a short period of time. However, the spectral and spatial configurations of current aquatic satellite sensors are not suitable for inland water quality monitoring. In most cases they are not suitable for phytoplankton monitoring in lakes due to their spectral configuration and poor spatial resolution (typically from several hundred meters to 1,000 m). The low spatial resolution of most satellite data can produce sources of error in empirical approaches used to assess water quality indicators. For example, a single *in situ* sample may not be representative of an entire pixel area. In most cases, a single pixel is greater than several meters in diameter, and it is rare for a single object or target feature to fill any one pixel. Thus, the characteristics of any pixel can rarely be considered truly homogenous (Tsi and Philpot, 1998). In addition, the accuracy of locating the

pixel that corresponds to the *in situ* sample may be uncertain depending on the geolocation method used (Giardino et al., 2001).

Spaceborne sensors provide the global coverage of the Earth's surface conditions at different spatial and temporal resolutions, but the efficacy of all current spaceborne remote sensing systems for detailed characterization of water quality parameters is limited by their spatial and spectral resolutions. Sensors with high spatial resolution do not have a sufficient number of narrow spectral bands (e.g., IKONOS, QuickBird, Landsat, and ASTER), while narrow-waveband spaceborne sensors usually have coarse spatial resolution (e.g., MODIS). Satellite sensor systems such as Landsat TM and ETM+, and ASTER currently provide data of sufficient spatial resolution for inland lake applications. However, their spectral resolution is questionable. It is important to recognize that these sensors average the spectral information over the entire width of the spectral band (Dekker et al., 1992). Narrow-waveband sensors may provide better fundamental information about the biophysical characteristics of inland waters. Various ground-based radiometers have been used with different bandpass filters to mimic the operational airborne radiometers and spaceborne scanners. Airborne sensors are generally designed to serve as a prototype for future spaceborne sensor systems.

#### **1.4 Hyperspectral Remote Sensing**

Hyperspectral sensors (0.4  $\mu\text{m}$  – 2.5  $\mu\text{m}$  wavelength range) capture the hopefully unique spectra (or 'spectral signature') of an object. These signatures

can be used to identify and quantify the materials of which it is composed (The Canadian Space Agency, 2003). With this principle, hyperspectral data enable the identification of the Earth's surface features with greater thematic accuracy. Airborne imaging spectrometers have been used to assess the trophic status of lakes and to map the spatial distribution of phytoplankton (Malthus et al., 1996). The analysis of hyperspectral imagery involves the decomposition of each reflectance pixel into its biophysical constituents. The identity of these constituents is determined by comparison with 'library' spectra of known materials measured in the field or in the laboratory (Richards and Jia, 1999).

The previous generation of spaceborne optical imagers are limited to either panchromatic or multispectral devices providing only a few spectral bands and limited resolving power. Numerous effective methods, mostly derived from multivariate statistics, have been developed and applied successfully for spatial or spectral analysis of these data (Tsai and Philpot, 1998). Hyperspectral imagers typically collect data in tens to several hundred contiguous, narrow bands in the electromagnetic spectrum. The large numbers of bands that are simultaneously imaged produce vast quantities of information. With higher resolution, spectrally continuous data, researchers tended to select a subset of suitable bands to optimize the existing algorithms for multispectral data analysis or to generate new algorithms based on traditional multispectral concepts (Penueles et al., 1994; Martin and Aber, 1993; Chappelle et al., 1992; Curran et al., 1992).

The new generation of airborne imaging spectrometers, such as the Airborne Imaging Spectrometer for Applications (AISA) and the Compact Airborne Spectrographic Imager (CASI), offer considerable advances in terms of radiometric sensitivity and operational flexibility (George and Malthus, 2001). The main problems with hyperspectral data are the substantial redundancy of the information, the difficulties in identifying the optical bandwidth and center wavelength of the bands that maximize the explanation of biophysical attributes, and the system limitations associated with the storage of the image data volumes.

#### **1.4.1 Spectral Data Characteristics**

Given the enormous number of wavebands recorded, the data produced by the imaging spectrometers are different from those of multispectral scanners – leading to the term *hyperspectral*. The data produced for a given geographical area can be viewed as a cube, as shown in Figure 1-1, having three dimensions that represent spatial location (two dimension) and spectral wavelength (the third dimension) (Richards and Jia, 1999).

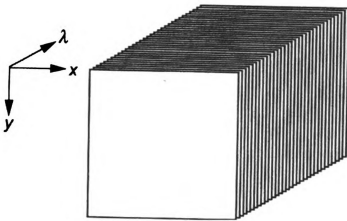


Figure 1-1 Hyperspectral “cube” of image data such as recorded by an imaging spectrometer (after Richard and Jia, 1999)

When displaying remotely sensed data on the display device, only three of the spectral bands are usually assigned to the red, green and blue color elements of the device. Careful band selection ensures the most informative display. This is relatively simple for multispectral data, such as the six 30 m bands from Landsat, but with hyperspectral data, selecting the three bands to display can be challenging. Choosing the most appropriate three channels to display is not straightforward and, in any case, would lead to substantial loss of the spectral benefits offered by these type of data. However, unless spectral transformations are employed, a set of three bands comparable to those used with multispectral imagery are often adopted (near IR, red, green) for simple display of the data (Richards and Jia, 1999).

#### **1.4.2 Hyperspectral Data Volume and Redundancy**

It is obvious that the major differences between multispectral and hyperspectral data (e.g., Landsat versus AVIRIS) is the number of wavebands (7 versus 224) and the radiometric quantization (8 versus 10 bits per pixel per band).

Disregarding differences in spatial resolution, the relative data volume per pixel are  $7 \times 8$  vs.  $224 \times 10$  – i.e., 56 : 2240 bits per pixel. For each pixel, there are 40 times as many bits for AVIRIS as for TM data. Consequently, storage and transmission of hyperspectral data are issues for consideration (Richards and Jia, 1999).

Unfortunately, 40 times as much data per pixel does not imply 40 times as much information can be extracted about the ground cover types being imaged. Even though additional data often enhance the possibility in discovering that information, much of it does not add to the potential information content. Hyperspectral data often contain substantial overlap or redundancy of information content among the bands of data recorded for a given pixel. Spectral redundancy means that the information content of one band can be fully or partly predicted from the other bands in the data (Richards and Jia, 1999).

#### **1.5 Research Objectives**

The objectives of this study are to:

- (1) identify the optimal spectral bands that are most sensitive to water quality indicators in the various water bodies within Michigan;
- (2) develop improved spectral water quality indicators; and

(3) determine the most effective filters for noise removal in hyperspectral remote sensing data.

Many previous studies relied on the correlation of local *in situ* measurements of chlorophyll *a*, suspended sediment, with the remote sensing data. These algorithms are not truly generalizable. They are only good for the particular location and cannot usually be generalized across space or time. This study attempts to develop generalizable algorithms that are spatially and temporally independent. The main purpose is to detect absorption and reflectance features within the spectral data, and then to develop the spectral indicators, such as under-curve area, curve height/width ratio, or narrow-waveband indices, that could estimate the water quality parameters (chlorophyll *a*, Secchi depth, total suspended sediment, non-purgable organic carbon, and algae biomass).

## **CHAPTER 2**

### **LITERATURE REVIEW**

Several remote sensing studies have estimated water quality parameters such as Secchi depth, chlorophyll *a*, and bluegreen algae. Some researchers used multispectral remote sensing data to map the general water quality indicator for Secchi depth; however, the data do not provide enough spectral resolution for the detection of algae or accurate assessment of chlorophyll *a*. Other researchers used hyperspectral data to predict suspended sediment, chlorophyll *a* and harmful bluegreen algae in the ocean where concentration of complicating optical factors (e.g., total suspended sediment and dissolved organic carbon) are very low. Various studies used different analytical techniques, such as principle component analysis (PCA), derivative spectroscopy, and regression techniques, to identify optimal narrow spectral wavebands and develop water quality models. None of the reviewed studies developed water quality indicators by fitting polynomial curves in the region-wavebands as presented in this study (Chapter 3). The region-waveband indicators can be more sensitive to changes in biophysical variables and less affected by noise from the atmosphere or the sensor itself than the narrow-waveband indicators. The literature review presented in this chapter served as a guideline of what has been done and what can be done to improve water quality assessment algorithms.

## **2.1 Spectral Response of Water Bodies**

When conducting remote sensing investigations on water bodies, it is useful to understand how pure water selectively absorbs and scatters incident solar.

Bukata et al. (1995) summarized the absorption coefficient  $a(\lambda)$ , the scattering coefficient  $b(\lambda)$ , and the total attenuation coefficient  $c(\lambda)$  of pure water molecules at wavelengths from 250 nm – 800 nm from a number of studies (Table 2-1).

Several important relationships were observed when the absorption and scattering data were graphed, as shown in Figure 2-1 (Jensen, 2000).

Table 2-1 Optical properties of pure water (derived from various sources by Bukata et al., 1995)

Wavelength (nm)	Absorption $a(\lambda)$ ( $m^{-1}$ )	Scattering $b(\lambda)$ ( $m^{-1}$ )	Total Attenuation $c(\lambda)$ ( $m^{-1}$ )
250 – ultraviolet	0.190	0.0320	0.2200
300 – ultraviolet	0.040	0.0150	0.0550
320 – ultraviolet	0.020	0.0120	0.0320
350 – ultraviolet	0.012	0.0082	0.0202
400 – violet	0.006	0.0048	0.0108
420 – violet	0.005	0.0040	0.0090
440 – violet	0.004	0.0032	0.0072
460 – dark blue	0.002	0.0027	0.0047
480 – dark blue	0.003	0.0022	0.0052
500 – light blue	0.006	0.0019	0.0079
520 – green	0.014	0.0016	0.0156
540 – green	0.029	0.0014	0.0304
560 – green	0.039	0.0012	0.0402
580 – yellow	0.074	0.0011	0.0751
600 – orange	0.200	0.0009	0.2009
620 – orange	0.240	0.0008	0.2408
640 – red	0.270	0.0007	0.2707
660 – red	0.310	0.0006	0.3106
680 – red	0.380	0.0005	0.3806
700 – red	0.600	0.0005	0.6005
740 – near-infrared	2.250	0.0004	2.2504
760 – near-infrared	2.560	0.0004	2.5604
800 – near-infrared	2.020	0.0003	2.0203

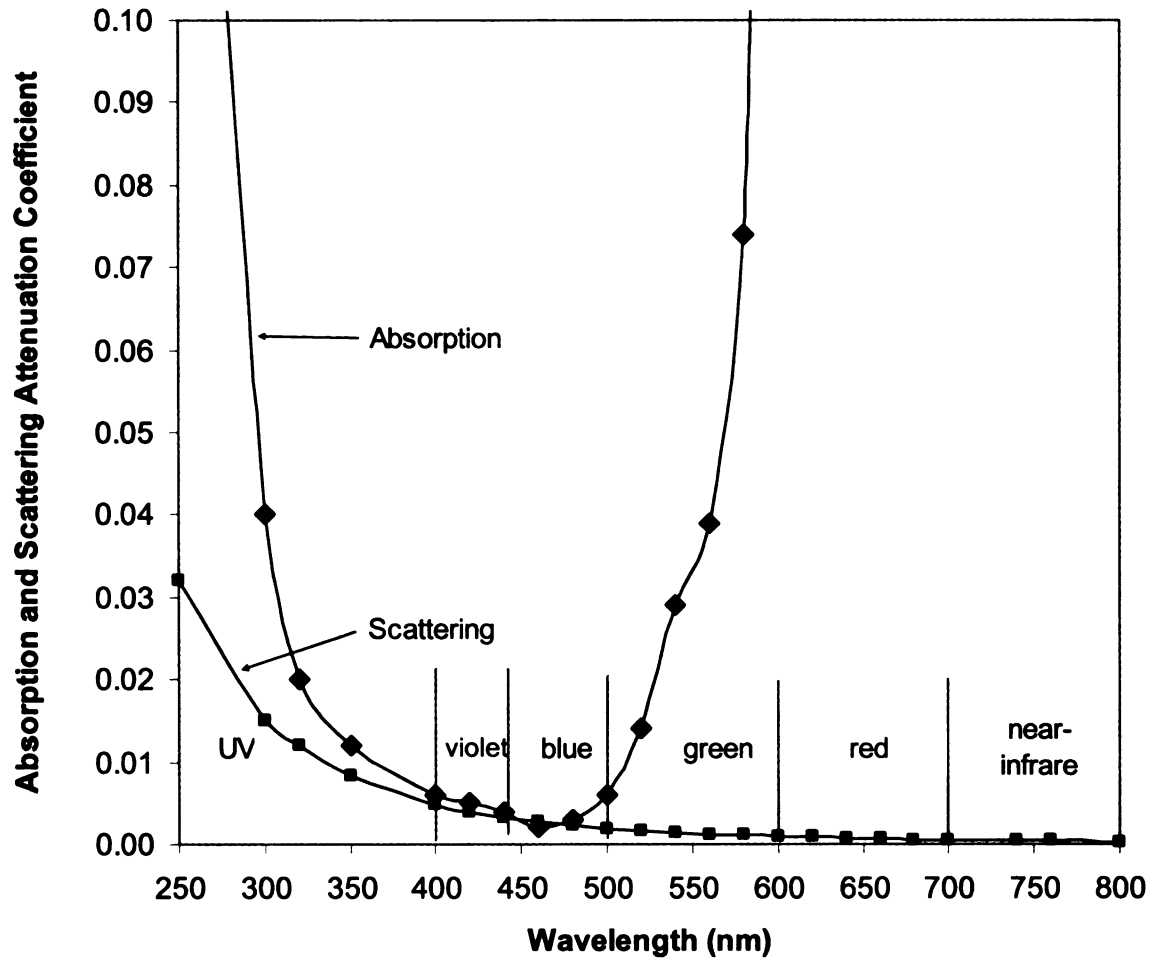


Figure 2-1 Absorption and scattering of light in pure water (after Jensen, 2000)

Blue wavelength region from approximately 400 nm – 500 nm had the least amount of absorption and scattering of incident light in the water column, with the minimum absorption at 460 nm – 480 nm. The wavelengths of violet to light blue light penetrated further than any other range of light into the water column because they had the best transmission (Clark et al., 1997). The water column absorbed incoming irradiance in the green and yellow wavelengths from 520 nm – 580 nm very well with relatively little scattering taking place. Almost

all of the incident red and infrared (580 nm – 3,000 nm) radiance entering deep pure water was absorbed with negligible scattering (Figure 2-1). Consequently, pure water appeared blue to our eyes due to the combined effect of molecular scattering of violet and blue light (< 520 nm) and significant absorption of green and red light (520 nm – 700 nm) in the same water column. Blue colored waters are typically found in pure mid-ocean water and deep non-turbid inland water bodies (Jensen, 2000).

In the natural environment, the spectrum shape characteristics of water from different lakes differed significantly depending on dissolved and suspended constituents within the water. The trophic state of water strongly influenced the spectral signatures (Pulliainen et al., 2001).

## **2.2 Spectral Characteristics of Chlorophyll *a***

The spectral reflectance characteristics of pure water changed when chlorophyll *a* was introduced. For example, Figure 2-2 depicted the spectral reflectance characteristics of clear water and the same water laden with algae consisting primarily of chlorophyll *a* (Han, 1997). Basically, as chlorophyll *a* concentration increased in the water column, the amount of energy reflected in the blue and red wavelengths significantly decreased but that in green wavelength increased. Clear water reflected approximately 2 percent between 400 nm and 500 nm and dropped gradually to less than 1 percent at wavelengths beyond 710 nm (Jensen, 2000). Conversely, the algae-laden water

presents four pronounced scattering/absorption features of chlorophyll (Figure 2-2; Jensen, 2000; Han, 1997; Rundquist et al., 1995; Gitelson, 1992):

- (1) strong chlorophyll *a* absorption in blue region between 400 nm and 500 nm;
- (2) maximum reflectance in green wavelengths around 550 nm (green peak) caused by *relatively* lower absorption of green light by algae;
- (3) strong chlorophyll *a* absorption in red wavelengths at approximately 675 nm; and
- (4) prominent reflectance peak between 690 nm – 700 nm caused by an interaction of algal-cell scattering and a combined effect of minimum pigment and water absorption. The height of this peak above the baseline (absorption trough) has been used to accurately measure chlorophyll amount.

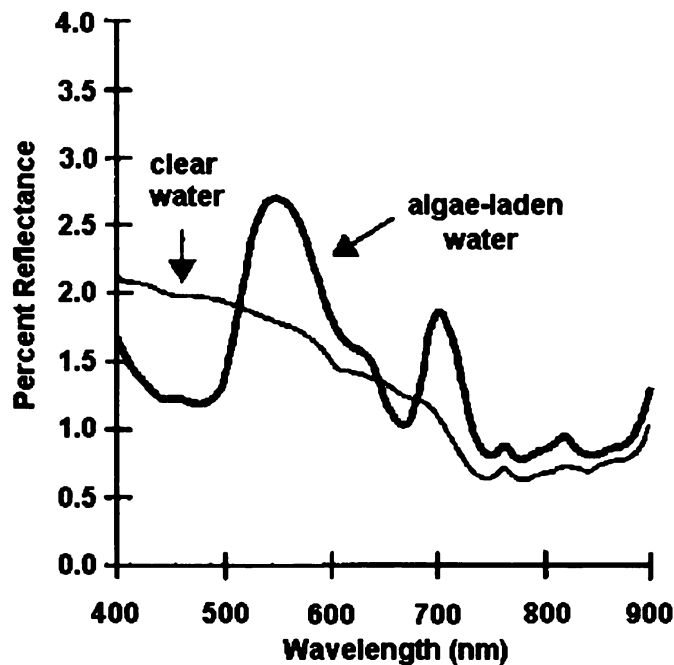


Figure 2-2 Percent reflectance of clear and algae-laden water based on *in situ* spectroradiometer measurements (after Han, 1997)

Dekker et al. (2001) illustrated the key spectral features in lake water signature curves. From their measured reflectance spectra in Figure 2-3, it was obvious that the absorption and scattering of the various constituents created a distinctive reflectance spectrum for each of the water samples. In general, there was little reflectance at shorter wavelengths of 400 nm – 500 nm, due to the combined effects of absorption by colored dissolved organic matter (CDOM), inanimate particles (tripton) and phytoplankton pigments. A local maximum in reflectance, caused by a local minimum in the combined absorption effects of CDOM and tripton absorption (which both exponentially decline with increasing wavelength) and a low phytoplankton pigment absorption efficiency, was found at approximately 550 nm – 580 nm. The local minimum in reflectance at 630 nm is caused by the combined effects of cyanophycocyanin absorption and a first shoulder in the absorption of water was noticeable. As this local minimum became more pronounced, the relative contribution of cyanobacteria to the total algal components increased. The local reflectance peak at 650 nm is due to a local minimum in absorption by pigments and an increasingly smaller contribution from CDOM and tripton absorption. A narrow reflectance minimum is centered at 676 nm, which was the *in vivo* chlorophyll *a* maximum absorption peak. Beyond 680 nm, reflectance increased significantly to a maximum of 14 percent at 706 nm. In the studied lake there was a vast amount of algae identifiable by the large reflectance at 706 nm, and the major algal pigment absorption at wavelengths from 400 nm – 680 nm (Figure 2-3).

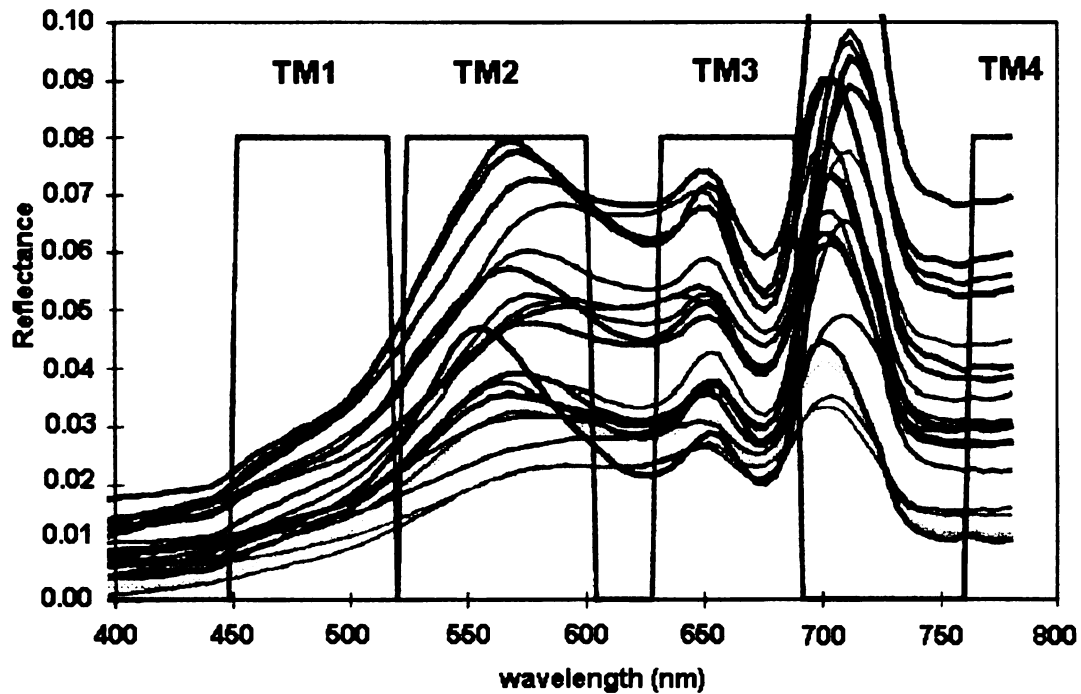


Figure 2-3 Spectra reflectance of Frisian waters, measured *in situ* in August 1995, with Landsat TM bands 1-4 superimposed (after Dekker et al., 2001)

Over the full spectral range, the shape of the spectral signature for water was broadly determined by the spectral absorption of dissolved organic matter in the blue, and by the absorption of chlorophyll *a* and water itself in the red and near-infrared (Figure 2-4). Attention had concentrated on the wavelength range from 600 nm to 740 nm, which included the effect of the interaction of the water absorption (with a peak absorption near 770 nm; Figure 2-4) and the chlorophyll *a* absorption (with a peak near 675 nm). This effect produced a minimum in absorption and thus a peak in reflectance, at about 700 nm. As chlorophyll *a* increased the peak size near 700 nm, measured with respect to adjacent wavelengths, increased in a non-linear fashion with shift to longer

wavelengths (i.e., Figure 3-2 showed the peak near 720 nm). Many studies used red/NIR spectral region in their spectral indices (Kallio et al., 2003; Harma et al., 2001; Kallio et al., 2001; Gitelson et al., 1993). A notable consequence of the use of these wavelengths was the negligible effects of DOM in the chlorophyll *a* retrieval compared with techniques using blue and green wavelengths (Green, 1998; Sathyendranath and Platt, 1989; Tassan, 1988).

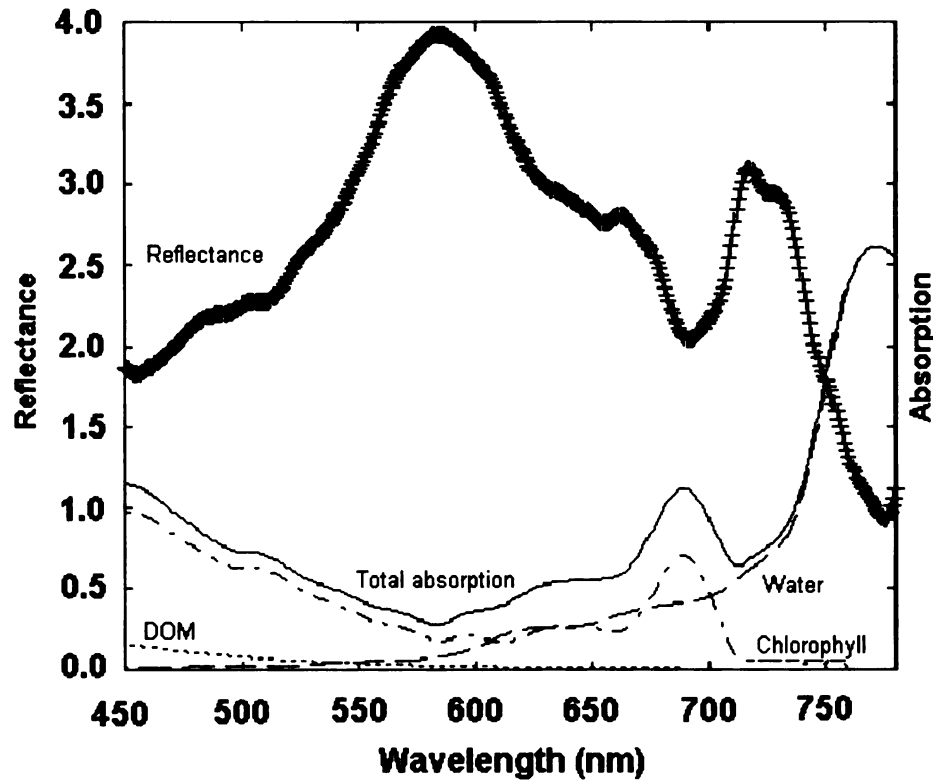


Figure 2-4 The lower three curves represent the absorption of water and its constituents: the dashed curve the absorption of water, the (---) absorption of 60 mg/l of chlorophyll, the dotted curve is the DOM absorption (0.14 /m @440 nm) and the solid represents the sum of the water, chlorophyll and DOM absorption. The upper hatched curve is an observed reflectance spectrum over the lake (after Green 1998)

Figure 2-5 presented an example reflectance spectrum of a lake with high chlorophyll *a* content and one with very little chlorophyll (Green, 1998).

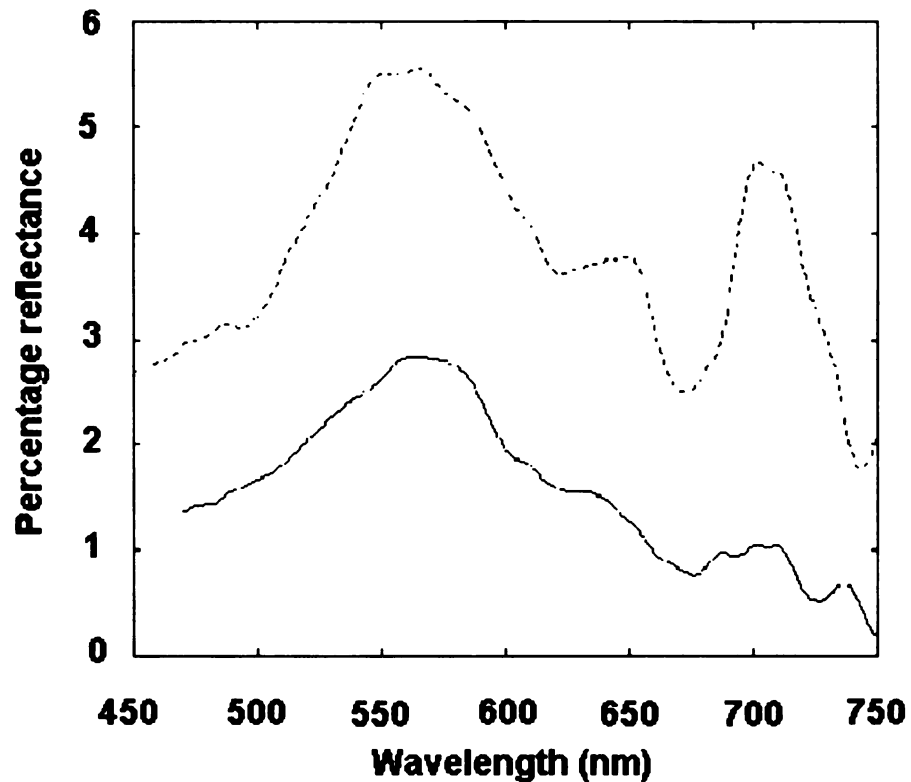


Figure 2-5 Example reflectance from a high chlorophyll content lake (85 mg/l – dash line) and one from a low chlorophyll content lake (3 mg/l; TSM 3.5 mg/l – solid line) (after Green, 1998)

With continued increase in chlorophyll *a* content, the reflectance peak of water shifted toward longer wavelengths (Figure 2-6; Gitelson, 1992). Thus, the indicator of the chlorophyll *a* concentration of the water column was related to the shape of the reflectance curve in this region, and not simply the peak height (Green, 1998).

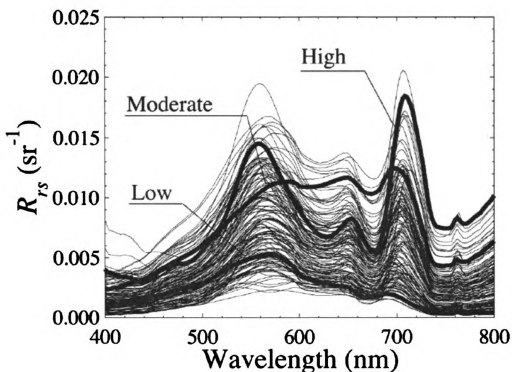


Figure 2-6 Reflectance spectra of the water bodies studied in Dall'Olmo and Gitelson (2005). Some examples are highlighted: curve “Low” (Chl-a = 11 mg/l; TSS = 5 mg/l), curve “High” (Chl-a = 89 mg/l; TSS = 21 mg/l), and curve “Moderate” (Chl-a = 24 mg/l; TSS = 55 mg/l)

### 2.3 Spectral Characteristics of Complicating Factors (TSS and DOC)

A general problem concerning remote sensing of all waters was that the reflectance signals were very weak and often also wavelength-specific (Ostlund et al., 2001). The radiance leaving water was a function of solar intensity and angle and the optical properties of the water attenuation, absorption, and scattering. While solar incoming radiation varied in time, optical properties varied in relation to the concentrations of optically active constituents, e.g.,

phytoplankton pigments, particulate substances, and aquatic humus (Pepe et al., 2001). The water column contained a mixture of dissolved organics, inorganic suspended sediments, and chlorophyll *a*, which masked and interfered with the spectral identification of the chlorophyll *a* alone, especially since the inorganic suspended sediment is a much brighter target than the chlorophyll.

In the deep ocean environment, dissolved and suspended matter seldom played important roles and often only one species of algae dominated (Ostlund et al., 2001). Remote sensing spectral signature of chlorophyll *a* in the 400 nm – 550 nm region was used to estimate phytoplankton in the oceans (O'Reilly et al., 1998). Such chlorophyll retrieval algorithms were derived solely from regression techniques and ignore the specific absorption and scattering properties of the water body being remotely sensed. The success of these algorithms was largely a consequence of the optically simple characteristics of mid-ocean and many near-coastal waters. Even though the optical properties of deep off shore waters were primarily a function of phytoplankton concentration, coastal and inland waters represented a much more complex optical environment. Water bodies strongly influenced by land masses displayed higher orders of optical complexity. This was a result of an increased number of optically-active components co-existing within the water column, as well as greater ranges in the variations of the concentrations of these aquatic components. Due to the optically competitive compositions of coastal, estuarine, lake, and river water masses, mathematical models developed mainly

on marine waters might not adequately describe the same variables of interest in lakes. The same wavelength region could not be applied in lakes, mainly because absorption by colored dissolved organic matter hid the spectral signature of chlorophyll *a* at these wavelengths. Instead, the interpretation of chlorophyll *a* from remote sensing data in lakes was usually based on the 660 nm – 715 nm spectral region (Kallio et al., 2003; Kallio et al., 2001; Gitelson et al., 1993). Harma et al. (2001) suggested that humic lakes needed to be separated and interpreted using specific models developed for these types of water bodies. Suspended sediment in lakes also had a significant effect on chlorophyll *a* signature extraction because its reflectance was much higher; therefore, it masked out the chlorophyll *a* absorption feature. Because of the same reason, oligotrophic lakes might need to be interpreted separately. Oligotrophic waters had weak signatures that could be interfered easily by other substances in the water.

Inland water color was related to the types and amounts of these substances in the water column which interacted with light absorbing or scattering it (Flink et al., 2001). The optical properties of natural bodies of water were influenced by three main components, which could vary independently from each other (Figure 2-7). These are (IOCCG Report Number 3, 2000):

(1) Phytoplankton – includes phytoplankton and other microscopic free-floating organisms found in the illuminated surface layers of water. They were the living organisms that form the base of the aquatic food web, and were an important component of the global carbon cycle. The concentration of the main

phytoplankton pigment, chlorophyll *a*, was often taken as an index of phytoplankton biomass;

(2) Suspended inorganic material – included all inorganic particulate material that was not included in the phytoplankton component; and

(3) Yellow substances – included the colored, dissolved organic substances, and also “detrital” particulate material, for example from the degradation of phytoplankton cells and other organic particles.

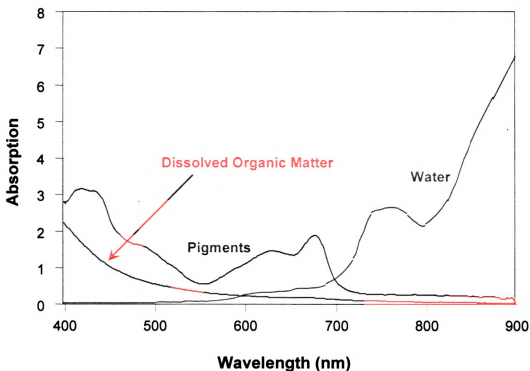


Figure 2-7 Absorption spectral properties of optically active constituents in water (after Dall’Olmo, 2005)

Extracting quantitative information about the constituents of interest from the remotely sensed data from natural water that contained a mixture of materials

was one of the greatest challenges in remote sensing (Goodin et al., 1993). To begin with, it would be instructive to look at the effect that each of these constituents had on the spectral reflectance characteristics of a water column (Jensen, 2000).

### **2.3.1 Spectral Characteristics of Suspended Sediments**

Sediment came from a variety of sources, such as agricultural cropland erosion and urban surface runoff. The particles ranged from fine clay particles (3  $\mu\text{m}$  – 4  $\mu\text{m}$  in diameter), to silt (5  $\mu\text{m}$  – 40  $\mu\text{m}$ ), to fine-grain sand (41  $\mu\text{m}$  – 130  $\mu\text{m}$ ), and coarse grain sand (131  $\mu\text{m}$  – 250  $\mu\text{m}$ ). Most of the suspended mineral sediment was concentrated in the inland and nearshore water bodies (Bukata et al., 1995). Thus, suspended mineral concentration was usually of no significance to deep ocean remote sensing studies. On the other hand, inland water bodies might carry a significant load of suspended sediment that could dramatically impact the spectral reflectance characteristics of the water bodies (Jensen, 2000; Nanu, 1993).

For several reasons, it was important to monitor the type, amount, and spatial distribution of suspended minerals in inland water bodies. First, sediment affected water quality and its suitability for drinking, recreation, and industrial purposes. Second, sediment served as a carrier and storage agent of pesticides, absorbed phosphorus, nitrogen, and organic compounds and could be an indicator of pollution. Third, photosynthesis by phytoplankton and submerged aquatic vegetation could be significantly impacted as suspended sediments

impede the transmission of solar radiation in the water column. These phytoplankton and aquatic vegetation played a vital role in the food chain of the aquatic ecosystem (Jensen, 2000).

Fortunately, remote sensing had been used to monitor the suspended mineral concentrations in water bodies. The *in situ* measurements of suspended mineral concentrations were usually required to derive a quantitative relationship with the remote sensor data. When collecting samples, the remote sensor data and the *in situ* suspended sediment measurements should be collected on days that have little wind because wind-roughened surface water created specula reflections (Jensen, 2000; Han and Rundquist, 1998).

When both suspended mineral sediment and chlorophyll were present in the water body at the same time, a dramatically different spectral response was produced. For example, Figure 2-8 illustrated the spectral response of water as red loam sediment concentrations from 0 – 500 mg/l were added to water that contained algae. For algae laden water, the green peak reflectance shifted from 547 nm at 0 mg/l to 596 nm at 500 mg/l (Jensen, 2000).

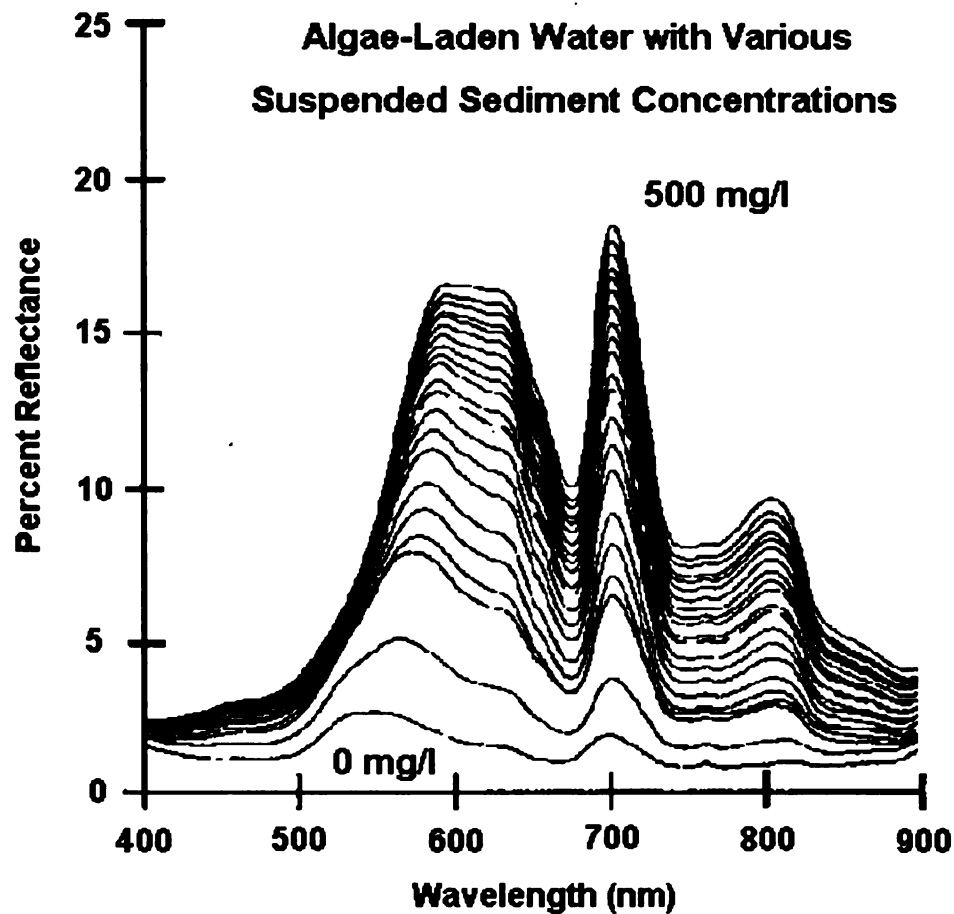


Figure 2-8 Percent reflectance of algae-laden water with various concentrations of suspended sediment ranging from 0 – 500 mg/l (after Han, 1997)

Figure 2-9 depicted the spectral reflectance of clear water and water with varying suspended sediment concentrations of two different type of soils; clayey and silty. For a deep clear water, spectral reflectance dropped continuously after approximately 580 nm due to increased absorption in the water column. Increased in suspended particulates (either inorganic or organic) were related to increase in overall brightness (Shafique et al., 2001). A water body with suspended sediment in it would generally appear brighter in imagery than a

water body without any suspended sediment. The clayey soil (Figure 2-9b) had approximately 10 percent lower reflectance at all wavelengths than the light-colored silty soil because it contained more organic matter and was darker in color (Figure 2-9a). If the suspended particulates were organic in nature, the reflectance data indicated a relative increase at about 705 nm (Shafique et al., 2001). Reflectance increased in the 580 nm – 690 nm region and in the near-infrared region as more mineral sediments were added to the water bodies. Thus, the peak reflectance shifted toward longer wavelengths in the visible region as suspended sediments increased (Jensen, 2000). These results suggested that: (1) the *type* of suspended sediments (soil) in waters might be assessed using the visible wavelength range of 580 nm – 690 nm; and (2) the *amount* of suspended minerals in waters where suspended minerals were the predominant constituent might be estimated using the near-infrared wavelength range of 714 nm – 880 nm.

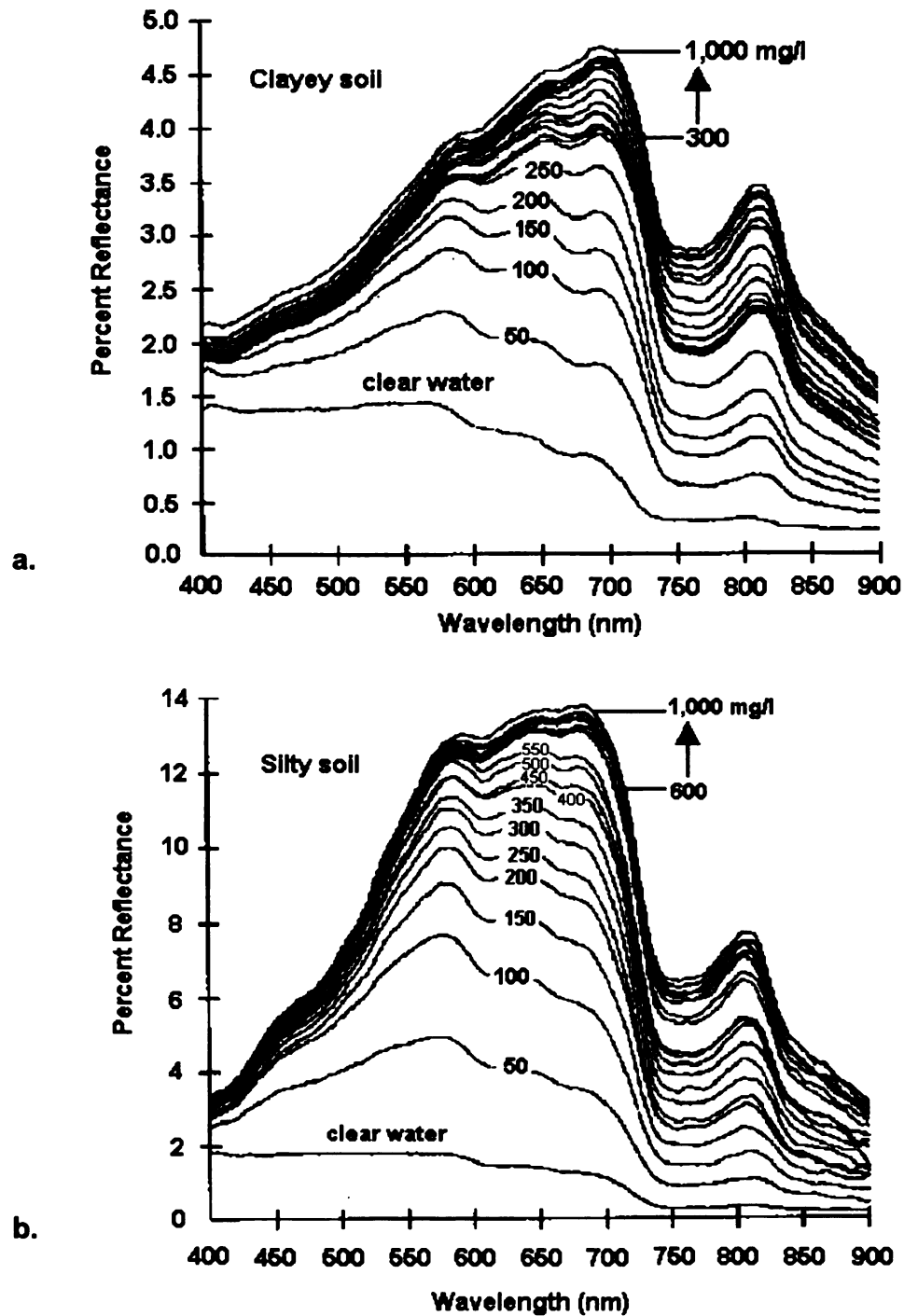


Figure 2-9 (a) *In situ* spectral reflectance measurements of clear water and clear water with various levels of clayey soil suspended sediment concentrations from 0 – 1,000 mg/l. (b) *In situ* spectral reflectance measurements of clear water and clear water with various levels of silty soil suspended sediment concentrations (after Lodhi et al., 1997)

### **2.3.2 Spectral Characteristics of Dissolved Organic Carbon**

A group of lakes that have high humic concentration made the interpretation of present multispectral remote sensing data practically impossible. The remotely measured signal was very low from these lakes due to strong absorption caused by high concentrations of colored dissolved organic matter (DOM), and low concentrations of particles causing scattering (Kutser et al., 2001).

The effects of dissolved organic compounds on the absorption of light energy were marked (Wetzel, 2001). Sunlight penetrates into the water column at certain *photoc depth* (the vertical distance from the water surface to the 1 percent subsurface irradiance level). Within this depth, phytoplankton consumed nutrients and converted them into organic matter via photosynthesis. The process was called *primary production*. Zooplankton also consumed the phytoplankton and created organic matter. Bacterioplankton decomposed these organic material. All the conversion produced dissolved organic matter (DOM) in the water bodies. The more productive the phytoplankton, the greater the released of dissolved organic matter. In certain instances, there might be sufficient dissolved organic matter in the water to reduce the penetration of light in the water column (Jensen, 2000; Bukata et al., 1995).

These dissolved humic substances were called *yellow substance* and could (1) impact the absorption and scattering of light in the water column, and (2) change the color of the water (Jensen, 2000). In comparison to pure water, lake

water with increasing concentrations of dissolved organic compounds, particularly humic acids, not only drastically reduced the transmission of light but shifted absorption selectively. Clear waters had a very high absorption in red and infrared wavelengths, but a relatively little absorption in UV wavelengths (300 nm – 400 nm; Figure 2-1). Very low concentrations of dissolved organic compounds increased UV absorption greatly. Most of the irradiance in UV, blue, and green wavelengths were essentially absorbed in much less than a depth of 1 m in lakes highly stained with humic compounds (Wetzel, 2001).

Phytoplankton was not the only source of dissolved organic matter. For example, the brownish-yellow color of the water in many rivers in the northern United States was due to the high concentrations of tannin from the eastern hemlock (*Tsuga Canadensis*) and various other species of trees and plants grown in bogs in these areas. These tannins potentially create problems with remote sensing of inland water bodies (Jensen, 2000).

Information about the phytoplankton pigments from remotely sensed data of natural inland water body that was effected by dissolved organic matter (DOM) was often more difficult to unwind. Figure 2-10 showed the spectra of natural waters that were dominated by different concentration of chlorophyll *a* and dissolved organic matter.

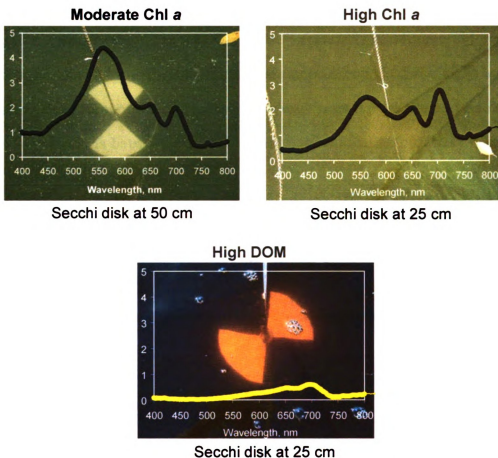


Figure 2-10 Examples of water reflectance for different chlorophyll  $a$  concentrations in natural waters (after Dall'Olmo, 2005)

#### 2.4 Spectral Characteristics of Algae

Algae were extremely diverse, and many exhibited a very wide tolerance to environmental conditions found under natural limnological situations. Nonetheless, certain characteristic phytoplanktonic associations occurred repeatedly in lakes of increasing nutrient enrichment. Some of the commonly observed major associations were described in Table 2-2 based on the detailed discussion of Hutchinson (1967) as cited in Wetzel (2001). However, the wide

spectrum of intergradations was often observed, and species composition shifts occurred seasonally from one type to another, especially among more productive waters. Nevertheless, such characterizations yielded insight into regulating environmental factors, thus they were useful from the standpoint of general correlations between qualitative and quantitative abundance of the algae and available nutrients.

Table 2-2 Characteristics of common major associations of the phytoplankton in relation to increasing lake fertility (after Hutchinson, 1967 as cited in Wetzel, 2001)

<b>General lake trophy</b>	<b>Water characteristics</b>	<b>Dominant algae</b>	<b>Other commonly occurring algae</b>
Oligotrophic	Slightly acidic; very low salinity	Desmids <i>Staurodesmus</i> , <i>Staurastrum</i>	<i>Sphaerocystis</i> , <i>Gloeocystis</i> , <i>Rhizosolenia</i> , <i>Tabellaria</i>
Oligotrophic	Neutral to slightly alkaline; nutrient-poor lakes	Diatoms, especially <i>Cyclotella</i> and <i>Tabellaria</i>	Some <i>Asterionella</i> spp., some <i>Melosira</i> spp., <i>Dinobryon</i>
Oligotrophic	Neutral to slightly alkaline; nutrient-poor lakes or more productive lakes at seasons of nutrient reduction	Chrysophycean algae, especially <i>Dinobryon</i> , some <i>Mallomonas</i>	Other chrysophyceans, (e.g., <i>Synura</i> and <i>Uroglena</i> ); diatom <i>Tabellaria</i>
Oligotrophic	Neutral to slightly alkaline; nutrient-poor lakes	Chlorococcal <i>Oocystis</i> or chrysophycean <i>Botryococcus</i>	Oligotrophic diatoms

Oligotrophic	Neutral to slightly alkaline; generally nutrient poor; common in shallow Arctic lakes	Dinoflagellates, especially some <i>Peridinium</i> and <i>Ceratium</i> spp.	Small chrysophytes, cryptophytes, and diatoms
Mesotrophic or eutrophic	Neutral to slightly alkaline; annual dominants or in eutrophic lakes at certain seasons	Dinoflagellates, some <i>Peridinium</i> and <i>Ceratium</i> spp.	<i>Glenodinium</i> and many other algae
Eutrophic	Usually alkaline lakes with nutrient enrichment	Diatoms much of year, especially <i>Asterionella</i> spp., <i>Fragilaria crotonensis</i> , <i>Synedra</i> , <i>Stephanodiscus</i> , and <i>Melosira granulata</i>	Many other algae, especially greens and cyanobacteria during warmer periods of year; desmids if dissolved organic matter is fairly high
Eutrophic	Usually alkaline; nutrient enriched; common in warmer periods of temperate lakes or perennially in enriched tropical lakes	Cyanobacteria, especially <i>Anacystis</i> (=Microcystis), <i>Aphanizomenon</i> , <i>Anabaena</i>	Other cyanobacteria; euglenophytes if organically enriched or polluted

#### 2.4.1 Spectral Characteristics of Algal Pigments

The amount of chlorophyll *a* was considered a reasonable representative for the organic component of optically complex natural waters (Bukata et al., 1995). It was a good indicator of the quality of lake water as it correlated well with the total productivity of a lake and; therefore, with the nutrient load and overall condition of the lake (Koponen et al., 2001).

Algae contained colored pigments – the chlorophylls, carotenoids, and biliproteins, which gave them characteristic spectral features. The pigments were used in the photosynthetic process. All algae and cyanobacteria contained the photosynthetically active pigment chlorophyll *a* as it was the primary photosynthetic pigment of all oxygen-evolving photosynthetic organisms. Chlorophyll *a* absorbed light in the blue (near 430 nm) and red (660 nm – 665 nm) parts of the spectrum, thus giving the substance itself a green color (Wetzel, 2001). Bluegreen algae, or cyanobacteria had other important phytoplankton photosynthesizing agents: carotenoids, and phycobilins (primary phycocyanin in freshwater, and phycoerythrin in marine environments). Phycocyanin absorbed more toward the yellow and green part of the spectrum giving the pigment a blue shade.

Fortunately, different genus of phytoplankton appeared as different colors to sensitive remote sensors because they had different types and concentrations of pigments (Figure 2-11). The wavelengths of pigment absorptions could be used together with nearby wavelengths, which were less affected by the pigment absorption, to detect the presence of the pigment. Often indices, which were used for quantification, were constructed from reflectance at pigment absorption wavelengths (Flink et al., 2001). Thus, the amount and general type of phytoplankton might be estimated by recording the optical spectra of the water body, and information about the health and chemistry of the water body could be assessed. Changes of optical water condition over time could be monitored by comparing images taken at different times (Jensen, 2000).

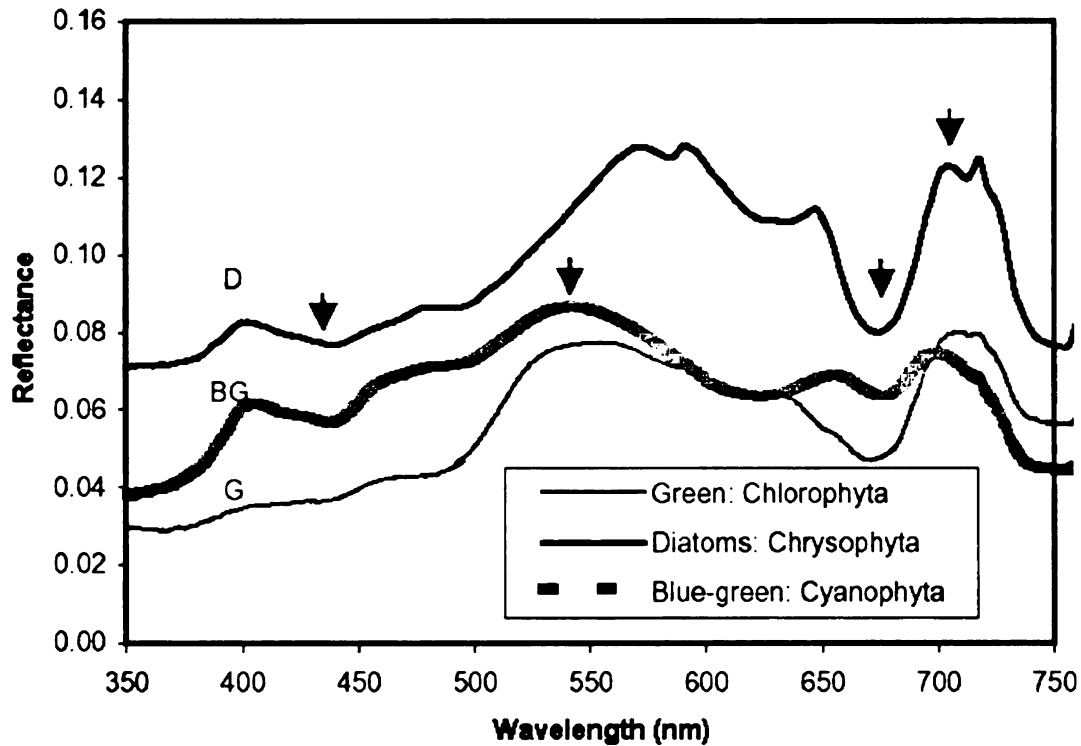


Figure 2-11 Maximum and minimum absorption values in the reflectance spectra of pure algal culture (after Shafique et al., 2001)

In addition, other pigment peaks might also be apparent in the reflectance curves. The measurement of *phycocyanin* spectral characteristic done in a controlled laboratory environment resulted in a maximum absorption at 630 nm. The absorption feature should also be observable as a trough in the *in situ* reflectance curve. In Figure 2-12, the effect of this additional pigment absorption was demonstrated. The two lakes, with similar chlorophyll concentrations, differed in that one was predominately by green algae while the other was predominate by cyanobacteria. The relative size of the chlorophyll *a*/water peak near 700 nm was the same; the extra absorption in this region, most notably at 630 nm, was due to the phycocyanin content. This showed the

potential of the remote sensing as “cyanobacteria detectors” which could benefit environmental monitoring because some of these blue-green algae are toxic (Green, 1998).

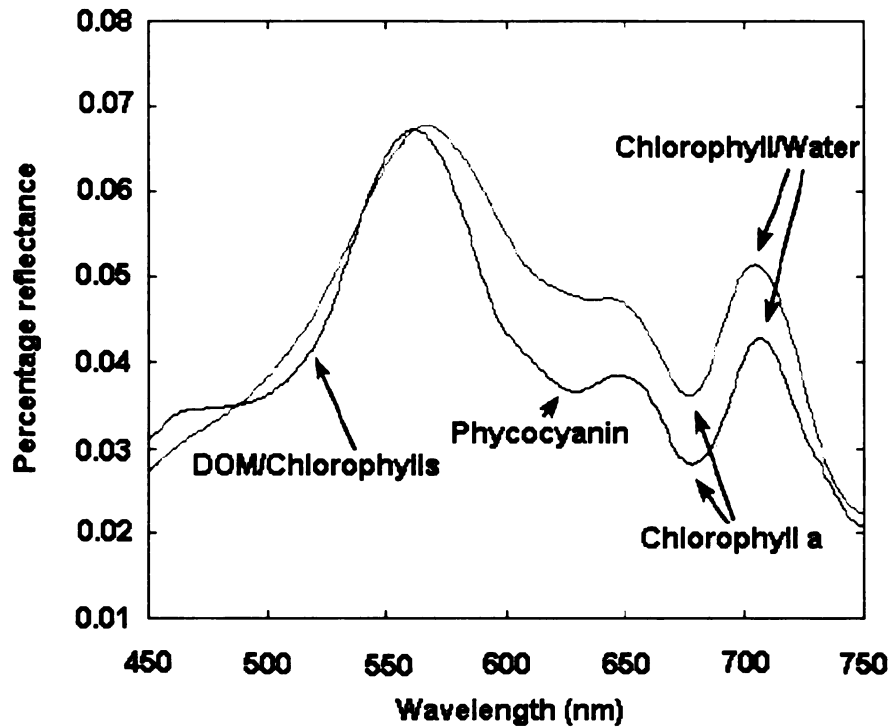


Figure 2-12 Two reflectance curves from lakes with similar high levels of chlorophyll – but one contains phycocyanin, indicating a cyanobacteria (the phycocyanin absorption peak at 630 nm is expressed as a trough in reflectance), while the other exhibits the properties of green algae (after Green, 1998)

#### **2.4.2 Cyanobacteria (Bluegreen Algae) Detection (Potential Toxic Algal Detection)**

Subramaniam et al. (1999) parameterized a standard remote-sensing reflectance model using measured values of *Trichodesmium's* inherent optical properties, namely the spectral dependence of the chlorophyll-specific optical absorption cross-sections and the spectral dependence of the chlorophyll-specific backscatter cross-sections. Sea truth and data from the Advanced Very High Resolution Radiometer (AVHRR) were used to map a 300,000 km<sup>2</sup> *Trichodesmium* bloom off the Somali Coast in May 1995.

In biological oceanography, changes in optical properties had been used to infer upper ocean chlorophyll *a* concentrations, which could, in turn, be related to primary productivity. It had been very difficult, however, to quantify the temporal and spatial extent of new production in the oceans, let alone the contribution of N<sub>2</sub> fixation to that flux. The nonheterocystous, colonial cyanobacterium, *Trichodesmium* spp., was responsible for most of the N<sub>2</sub> fixation in the open oceans (Capone et al., 1997). Hence, a remote-sensing algorithm capable of distinguishing these organisms from all other phytoplankton would be of enormous value in constraining estimates of N<sub>2</sub> fixation in the world's oceans.

Together, the optical properties and physiological behavior of *Trichodesmium* potentially provided a basis for developing algorithms capable of uniquely identifying and quantifying their distributions based on remotely sensed

information (Subramaniam and Carpenter, 1994). The research analyzed the backscatter properties, in conjunction with absorption properties, of *Trichodesmium* and parameterized a remote sensing reflectance model which derive satellite observations of ocean color in the visible and near-infrared (Subramaniam et al., 1999).

The backscatter coefficient for *Trichodesmium* was wavelength dependent. “Backscatter” peaks centered between 550 nm and 579 nm and at 640 nm were a consequence of phycoerythrin and allophycocyanin fluorescence, respectively, rather than true elastic backscatter. Typically, chlorophyll *a* fluorescence emission overwhelmed the red absorption band, such that the backscatter spectrum revealed a peak in this region (Ahn et al., 1992). Remote sensing reflectance spectra of phytoplankton blooms typically contained a “green peak,” centered around 575 nm. The peak was a consequence of an absorption minimum in that portion of the spectrum in most phytoplankton taxa, coupled with a sharp increase in the water absorption spectrum. As a consequence of both the intrinsically high backscatter and phycoerythrin fluorescence, the remote-sensing reflectance was extremely high around 575 nm for blooms of *Trichodesmium*. The reflectance was approximately fivefold higher than that for *Synechococcus* or typical phytoplankton at high densities of chlorophyll biomass (10 mg Chl m<sup>-3</sup>; Figure 2-13).

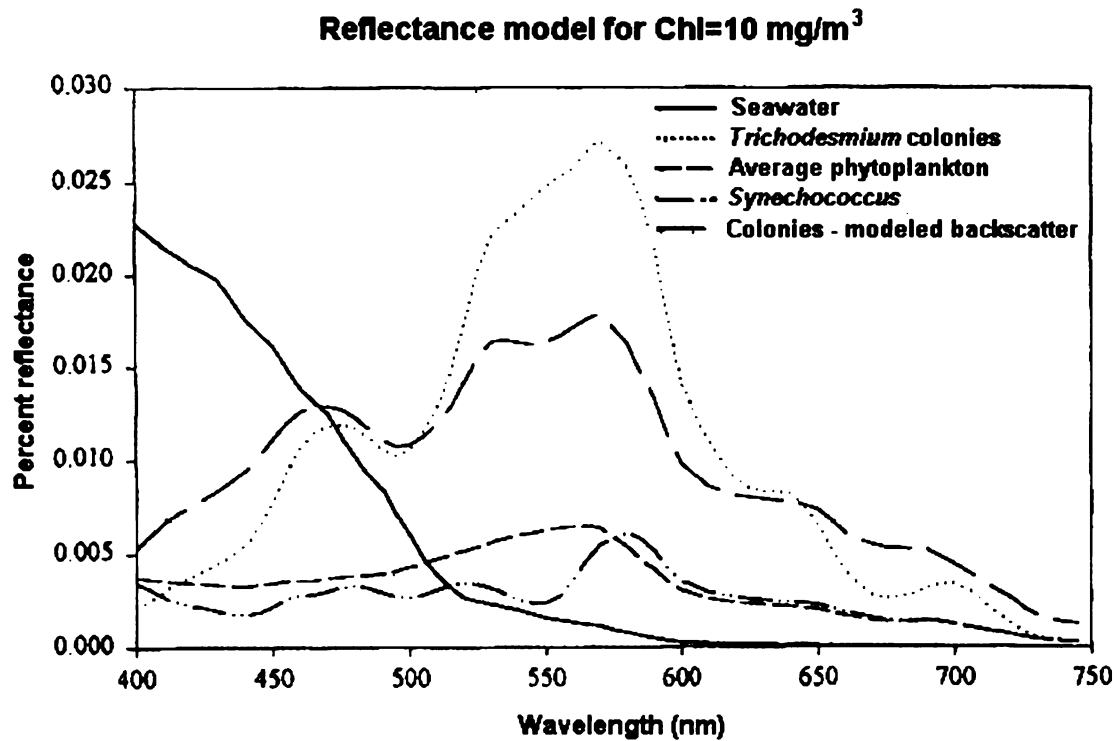


Figure 2-13 Reflectance model for chlorophyll = 10 mg/m<sup>3</sup> (after Subramaniam et al., 1999)

Although remote sensing of phytoplankton in the ocean was primarily based on water-leaving radiance in the visible, the colonial and buoyancy behaviors of gas vacuolated cyanobacteria offered opportunities to exploit the red and near-infrared regions of the spectrum as well. In the specific case of *Trichodesmium*, the virtual absence of solar-induced fluorescence of Chlorophyll *a*, the optical brightness resulting from gas vacuoles, and the removal of absorption by water in the near-infrared permitted the development of simple two-channel reflectance difference indices from AVHRR data to map distributions of surface blooms. While this approach was inferior to that utilizing visible color

information, AVHRR data could be used to map, retrospectively, the distribution of surface blooms where there was simultaneous *in situ* information identifying the bloom organism.

### **2.5 Most Sensitive Spectral Bands**

Spectral wavebands that were successfully used in the reviewed researches were summarized in Table 2-3. Several studies have shown spectral bands that were found link to water quality variables were in common spectral regions. However, a slight shift in wavelengths might occur due to the different nature of research (e.g., controlled laboratory setting versus natural condition) and/or different condition of water (e.g., high DOC and TSS). When Chlorophyll increased, the near-infrared peak often shifted to the longer wavelength as well. The spectral bands that were found to be significant from previous studies were used as a general guide in the optimal spectral band identification process in later sections.

Table 2-3 Summary of wavebands from literature review

<b>Parameter</b>	<b>Wavelength (nm)</b>	<b>Optical Properties</b>	<b>Reference</b>
Chlorophyll <i>a</i>	440-450	Distinct absorbance in blue	Shafique et al., 2001
	575	“Green peak” from min algae abs + sharp increase water abs	Subramanium et al., 1999
	650	Min absorbance	Dekker et al., 1992
	670-680	Distinct max absorbance in red	Kallio et al., 2003 Shafique et al., 2001 Dekker et al., 1992
	705	Local peak due to max abs at 670 + growing water absorption	Kallio et al., 2003 Shafique et al., 2001
SS	705	Type of sediment	Shafique et al., 2001
	580-690	Amount of sediment	
Cyanobacteria	550-579	Phycoerythrin	Subramanium et al., 1999
	625	Phycocyanin	Jupp et al., 1994
	630	Local minimum reflectance	Dekker et al., 1992
	640	Allophycocyanin	Subramanium et al., 1999

## **2.6 Spectral Band Selection Methods**

Several analytical methods were used to determine wavebands that best described biophysical variables. The methods that were used most frequently in the remote sensing of water studies were principle component analysis and the spectral derivative analysis.

### **2.6.1 Principle Component Analysis (PCA)**

In order to create an index suitable for water quality variable mapping, the wavelengths where substance-specific features existed must be identified. Such an index should exhibit high variance, which will reduce the influence of noise in subsequent regression analysis. The amount of data collected by hyperspectral spectrometers is immense and it is, therefore, often necessary to remove redundancy in the dataset. Principal Component Analysis (PCA) can be used to determine the inherent dimensionality of the dataset. Flink et al. (2001) used reflectance values derived from CASI bands 35-288. Figure 2-14 showed the standard deviation as a function of wavelength. Low variation was associated with the chlorophyll *a* absorption wavelengths.

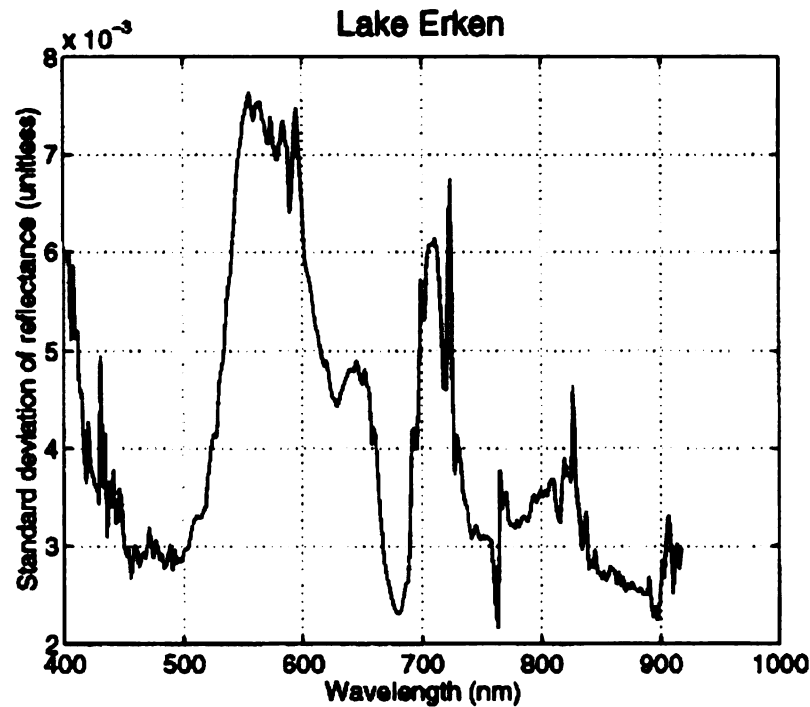


Figure 2-14 Standard deviation of the data at different wavelengths for Lake Erken (after Flink et al., 2001)

A PCA was performed on these correlation matrix, and constructed new variables called principal components (PCs) as linear combinations of the original variables. PCA also concentrates the majority of the variance of the dataset into a few new non-correlated components, thus reducing redundancy. In this study, more than 96 percent of the total variance of the data was contained in only three PCs (i.e., any spectra in the lakes could be fairly well approximated by a weighted sum of only three PCs). Flink et al. (2001) reconstructed all 100 lake spectra from their three first PCs and then subtracted them from the corresponding original spectra to derive the approximation error. Flink et al. (2001) cautioned that PCA should be used

with care. The PCs should be identified with physical phenomena only when there are obvious connections, as in previous work, e.g., Doerffer et al. (1989), where they interpreted PCs calculated from TM data as physical variables based on factor analysis. Their identified factors were temperature, suspended matter and aerosol effect. These factors were likely to have been uncorrelated, just as are the PCs. Other variables such as chlorophyll *a* and suspended particulate matter (SPM) (and even suspended inorganic material) were often highly correlated. One should keep in mind that a PCA gave uncorrelated variables as its result; therefore, the PCs should be interpreted with care. Measurements of variables were very seldom uncorrelated in reality, either because the variables were inherently correlated or because the method used for measuring them yielded a correlation (Flink et al., 2001).

Many single band algorithms performed well in Lake Erken data, e.g., Band 550 nm gives an  $R^2$  of 0.94 between lake spectra and chlorophyll *a*. However, at the corresponding wavelength (550 nm) it was difficult to determine if the variations were caused by chlorophyll *a* or by some other substance in the water. Thus, mapping by means of one single band was possible, as long as chlorophyll *a* constitutes almost the entire amount of material in the lake. A physically sound model, however, should include bands at chlorophyll-specific features (e.g., a ratio between bands at 708 nm and 680 nm), which is probably the most widespread way of measuring chlorophyll *a*.

### 2.6.2 Spectral Derivative Analysis

Spectroscopic derivatives are obtained by taking the difference between the reflectance of two bands and dividing that value by the difference between the wavelengths separating the two bands (Philpot, 1991). When the two bands used in the calculation are adjacent to one another, the result is the first derivative (Shafique et al., 2001). Pepe et al. (2001) developed the chlorophyll *a* model using derivative method. The model based on the higher sensitivity of reflectance 1<sup>st</sup> derivative spectra to concentrations of optically active substances than the radiance reflectance spectra themselves. Correlation analyses were carried out with a first derivative at each hand-held spectroradiometer band pass. Spectral band at 676 nm proved to be the best-correlating wavelength in most cases, corresponding with a peak in chlorophyll *a* absorption (Han and Rundquist, 1997). On the basis of those results, 676 nm as a sole wavelength was used to evaluate the applicability of the first derivative spectra model to every lake condition. Considering the results of the first-derivative model over the complete acquired spectrum (380 nm – 780 nm), the result showed that higher correlation values were dependent on wavelength with respect to chlorophyll contents and sampling depths. In any case 676 nm proved to be the most often correlated wavelength. The first derivative of reflectance at 676 nm was sufficiently reliable only when average chlorophyll *a* contents higher than 2 µg/l; and when the *Cyanophyceae* (bluegreen algae) presence less than 20 percent in the phytoplankton biomass. The accuracy of 1<sup>st</sup> derivative method and the near-infrared/red reflectance ratio (NIR/red) were tested in the study. The NIR/red model was based on the contrast between a local

reflectance peak feature at approximately 705 nm due to a minimum absorption by the pigment and the water, and a local reflectance minimum feature at approximately 670 nm due to the absorption maximum of chlorophyll *a*. The results showed that NIR/red model results were less satisfactory than the first derivative one.

Rencz (1999), and Huguenin and Jones (1986) examined a variety of higher-order derivatives of spectra in an effort to identify the location of individual absorption regions. While assuming that each absorption was symmetric around its band center, the method did not require that absorptions have a specific shape. Band centers were identified where the second derivative of the spectrum was negative, the fourth derivative was positive, and the fifth derivative was zero. Like any derivative analysis, this method was highly sensitive to noise. Therefore, the Huguenin and Jones (1986) approach was critically dependent on an intelligent smoothing algorithm. Nonetheless, their approach was capable of resolving overlapping band centers separated by as little as 0.1 to 1.0 of the full width at half maximum (assuming Gaussian shaped absorptions). Although derivative technique was sensitive to noise, Tsai and Philpot (1998) concluded that an algorithm for derivative analysis of hyperspectral data was a tool that treated hyperspectral data as truly spectrally continuous data. Moreover, the approach could be used with no need to assume that the data were generated in highly controlled environments.

## 2.7 Spectral Indicators

In order to assess water quality by using remote sensing data, the relationship between spectral data and water quality variables such as Secchi depth, chlorophyll *a*, and suspended sediment need to be identified and quantified. A variety of statistical methods such as band rationing and regression techniques have been used to derive these water quality modeling. Wavebands that were identified to be important for water quality indicators were usually set as the dependant variables while water quality parameters were independent variables.

### 2.7.1 Spectral Band Ratio Method

Certain band ratios , could be used successfully for chlorophyll mapping in inland waters (Koponen et al., 2001; Gitelson et al., 1993). Dekker (1993) and Gitelson et al. (1993) found that the optimum ratio of spectral radiance or reflectance at two wavelengths ( $\lambda_x$ ) and ( $\lambda_y$ ) is achieved where ( $\lambda_x$ ) was in the range from approximately 680 nm – 710 nm (corresponding to the chlorophyll *a* fluorescence peak and volume scattering from particulate matter) and ( $\lambda_y$ ) was at approximately 665 nm – 680 nm (the region of the chlorophyll *a* absorption maximum).

$$Chla(\mu g / l) = a_0 + a_1 \left( \frac{L(\lambda_x)}{L(\lambda_y)} \right) \quad (\text{Eq 2-1})$$

Pulliainen et al. (2001) employed the wavelength ranges suggested by Gitelson et al. (1993) in their chlorophyll *a* retrieval algorithms. The optimum channel

ratio was selected empirically using a training data set to determine the highest correlation with chlorophyll *a* concentration. A linear regression model employing the channel ratio  $L_{702\text{nm}} / L_{665\text{nm}}$  yielded a maximum value of  $R^2 = 0.94$ . However, when the predicting waters were affected by various substrates besides chlorophyll (e.g., humic and high suspended sediment), application of Eq 2-1 with remote sensing data may encounter some problems especially if other parameters in addition to chlorophyll *a* affect the ratio  $L(\lambda_x) / L(\lambda_y)$ . This method might require the data set to be pre-classified into different sub-groups, e.g., based on the shape of the measured radiance spectra, in order to increase the chlorophyll *a* estimation accuracy.

Koponen et al. (2001) also used the AISA data to measure chlorophyll *a* concentration in lakes. The study found the 702 nm/ 673 nm band ratio produced the best result. Their results confirmed that an airborne spectrometer was a useful tool for chlorophyll *a* monitoring in lakes. The result corresponded well to the finding of other authors (e.g., Dekker et al., 1992 or Gitelson et al., 1993).

George and Malthus (2001) used an array of wavelength-specific correlation coefficients to determine the 'single band.' Low coefficient values indicated that the radiance values at these wavelengths were not influenced by the presence of phytoplankton. High positive or negative values indicated that the radiance values were strongly influenced by the concentration of phytoplankton. The strongest correlation between the two variables was recorded in the green and

red portions of the spectrum where the 'r' values were positive and reached a maximum value of 0.86 ( $P < 0.05$ ). Then, the correlation between all possible combinations and the measured concentration of chlorophyll *a* was calculated. The results suggested that the most effective multi-band algorithm would contrast the amount of 'green' light reflected with that absorbed at the 'blue' end of the spectrum. The ratio of measurements centered at 550 nm and 440 nm (the ratio identical to the blue/green ratio suggested by Clarke et al., 1970) was found to perform best for chlorophyll prediction, and the ratio of measurements at 685 nm and 745 nm (rather similar to the long-waveband ratio recommended by Dekker, 1993) performed well for waters containing high concentrations of dissolved organic matter.

### **2.7.2 Statistical Method**

Multivariate statistics have been developed and applied successfully for spatial or spectral analysis of remote sensing data, usually derived from established methods in multivariate statistics (Tsi and Philpot, 1998; Richards, 1993; Duda and Hart, 1973). Giardino et al. (2001) adopted several statistical techniques to examine the relationship between *in situ* measured parameters (i.e., Secchi disk and chlorophyll *a*) and remote sensing reflectance values from the Landsat Thematic Mapper sensor. These models included linear, exponential and log transformations. A few previous studies used nonlinear power models ( $y=aX^b$ ) to address the curvilinear behavior of this relationship (e.g., Cox et al., 1998; Lathrop, 1992). Although a power model provided a strong correlation, residuals from it were not normally distributed. In contrast, the semilog

equation used by Kloiber et al. (2002) met the model assumptions. A similar result had been found by Pattiaratchi et al. (1994). Regression models were used to determine the relationship between the difference between reflectance values difference between TM bands 1 and 3 ( $TM1 - TM3$ ), and the ratio between TM bands 1 and 2 ( $TM1/TM2$ ). These models allowed the surface distribution of chlorophyll *a* concentrations and Secchi disk depths to be determined with good confidence (the coefficients of determination were 0.99 and 0.85, respectively; Giardino et al., 2001).

Kloiber et al. (2002) took a further step to develop a standard model that used a consistent equation form for using satellite remote sensing data to estimate key variables related to lake management issues, such as trophic state condition and water clarity. Rather than using regression equations where the independent variables were different for each image, the feasibility of using a consistent equation form to relate ground observations and satellite data was examined. A Pearson correlation matrix was developed to examine the relative strength of correlation between Secchi disk transparency depth (SD) and various Landsat TM bands and band ratios. Results indicated that regressed log-transformed SD versus the  $TM1/TM3$  ratio plus  $TM1$  ( $TM1/TM3 + TM1$ ) provided strong predictive relationships for multiple images over a 25-year period. However, the effect of increased scattering by suspended particles impacted much of the visible and near-infrared portion of the spectrum from about 500 nm to about 850 nm. This scattering effect overwhelmed the subtler influence of other features such as the chlorophyll *a* minimum. Although a

relationship between water clarity and Landsat measured reflectance can be established, this should not be construed to imply that such relationships could be developed for other water quality variables such as chlorophyll *a*.

Kloiber et al. (2002) noted the importance of radiometric calibration. The brightness values of the pixels in a satellite image were affected by sun angle, atmospheric interference, changes in detector response, and numerous other factors. If radiometric correction techniques accounted for these factors, then the coefficients for the models would be more consistent, and one set of coefficients would apply for different images across time and space.

All relevant publications on techniques that were used with hyperspectral data were reviewed and discussed, specifically what had been done, and what needed to be done in order to improve remote sensing of water quality.

Although some of the spectral bands were identified in the previous studies, they were not generalizable due to the disadvantages of empirical methods that are data dependant. An empirical model was often derived based on relationship between dependant and independent variables from a specific set of data. Spectral indicators based on correlations between local *in situ* measurements of water quality and spectral variables at one location may not represent the relationship between the same variables at different locations. Spectral indicators developed from wavebands that truly explain optical properties of the variables such as absorption and reflectance features are the potential solution. However, very few studies have been conducted on deriving

the spectral features of water, such as spectral library development, when compared to those in mineral and vegetation sciences. In addition, the spectral bands identified by these derivative techniques were mostly derived from a specially controlled environment. Therefore, they may not be applicable in the real natural environment. Water quality studies should be conducted on a spatial extent large enough to account for the local biophysical conditions, such as dissolved organic carbon from woods in nearby swamps or suspended inorganic sediment areas with high slopes, in order for the method to be generalizable. A study to use spectral bands that were developed based on optical properties of water quality variables to quantify the relationship between water quality and spectral data within a natural biophysical condition needed to be conducted at large scales. This study attempts to develop in the remaining chapters generalizable algorithms that are spatially and temporally independent. The objectives of this study are to (1) identify optimal spectral bands that are most sensitive to water quality indicators in the various water bodies within Michigan; (2) develop improved spectral water quality indicators; and (3) determine the most effective filters for noise removal in hyperspectral remote sensing data.

## **CHAPTER 3**

### **EXPERIMENTAL DESIGN**

Fieldwork was conducted throughout the Lower Peninsula of Michigan. A majority of the sampled lakes was in the Muskegon River Watershed due to the extensive amount of ecological research that had been going on within this watershed. Muskegon River Watershed attracts researchers because it contains high variation in topography and land use/ land cover types. However, the experiment was designed to include lakes in a wide trophic range. The study site was therefore extended to the entire Lower Peninsula of Michigan. One purpose of this study was to quantify the relationship between spectral information and biophysical variables that indicate water quality. Bathymetric maps were used to predetermine the sample sites within the lakes in order to diminish the effects of other features, such as lake bottoms and submerge vegetations. Data were collected when the sky was cloud and haze free to minimize inconsistency in down-welling radiance and the effect of atmospheric gases, and when the sun elevation was high above the horizon to reduce the sun-glint (hotspot) effects. The characteristics of the study area, spectral and water quality data acquisition procedures along with analytical methods are presented in the following sections.

### **3.1 Description of the Study Area**

The study site covered almost the entire Lower Peninsula of Michigan.

Therefore, biotic and abiotic components of the Lower Peninsula were described following (Albert, 1995; Schuette and Skjaerlund, 1994; Veatch, 1941).

#### **3.1.1 Climate**

The weather of Michigan was controlled by three major air masses, the *Continental Polar*, *Maritime Tropical*, and the *Maritime Polar* (Eichenlaub, 1979).

The Continental Polar air mass, forming over land in the Arctic, brought cold, dry weather in the winter and cool conditions in the summer. The Maritime Tropical, forming over the waters of the Gulf of Mexico to the south, brought warm moist winter weather and hot humid summer conditions. The Maritime Polar air mass originated in the northern Pacific Ocean, although it originally carried large amounts of moisture, much of this was lost on the western slope of the Rocky Mountains. The air warmed as it descended from the mountains. The Maritime Polar air mass brought mild weather with little precipitation to the Midwest.

The Great Lakes were another major control on climate for Michigan. These effects increased the amount of storms over and nearby to the lakes during the winter, but decreased the intensity of storms and increased the stability of air masses over the lakes during the spring and summer. Areas where elevation increases rapidly near lakes receive the most lake-effect precipitation. Climate was responsible for major differences in both soils and vegetation. Along the

Great Lakes, the air near the coast warms more slowly in the spring and cools more slowly in the fall than in the continental climate area.

### **3.1.2 Bedrock Geology**

The continental interior of North America, including all of Michigan, Minnesota, and Wisconsin, was known as the *Central Stable Region* or *craton*, an area that was relatively stable during the Paleozoic (Dorr and Eschman, 1984). During the Paleozoic, from Cambrian to Pennsylvanian times, the southern portion of the craton, including Michigan, Minnesota, and Wisconsin, was intermittently submerged beneath shallow seas. Marine and near shore sediments, including limestone, dolomite, evaporites, sandstone, and shale, were deposited over Precambrian bedrock.

Roughly 31.6 percent of Michigan was comprised of poorly drained soil (Veatch, 1941). The terms “clay soil,” often referred to land underlain by clay at a depth of a few inches to approximately one foot. This broad group of soil constituted the greater part of the highly productive and durable agricultural land in the State of Michigan. An estimated 70 – 75 percent of the original wet or shrub land underlain by clay had been cleared and drained for some sort of agricultural use by 1941 (Veatch, 1941).

### **3.1.3 Physiography**

Modern physiography and soils were the result of postglacial erosion and soil formation processes as the result of glacial deposits during the Wisconsinan Glaciation of the Pleistocene Epoch. Erosion of bedrock and unconsolidated materials occurred beneath the advancing glacier. The advancing ice scoured the bedrock uplands, producing rounded knobs. Rocks and soil materials were carried in the glacial ice and later redeposited and formed diverse features, including moraines, drumlins, eskers, kames, and outwash plains. Lakes and depressions were common in the glacial landscape. Many lakes formed when large blocks of ice were surrounded by outwash sands as the glacier melted. Lakes also formed in linear depressions that had been scoured out by the glacier. Swamps and marshes occur where vegetation colonized shallow depressions. Michigan's unique geographical location provided its citizens with rich freshwater resources including over 11,000 inland lakes. In addition to ecological value, lakes provided tremendous aesthetic and recreational value for people in Michigan.

### **3.1.4 History of Land use/ Land cover in Michigan**

The present-day vegetation of Michigan resulted from the physical environment, post-Pleistocene species migration patterns (Albert, 1995), and human alteration of lands and plant communities. Disturbances such as logging, agriculture, drainage, fire, and fire exclusion had significantly altered plant cover and composition (Albert, 1995). Located in the Midwestern Corn Belt, Michigan has an enormous area of agricultural land. Most farmers apply

nutrients to maximize their crop yields, but excessive nutrients carried by water runoff became pollutants downstream. The tile-drained soil of Michigan enhanced the severity of the nutrient pollution problem by preventing penetration of nutrients into the ground. As a result, considerable amounts of fertilizers accumulated into nearby lakes.

During the past 100 – 125 years the natural landscape of Michigan had been altered by human actions (Veatch, 1953). Humans cannot change the major elements of the environment, such as the climate, the land forms, the composition of the Glacial drift covering, or the bedrock; however, they can make alterations in the cover of vegetation, the fauna, the soil, and the waters. The effects of man's activities after 100 years were not geographically uniform throughout the state, partly because of the differences in regional climate, topography, soil and other resources. Those variable impacts resulted in part from the spatial distribution of the population in Michigan. Historically, approximately 90 percent of the people in the state lived in the southern half of the region with only 5 percent in the entire Upper Peninsula (Veatch, 1953). Out of the approximately 149,734 km<sup>2</sup> of the land area of Michigan, 72,843 km<sup>2</sup> (48.6 percent) were classified by the U.S. Census (1953) as farmland and as much as 8,094 km<sup>2</sup> as cities, industrial sites, highways, and rural homes (Veatch, 1953). Agriculture contributed more than 37 billion dollars annually to the state economy (Schuette and Skjaerlund, 1994). Michigan has many agricultural advantages, such as an abundance of inland fresh water, fertile soils and a mild climate moderated by the Great Lakes. Because of its unique

micro-climates, the state of Michigan was ranked second in the nation with agricultural diversity. Over 100 different food and fiber products had been produced in Michigan. The state has been the lead producer of tart cherries, blueberries, flowers and edible beans (Schuette and Skjaerlund, 1994).

Land use in Michigan has decreased in agricultural land and pasture. This decrease in agricultural acreage occurred in concert with increases in urban and built-up land (National Resources Inventory, 1987). Agriculture was directly impacted by recent trends in land use patterns. Michigan had not experienced significant increases in population during the last 20-25 years, although a dramatic shift in the location of residential development had occurred. As a result, the amount of land used for residential housing had continued to increase at a rapid rate, placing additional pressures on agricultural land. When suburbs expanded, they often invaded lands previously planned in agricultural crops (Schuette and Skjaerlund, 1994). The impact of increasing residential development was not only in the loss of farmland, but also impacts existing farm operations. Decreasing farm size led to increase in crop production by intensification of cultivation and improvement of farm management. Where the natural fertility was not favorable, increased use of commercial fertilizers was an alternative to help boost production (Veatch, 1953). This change in farm operations could magnify the non-point source pollution problem.

### **3.1.5 Selected Lakes in this Study**

*In situ* data were collected from 42 lakes in Michigan from April 24 to August 26, 2004 (Figure 3-1). Some lakes were revisited in both spring and summer resulting in 49 independent *in situ* measurements of chlorophyll *a* (CHL), total suspended sediment (TSS), Secchi disk depth (SD), total nitrogen (TN), total phosphorus (TP), non-purgable organic carbon (NPOC), light extinction profile, dissolved oxygen (DO) profile, temperature profile, phytoplankton species composition, and reflectance spectra. *In situ* upwelling radiance from the water column was measured with the hand-held spectroradiometer (LabSpec® Pro, Range 350 nm – 2,500 nm with sampling interval 1.4 nm @ 350 – 1050 nm and 2 nm @ 1,000 nm – 2,500 nm). An intensive ground truth data set was collected between July 24 – 28, 2004 within days of the airborne hyperspectral imagery acquisition (July 24 and July 26, 2004), respectively.

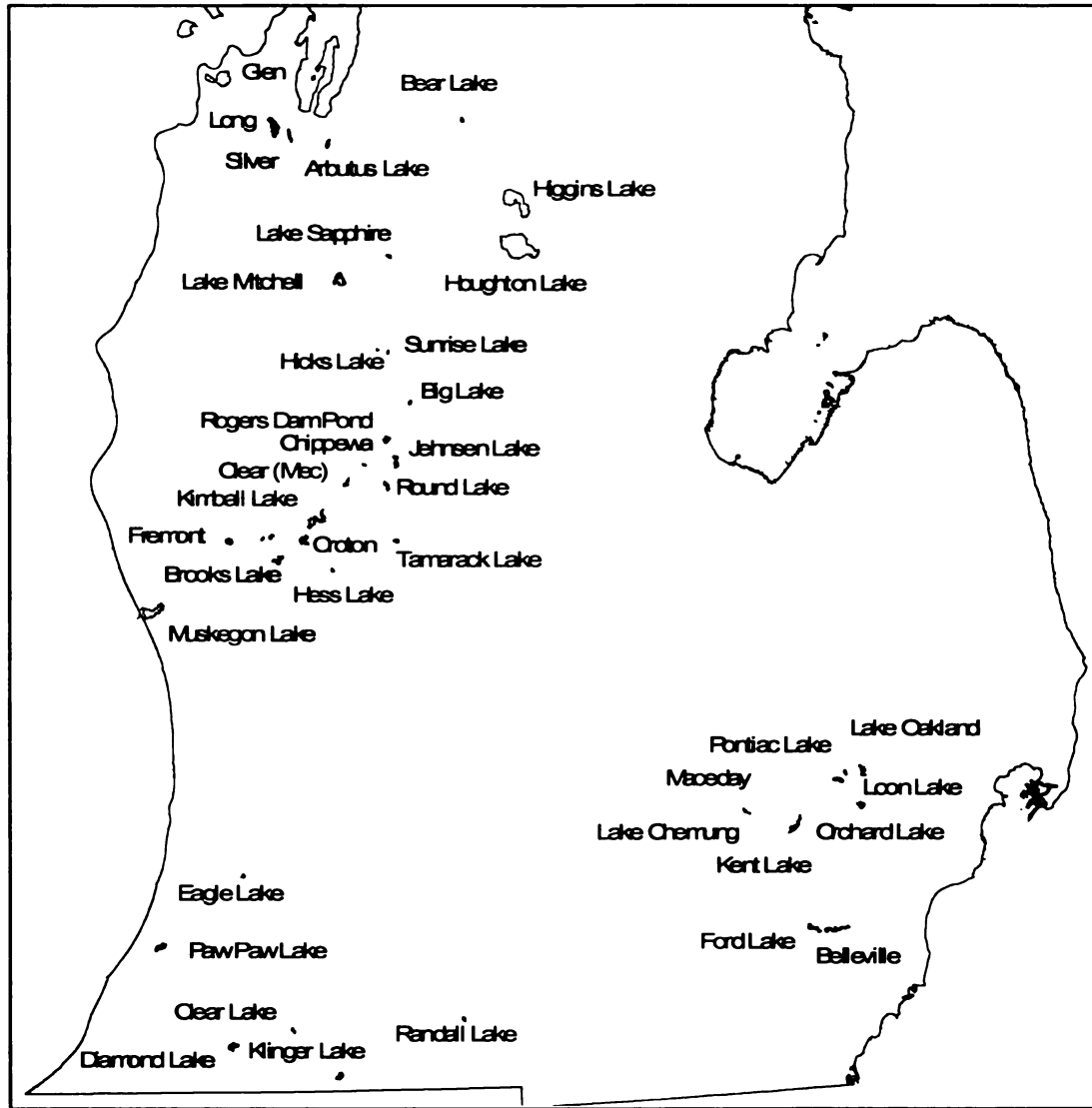


Figure 3-1 Geographic location of the lakes sampled in the study

The field measurement lakes were selected to represent a wide range of water quality characteristics (from hypertrophic waters to oligotrophic waters) based on the preliminary trophic state data estimated from historic CHL and SD measurements from three sampling programs: (1) the Michigan Department of Environmental Quality's (MDEQ) Lake Water Quality Assessment (LWQA)

Monitoring Program, (2) the Michigan Cooperative Lake Monitoring Program (CLMP), and (3) Professor R. Jan Stevenson's algal ecology lab, MSU Department of Zoology. These data were collected in spring and summer between May - August of 2001 to 2003. Water conditions of the sample lakes varied from clear (SD 8.5 m) oligotrophic lakes to turbid (SD 0.5 m) hypertrophic lakes. Approximately 86 percent of the water depth at the sampling sites was, at a minimum, twice the Secchi depth. Therefore, the effect of bottom reflections on remote sensing observations was negligible. The rest of the sample sites were collected at the deepest basins where the bottom was not visible, although water depth was less than twice the SD. The detailed field procedure is included in Appendix A.

### **3.2 Remote Sensing Data Acquisition**

Two sets of hyperspectral remote sensing data were used in the study. The two data sets were acquired from a hand-held ASD sensor and an airborne AISA sensor.

#### **3.2.1 Hand-held Analytical Spectral Devices (ASD)**

Upwelling radiance data (for determination of reflectance spectra) were collected at the same time as water sampling from 42 lakes (48 spectra, 6 revisited). Recorded radiance represented the vertical flux of energy upward from the water surface (primarily solar energy backscattered within the water column and emerging from the water surface). These nadir optical measurements were collected using the LabSpec FR instrument from Analytical Spectral Devices

(ASD, Inc., 2006), positioned approximately 1 m above the water surface and approximately 0.7 m from the side of the boat not affected by a shadow. The radiance samples were taken from the deepest basins of the lakes except for Higgins Lake because the deepest site was too far for the sampling team to be in a safe working condition. The samples from Higgins Lake were taken approximately 3 km offshore where the water was extremely deep (>35 m); therefore, bottom effect was negligible.

Forty eight representative radiance spectra were recorded consisting of 2,150 spectral bands ranging from 350 nm to 2,500 nm at 1-nm intervals. At least 10 replicate upwelling and downwelling scans were recorded at each sampling location. These spectra were averaged to produce a representative reflectance signature for each lake. Down-welling irradiance was indirectly evaluated by measuring the reflected light from a white, near-lambertain reference Spectralon plate® (LabSphere, Inc., 2006). This reference panel is made from sintered polytetrafluoroethylene that is a near-perfect Lambertian reflector. Figure 3-2 showed the variation of up- and down-welling radiance of a high trophic lake (Hess) and a low trophic lake (Higgins).

In summary, spectra collection performed at each sample site comprised (1) the average of approximately 10 radiance spectra of the reference panel at the *beginning* of each measuring session; (2) the up-welling nadir radiance, where each measurement was an average of approximately 15 spectra collected at

every sampling site; and (3) another average of approximately 10 spectra of the reflectance panel at the *end* of the measuring session.

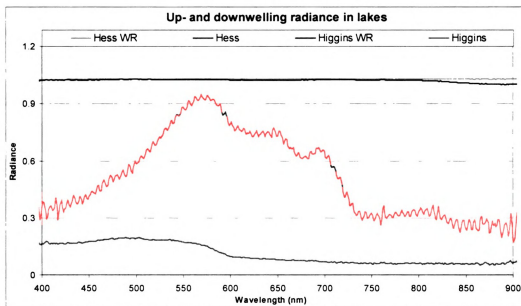


Figure 3-2 The variation of up- and down-welling radiance as measured from ASD. The 10x of mean of upwelling radiance are plotted to scale the reflectance values up for visual comparison with the downwelling radiance

The fraction of light reflected from lake water was very small compared to other natural surfaces, such as soils and vegetation. Water-leaving radiances from natural water bodies are commonly less than 10 percent of the total radiance measured at the sensor. Most of them are even often less than 1 percent (Gordon, 1987). Typically, in clear water, the radiance is maximal in the blue ( $\lambda \approx 440$  nm), medium in the green ( $\lambda \approx 550$  nm) and negligible in the near-infrared ( $\lambda \geq 750$  nm). Since the desired water-leaving radiance is only a small part of the signal recorded by the sensor, accurate radiometric correction is critical (Gordon, 1987). To extract the true representative reflectance of substances in

water column, the collected spectra needed to be transformed to reflectance values at different wavelengths that: (1) maximally relate to the concentration of the constituent of interest; and (2) minimize the effects of other optically active constituents and survey conditions.

### **3.2.2 Airborne Imaging Spectrometer for Applications (AISA)**

Another spectrometer used in the surveys was the Airborne Imaging Spectrometer for Applications (AISA). AISA is a pushbroom imager with a charge-coupled device (CCD) array. The two-dimensional array consisted of a spatial axis of 364 detectors, and a spectral axis of 286 detectors. The instantaneous field of view across the track was one milliradian, which resulted in 1-m-wide pixels from an altitude of 1,000 m. The channel combinations of the two surveys differed slightly: the number of channels was 20 on July 24 acquisition, and 30 on July 26 acquisition. The integration time in the surveys was 30 ms for 20 bands imagery acquired on July 24, 2004 and 20 ms for 30 bands acquired on July 26, 2004. During the surveys, the flight altitudes were approximately 1,200 m. The 20 band imagery pixel length along the track was approximately 1.45 m, and across track was approximately 1.09 m (1.09 m x 1.45 m). Ground resolution of the 30 band imagery was approximately 1.06 m x 1.11 m.

The AISA has flexibility in selecting the sensor's spatial and spectral resolution characteristics. It operates at a wavelength range of 430 nm – 900 nm with a maximum number of 286 channels (width programmable from 2 nm – 10 nm).

The data rate associated with the short integration times (sampling rates) required of the sensor in most operational/flight modes, limits the number of channels. The selected channels for this study covered the wavelength range between 434 nm – 900 nm almost continuously with a channel width of 3 nm – 8 nm. Tables 3-1 and 3-2 listed the band-sets selected and indicate the range of wavelengths covered by each band.

Table 3-1 Spectral configurations of the 20 band AISA data

<b>Nbr</b>	<b>channel</b>	<b>Min wvl</b>	<b>center wvl</b>	<b>Max wvl</b>	<b>Fwhm*</b>	<b>avg.offset</b>	<b>avg.gain</b>
1	6	434.45	438.43	442.40	7.95	0	21.8771
2	17	451.94	455.92	459.89	7.95	0	17.8561
3	22	459.89	463.87	467.84	7.95	0	15.9328
4	47	499.64	503.62	507.59	7.95	0	7.1509
5	59	518.72	522.70	526.67	7.95	0	5.6548
6	94	575.56	579.73	583.91	8.35	0	3.382
7	100	585.58	589.75	593.93	8.35	0	3.2076
8	121	620.65	624.82	629.00	8.35	0	2.9989
9	135	644.03	648.20	652.38	8.35	0	2.9429
10	141	654.05	658.22	662.40	8.35	0	2.8382
11	153	674.09	676.60	679.10	5.01	0	3.9341
12	159	684.11	685.78	687.45	3.34	0	5.3284
13	162	689.12	691.62	694.13	5.01	0	3.4042
14	182	723.06	725.65	728.25	5.19	0	3.4821
15	187	731.71	734.31	736.90	5.19	0	3.5483
16	191	738.63	741.23	743.82	5.19	0	3.6101
17	202	757.66	760.25	762.85	5.19	0	4.0223
18	217	783.61	786.21	788.80	5.19	0	5.2317
19	246	833.78	836.38	838.97	5.19	0	5.8467
20	271	877.03	879.62	882.22	5.19	0	7.3689

\*Fwhm: Full-width, half maximum in nanometers

Table 3-2 Spectral configurations of the 30 band AISA data

<b>Nbr</b>	<b>channel</b>	<b>min.wvl</b>	<b>center wvl</b>	<b>max.wvl</b>	<b>Fwhm*</b>	<b>avg.offset</b>	<b>avg.gain</b>
1	6	434.45	438.43	442.40	7.95	0	32.8156
2	11	442.40	446.38	450.35	7.95	0	30.5965
3	17	451.94	455.92	459.89	7.95	0	26.7842
4	22	459.89	463.87	467.84	7.95	0	23.8992
5	34	478.97	482.95	486.92	7.95	0	17.0929
6	47	499.64	503.62	507.59	7.95	0	10.7264
7	59	518.72	522.70	526.67	7.95	0	8.4822
8	77	547.34	551.32	555.29	7.95	0	6.4266
9	94	575.56	579.73	583.91	8.35	0	5.0729
10	100	585.58	589.75	593.93	8.35	0	4.8114
11	121	620.65	624.82	629.00	8.35	0	4.4983
12	135	644.03	648.20	652.38	8.35	0	4.4144
13	141	654.05	658.22	662.40	8.35	0	4.2573
14	153	674.09	676.60	679.10	5.01	0	5.9012
15	159	684.11	685.78	687.45	3.34	0	7.9926
16	162	689.12	691.62	694.13	5.01	0	5.1063
17	170	702.48	704.99	707.49	5.01	0	5.0089
18	182	723.06	725.65	728.25	5.19	0	5.2232
19	187	731.71	734.31	736.90	5.19	0	5.3224
20	191	738.63	741.23	743.82	5.19	0	5.4151
21	202	757.66	760.25	762.85	5.19	0	6.0335
22	207	766.31	768.90	771.50	5.19	0	6.5596
23	217	783.61	786.21	788.80	5.19	0	7.8476
24	222	792.26	794.86	797.45	5.19	0	8.3681
25	232	809.56	812.15	814.75	5.19	0	8.743
26	246	833.78	836.38	838.97	5.19	0	8.77
27	257	852.81	855.40	858.00	5.19	0	9.0624
28	261	859.73	862.33	864.92	5.19	0	9.4207
29	271	877.03	879.62	882.22	5.19	0	11.0533
30	278	889.14	891.74	894.33	5.19	0	12.7728

\*Fwhm: Full-width, half maximum in nanometers

The coordinates of the sampling stations were determined in advance. The AISA sensor was installed aboard an aircraft, which was equipped with a differential GPS navigation system that made it possible to accurately overfly the sampling stations. The AISA sensor system also incorporates the Fiber Optic Downwelling Irradiance System (FODIS). FODIS allows for the concurrent measurement of downwelling and upwelling radiance by the AISA sensor head. A diffuse collector installed on the top of the plane is connected to the AISA head via a fiber optic cable and collects downwelling irradiance in the same bandwidth configurations as the areas being imaged. The calibration of the FODIS coupled with the AISA sensor allows for the calculation of apparent at-platform reflectance. The AISA pre-processing software (CaliGeo) provides for the automatic geometric correction, rectification, mosaicing, and calculation of radiance or apparent at-platform reflectance (FODIS ratio). The program uses the GPS and attitude information to perform the geometric, georeferencing and mosaicing operations. The AISA data used in this study were radiometrically and geometrically corrected to apparent reflectance at sensor level.

### **3.3 Water Quality Parameter Data**

Field activities at the sites included collection of water samples for laboratory analysis of CHL, TSS, TN, TP, NPOC, and phytoplankton types, and the on-site measurement of SD, lake depth, light-extinction profile, DO, and temperature profile. SD was measured by lowered a Secchi disc (a 20-centimeter diameter, black and white disc attached to a calibrated rope with permanent ink marks) into the water while observing the depth at which it disappeared. The disc was

lowered more and then raised until it reappeared. The depth of the water where the disc vanishes and reappears is the Secchi depth. DO and temperature were measured using a YSI® 55 Dissolved Oxygen Meter, and the underwater light was measured using an LI-250 light meter with the LI-193SA underwater spherical quantum sensor attached to a 30-meter underwater cable.

The water samples for the chlorophyll *a* and TSS analyses were collected in bottles, kept in the dark and filtered at the end of the field day through 47 mm Whatman GF/F filters (0.7- $\mu$ m pore size membrane). The filters for pigment analysis were wrapped in aluminum foil, stored in an ice cooler, transfer and storage in a freezer, and then analysis was carried out. This occurred within five weeks from storage. The filters for TSS measurement were also wrapped with aluminum foil and stored in the freezer. Water samples (850 ml) for phytoplankton analysis were immediately fixed with the iodine solution (M3) on site. The samples were then concentrated in the laboratory and stored in the 30 ml vials until analysis. Samples for NPOC analysis were stored in 30 ml vials at the sample site, wrapped in aluminum foil, and stored in a refrigerator until analysis.

### **3.3.1 Lab Analytical Methods for Chlorophyll *a***

Samples were removed from the freezer and brought to the dark room, which only had yellow and orange light. Aluminum wrap were not removed until the fluorescence light was turned off. Each sample was supplemented with 9 mL 90 percent ETOH and was tightly covered with the cap and the aluminum foil.

The samples were sonicated for 15 minutes, covered entirely with aluminum foil, and then placed in the fridge for 24 hours. Then filters were removed and the remaining ETOH solutions were centrifuged for 10 minutes. A text file (.txt) was created in the computer connected to the fluorometer to allow file transfer. A new Excel spreadsheet was also created and all sample information (sample site, sample number, date, and filtered volume) were input into the spreadsheet. Once the samples were centrifuged, they were ready to be measured. Sample adaptor in the fluorometer was replaced with the solid standard. The standard was measured by pressing the [\*]. The standard values should be confirmed to match with the calibration values. The solid standard was then replaced with the sample adaptor. The supernatant of centrifuged samples were pipetted into 13 mm sample cuvette until approximately 75 percent full. Blank sample was inserted into the fluorometer and measured for the fluorescence value. The value was confirmed to be near zero (~0.05), if not a new blank would be made and used immediately. Fluorescence of all samples were measured (Rd) and recorded into the spreadsheet. Samples with high chlorophyll concentration were diluted with the ratio of 1:5 (1 mL sample with 5 mL 90 percent ETOH). Each sample was acidified by adding 8 drops of 0.1 N HCL (0.15 mL for every 5.0 mL of sample) and stirring thoroughly. Approximately 90 seconds after mixing the acid, the samples were measured again for the fluorescence values (Rc).

### **3.3.2 Lab Analytical Methods for Total Suspended Sediment**

TSS determination followed the Filter TSS/ISS method. Approximately eight TSS samples were taken out from the freezer at a time. Information from the label (e.g., site, date, volume, filter number) was recorded. Next, the aluminum dishes used in the process were labeled and weighed (Dish number. and Dish Wt). Sample filters were then individually placed in the dishes, and dried in the oven for 1 hour at ~105°C. The dishes were transferred into the desiccator for 1 hour before being weighed again for dried weight (Dried Wt). The dish and sediment were placed in muffle furnace at 500 °C for 15 minutes, and transferred to the desiccator for 1 hour. The samples were then weighed to determine loss on ignition (LOI). TSS was calculated using Eq 3-1 and 3-2).

$$\text{TSS (mg/L)} = (\text{Dried Wt} - \text{Dish Wt} - \text{Filter Wt}) / (\text{Volume Filtered} * 1,000) \quad (\text{Eq 3-1})$$

$$\text{ISS (mg/L)} = (\text{LOI} - \text{Dish Wt} - \text{Filter Wt}) / (\text{Volume Filtered} * 1,000) \quad (\text{Eq 3-2})$$

### **3.3.3 Lab Analytical Methods for Non - Purgable Organic Carbon**

NPOC were analyzed at Hamilton's laboratory at Kellogg Biological Station, MSU. The NPOC analytical method was slightly modified from Hamilton lab NPOC/DOC protocol written by Dave Weed. The method was written for the Shimadzu TOC-Vcph carbon analyzer with the total nitrogen module (TNM-1), and the ASI-V autosampler. The system was set up to automatically add portions of 2M Hydrochloric acid to each standard and sample, and to sparge each of them with chromatographic grade or zero air for a predetermined time

period. Each sample was sparged just prior to injection onto a combustion chamber containing platinum catalyst. The vaporized sample then traveled out to a CO<sub>2</sub> detector and to the TNM-1 module for chemiluminescence detection of nitrogen.

(1) Acid Preparation: 2M hydrochloric acid (HCl) was made by adding 41 – 42 mL concentrated HCl to approximately 200 mL of deionized water in a 250 mL volumetric flask, then diluted to the mark with deionized water.

(2) Standard Preparation: Carbon analysis stock standard was made by drying potassium hydrogen phthalate (KHP) at 105 – 120°C for 1 hour and cool in desiccator. The 2.1254 grams KHP was accurately weighed into weigh boat before transferred to 1 L volumetric flask and diluted to mark with deionized water (use zero grade water if available for the best results). Nitrogen analysis stock standard was made by drying potassium nitrate (KNO<sub>3</sub>) at 105-120°C for three hours and cool in desiccator. The 7.1282 gm KNO<sub>3</sub> was accurately weighed into weigh boat before transferred into 1L volumetric flask and diluted to mark with deionized water (use zero grade water if available for the best results).

(3) Mixed C/N standards: The following standards were typically made for a combination NPOC/TN analysis: 5, 10, 25, 50, and 100 parts per million Carbon and Nitrogen.

(4) Autosampler Rack Preparation: The autosampler rack had 93 positions and used 24 mL vials with corresponding caps and septa. A complete set of standards (including blanks) were placed at the beginning and end of the rack, and check standards (either 5ppm C, N or 10 ppm C, N) were placed among every 15-20 samples. Approximately 20 mL each of sample or standard were poured off into 24 mL vials, then capped with open-hole caps and septa, and placed into rack. The sample level in the vial was usually even with the top of the rack.

(5) Instrument Preparation: The two outside rinse water reservoirs were checked to make sure they were filled with deionized water. Front panel was opened to make sure that the two water traps on the bottom right internal area of the instrument had water at the correct levels. The front trap had high and low markings; the back trap should be filled to the level of the clamp that holds it. The 2M hydrochloric acid reservoir should be filled if low. A full HCl reservoir should contain enough acid to run about five complete racks (93 samples per rack), if not more. The main cylinder valve (large silver knob on top of cylinder) and the regulator valve (black knob) were opened on the zero air compressed gas cylinder. The instruments were powered on to open gas lines to the instrument and turn the fans on. The actual instrument settings were initialized using the TOC software located on the Dell Computer next to the Ion Chromatograph.

(6) Setup using TOC software: The TOC oven must be heated to 720°C and stabilize prior to running samples/standards. The TN module also required some stabilization time. This process took at least 20-30 minutes.

(7) Sample Table: The sample table was used to assign methods and rack positions for each standard and sample. The software was capable of running the calibration standards, but typically all standards were run as unknowns. Afterwards, the data was used with MS Excel to create calibration curves.

The principle of Non-purgable organic carbon analysis was to measure samples that were acidified (pH less than 2.0) and sparged with CO<sub>2</sub> free air. The sample was injected into a TC (Total Carbon) combustion tube, which had been filled with oxidation catalyst and heated to 720°C. The sample was combusted or decomposed to CO<sub>2</sub>. The combustion product was sent through an IC reaction vessel, cooled, dried by a dehumidifier and then sent through a halogen scrubber. The NPOC component was detected for CO<sub>2</sub> in a non-dispersive infrared gas analyzer (NDIR). The peak area count was proportional to the NPOC concentration of the sample.

#### **3.3.4 Lab Analytical Methods for Algal Community Counting**

Phytoplankton community counts used the Soft Algae Counts method. Species composition and biomass was determined by counting a known volume sample under a microscope followed the steps:

(1) A sample list was created to indicate initial volumes (collected from field), sample ID (what lake and date the sample was from), volume of sample (in lab before counting).

(2) The initial volume of the sample was measured by comparison with a marked 'Standard bottle.' The standard bottle was made by marking the outside surface of the empty bottle that was exactly the same as the bottles in which the original samples were collected with lines that correspond to volumes precisely measured with a graduated cylinder. The reference 35 mL bottle was marked every 1 mL.

(3) The outside of the sample bottle that represented lower meniscus level of the sample was marked with a fine tip permanent marker to precisely measure the sample volume without transferring the sample into a graduated cylinder or beaker, which was time consuming and required adding rinse water. The mark was compared with the closest measure on the 'Standard bottle' and the volume was measured and recorded. Measurement and recording volumes were done with all samples.

(4) A pipette was used to transfer 0.1 mL sample into the Palmer-Maloney Counting Cell. There should be approximately 15-30 natural units in a field of view in order to count a sample in a timely manner without drying of the subsample in Palmer Maloney counting chamber. If algal density met the requirement, start counting. If not, the sample needed to be diluted or

concentrated further. Algal division, size, and number of colonies were recorded along with the counting distance on the microscope (for area calculation).

(5) Representative biovolume for each algal category was determined. Known algal genera were recorded when counting. The biovolume of these genera were derived from Stevenson et al. (1996), Buzzi (2002), and the biovolumes of algal taxa in samples collected by the USGS National Water Quality Assessment (NAWQA) Program 2004 (The Academy of Natural Sciences, 2006). Biovolume for several genera in each category was averaged to obtain the representative biovolume. These biovolumes were used to multiply cell density for each class for each sample.

### 3.4 Spectral Analytical Methods

The spectral analytical process followed the flow diagram showed in Figure 3-3.

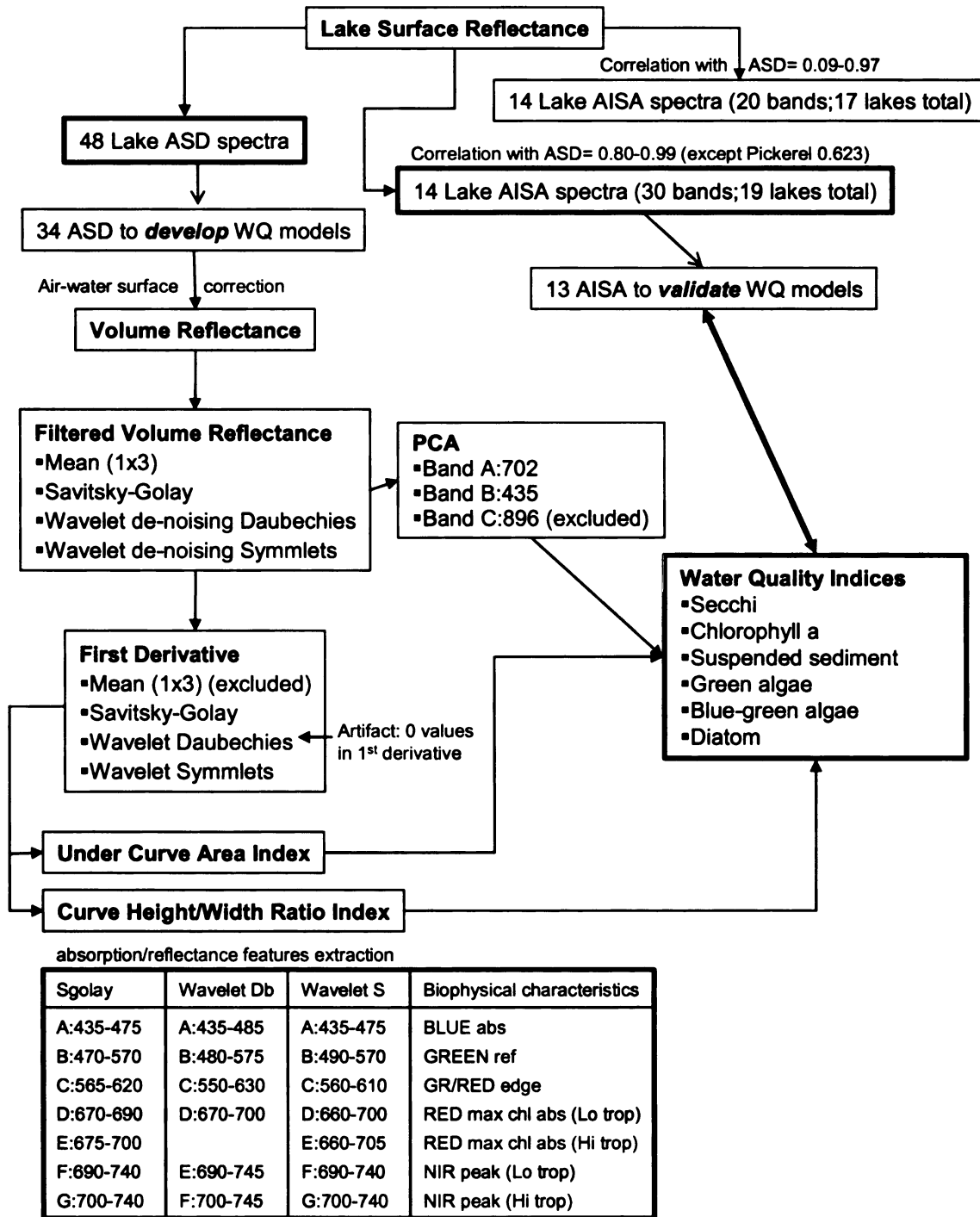


Figure 3-3 Spectral analytical procedure flow diagrams

### 3.4.1 ASD Data Preprocessing

Reflectance is the percentage of light reflected by a target. It minimizes the effect of different illumination conditions, thus allows a better quantitative measuring of the water color. Radiance measurements from the field were converted to surface reflectance by using nearly coincident measurements over the spectralon panel (Eq 3-3). These reflectance data represent the ratio of reflected energy to incident energy with values ranging from 0.0 to 1.0 (0.0 for no reflectance and 1.0 for 100 percent reflectance). The multiple spectra collected from each site were averaged to determine a mean spectral response for that lake.

$$\rho^a_{\text{in-situ}} = E\uparrow_{\text{in-situ}} / E\uparrow_{\text{spec}} * \rho^a_{\text{spec}} \quad (\text{Eq 3-3})$$

Where:

$$\rho^a_{\text{in-situ}} = \text{In situ target percent reflectance}$$

$$E\uparrow_{\text{in-situ}} = \text{In situ target radiance}$$

$$E\uparrow_{\text{spec}} = \text{Linearly interpolated reference panel radiance}$$

$$\rho^a_{\text{spec}} = \text{Reference panel reflectance coefficient}$$

Reflectance of forty eight spectra of water bodies are shown in Figure 3-4. It is notable that reflectance below 400 nm and above 900 nm are dominated by noise. The relatively small amounts of solar energy outside the 400 nm – 900 nm range result in data with comparatively high levels of noise (Harrington and Repic, 1995). Further spectral processing and analysis in this research will be based on the spectral data between 400 nm – 900 nm (Figure 3-5). This range

of wavelength has been used in a number of studies on inland waters (Dekker et al., 2001; Flink et al., 2001; George and Malthus, 2001; Harma et al., 2001; Koponen et al., 2001; Pepe et al., 2001; Pulliainen et al., 2001; Shafique et al., 2001; Jensen, 2000; Subramaniam et al., 1999).

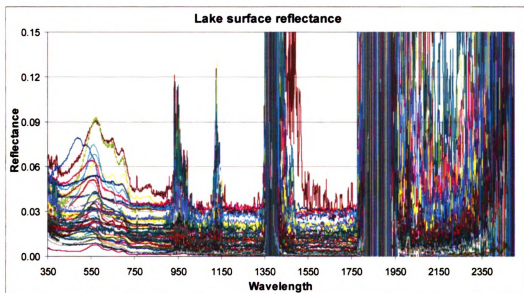


Figure 3-4 ASD spectral signatures (350 nm – 2,500 nm) of 48 representative water samples

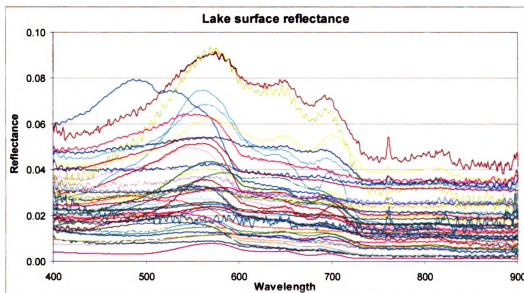


Figure 3-5 ASD spectral signatures (400 nm – 900 nm) of 48 representative water samples

Optical characteristics of different biophysical conditions in water are shown in Figure 3-6. Pickerel Lake and Ford Lake exhibit high trophic conditions (CHL = 113.79 mg/L and CHL = 80.54 mg/L, respectively). The difference between the two water bodies is that Ford Lake had a much shallower Secchi depth of 0.95 m, while the SD in Pickerel Lake was 2.20 m. Lower SD lakes have higher reflectance. Both reflectance curves show the unique CHL signature features such as high reflectance in green wavelengths (500 nm – 600 nm), absorption in red wavelengths (650 nm – 700 nm), and a secondary peak reflectance at near-infrared wavelengths (near 700 nm). The reflectance curves for Brooks Lake and Tamarack Lake are indicative of waters with moderate concentrations of suspended sediment (TSS = 64.00 mg/L and TSS = 51.40 mg/L). These two lakes had the highest TSS of all lakes sampled.

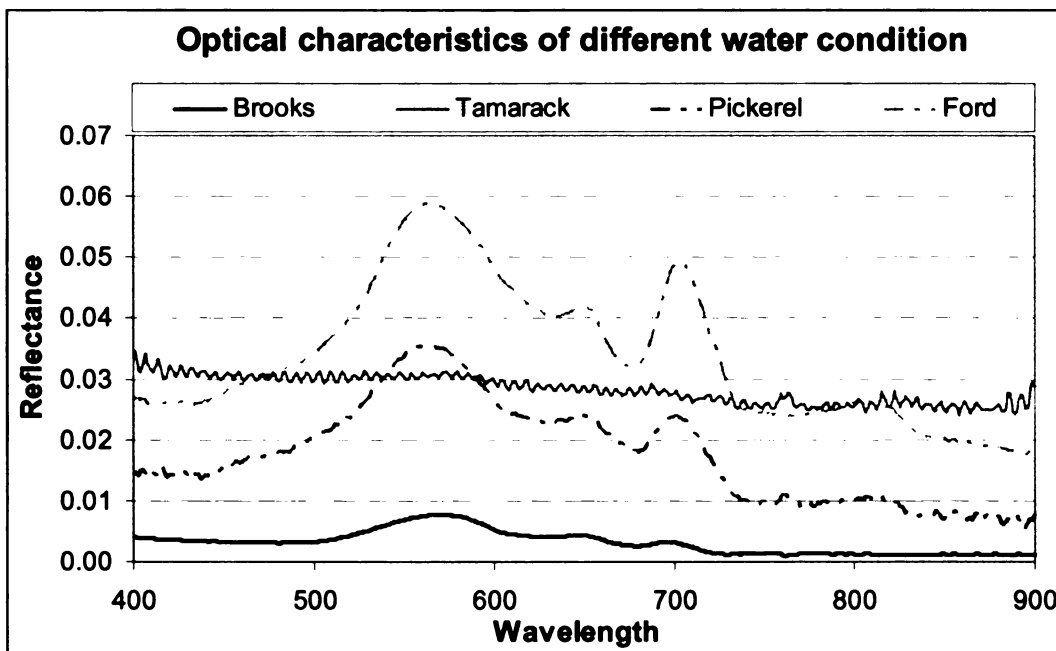


Figure 3-6 ASD spectral characteristics of different biophysical dominate in waters

### **3.4.2 AISA Image Preprocessing**

Representative reflectance values for each ground-truth site were extracted for each band at locations that coincided with the sampling stations. Mean values were calculated within 3 x 3 pixels window (approximately 3.2 x 3.3 meters) around the sampling station. This pixel window size was reasonable enough to smooth out noise or errors in the spectral data, yet maintain homogeneous water quality. Pearson correlations were used to investigate the relationship between the airborne AISA spectra and the hand-held ASD measurements. The AISA 20-band data set had low, and some negative, correlations with ground-truth ASD (Table 3-3; Figure 3-7). On the other hand, the 30-band AISA data set produced very high correlations with the ground measurement ASD (Table 3-4; Figure 3-8). Despite the fact that some of the AISA spectra were correlated with the ASD spectra of different dates (May and June, due to the lack of ASD data near the date), and atmospheric effects could play an important role in low correlations, the sky on July 24 was overcast with patchy clouds that could have constantly change the incident light. The sky was clear when measurements were made on July 26. As a consequence, only the 30 band data set will be used in further analysis. Figures of 20-band and 30-band AISA imagery are provided in Appendix B.

Table 3-3 Pearson correlation between 20 band AISA and ASD spectra

<b>Lakes</b>	<b>AISA Date</b>	<b>ASD Date</b>	<b>Correlation</b>
Brooks	7/24/2004	7/27/2004	0.928
Clear (@Mecosta)	7/24/2004	7/24/2004	-0.249
Hess	7/24/2004	7/27/2004	0.973
Higgins	7/24/2004	7/27/2004	0.776
Houghton	7/24/2004	7/26/2004	0.908
Jehnsen	7/24/2004	5/19/2004*	-0.368
Kimball	7/24/2004	5/26/2004*	0.229
Marl	7/24/2004	7/27/2004	-0.879
Mecosta	7/24/2004	7/24/2004	-0.323
Mitchell	7/24/2004	7/25/2004	0.627
Muskegon	7/24/2004	7/28/2004	0.424
Roger dam pond	7/24/2004	7/24/2004	0.351
Round	7/24/2004	7/24/2004	0.020
Silver	7/24/2004	7/25/2004	0.801
Tamarack	7/24/2004	6/5/2004*	0.090

\* Lakes that ASD was not measured at the same period

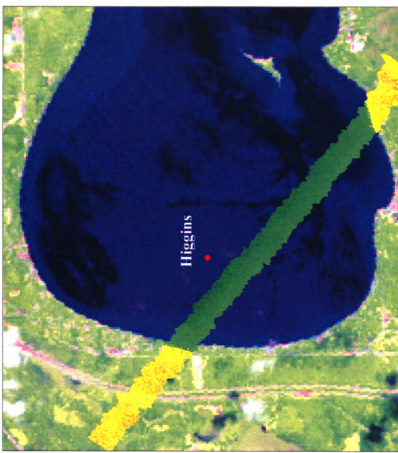
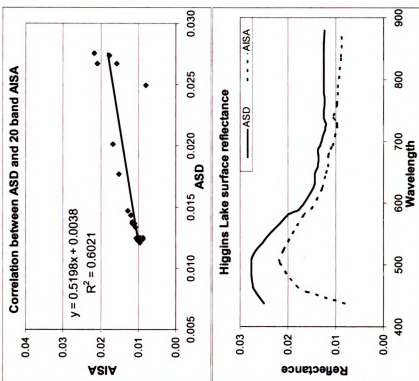


Figure 3-7 Comparison between ASD and 20 band AISA spectral signatures of Higgins Lake. AISA stripe image overlay on Landsat image. Red point represents the corresponding sample site

Table 3-4 Pearson correlation between 30 band AISA and ASD spectra

<b>Lakes</b>	<b>AISA Date</b>	<b>ASD Date</b>	<b>Correlation</b>
Arbutus	7/26/2004	7/26/2004	0.971
Brooks	7/26/2004	7/27/2004	0.982
Clear (@Mecosta)	7/26/2004	7/24/2004	0.934
Hess	7/26/2004	7/27/2004	0.987
Higgins	7/26/2004	7/27/2004	0.985
Houghton	7/26/2004	7/26/2004	0.914
Jehnsen	7/26/2004	5/19/2004*	0.936
Kimball	7/26/2004	5/26/2004*	0.591
Marl	7/26/2004	7/27/2004	0.915
Mitchell	7/26/2004	7/25/2004	0.832
Muskegon	7/26/2004	7/28/2004	0.801
Pickerel	7/26/2004	5/26/2004*	0.623
Roger dam pond	7/26/2004	7/24/2004	0.892
Sapphire	7/26/2004	7/25/2004	0.989
Tamarack	7/26/2004	6/5/2004*	0.950

\* Lakes that ASD was not measured at the same period

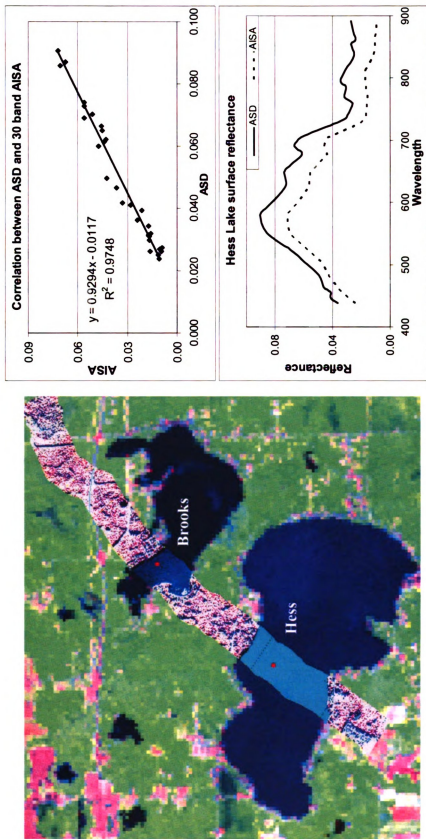


Figure 3-8 Comparison between ASD and 30 band AISA spectral signatures of Hess Lake. AISA stripe image overlay on Landsat image. Red point represents the corresponding sample site

### 3.4.3 Air-Water Interface Correction

The total radiance, ( $L_t$ ) recorded by the remote sensor is a function of the electromagnetic energy from the four sources identified in Figure 3-9 (Eq 3-4) (Jensen, 2000).

$$L_t = L_p + L_s + L_v + L_b \quad (\text{Eq 3-4})$$

Where:

$L_p$  is an atmospheric noise commonly referred to as *path radiance*. It is the portion of the radiance recorded by a remote sensing instrument resulting from the downwelling solar ( $E_{sun}$ ) and sky ( $E_{sky}$ ) radiation that never actually reaches the water surface.

$L_s$  is sometimes called the *free-surface layer* or *boundary layer*. It is the radiance from the downwelling solar radiance that reaches the air-water interface but only penetrates it a millimeter or so and is then reflected from the water surface. This reflected energy contains spectral information about the near-surface characteristics of the water body. Unfortunately, if the solar zenith angle and sensor viewing angle are almost identical, this spectral component presents only a purely specular reflection (*sun-glint* effect).

$L_v$  is the *subsurface volumetric radiance*. It is the radiance that actually penetrates the air-water interface, interacts with the water and organic/inorganic constituents and then exits the water column without

encountering the bottom. This radiance provides valuable information about the characteristics of the water column.

$L_b$  is the portion of the radiance that reflected back from the bottom of the waterbody. If the objective of the study is to obtain information about the bottom, i.e. bathymetric mapping or coral reef mapping, then this radiance component may be of significant value. However, in water column study, radiance from the bottom causes difficulty for properly a characterizing the water column above it.

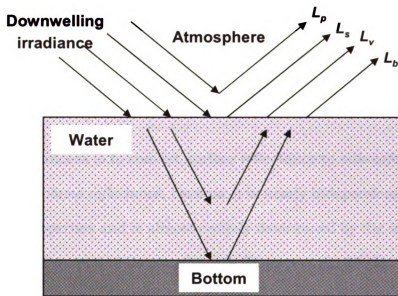


Figure 3-9 Down- and up-welling radiances from water bodies (after Jensen, 2000)

To achieve the goal of identifying the organic and inorganic constituents in the water column, volumetric radiance ( $L_v$ ) needs to be extracted from all the other radiance components being recorded by the sensor (Eq 3-5).

$$L_v = L_t - (L_p + L_s + L_b) \quad (\text{Eq 3-5})$$

The data used in this study were collected 1 m from the water surface with a hand-held ASD and 1 km above surface on a very clear day with an airborne AISA. Therefore, atmospheric attenuation ( $L_p$ ) should not have much effect on these data. Bottom reflectance ( $L_b$ ) was carefully avoided during field sampling (see Appendix B). However, surface sunglint and other surface reflection ( $L_s$ ) needed to be corrected because it was impossible to avoid in the field measurements.

The analytical process is to convert surface reflectance to *subsurface volume reflectance*, or *volume reflectance*, because it is nearly independent of atmospheric properties and is almost entirely determined by the optical properties of the water and its constituents (Bukata et al., 1995). The equation used by Morel and Gentili (1993; Eq 3-6) was modified to Eq 3-7, which was applied to the data to convert the surface reflectance (remote sensing reflectance) into subsurface reflectance.

$$R_{rs} = \frac{(1-\rho) * (1-\rho') * R(0-)}{1-r * R(0-) * n^2 * Q} + R_{surf} \quad (\text{Eq 3-6})$$

$$R(0^-) = \frac{Rrs - Rsurf}{\frac{(1-\rho) * (1-\rho')}{n^2} + r * Q * (Rrs - Rsurf)} \quad (\text{Eq 3-7})$$

Where:

*Rrs* is the remote sensing reflectance

*R(0<sup>-</sup>)* is the volume reflectance

*Rsurf* is a specular reflectance from the surface of the water body

*Q* is a ratio of downwelling irradiance to upwelling radiance (5 sr<sup>-1</sup>)

$\rho$  is an internal Fresnel reflectance (0.03)

$\rho'$  is an air-water Fresnel reflection at the interface (0.54)

*n* is a refractive index of water (1.34)

*r* is the water-air reflection (0.54)

Gege (2001) applied this model for calculating remote sensing reflectance in the WASI 2.0 (Water Colour Simulator) software. Default values indicated in the brackets of the key of Equation 3-7 were taken from the WASI 2.0 (Gege, 2001).

Upwelling spectra measured above the water can be affected by sun glint from the water surface (specular reflectance, *R<sub>surf</sub>*) due to waves. The assumption that light absorption by pure water is predominant in NIR (970 nm – 1,000 nm), and the water-leaving radiance in this region is zero, was suggested to estimate *R<sub>surf</sub>* in the measured spectra (Ouillon et al., 1997). It should be noted that this assumption may not hold valid in highly turbid waters (Doxaran et al., 2002). However, the TSS range of the study sites were

considered low to moderate; therefore, the waters were assumed not highly turbid and the assumption of Ouillon et al. (1997) was implemented. Due to the high noise levels of the collected spectra, the spectral range between 1,250 nm – 1,260 nm were found more stable than other NIR regions (Figure 3-4). The average reflectance from this range was used to remove specular reflectance and wave effects by subtracting it from the whole spectra (Eq 3-7). Figure 3-10 and 3-11 show the reflectance before and after corrected for air-water interface. The corrected volume spectra are generally higher than the measured surface reflectance. The volume reflectance spectrum that was below zero was Round Lake. The samples were taken from this lake late in the evening and the sun elevation angle was very low. There was a fair amount of sun glint reflected from the water surface, which causes a problem when converting from surface reflectance to subsurface volume reflectance.

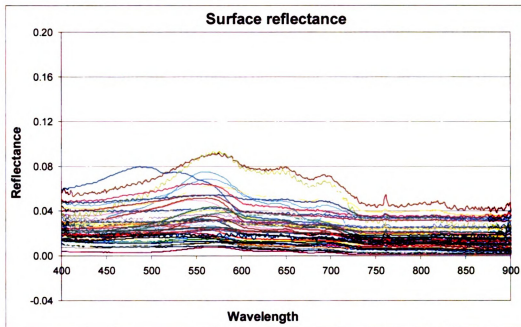


Figure 3-10 Remote sensing reflectance  $R_{rs}$

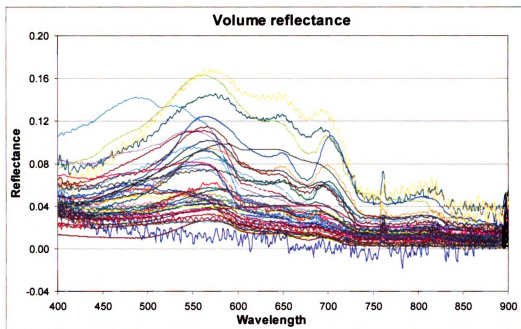


Figure 3-11 Subsurface volume reflectance  $R(O-)$

#### **3.4.4 Noise Reduction**

The volume reflectance were used in the principle component analysis (PCA) and the derivative analysis in order to determine the optimal spectral bands that best related to biophysical parameters within the water column. Both PCA and derivative techniques are based on the variation within the data; therefore, they are very sensitive to noise in the data. Noise can obscure important features such as peaks, valleys, or peak widths, or make calculation of signal features such as slopes, areas, peak widths and so forth difficult. The volume reflectance spectra needed to be filtered to produce the data that are uncontaminated by noise signal from the atmosphere or the sensor itself. The filter should maintain the sharpest absorption/reflectance features in the original signal. Mean and Savitsky Golay filter, and Daubechies and symlet wavelet de-noising transformations were used (Schmidth and Skidmore, 2004). Several configurations of these methods were applied to the volumetric reflectance (Appendix C). The methods were compared based on the criteria that the selected model must smooth out high frequency noise while maintaining the smallest features that could be associated with biophysical attributes (absorption troughs and reflectance peaks). If the higher wavelet order and level did not provide more optical information than the lower ones, the simpler models were selected.

In this process, the volume spectra were filtered with: Mean 1x3, Savitsky Golay (Sgolay), Daubechies de-noising wavelet, and Symlet de-noising wavelet. Mean filter is the simplest method. Savitzky Golay seeks to preserve shapes of

reflectance peaks. The Savitzky Golay filter method essentially performs a local polynomial regression to determine the smoothed value for each data point. This method is superior to adjacent averaging because it tends to preserve features such as peak height and width, which are usually 'washed out' by adjacent averaging (Figure 3-12).

The general wavelet de-noising procedure involves three principle steps: decomposition, threshold selection, and reconstruction. First, a wavelet is selected and a level at which the wavelet decomposition will be computed. In this study, two wavelets were selected as the best wavelet options, Daubechies order 1 level 3 (db1) and Symlet order 8 level 3 (s8). The coefficients of all component of a third-level decomposition (that is the third-level approximation and the first three levels of detail) are returned concatenated into one vector, C. Vector L gives the lengths of each component. Second, select a threshold such as global thresholding (gbl) and apply it to the detail coefficients. Third, compute wavelet reconstruction using the original approximation coefficients and the modified detail coefficients (Figure 3-13; The MathWorks Inc., 2006).

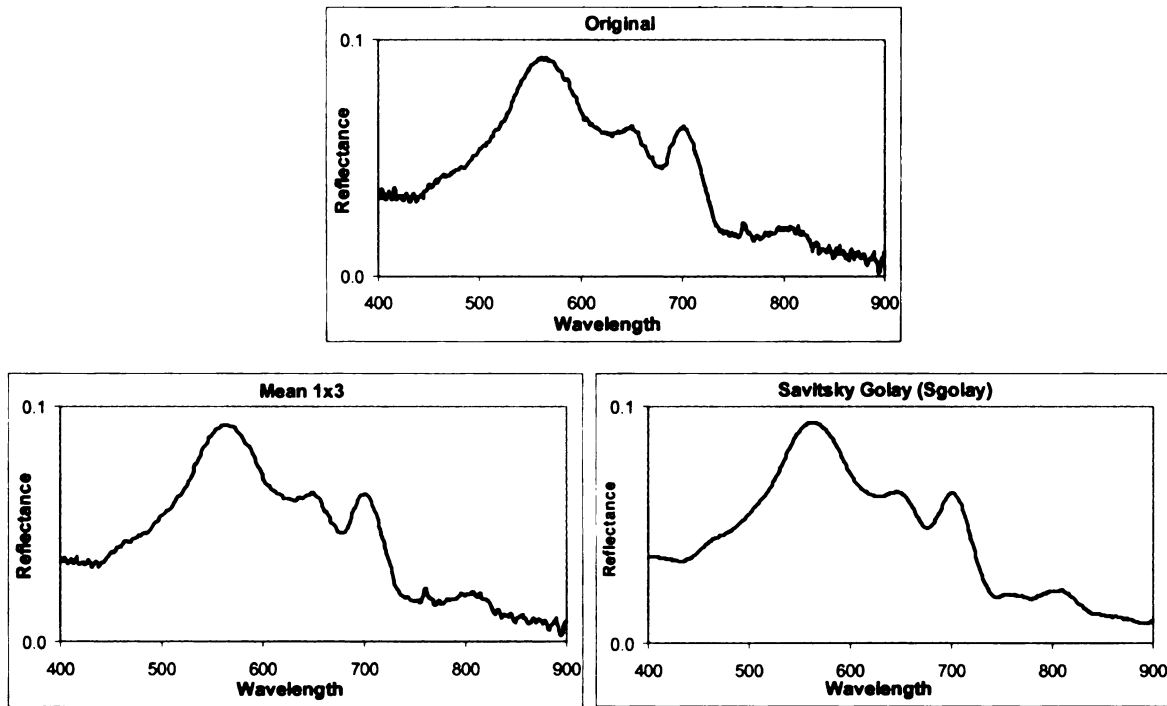


Figure 3-12 Examples of Mean and Savitsky Golay (Sgolay) filter transformation on Pickerel Lake

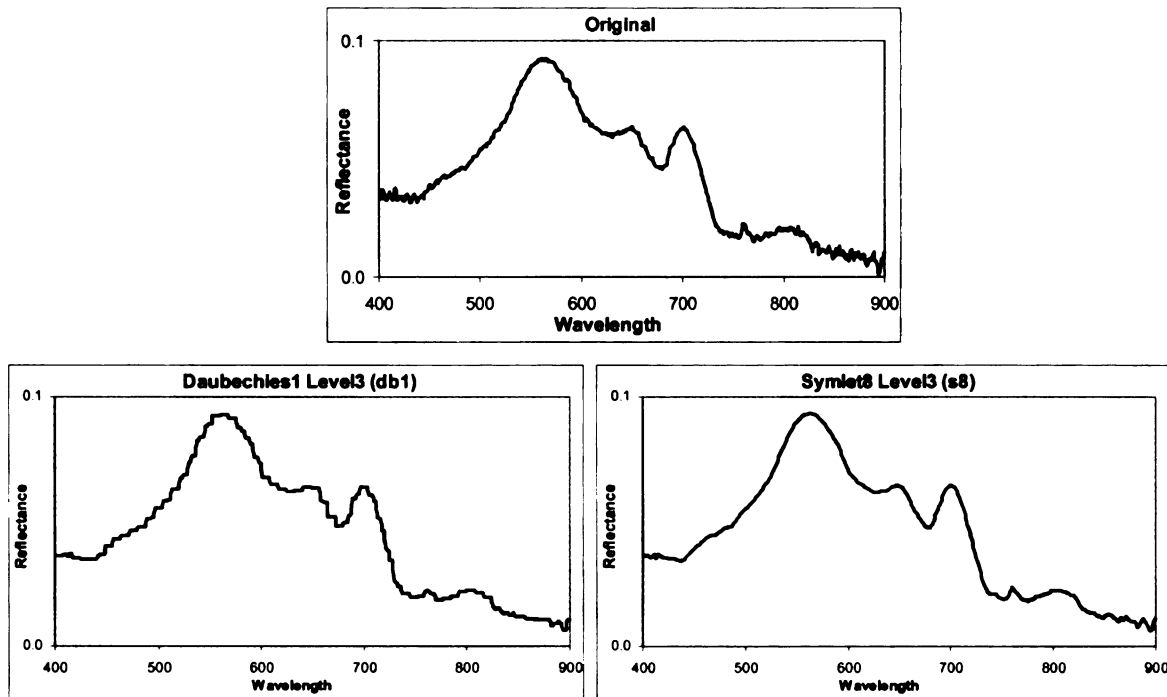


Figure 3-13 Examples of Daubechies (db1) and Symlet (s8) wavelet de-noising transformation on Pickerel Lake

### **3.4.5 Narrow-Waveband (1 nm) Indicator: Principal Component Analysis**

A number of approaches have been developed to maximize the spectral variance of remote sensing data to assist in the discrimination of different surface materials. The most widely used of these techniques is principal components analysis (PCA) (e.g., Becker et al., 2005; Lillesand and Kiefer, 2000; Jensen, 1996; Davis, 1986). PCA has been effectively used with multispectral data through the compression of the information into fewer, independent (orthogonal channels) components. The principal components transformation assists removing the inherent redundancy through a decorrelation process followed by the discarding of low variance components (Richards and Jia, 1999). It is sometimes used as a tool for feature reduction in multispectral data analysis. When employing the method with hyperspectral data, the high computational load is the main concern (Richards and Jia, 1999).

PCA requires no *a priori* information and is based on the entire spectral domain of the data set (Rencz, 1999). PCA is generally based on the correlation matrix between spectral channels. Conceptually, the process defines a new set of orthogonal uncorrelated coordinate system or vector space that maximizes the amount of variance that each axis describes. In doing so, it produces a space in which the data have the most variance along its first axis, the next largest variance along a second orthogonal axis, and so on. In general, the later principal components would be expected to show little variance and thus can be ignored. Eigenvalues explain the amount of the spectral variability contained in each component, and the eigenvectors explain the relative proportion or

contribution of each band to that component (Rencz, 1999). The technique is only of value however if the spectral structure of the data is distributed substantially along the first few axes (Richards and Jia, 1999).

Generally, high data variance is usually needed for separating different features in the data. Thus, higher order components with low variance can be discarded without significant information loss. The first few high variance features (principal components) are usually selected. Increasing use of high spectral resolution remote sensing requires larger image storage. Bandwidth compression has become more important. Another advantage of PCA is that the original spectral or image data can be reconstructed from the reduced representation (using an inverse principal components transform) although with loss of information. Since the reconstructed data may differ, the information loss is sometimes referred to as distortion from the original (Richards and Jia, 1999).

PCA is thus an effective tool for summarizing the common components of spectral variability of the hyperspectral data into a small number of variables. The separation of materials in a remote sensing scene by PCA is driven by the spectral variability of the substances and is thus linked to spectral properties (Rencz, 1999). However, it is important to recognize that some features selected in this way may be misleading. For example, original noisy bands will lead to some principal components with high variance but low separability (Richards and Jia, 1999).

Fourteen out of 48 water spectra were separated for validation. Thirty four filtered spectra were used to develop the spectral indicators for water quality. These 34 filtered volume reflectance at wavelength between 400 nm – 900 nm were used in the PCA analysis. The spectral data were arranged in the format that each row represented spectral data of the lake and each column referenced a specific waveband. SPSS® software package was used to perform PCA and transform the 500 independent spectral bands into their principal components.

Band number was the independent variable. PCA was performed with the minimum eigenvalue: 1.0. Correlation-based and covariance-based PCA were performed to compare the efficiency of the two methods. Both PCA methods used standardized input variables that have a mean of zero and a variance of one. This standardization tends to inflate the contribution of variables whose variance is small, and reduce the influence of variables whose variations are large (Davis, 1986). PC analyses based on correlation matrices generate dimensions that emphasize the features that best capture the predominant *similarities* among the variables (Davis, 1986). PCA based on covariance matrices generate dimensions that emphasize the features that best capture predominant target *differences*. Both methods were investigated and compared.

Unrotated PCs from both methods produced a very high percent of total variance explained in the 1<sup>st</sup> component, which made meaningful interpretation difficult. Rotation of the factors to right angles (uncorrelated) with the first removes the effects of variables highly loaded on the first factor and enables an

assessment of patterns independent of them (Rummel, 1970). PCA was performed again with the varimax rotation. Rotated correlation-based and rotated covariance-based PCA produced almost the same results with the same ranges of high component loadings, but different loading values. The results consistently showed that there were three significant components to extract from the spectra of 34 lakes. The percent variance explained by the 4<sup>th</sup> component dropped dramatically from the first three. Although both PCA methods produced consistent results, principle components from correlation-based PCA provided more confidence in locating the spectral bands because of the more defined peak. Therefore, three principle components, which explain the whole data set while significantly reduce redundancy in dataset from 500 bands to 3 principle bands, were produced from correlation-based PCA. The three principle components (Figure 3-14) consisted of PC1: band 700 nm (NIR peak), PC2: band 435 nm and 455 nm (blue absorption) for different filter methods, and PC3: band 896 nm which was suspected to detect the atmospheric effect because water absorbed most incident light after 800 nm. These bands were selected repeatedly as the principle components regardless of different filter and different PCA methods. Each component explained 36 percent, 37 percent, and 26 percent of the variance of the data. The first three components together explained more than 99 percent of the variance of the data. However, only PC1 and PC2 will be used in the water quality indicator model development because they contain information about biophysical characteristics in waters.

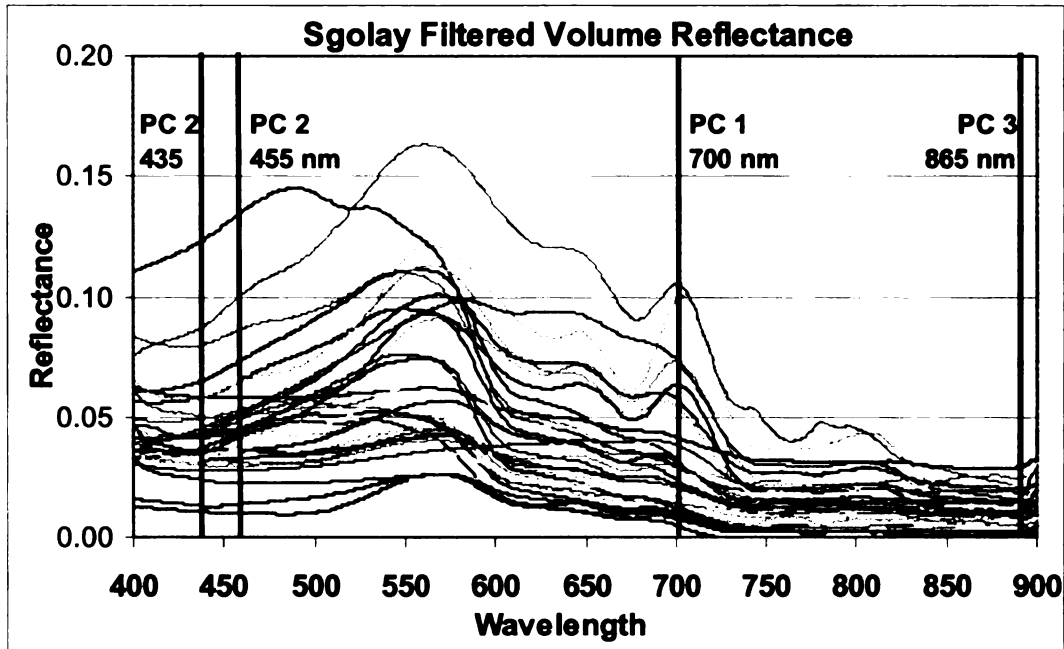


Figure 3-14 Example of PCA result

The first principle waveband was located precisely at the near-infrared reflectance peak of high trophic lake spectra. The second principle wavebands, especially band 435 nm, were located close to blue absorption region.

### 3.4.6 Spectral Derivative Analysis

Although the massive amount of hyperspectral data (the hundreds of spectral bands) may cause difficulties in traditional image processing and data handling techniques, it provides information to allow analyses based on a knowledge of spectroscopic principles. Data used in spectroscopy are usually collected under controlled laboratory conditions with full control of the intensity and spectral distribution of the illumination as well as viewing geometry (Tsai and Philpot,

1998). However, having a well-defined spectrum and knowledge of spectral features means that a scientific approach to interpretation of the real world features can be carried out (Richards and Jia, 1999). Absorption features (seen as localized dips) are often observed in the reflectance spectra of specific substances. These features provide characteristics of the substrates of interest when sufficient spectral resolution is obtained. Characterization, and thus automatic detection of such absorption features, is of particular interest in hyperspectral image recognition. Absorption features can be characterized by their locations (bands), relative depths and widths (full width at half the maximum depth). A complete spectrum is divided into several regions and absorption features (Richards and Jia, 1999).

*Derivative spectroscopy* is particularly promising tool among the techniques developed in spectroscopy for use with remote sensing data (Tsai and Philpot, 1998). Spectral derivative techniques have long been applied in spectral studies, and have been found to eliminate background signals, differentiate overlapping signatures, and reduce the affects of turbidity in aquatic chlorophyll *a* investigations (Demetriades-Shah, 1990). In hyperspectral analyses, derivatives are found to be very sensitive to noise. Derivatives of the second order or higher should be relatively insensitive to variations in illumination. Nonetheless, first and second order derivatives have been the most commonly used by scientists (Tsai and Philpot, 1998; Fell and Smith, 1982; Butler and Hopkins, 1970).

After random noise was minimized from the 34 spectral measurements, the derivatives were calculated from volume reflectance for each of the four filter methods: Mean, Sgolay, db1 and s8 (Figure 3-15). Spectroscopic first derivatives were obtained by taking the difference between the reflectance of two bands and dividing that value by the difference between the wavelengths separating the two bands. The first step is to determine the slope of a line segment by simply dividing reflectance value differences by the wavelength interval separating them (rise/ run) as indicated by Eq 3-8.

$$d^{1st} = (\rho_{n+1} - \rho_n) / (\lambda_{n+1} - \lambda_n) \quad (\text{Eq 3-8})$$

where:

n = band number

$d^{1st}$  = 1<sup>st</sup>-derivative (line segment slope)

$\rho$  = percent reflectance

$\lambda$  = wavelength (nm)

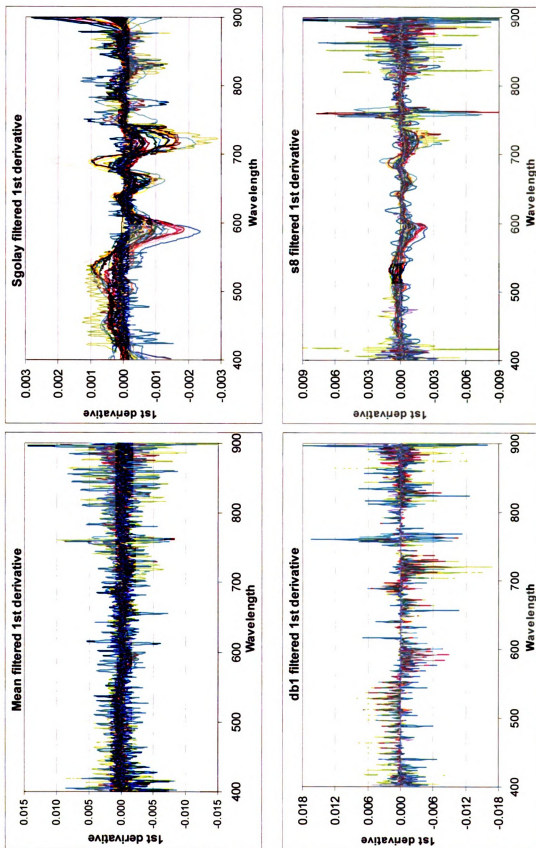


Figure 3-15 First derivatives approximation from 4 different filtrations of the volume reflectance spectra

Spectral absorption/reflectance features were revealed in the 1<sup>st</sup> derivative products, especially in Savitsky Golay filter method. These optical characteristics are related to the various constituents in the water column. For example, green reflectance of CHL between 560 nm – 620 nm and maximum red absorption of CHL near 680 nm. The derivative transformation reveals waveband regions that are most appropriate for the differentiation of the input spectra. The mean filter method did not provide useful wavebands; it was thus omitted from further consideration.

The 2<sup>nd</sup> derivative approximations are calculated using Eq 3-9 to investigate whether more pattern or information can be extracted (Figure 3-16). An expansion multiplier (0.5) was incorporated in the denominator as this was found to enhance the differences in reflectance amplitude (Becker et al., 2005).

$$d^{2nd} = (d^{1st}_{n+1} - d^{1st}_n) / 0.5 (\lambda_{n+2} - \lambda_n) \quad (\text{Eq 3-9})$$

where:

n = band number

d<sup>1st</sup> = 1<sup>st</sup> derivative

d<sup>2nd</sup> = 2<sup>nd</sup> derivative approximation

λ = wavelength (nm)

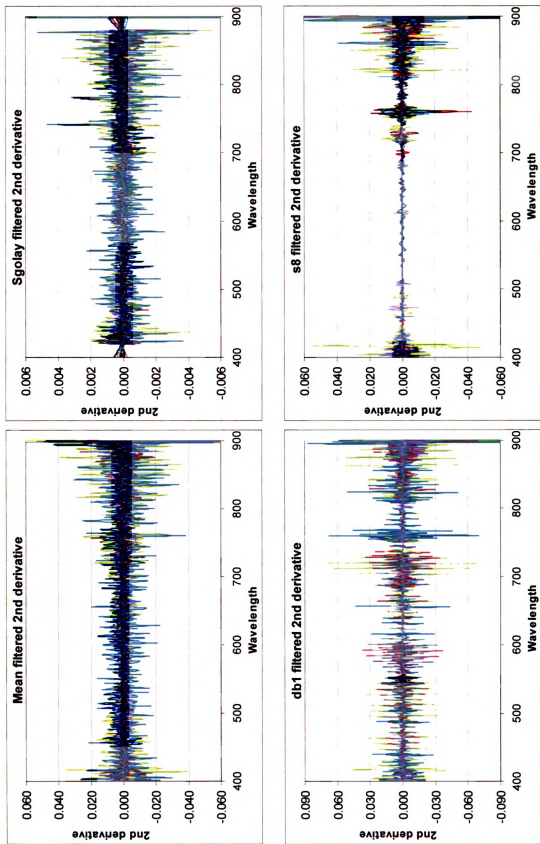


Figure 3-16 Second derivatives approximation from 4 different filtrations of the volume reflectance spectra

Second derivatives did not provide much information compared to the first derivative because no additional clear absorption or reflectance features could be extracted. Therefore, only the 1<sup>st</sup> derivatives will be used in further analyses.

### **3.4.7 Region-Waveband**

Region-wavebands were determined based on the observed features in derivative curves and the reviewed literature (Table 3-5, Figure 3-17). Previous studies indicate single spectral bands that were successfully used to explain water quality variables. None of the studies developed water quality indicators based on a region-waveband. In this study, region-wavebands were indicated using narrow band locations from the reviewed researches as a guideline. The first-order derivatives from filtered volume reflectance spectra were used as a primary source in the waveband determination. Spectral features were obviously showed in Figure 3-17. These features indicate waveband regions that are most sensitive to changes in biophysical variables. Reviewed researches provided the information to associate each spectral region to its optical properties (Table 3-5). These wavebands were used to develop spectral indices for water quality in the next step. Lakes that have high and low trophic conditions have different optical properties. To insure the ability to differentiate the same biophysical characteristic but different lake trophic condition, some of the region-wavebands were overlapped.

Table 3-5 Selected waveband regions for water quality assessment

<b>Sgolay</b>	<b>db1</b>	<b>s8</b>	<b>Biophysical characteristics</b>
A:435-475	A:435-485	A:435-475	BLUE absorption
B:470-570	B:480-575	B:490-570	GREEN reflectance
C:565-620	C:550-630	C:560-610	GR/RED edge
D:670-690	D:670-700	D:660-700	RED max chl <i>a</i> absorption for Low trophic lake
E:675-700		E:660-705	RED max chl <i>a</i> absorption for High trophic lake
F:690-740	F:690-745	F:690-740	NIR peak for Low trophic lake
G:700-740	G:700-745	G:700-740	NIR peak for High trophic lake

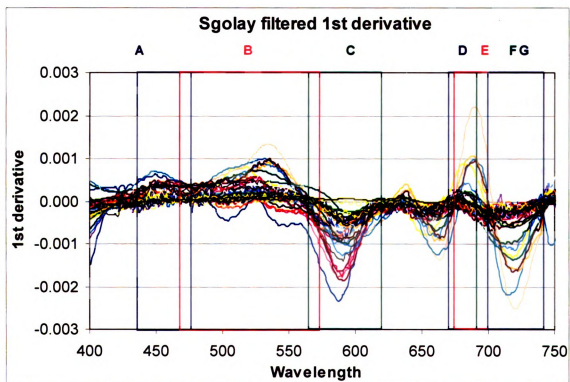
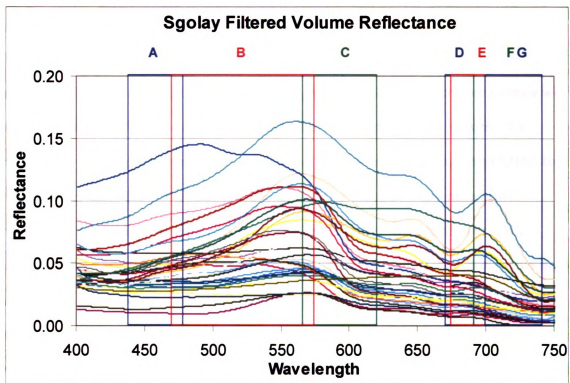


Figure 3-17 Example of region-waveband selection on Sgoly method

### **3.4.8 Area Under Spectral Curve Indicator**

First, derivative curves for each filter method are separated into region-wavebands (Table 3-5). Figure 3-17 displays spectral and derivative curves with continuous lines, but the data are in fact the series of discrete points. To extract the area under the curve, a 2<sup>nd</sup> order polynomial function was fitted to these data points for each lake (Figure 3-18). To calculate the area that represents relative inherent constituents (e.g., smaller area for lower CHL concentration and larger area for higher CHL concentration), the derivative data need to be adjusted such that all the data points fall above zero (for absorption curves) or below zero (for reflectance curves). For the absorption curves, the minimum value within the region was added to all data within the region. For reflectance curves, the maximum value was added to the rest of the data within the same region. Appendix D shows the area index for the three filters.

Daubechies wavelet created a staircase artifact in the filtered signals, which produce a large number of zero values in the 1<sup>st</sup> derivative product. Fitting a polynomial function to data that has numerous zero values weighs the curve down near zero. Db1 curve fitting was adjusted to eliminating all the zero values from the function in order to minimize the artifact of this filter method.

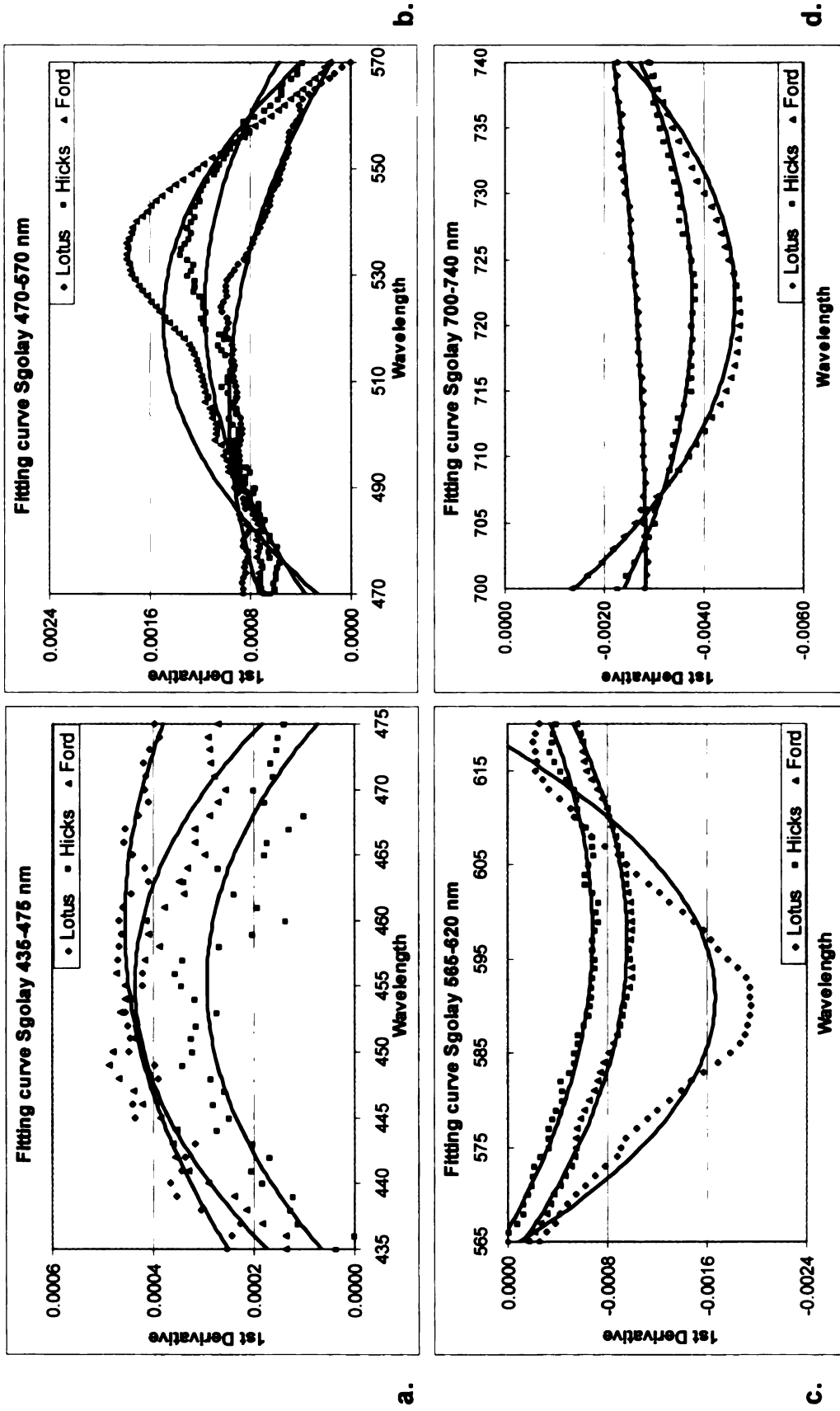


Figure 3-18 Examples of curve fitting on 1<sup>st</sup> derivative data. Graph (a) and (b) represent absorption curves, and (c) and (d) represent reflectance curves

### 3.4.9 Spectral Curve Height/Width Ratio Indicator

Maximum height of the same polynomial fitting function measured from  $y = 0$  was determined for each lake and each filter (Appendix E). The width used in calculation of height/width ratio is basically the width of the region-waveband (Figure 3-19).

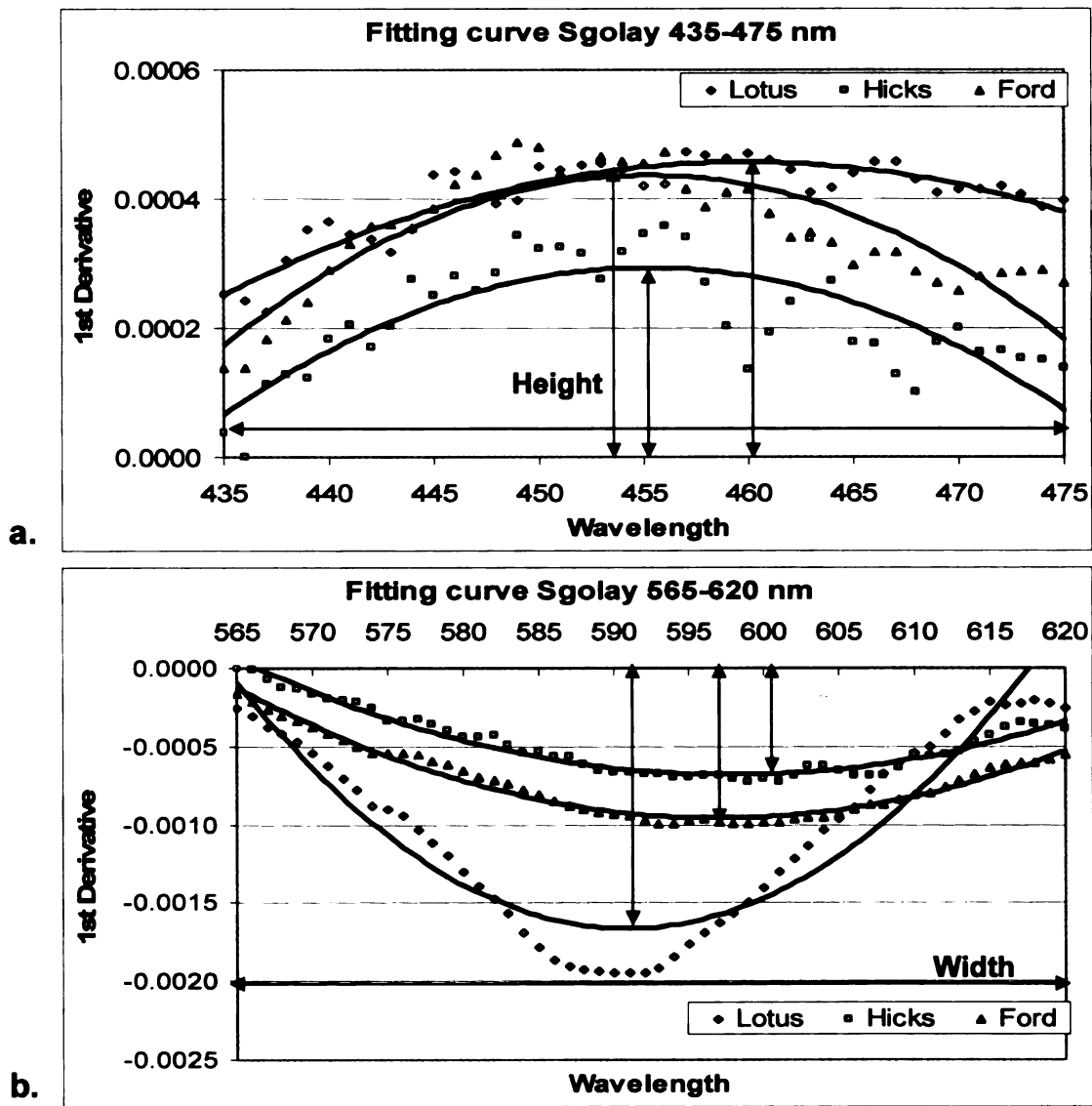


Figure 3-19 Examples of height and width measurements

### **3.4.10 Spectral Band Ratio Technique**

Band ratios have been most used extensively in the analyses of broadband sensors such as Landsat Multispectral Scanner (MSS), Thematic Mapper (TM), and Systeme Pour l'Observation de la Terre (SPOT). Ratios can also be used for the analysis of data from two major classes of absorption: visible to near-infrared absorptions such as the spectral characteristics of chlorophyll *a* and other photosynthetic pigments. Ratio indices, created by dividing one spectral channel by another, are widely used in biophysical investigations. The method has been used to enhance the discrimination of surface spectral characteristics. Band rationing can be very effective spectral analysis tools when applied with a well-formulated rationale and spectroscopic basis. The major advantages of the ratio indexes are that effects of bi-directional reflectance are removed and the relative color properties of substances are enhanced (Rencz, 1999). Common to spectroscopic tools, the data must be corrected for the system contribution (e.g., dark current) or environmental signal (e.g., atmospheric path radiance) that is additive to the measured radiance. These additive noises contribute significantly to errors in the results (Rencz, 1999).

Spectral features that are strong in biophysical characteristics (e.g., the green peak and red edge in chlorophyll spectra) can be used with band ratios to rapidly detect areas with these properties and therefore can be effective for environmental monitoring (Rencz, 1999). PCA and spectral derivative techniques were used to determine the optimal wavebands and region-waveband that are sensitive to changes in biophysical attributes in waters. The

selected bands will be used both as the single bands alone and the ratio bands. Single-band algorithms have an advantage of simplicity but multi-band algorithm has an advantage in that they can be applied in situations where the target is not evenly illuminated. Therefore, multi-band variables can be used in a wide range of circumstance (George and Malthus, 2001).

Ratios were calculated for both area and height/width region-waveband (e.g., A/B, A/C, A/D, ..., G/D, G/E, GF). The narrow-wavebands were originally selected by PCA. It was observed that these bands were closest to the lower edge wavelengths of the region-wavebands (e.g., 435 nm, 470 nm, 480 nm, 490 nm, 550 nm, 560 nm, 565 nm, 660 nm, 670 nm, 675 nm, 690 nm, and 700 nm). Therefore, narrow-wavebands (1-nm) from the lower edges of region wavebands were selected for the narrow-waveband indicators in addition (Appendix F). Ratios were calculated for all narrow-wavebands.

#### **3.4.11 Development of New Spectral Indicators for Water Quality**

The relationship between the spectral indicators (e.g., area, height/width, and narrow-waveband) and the water quality indicators (e.g., SD, CHL, TSS, NPOC, diatom, green and bluegreen algae) measured at the same sites was determined. Multiple regression methods were used to test the correlation of water quality observations and spectral data both with the region-waveband, and narrow-waveband and their multi-band ratio. The water quality parameters and corresponding ASD spectral indicators from 34 lake data set were used to develop the models and determine the empirical coefficients for SD, CHL, TSS,

NPOC, diatom, green, and bluegreen algae algorithms. Stepwise regression was first performed on all variables to investigate all possible combinations of spectral bands that potentially best explain biophysical characteristics in the water. These wavebands were then used in the determination for the final models based on their level of significance ( $P \leq 0.05$ , two-tailed analysis), correlation coefficient, distribution of residuals, tolerance value, and optical properties of the bands. The models will be validated by the 12 remaining ASD data to determine and compare the accuracy of the model to ASD sensor. The best performance models for each water quality variable will be applied to the AISA data set from the same 12 lakes to investigate an ability to expand the algorithm to an airborne hyperspectral data.

## **CHAPTER 4**

### **RESULTS AND DISCUSSION**

#### **4.1 Michigan Lake Water Quality from Field Observation**

Initial observations of water quality indicators include bar graphs, histograms and Pearson correlation matrices of the parameters (Figure 4-1 to 4-5; Table 4-1). The histograms (Figure 4-1 and 4-2) reveal that both Secchi depth (SD) and chlorophyll *a* (CHL) concentration varied widely among the sampled lakes, but some of the other biophysical parameters such as total suspended solids (TSS), non-purgable organic carbon (NPOC), diatom, green and bluegreen algae had only a few samples with high values, and the rest of the data values were low. This caused some of the variables to be non-normally distributed (Figure 4-3). Both logarithm base 10 (LOG) and natural logarithm (LN) transformations of these data were compared. Both transformations generated more normally distributed data, but the LN produced a range of values that were more appropriate to use in the regression models (Figure 4-4). Table 4-1 and Figure 4-5 demonstrated that Secchi depth (SD) had a relatively strong negative correlation with chlorophyll *a* (CHL) and total suspended solids (TSS), meaning that CHL and TSS are the major constituents that change clarity in the sample waters. The relationship between SD and CHL was stronger. SD and TSS had a relatively strong correlation with CHL and green algae, suggesting that most of the TSS was caused by algae rather than inorganic substances (e.g., silt).

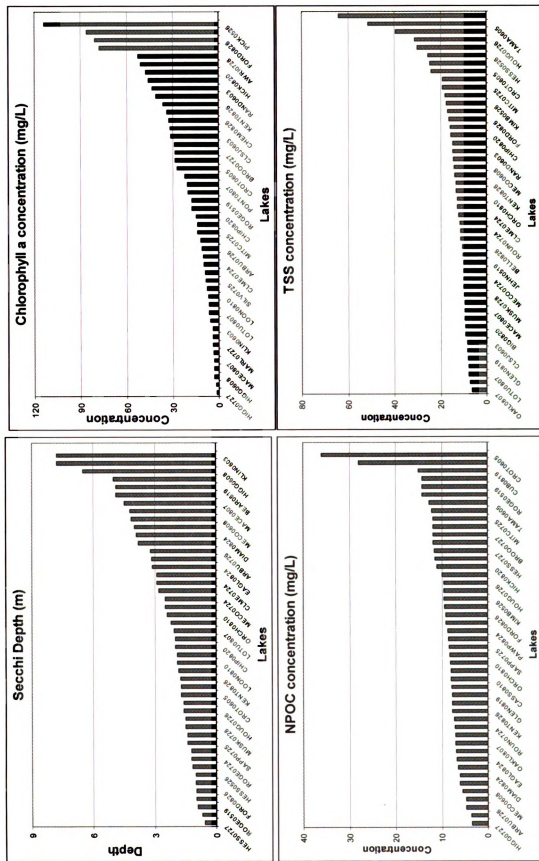


Figure 4-1 Bar graphs of SD, CHL, NPOC and TSS

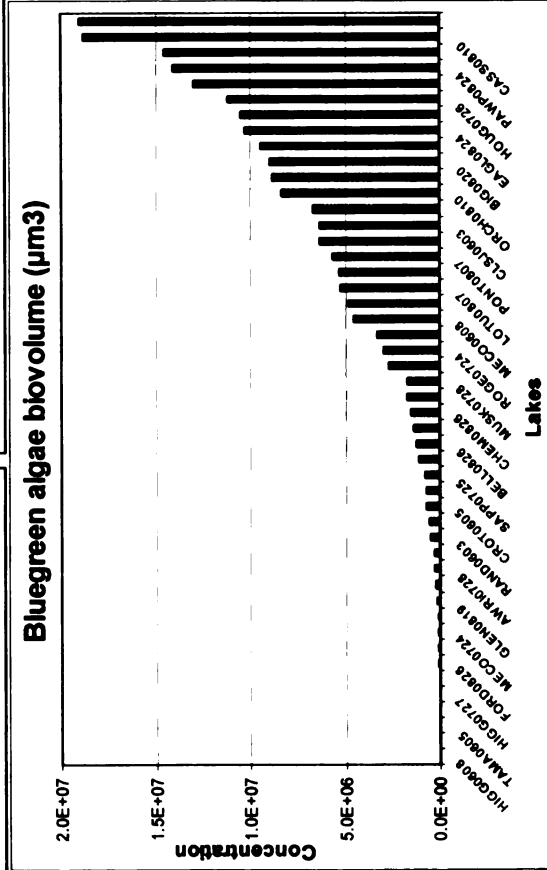
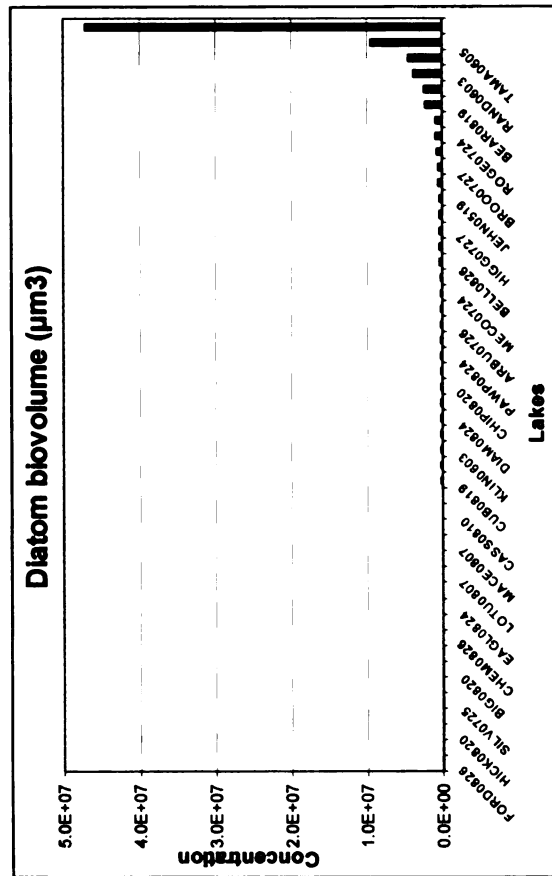
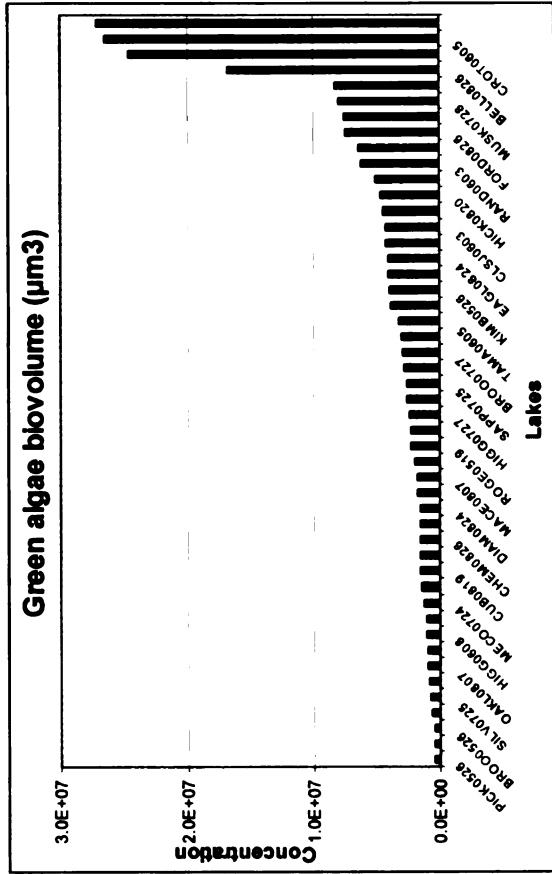


Figure 4-2 Bar graphs of diatom, green and bluegreen algae

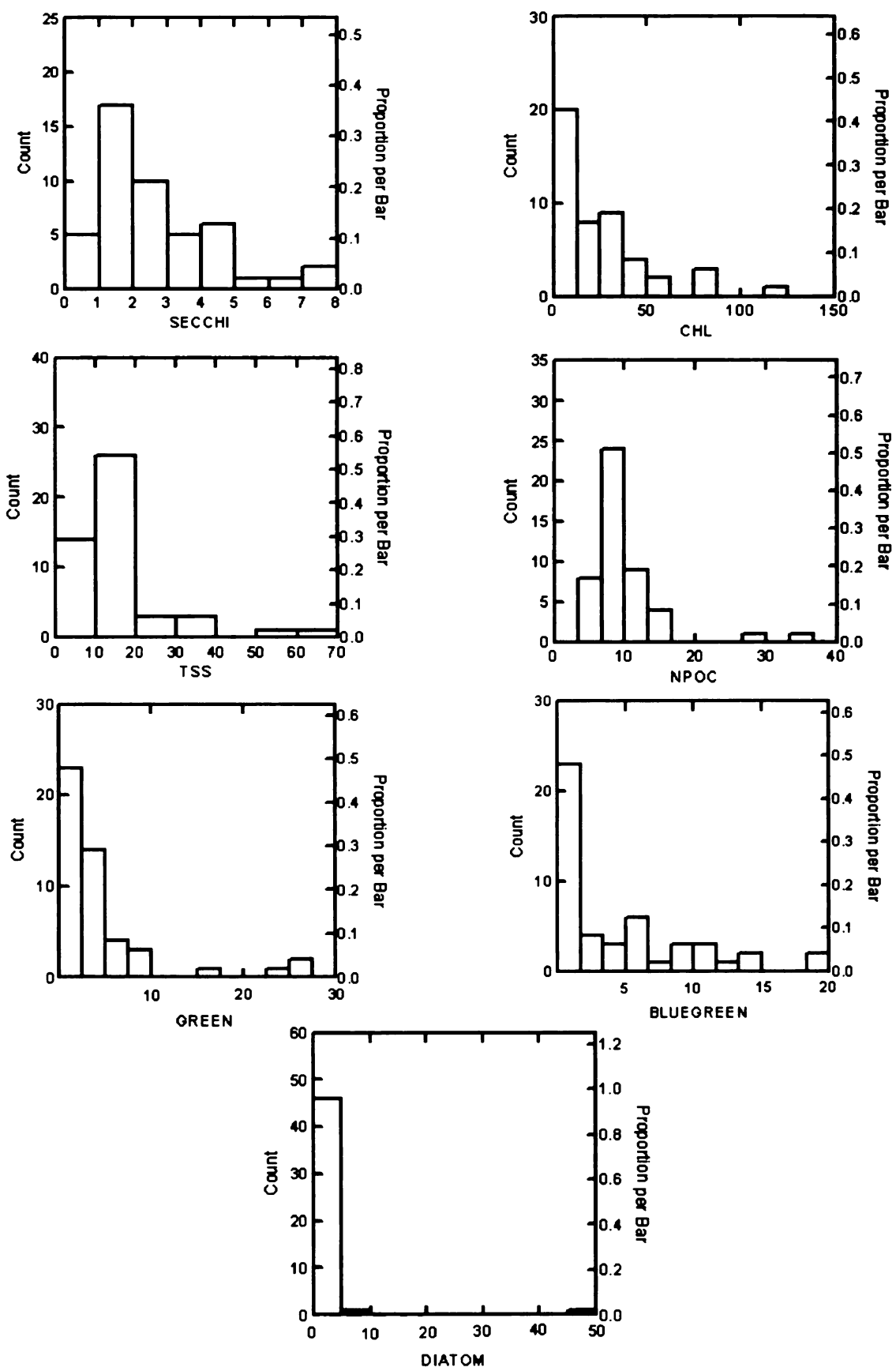


Figure 4-3 Histogram distributions of the raw water quality parameters

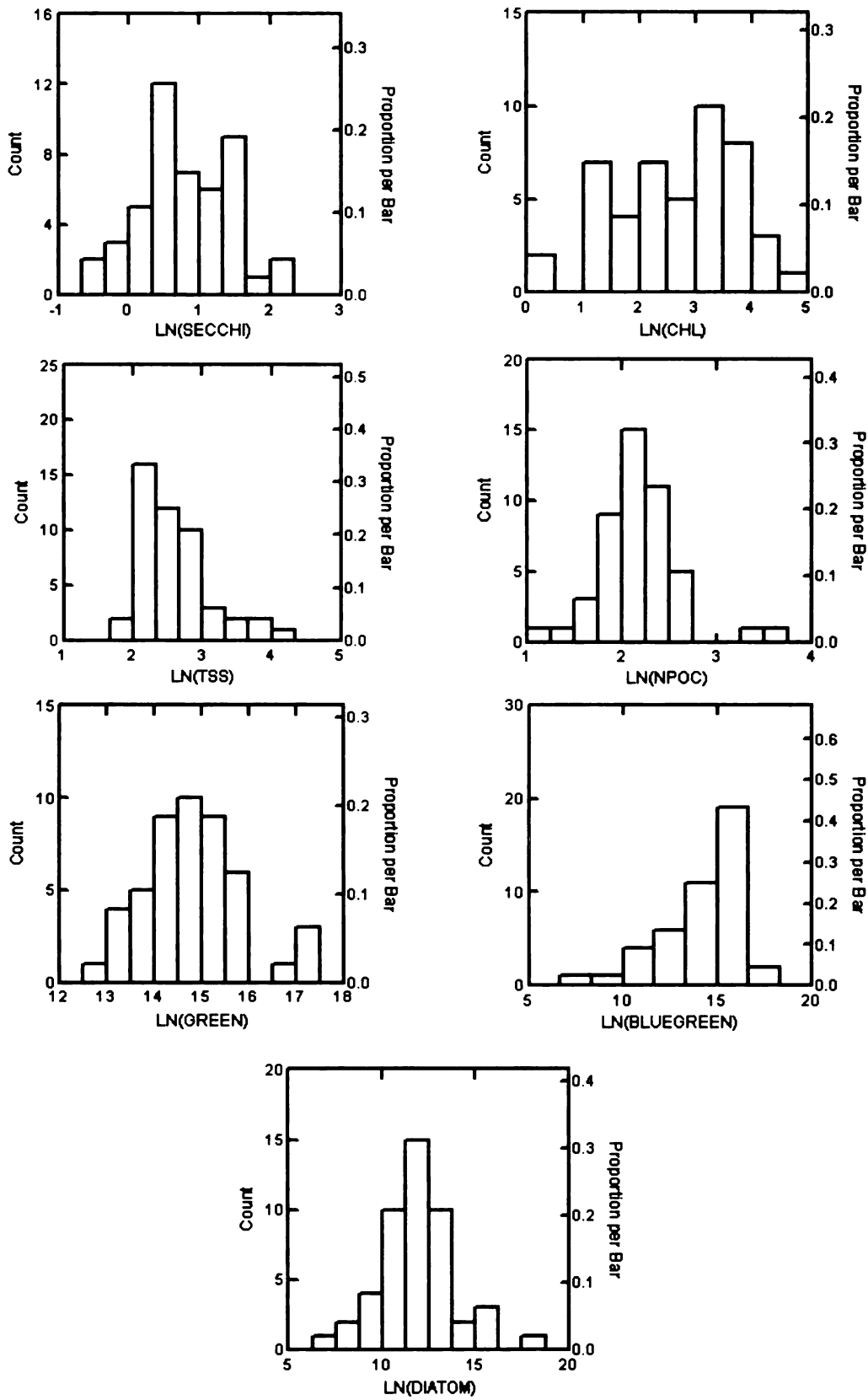


Figure 4-4 Histogram distributions of LN transformed water quality parameters

Table 4-1 Pearson correlation matrix of water quality indicators

	<b>SD</b>	<b>CHL</b>	<b>TSS</b>	<b>NPOC</b>	<b>DIATOM</b>	<b>GREEN</b>	<b>BLUEGREEN</b>
<b>SD</b>	1.000						
<b>CHL</b>	<b>-0.546</b>	1.000					
<b>TSS</b>	<b>-0.463</b>	<b>0.377</b>	1.000				
<b>NPOC</b>	-0.151	0.050	0.357	1.000			
<b>DIATOM</b>	-0.135	0.042	0.305	0.720	1.000		
<b>GREEN</b>	-0.388	<b>0.393</b>	<b>0.370</b>	0.554	0.653	1.000	
<b>BLUEGREEN</b>	-0.343	0.268	0.284	-0.069	-0.125	0.137	1.000

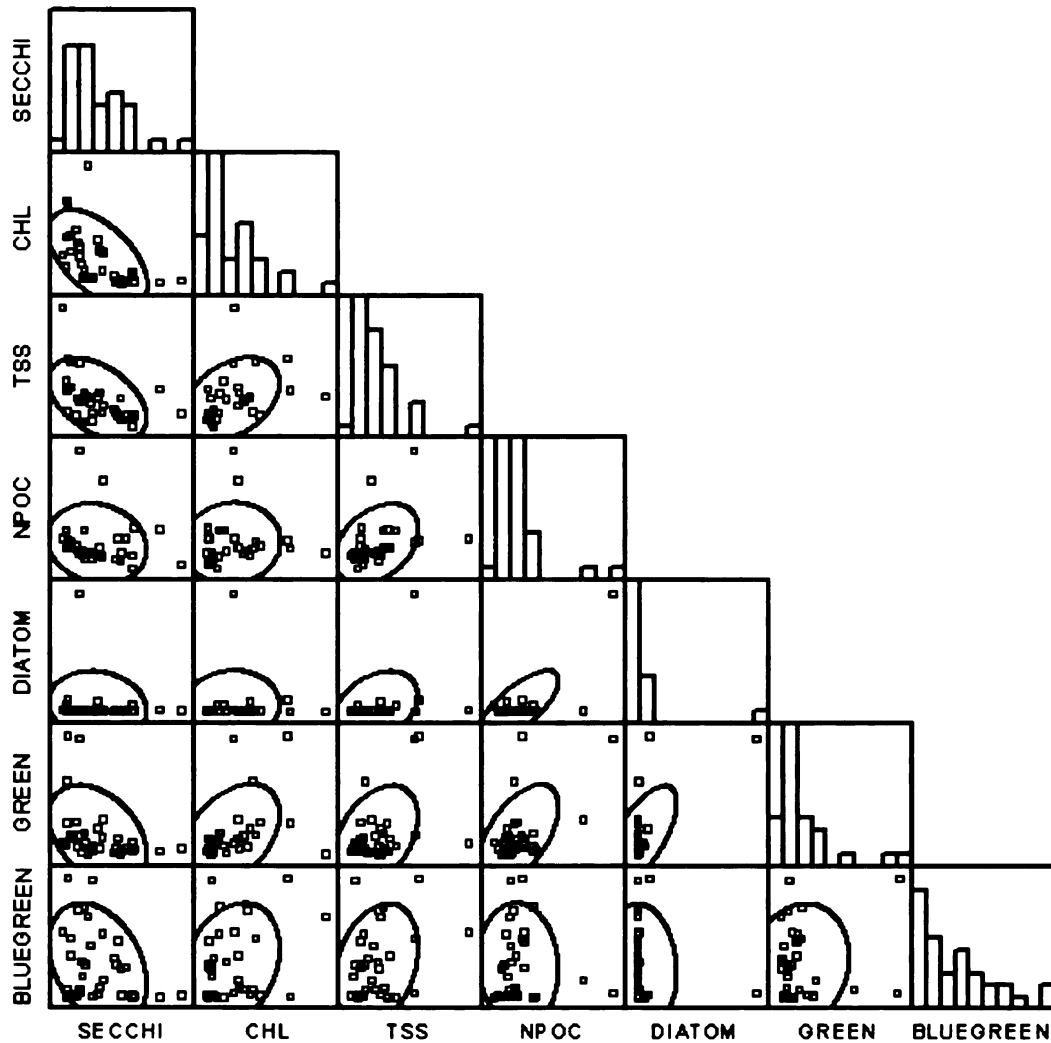


Figure 4-5 Pearson correlation graphs and histogram plots of water quality indicators

## 4.2 Optimal Spectral Bands

Two types of optimal spectral wavebands were identified, the region-wavebands and the narrow-wavebands (Tables 4-2 and 4-3). Region-wavebands were determined using the spectral derivative spectroscopy method. Important absorption and reflectance features that associated with optical water quality variables were extracted from the first derivative curves. Narrow-wavebands were determined using Principle Component Analysis together with the results from the region-waveband determination. PCA identified three principle wavebands that explained over 90 percent of variation in the 500 wavebands. One of the waveband was suspected to cause by atmospheric noise and therefore excluded from the final optimal waveband set. The wavebands at the lower edge of the region-wavebands were added to the narrow-waveband set because these wavebands represented the maximum peak or trough in water spectral signatures.

Table 4-2 Identified region-wavebands

<b>Sgolay</b>	<b>db1</b>	<b>s8</b>	<b>Biophysical characteristics</b>
A:435-475	A:435-485	A:435-475	BLUE absorption
B:470-570	B:480-575	B:490-570	GREEN reflectance
C:565-620	C:550-630	C:560-610	GR/RED edge
D:670-690	D:670-700	D:660-700	RED max chl <i>a</i> absorption for Low trophic waters
E:675-700		E:660-705	RED max chl <i>a</i> absorption for High trophic waters
F:690-740	F:690-745	F:690-740	NIR peak for Low trophic waters
G:700-740	G:700-745	G:700-740	NIR peak for High trophic waters

Table 4-3 Identified narrow-wavebands

<b>Narrow-band</b>	<b>Wavelength</b>	<b>Biophysical characteristics</b>
A	435	BLUE absorption
B	455	BLUE absorption from PCA
C	470	Beginning of GREEN reflectance
D	565	GREEN and RED edge
E	670	RED max chl <i>a</i> absorption for Low trophic waters
F	675	RED max chl <i>a</i> absorption for High trophic waters
G	690	NIR peak for Low trophic waters
H	700	NIR peak for High trophic waters

### 4.3 Spectral Indicators

Several optimum spectral indicators were developed to relate water quality variables with the spectral information of the same site. These indicators may be used to assess water quality parameters where adequate remote sensing data is available without the needs for *in situ* water samples.

#### 4.3.1 Spectral Indicators for Chlorophyll *a*

Spectral wavebands were determined using PCA and derivative methods (detailed description in Section 3.4.5 and 3.4.7) and are summarized in Tables 4-2 and 4-3. The selected wavebands from the three filter methods were regressed against LN(CHL). The final models were compared in Tables 4-4 to 4-5.

Table 4-4 Chlorophyll *a* area models using the optimal wavebands

<b>Filter</b>	<b>Band</b>	<b>Coefficient</b>	<b>Tolerance</b>	<b>P(2-tail)</b>	<b>R<sup>2</sup></b>	<b>Adjusted R<sup>2</sup></b>
<b>Sgolay</b>	AG	-1.687	0.472	0.000	0.787	<b>0.757</b>
	DG	1.509	0.175	0.028		
	FE	-0.331	0.708	0.003		
	GD	1.132	0.188	0.005		
	CONSTANT	3.234		0.003		

<b>db1</b>	AC	7.263	0.874	0.000	0.710	0.680
	AF	-3.081	0.935	0.000		
	DF	2.166	0.882	0.010		
	CONSTANT	2.160		0.064		

<b>s8</b>	AG	-3.268	0.912	0.000	0.765	0.749
	CE	-1.304	0.912	0.005		
	CONSTANT	7.352		0.000		

Table 4-5 Chlorophyll *a* height/width models using the optimal wavebands

<b>Filter</b>	<b>Band</b>	<b>Coefficient</b>	<b>Tolerance</b>	<b>P(2-tail)</b>	<b>R<sup>2</sup></b>	<b>Adjusted R<sup>2</sup></b>
<b>Sgolay</b>	HWAG	-1.930	0.800	0.000	0.718	<b>0.699</b>
	HWBD	-5.181	0.800	0.013		
	CONSTANT	5.891		0.000		

<b>db1</b>	HWCF	-4.891	0.592	0.000	0.599	0.572
	HWFB	-1.881	0.592	0.006		
	CONSTANT	10.042		0.000		

<b>s8</b>	HWAG	-2.244	0.787	0.000	0.709	0.690
	HWCD	-1.570	0.787	0.005		
	CONSTANT	6.139		0.000		

The regression models selected 2 – 4 variables out of 49 variables (7 single-bands and 42 ratio-bands). The wavebands that were selected most repeatedly are A (blue absorption) and G (NIR peak for high trophic). These two wavebands link directly to the optical characteristics of CHL as reviewed in Section 2.2. This regression result proves that the narrower region-waveband G (700 nm – 740 nm, which represents the waveband region of higher trophic lakes) correlated better to the CHL than the broader region-waveband F (690 nm – 740 nm, which represents lower trophic lakes). Bands D and E also appeared in the models, but they do not contribute as large an influence as bands A and G do (consider variable coefficients, e.g., larger positive or negative coefficient value suggested a larger influence of the variable in the model). Both band D and E represent the regions of maximum CHL absorption in the red wavelengths. They could be used to differentiate CHL in water because higher CHL should produce a deeper absorption feature (valley) in this region. It is notable that the shorter wavelength band D (670 nm – 690 nm) was selected more frequently than the longer wavelength band E (675 nm – 700 nm) in the region-waveband indices.

Table 4-6 Chlorophyll *a* narrow-waveband models using the optimal wavebands

<b>Filter</b>	<b>Band</b>	<b>Coefficient</b>	<b>Tolerance</b>	<b>P(2-tail)</b>	<b>R<sup>2</sup></b>	<b>Adjusted R<sup>2</sup></b>
<b>Sgolay</b>	A	-38.605	0.264	0.000	0.785	<b>0.754</b>
	E	42.536	0.125	0.004		
	EH	-5.108	0.367	0.000		
	GA	-1.549	0.102	0.025		
	CONSTANT	9.801		0.000		
<b>db1</b>	A	-18.323	0.649	0.011	0.709	0.679
	H	19.859	0.469	0.004		
	FG	-4.566	0.513	0.003		
	CONSTANT	7.414		0.000		
<b>s8</b>	A	-24.190	0.731	0.001	0.723	0.694
	E	17.116	0.488	0.017		
	EG	-3.598	0.605	0.000		
	CONSTANT	7.239		0.000		

The narrow-wavebands that were selected most frequently are A (435 nm, blue absorption), E (670 nm, maximum red absorption), and G (690 nm, NIR peak). Band A and G consistently performed well in the regression models for both narrow-waveband and region-waveband indicators. Band E was expected to appear to improve the prediction power of the model. It is noticed that between band G (690 nm) and H (700 nm), which both represent NIR peak of lower and higher trophic waters, band G was selected more often and had a larger influence in the models.

### 4.3.2 Spectral Indicators for Secchi Depth

Region-wavebands (area and height/width) indicators and narrow-wavebands reflectance indicators from three filter methods were regressed against LN(SD). The final models were compared in Tables 4-7 to 4-9.

Table 4-7 Secchi depth area models using the optimal wavebands

<b>Filter</b>	<b>Band</b>	<b>Coefficient</b>	<b>Tolerance</b>	<b>P(2-tail)</b>	<b>R<sup>2</sup></b>	<b>Adjusted R<sup>2</sup></b>
<b>Sgolay</b>	AB	-5.560	0.473	0.004	0.736	<b>0.700</b>
	AG	0.792	0.352	0.001		
	BF	-2.183	0.575	0.029		
	EC	-0.937	0.307	0.009		
	CONSTANT	3.955		0.012		
<b>db1</b>	BD	-0.252	0.636	0.006	0.638	0.615
	DC	-8.735	0.636	0.000		
	CONS	4.195		0.000		
<b>S8</b>	C	-36.227	0.166	0.000	0.718	0.679
	BC	-0.858	0.167	0.000		
	BE	-1.418	0.453	0.001		
	FD	1.69	0.378	0.000		
	CONSTANT	2.888		0.000		

Table 4-8 Secchi depth a height/width models using the optimal wavebands

<b>Filter</b>	<b>Band</b>	<b>Coefficient</b>	<b>Tolerance</b>	<b>P(2-tail)</b>	<b>R<sup>2</sup></b>	<b>Adjusted R<sup>2</sup></b>
<b>Sgolay</b>	HWC	-47.187	0.356	0.000	0.781	<b>0.759</b>
	HWBA	-1.742	0.426	0.000		
	HWGC	-0.597	0.762	0.000		
	CONSTANT	4.559		0.000		
<b>db1</b>	HWBC	-7.035	0.108	0.000	0.596	0.570
	HWCB	-1.912	0.108	0.027		
	CONSTANT	9.084		0.001		
<b>s8</b>	HWC	-23.473	0.249	0.049	0.741	0.716
	HWAG	0.909	0.537	0.001		
	HWBC	-1.297	0.182	0.002		
	CONSTANT	1.465		0.078		

The wavebands that were selected most repeatedly are band B (green reflectance) and C (green and red edge). These two wavebands together covered the entire green reflectance peak, which is the range that has the highest variation in reflectance (Figure 4-6). Savitsky Golay models produced the higher R<sup>2</sup> for both area and height/width methods, suggesting that 70 percent of the SD can be explained by the spectral indicators. Band A (blue absorption) also appeared in Sgolay and s8 models. This band can measure clarity of the water because it could penetrate deeper than other band regions (Figure 4-6). SD mostly related to overall reflectance of all particles suspended in the water column. Unlike CHL, SD does not need detail absorption/reflectance features to detect the differences among lakes.

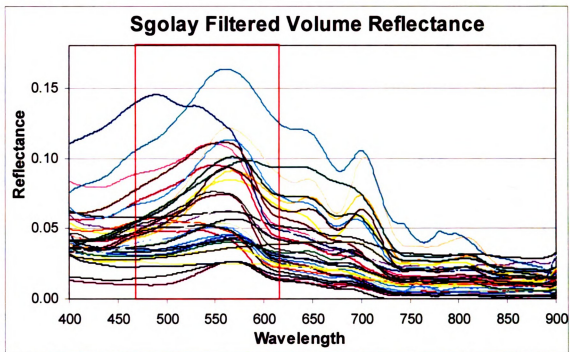


Figure 4-6 Volume reflectance curves

When looking at the volume reflectance within the waveband B and C regions, it was observed that the spectral signatures did not arrange from low SD to high SD (Figure 4-7). However, the 1<sup>st</sup> derivative curves shows a clear pattern of SD arranged from low to high (Figure 4-8). Derivative processes in this algorithm improve the ability to relate remote sensing spectra to water quality parameters.

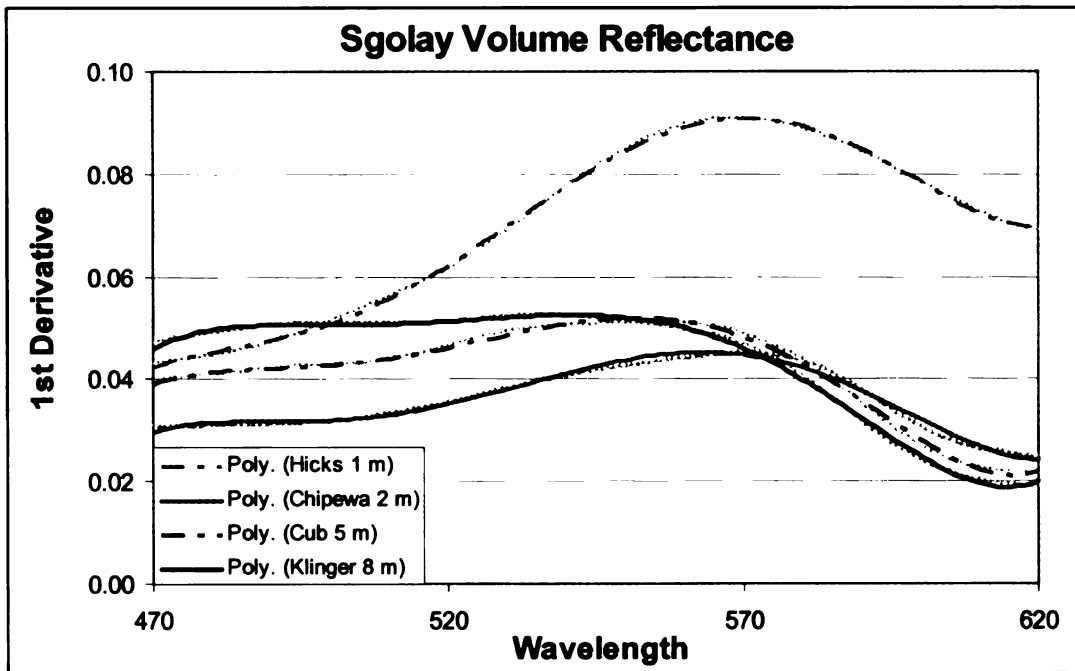


Figure 4-7 Examples of volume reflectance curves on different SD in B and C waveband regions

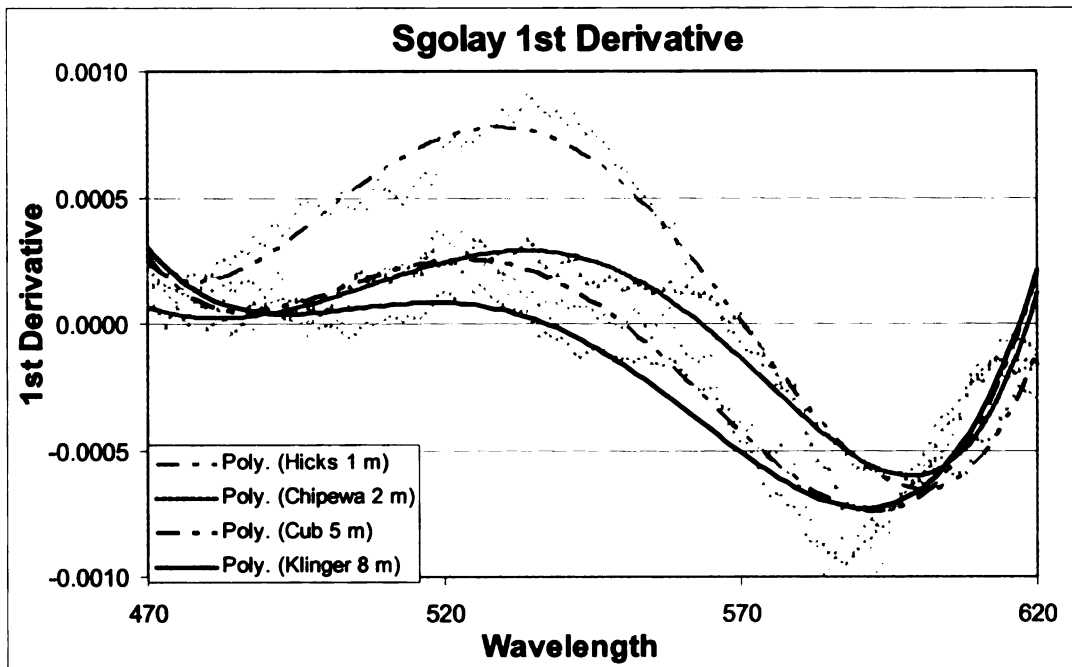


Figure 4-8 Examples of fitting curves on different SD in B and C waveband regions

Table 4-9 SD narrow-waveband models using the optimal wavebands

<b>Filter</b>	<b>Band</b>	<b>Coefficient</b>	<b>Tolerance</b>	<b>P(2-tail)</b>	<b>R<sup>2</sup></b>	<b>Adjusted R<sup>2</sup></b>
<b>Sgolay</b>	A	-7.1088	0.737	0.020	0.796	0.768
	DA	1.1003	0.115	0.001		
	DC	-1.8842	0.102	0.000		
	GC	-1.0169	0.583	0.000		
	CONSTANT	2.871		0.000		

<b>db1</b>	E	-11.875	0.289	0.000	0.877	<b>0.855</b>
	BA	6.929	0.386	0.000		
	ED	-0.791	0.558	0.000		
	GD	-1.36	0.291	0.000		
	GH	-2.212	0.258	0.004		
	CONSTANT	-1.115		0.304		

<b>s8</b>	D	-10.0724	0.387	0.000	0.865	0.841
	AB	-8.5365	0.313	0.000		
	BD	0.8514	0.439	0.017		
	DE	-0.2994	0.192	0.011		
	EC	-1.7623	0.159	0.000		
	CONSTANT	11.172		0.000		

The R<sup>2</sup> are very high for all narrow-waveband SD models. Similar to the region wavebands models, the narrow-waveband models also have band A (435 nm). Narrow-waveband models tend to select band G (690 nm, NIR peak for lower trophic waters) over band H (700 nm, NIR peak for higher trophic waters).

### 4.3.3 Spectral Indicators for TSS

Region-wavebands (area and height/width) indices and narrow-wavebands volume reflectance indicators from three filter methods were regressed against LN(TSS). The final models for TSS were compared in Tables 4-10 to 4-12.

Table 4-10 TSS area models using the optimal wavebands

Filter	Band	Coefficient	Tolerance	P(2-tail)	R <sup>2</sup>	Adjusted R <sup>2</sup>
<b>Sgolay</b>	DA	0.420	0.878	0.019	0.351	<b>0.286</b>
	ED	1.088	0.983	0.017		
	GE	0.295	0.870	0.047		
	CONSTANT	0.405		0.498		

<b>db1</b>	DC	3.171	1.000	0.001	0.286	0.264
	CONSTANT	1.748		0.000		

<b>s8</b>	EC	0.179	0.996	0.037	0.283	0.237
	GF	2.344	0.996	0.015		
	CONSTANT	1.375		0.000		

Table 4-11 TSS height/width models using the optimal wavebands

Filter	Band	Coefficient	Tolerance	P(2-tail)	R <sup>2</sup>	Adjusted R <sup>2</sup>
<b>Sgolay</b>	HWGC	0.213	1.000	0.004	0.231	0.207
	CONSTANT	2.273		0.000		

<b>db1</b>	HWEC	0.599	1.000	0.009	0.197	0.172
	CONSTANT	1.262		0.010		

<b>s8</b>	HWB	39.605	0.977	0.022	0.267	<b>0.220</b>
	HWCA	-0.874	0.977	0.012		
	CONSTANT	2.288		0.000		

Table 4-12 TSS narrow-waveband models using the optimal wavebands

Filter	Band	Coefficient	Tolerance	P(2-tail)	R <sup>2</sup>	Adjusted R <sup>2</sup>
<b>Sgolay</b>	FH	-1.224	1.000	0.000	0.346	0.326
	CONSTANT	3.876		0.000		
<b>db1</b>	FH	-1.073	1.000	0.001	0.318	0.296
	CONSTANT	3.737		0.000		
<b>s8</b>	E	8.3417	0.344	0.034	0.532	<b>0.468</b>
	BC	3.1053	0.444	0.002		
	DF	0.2785	0.213	0.015		
	EC	1.034	0.264	0.001		
	CONSTANT	-1.9603		0.102		

TSS models have low R<sup>2</sup> overall. Wavelet s8 produces better models in some cases but the reported R<sup>2</sup> are not much higher than Sgolay method. Several waveband regions were selected in the models including band D, E and C. These are the band range (565 nm – 700 nm) that varied the most when suspended sediments were added to the water (Figure 2-9).

The narrow-waveband models selected band F (675 nm) and H (700 nm). These are the maximum CHL absorption band and NIR peak band, which have been used extensively in vegetation indices. The combination of these two bands should indicate CHL. It is possible that these wavebands were selected because most of the TSS in the data set may be dominated by algal biomass, which also refers to CHL. TSS and CHL concentration distributions are actually look alike (Figure 4-1). However, correlation coefficients of TSS models are not as high as CHL. This may be because TSS lab analysis used the simple mass

measurement, which could encounter high error when TSS concentration is low. On the other hand, CHL analysis uses equipment that is very sensitive to CHL concentration.

#### 4.3.4 Spectral Indicators for NPOC

The final models for NPOC were compared in Tables 4-13 to 4-15.

Table 4-13 NPOC area models using the optimal wavebands

<b>Filter</b>	<b>Band</b>	<b>Coefficient</b>	<b>Tolerance</b>	<b>P(2-tail)</b>	<b>R<sup>2</sup></b>	<b>Adjusted R<sup>2</sup></b>
<b>Sgolay</b>	EC*	0.485	1.000	0.052	0.116	0.087
	CONSTANT	1.882		0.000		
<b>db1</b>	EA*	0.262	1.000	0.076	0.098	0.069
	CONSTANT	1.514		0.001		
<b>s8</b>	EC*	0.194	1.000	0.067	0.104	0.075
	CONSTANT	1.843		0.000		

\*Insignificant variable

Table 4-14 NPOC height/width models using the optimal wavebands

<b>Filter</b>	<b>Band</b>	<b>Coefficient</b>	<b>Tolerance</b>	<b>P(2-tail)</b>	<b>R<sup>2</sup></b>	<b>Adjusted R<sup>2</sup></b>
<b>Sgolay</b>	HWEC	0.100	1.000	0.037	0.133	0.105
	CONSTANT	1.902		0.000		
<b>db1</b>	HWEC	0.602	1.000	0.020	0.164	<b>0.137</b>
	CONSTANT	0.945		0.082		
<b>s8</b>	HWAC*	0.177	1.000	0.053	0.115	0.087
	CONSTANT	1.848		0.000		

\*Insignificant variable

Table 4-15 NPOC narrow-waveband models using the optimal wavebands

<b>Filter</b>	<b>Band</b>	<b>Coefficient</b>	<b>Tolerance</b>	<b>P(2-tail)</b>	<b>R<sup>2</sup></b>	<b>Adjusted R<sup>2</sup></b>
<b>Sgolay</b>	CH*	-0.0872	1.000	0.121	0.076	0.046
	CONSTANT	2.4076		0.000		
<b>db1</b>	DF*	-0.1206	1.000	0.124	0.075	0.045
	CONSTANT	2.4426		0.000		
<b>s8</b>	CE*	-0.1243	1.000	0.103	0.084	0.054
	CONSTANT	2.4441		0.000		

\*Insignificant variable

Most of the NPOC models are not valid and one that is valid has a very low R<sup>2</sup> because there are very few high NPOC lakes in the data set. Although the model was performed on LN(NPOC), which helped transformed the highly skewed data to a normally distributed data set, a wide range of NPOC data was lacking in the regression model development. Another reason could be that NPOC absorb incident light so much that the measured spectral signature of the two high NPOC lakes was so low and no spectral feature could be extracted from them. Figure 4-9 compared spectral signature of the highest NPOC Croton dam pond with the two other similar water condition lakes but lower NPOC.

It was almost consistent that band E and C have been selected very often, both in significant and insignificant models. NPOC absorb light significantly in shorter wavelengths; therefore, the useful wavebands (if there is one) should be located in longer wavelengths, such as band D to G (Figure 2-7 and 2-10).

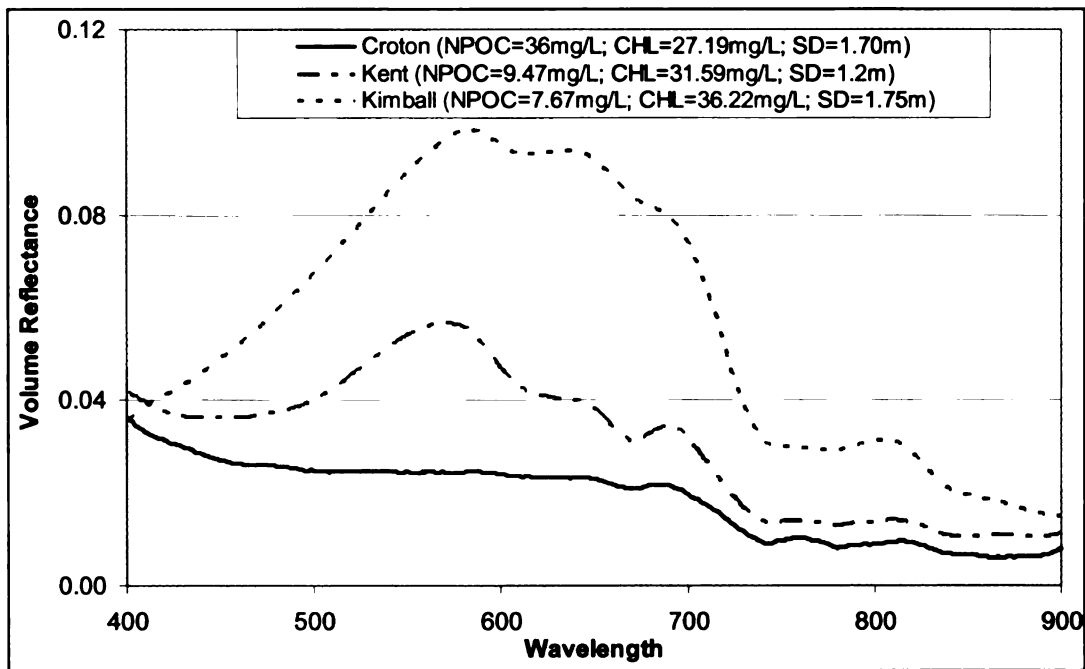


Figure 4-9 Comparison between high NPOC lake (Croton dam pond) and other lakes with similar water condition but lower NPOC

#### 4.3.5 Spectral Indicators for Diatom

Region-wavebands (area and height/width) indices and narrow-wavebands volume reflectance indices from three filter methods were regressed against LN(DIATOM), LN(GREEN) and LN(BLUEGREEN). The final models for diatom were compared in Tables 4-16 to 4-18.

Table 4-16 Diatom area models using the optimal wavebands

<b>Filter</b>	<b>Band</b>	<b>Coefficient</b>	<b>Tolerance</b>	<b>P(2-tail)</b>	<b>R<sup>2</sup></b>	<b>Adjusted R<sup>2</sup></b>
<b>Sgolay</b>	AD	2.670	0.322	0.048	0.280	<b>0.208</b>
	DC	10.127	0.186	0.003		
	GC	-3.522	0.345	0.004		
	CONSTANT	5.638		0.030		

<b>db1</b>	BD	-0.67	0.904	0.069	0.289	0.190
	CA*	-4.16	0.125	0.087		
	FA	3.852	0.148	0.020		
	GC	-17.065	0.336	0.022		
	CONSTANT	20.061		0.000		

<b>s8</b>	BA	-3.555	0.633	0.021	0.160	0.106
	CG*	-1.828	0.633	0.113		
	CONSTANT	19.298		0.000		

\*Insignificant variable

Table 4-17 Diatom height/width models using the optimal wavebands

<b>Filter</b>	<b>Band</b>	<b>Coefficient</b>	<b>Tolerance</b>	<b>P(2-tail)</b>	<b>R<sup>2</sup></b>	<b>Adjusted R<sup>2</sup></b>
<b>Sgolay</b>	HWEC	0.752	0.617	0.005	0.264	<b>0.216</b>
	HWGA	-1.729	0.617	0.005		
	CONSTANT	11.663		0.000		

<b>db1</b>	HWD	-26.578	0.230	0.011	0.203	0.151
	HWED	-12.835	0.230	0.011		
	CONSTANT	27.574		0.000		

<b>s8</b>	HWAC*	0.733	1.000	0.085	0.090	0.062
	CONSTANT	10.126		0.000		

\*Insignificant variable

Table 4-18 Diatom narrow-waveband models using the optimal wavebands

<b>Filter</b>	<b>Band</b>	<b>Coefficient</b>	<b>Tolerance</b>	<b>P(2-tail)</b>	<b>R<sup>2</sup></b>	<b>Adjusted R<sup>2</sup></b>
<b>Sgolay</b>	AD	4.718	1.000	0.004	0.230	<b>0.206</b>
	CONSTANT	8.474		0.000		
<b>db1</b>	FG	-20.348	0.177	0.006	0.248	0.200
	HF	-12.028	0.177	0.003		
	CONSTANT	43.596		0.000		
<b>s8</b>	AC	7.654	1.000	0.006	0.212	0.187
	CONSTANT	5.059		0.034		

There were only a few diatom dominated lakes in the data set. Almost all of these few lakes that had high diatom biomass also had high green algae biomass. Therefore, the diatom dominated signatures to use in the model development was lacking. The R<sup>2</sup> of all models were low; however, Sgolay produced better models than other methods in every case. Significance of the models was determined based on *P* value ( $P \leq 0.5$ ; two-tailed test). When *P* value of a variable was higher than 0.5, the model was considered invalid and the variable that was most insignificant was eliminated from the regression analyses. The regression model was performed again based on the remaining variables. In some cases, other variables became significant after the first variable was removed and the model became significant. Otherwise, the variable that had the next highest insignificant *P* value was removed and the regression model was performed again until all remaining variables produced a significant valid model.

The region wavebands that were selected repeatedly were D (maximum chlorophyll absorption in red) and C (green and red edge). Waveband C (565 nm – 620 nm) could represent the general CHL curve, which is the major pigment of all algae. According to Figure 2-11, The diatom spectral signature has the prominent trough around 670 nm – 690 nm, which is the region waveband D. The height/width model did not have band D, but it had band E which was very similar (675 nm – 700 nm). Other bands that were selected, band A and G, were the bands that were found to be the indicators of CHL.

The narrow-waveband models selected waveband in different region. According to Figure 2-11, band D (565 nm) selected by Sgolay method was the distinctive but very small valley appeared in diatom curve. This trough would be difficult to identify the region waveband indicators. Wavelet db1 method did selected band F (675 nm), which is the exact same prominent trough that showed in the region waveband models. However, Sgolay produced a slightly better result, therefore, it was used in validation process.

#### **4.3.6 Spectral Indicators for Green Algae**

Examples of green algal dominated lakes are shown in Figure 4-10, and the final models for green algae were compared in Tables 4-19 to 4-21.

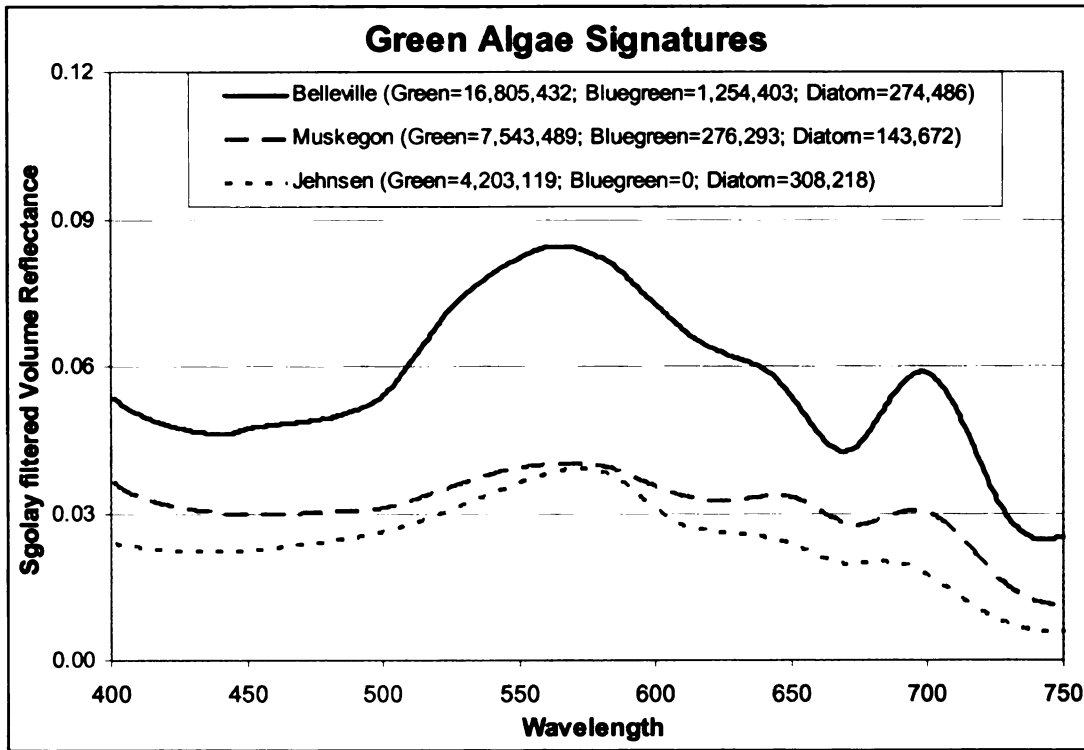


Figure 4-10 Examples of volume reflectance of green algal dominated waters

Table 4-19 Green algae area models using the optimal wavebands

Filter	Band	Coefficient	Tolerance	P(2-tail)	R <sup>2</sup>	Adjusted R <sup>2</sup>
<b>Sgolay</b>	AD	1.642	0.190	0.047	0.328	<b>0.285</b>
	EA	2.266	0.190	0.002		
	CONSTANT	9.847		0.000		
<b>db1</b>	DA	2.734	1.000	0.008	0.203	0.178
	CONSTANT	13.071		0.000		
<b>s8</b>	B*	-39.786	0.171	0.081	0.231	0.154
	AB	-6.883	0.167	0.019		
	GB	7.548	0.423	0.016		
	CONSTANT	19.238		0.000		

\*Insignificant variable

Table 4-20 Green algae height/width models using the optimal wavebands

<b>Filter</b>	<b>Band</b>	<b>Coefficient</b>	<b>Tolerance</b>	<b>P(2-tail)</b>	<b>R<sup>2</sup></b>	<b>Adjusted R<sup>2</sup></b>
<b>Sgolay</b>	HWEA	0.375	1.000	0.006	0.217	<b>0.192</b>
	CONSTANT	13.343		0.000		

<b>db1</b>	HWAF*	-1.267	1.000	0.064	0.103	0.075
	CONSTANT	16.098		0.000		

<b>s8</b>	HWAF	-4.772	1.000	0.013	0.177	0.151
	CONSTANT	17.84		0.000		

\*Insignificant variable

Table 4-21 Green algae narrow-waveband models using the optimal wavebands

<b>Filter</b>	<b>Band</b>	<b>Coefficient</b>	<b>Tolerance</b>	<b>P(2-tail)</b>	<b>R<sup>2</sup></b>	<b>Adjusted R<sup>2</sup></b>
<b>Sgolay</b>	A	-28.2	0.384	0.022	0.372	0.309
	D	34.403	0.210	0.001		
	AB	14.341	0.406	0.000		
	CONSTANT	-0.01		0.998		

<b>db1</b>	BA	-9.489	0.738	0.002	0.421	<b>0.363</b>
	BC	-78.591	0.740	0.006		
	GF	4.002	0.985	0.002		
	CONSTANT	99.102		0.001		

<b>s8</b>	A	-28.015	0.377	0.021	0.429	0.350
	H	56.429	0.142	0.001		
	AC	3.854	0.758	0.007		
	EA	-2.113	0.156	0.013		
	CONSTANT	12.596		0.000		

Area and narrow-waveband models tend to perform better than the height/width model for green algae. All the models produce relatively low  $R^2$ ; therefore, they could not be compared with a high confidence but it is observed that height/width may not be as sensitive indicator to green algae as area does. Due to the 2<sup>nd</sup> order polynomial fitting method, lakes with different algal biomass may produce fitting curves with different area but the same height. Figure 4-11 demonstrated how height may be less sensitive to changes in biophysical parameters than area.

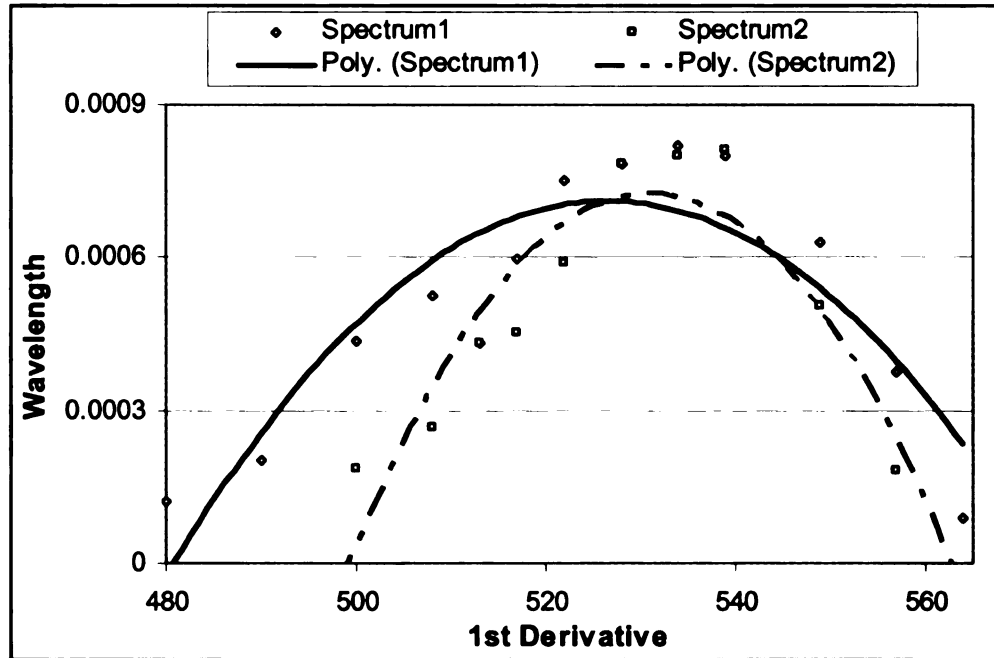


Figure 4-11 Examples of spectra that produce the same height but different under curve area

Although Sgolay did not produce the best models in every case, it was selected as the method to validate because it produced better results overall. Different filters to use for the same water quality parameter cause a difficulty in implementation.

The region-waveband that was selected most repeatedly was band A (blue absorption). Either or both band D and E (the maximum CHL absorption bands) were also appeared in every model. These wavebands are the indicators of chlorophyll pigment, which is the major component in green algae.

The narrow-waveband models selected band A (435 nm) and B (455 nm) most often. Both region-waveband and narrow-waveband model selected band A, which is the blue absorption. This band may be a good indicator of green algae.

#### 4.3.7 Spectral Indicators for Bluegreen Algae

Examples of bluegreen algal dominated lakes is showed in Figure 4-12, and the final models for bluegreen algae were compared in Tables 4-22 to 4-24.

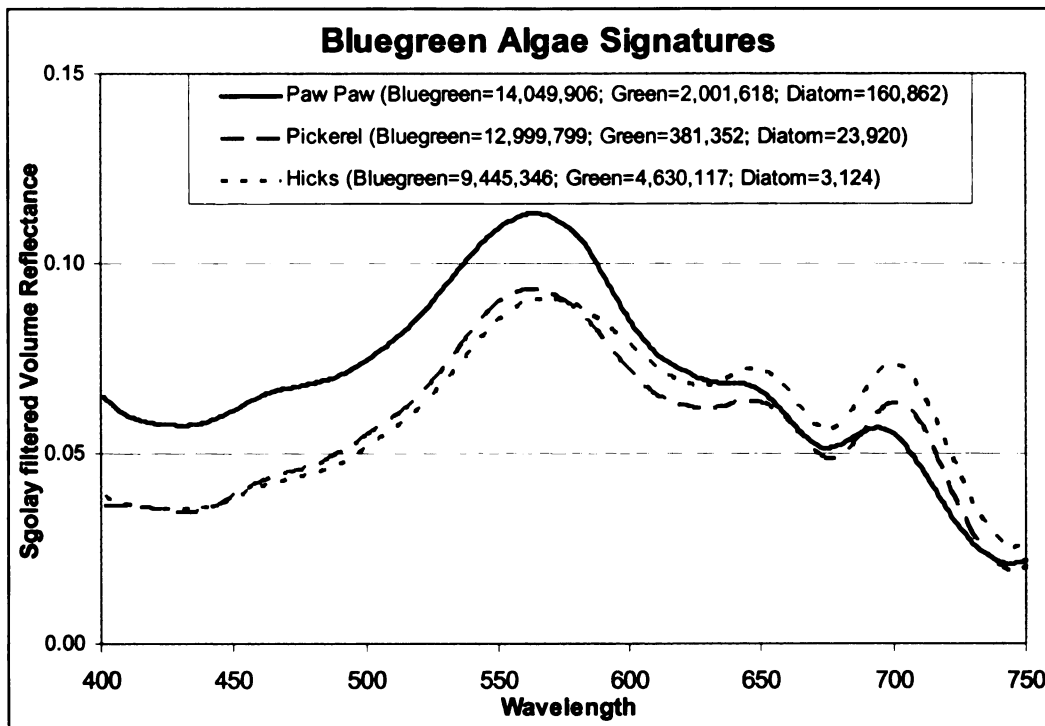


Figure 4-12 Examples of volume reflectance of bluegreen algal dominated waters

The first observation from the reflectance curve alone shows that the slight bumps in blue wavelengths around 435 nm – 475 nm are noticeable. This blue reflectance pattern did not appear clearly on the green algae curves (Figure 4-10) except for Belleville Lake, which also has a high bluegreen algal biomass.

Table 4-22 Bluegreen algae area models using the optimal wavebands

<b>Filter</b>	<b>Band</b>	<b>Coefficient</b>	<b>Tolerance</b>	<b>P(2-tail)</b>	<b>R<sup>2</sup></b>	<b>Adjusted R<sup>2</sup></b>
<b>Sgolay</b>	AG	-3.123	0.646	0.000	0.634	<b>0.580</b>
	CA	1.977	0.756	0.005		
	DB	-66.849	0.788	0.000		
	DE	-7.727	0.811	0.044		
	CONSTANT	28.569		0.000		
<b>Db1</b>	DB	-22.962	0.644	0.013	0.200	0.144
	DC*	12.158	0.644	0.066		
	CONSTANT	16.569				
<b>s8</b>	D	-192.032	0.618	0.001	0.370	0.326
	BA	5.106	0.618	0.001		
	CONSTANT	18.946		0.000		

\*Insignificant variable

Table 4-23 Bluegreen algae height/width models using the optimal wavebands

<b>Filter</b>	<b>Band</b>	<b>Coefficient</b>	<b>Tolerance</b>	<b>P(2-tail)</b>	<b>R<sup>2</sup></b>	<b>Adjusted R<sup>2</sup></b>
<b>Sgolay</b>	HWF	133.395	0.542	0.001	0.436	<b>0.353</b>
	HWAF	-35.544	0.212	0.001		
	HWBF	69.307	0.495	0.001		
	HWDA	-1.191	0.239	0.004		
	CONSTANT	1.266		0.834		
<b>Db1</b>	HWBE	20.307	1.000	0.008	0.213	0.187
	CONSTANT	6.387		0.032		
<b>s8</b>	HWDB	-3.233	1.000	0.000	0.373	0.352
	CONSTANT	23.298		0.000		

Table 4-24 Bluegreen algae narrow-waveband models using the optimal wavebands

<b>Filter</b>	<b>Band</b>	<b>Coefficient</b>	<b>Tolerance</b>	<b>P(2-tail)</b>	<b>R<sup>2</sup></b>	<b>Adjusted R<sup>2</sup></b>
<b>Sgolay</b>	BE	-2.107	0.405	0.000	0.364	0.320
	HC	-2.776	0.405	0.021		
	CONSTANT	19.926		0.000		
<b>Db1</b>	BF	-2.328	0.383	0.000	0.569	<b>0.505</b>
	GH	-15.242	0.204	0.006		
	HE	-7.000	0.221	0.009		
	HF	-7.160	0.209	0.015		
	CONSTANT	44.931		0.000		
<b>s8</b>	BE	-1.429	0.961	0.000	0.477	0.441
	EF	10.362	0.961	0.002		
	CONSTANT	5.577		0.088		

Again, area and narrow-waveband models perform better than the height/width model for bluegreen algae (discussed in Section 4.3.6; Figure 4-11). The models produce fairly good  $R^2$ , approximately 50 – 60 percent of the bluegreen algal biomass could be predicted by the area and the narrow-waveband spectral indicator models. There were not as many toxicity lakes that were dominated with bluegreen algae comparing to green algae. Nevertheless, the models select spectral regions that could detect bluegreen algae. Giving a potential toxic of this type of algae and the importance to assess and monitor for it in the real ecosystem environment, 50 percent chance of detecting it with remote sensing technology is useful. This hyperspectral remote sensing algorithm does not require as much time as the traditional way of taking samples back to the lab analysis. It allows a frequent monitoring by a hand-held sensor, or even a spatial overview with an airborne or a satellite sensor. Hyperspectral satellite sensors suitable for inland water monitoring are currently unavailable. However, research on locating waveband regions and spectral band width such as this study would help facilitate the future sensor configurations.

The region wavebands selected most frequently were band A (435 nm – 475 nm, blue absorption) and D (670 nm – 690 nm, maximum red absorption). Band A is a good indicator of blue green algae. It separates bluegreen algae from other algae type because bluegreen algae reflect light in blue wavelength regions, whereas other algae absorb light in these regions (Figure 4-10 and 4-12). Waveband D is an indicator of chlorophyll maximum absorption. It is expected to present in the models because most of the lakes that were dominated by

bluegreen algae had relatively high trophic. Waters that have high chlorophyll would have a clear prominent absorption feature in band D. The narrow-waveband models selected band B (455 nm) and E (670 nm), which are in the ranges of band A and D in the region-waveband indicators. The narrow-waveband indices show that wavelength 455 nm, which is close to the center of the slight bump in blue wavelengths, is a good indicator of bluegreen algae. Band H appears in the models as it is an indicator of higher CHL spectral signature.

#### **4.4 Model Validation**

The spectral indicators for each water quality variable were validated with 14 samples from both ASD and AISA data set.

##### **4.4.1 Chlorophyll $\alpha$ Model Validation**

AISA sensor was flown on 14 lakes on July 26, 2004. Of all the 14 lakes, ASD data are available for 13 of these lakes. Most of the measurements were made within 3 days of the AISA fly-over. One of these 13 lakes, Marl Lake, was extremely shallow. The deepest basin of the lake was only 1.5 meters and it was impossible to launch the boat to collect the sample. ASD and water samples were collected at the dock, which did not fall within the path of the AISA image. The ASD reading was impacted largely by the bottom effect. Spectral signature of this site did not purely represent inherent constituents within the water column. Therefore, it was appropriate to exclude the lake from

the validation data set. Consequently, the validation data set contained 12 ASD and 12 AISA spectra of the same lakes.

#### **4.4.1.1 Chlorophyll $\alpha$ ASD Validation**

The best spectral indicator for CHL was from Sgolay method. This method consistently performed better than the other approaches, and was therefore selected to use in the validation process. Although the area indicator tended to produce better results than the height/width index and narrow-waveband index in general (in terms of correlation coefficient and distribution of residual), all three indices were validated.

The ASD radiance spectra from 12 lakes were converted to volume reflectance and filtered with Savitsky Golay method. The filtered volume reflectances were then calculated for the 1<sup>st</sup> derivative. The derivative products were separated into narrow-wavebands and region-wavebands according to Table 4-2 and 4-3. Second order polynomial functions were fitted to the derivative data of region-waveband, and area under the curve, height and width of the function were calculated (detail described in Section 3.4.7 to 3.4.9). These waveband variables were used in the CHL models (Tables 4-4 to 4-6) to calculate the predicted CHL concentration for each lake (Table 4-25). The predicted CHL was then correlated with the real CHL concentration measured from the sampled water of the same site (Table 4-26; Figure 4-13).

Table 4-25 Chlorophyll ASD validation

Lake	Actual LNchl	Predicted LNchl		
		Area	Height/Width	Narrow Band
HIGG0727	0.122	0.857	0.096	1.465
CLME0724	2.270	2.505	2.718	2.482
SAPP0725	2.315	2.787	2.800	2.725
ARBU0726	2.371	1.922	1.882	1.903
MITC0725	2.612	2.919	3.228	2.907
HOUG0726	2.851	2.577	2.641	2.633
ROGE0724	3.001	2.967	3.365	3.179
MUSK0728	3.334	3.626	3.928	3.377
JEHN0519	3.359	2.664	2.890	2.781
HESS0727	3.515	4.901	3.336	4.215
BROO0727	3.928	4.199	3.514	3.713
TAMA0605	4.456	3.133	3.304	2.866

Table 4-26 Pearson correlation matrix of actual and predicted chlorophyll from ASD

Predicted CHL	Area Method	Height/Width Method	Narrow Band Method
Actual CHL	0.782	0.865	0.749

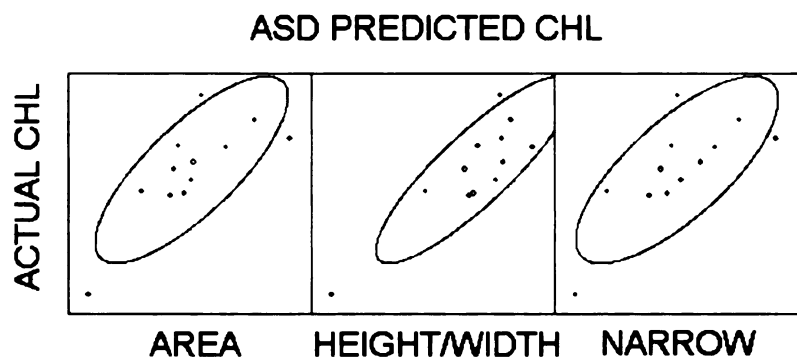


Figure 4-13 Correlation graphs between actual and predicted CHL from ASD

Correlations between actual and predicted CHL were quite strong for all methods. In a complex real natural ecosystem, many organic and inorganic

constituents coexist at the same time. These substances have different optical properties that could interfere or mask the signal of CHL in water. Therefore, the correlation coefficients of 0.75 – 0.87 were considered to be high especially for the studies that base on the natural environment rather than a controlled laboratory experimental condition. The CHL models selected spectral bands that are strongly related to the optical properties of CHL. These spectral bands were able to differentiate and provide a very good indication of CHL concentration of various trophic states in Michigan’s inland lake waters.

#### **4.4.1.2 Chlorophyll $\alpha$ AISA Validation**

AISA spectra were extracted from the 30 bands AISA imagery using the 3x3 area of interest (AOI). The average reflectance values within the AOI were used as the representative spectra of the lakes. These spectra were converted to volume reflectance. The AISA volume reflectances did not need to be filtered because the high frequency noise was not present. The average bandwidth was 5 nm – 8 nm. Filtering these spectra could result in losing useful absorption/reflectance features. The filtered volume reflectance was calculated for the 1<sup>st</sup> derivative. The derivative was then separated into narrow- and region-wavebands according to the Sgolay spectral indicator model. Polynomial functions 2<sup>nd</sup> order were fitted to the derivative data for each band regions, and under curve area, height and width of the function were calculated (detail described in Section 3.4.7 to 3.4.9). These spectral indicators were used to predict CHL concentration for each lake (Table 4-27). The predicted CHL was then correlated with the real CHL concentration measured from the sampled water of the same site (Table 4-28; Figure 4-14).

Table 4-27 Chlorophyll AISA validation

Lake	Actual LNchl	Predicted LNchl		
		Area	Height/Width	Narrow Band
HIGG0727	0.122	2.978	0.071	0.905
CLME0724	2.270	2.560	1.493	1.821
SAPP0725	2.315	2.371	2.688	2.438
ARBU0726	2.371	3.201	-0.181	1.652
TAMA0726	2.543	2.289	2.852	2.170
MITC0725	2.612	2.461	0.806	2.603
HOUG0726	2.851	2.319	2.917	2.090
JEHN0726	2.866	2.714	2.016	1.849
ROGE0724	3.001	1.467	4.617	2.657
MUSK0728	3.334	1.969	-0.293	1.204
HESS0727	3.515	1.713	3.689	3.962
BROO0727	3.928	2.053	3.019	3.591

Table 4-28 Pearson correlation matrix of actual and predicted chlorophyll from AISA

Predicted CHL	Area Method	Height/Width Method	Narrow Band Method
Actual CHL	-0.646	0.463	0.668

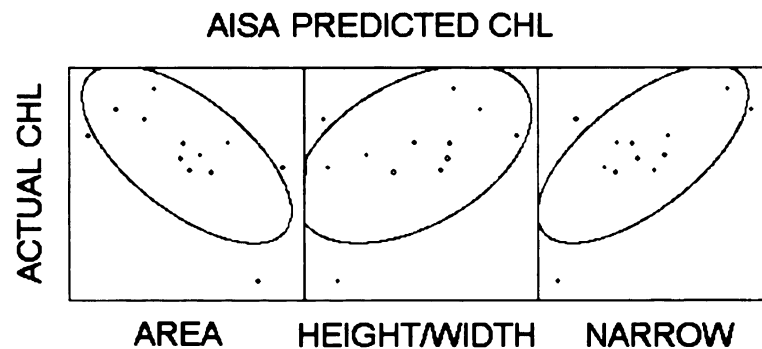


Figure 4-14 Correlation graphs between actual and predicted CHL from AISA

Correlation between the actual and predicted CHL from AISA data was lower than expected. Two of the 12 AISA spectra were not reliable. Mitchell Lake

image could not be successfully processed in an image export. However, part of the image that was successfully exported, although far from the *in situ* sample location, was used. The reflectance value was extracted from that part of the image. Muskegon Lake contained a large amount of bad scan lines (Appendix G). It was almost impossible to extract reflectance in 3x3 pixel window that was not affected by the defective scan lines. These two lakes were excluded from the data in the correlation process. The result shows a significant improvement on height/width and narrow-waveband indicators (Table 4-29; Figure 4-15).

Table 4-29 Pearson correlation matrix of actual and predicted chlorophyll from AISA without Mitchell and Muskegon Lakes

Predicted CHL	Area Method	Height/Width Method	Narrow Band Method
Actual CHL	-0.627	0.685	0.836

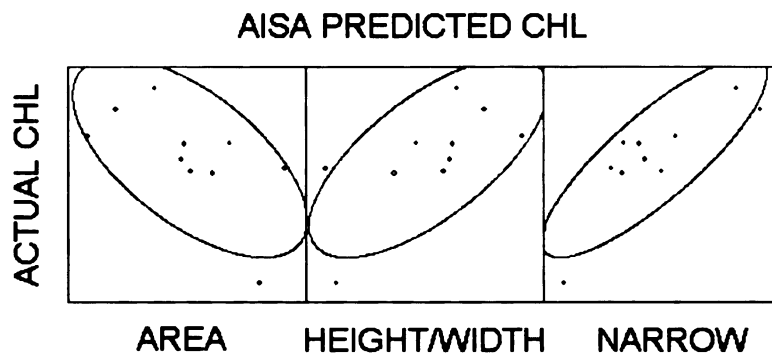


Figure 4-15 Correlation graphs between actual and predicted CHL from AISA without Mitchell and Muskegon Lakes

#### 4.4.2 Secchi Depth Model Validation

Validation is tested on the ASD and the AISA data from the same 12 lakes.

Spectral radiance from both data sets was transformed to surface reflectance.

Air-water interface correction and was applied to the reflectance. Three de-noising filters were performed on the ASD data, and the 1<sup>st</sup> derivative was calculated for each lake. The derivative products were then separated into regions determined in the previous section (section 3.4.7). Under curve area, height and width rationing were calculated. These indices, as well as the narrow-waveband reflectance values were used in the multivariate regression models. Since Sgolay produced the better results in the most biophysical models, it was used to validate the efficiency of the models. Although Sgolay did not produce the best SD model in the narrow-waveband model, the R<sup>2</sup> was not low. For an implementation purpose, it is more practical for the decision makers to use the models that were calculated from one filter method to predict water quality variables rather than applying different filters to the data for different variables.

#### **4.4.2.1 Secchi Depth ASD Validation**

The ASD radiance spectra from 12 lakes were converted to volume reflectance and filtered with Savitsky Golay method. The filtered volume reflectance was then calculated for the 1<sup>st</sup> derivative. The derivative products were separated into narrow-wavebands and region-wavebands according to Tables 4-2 and 4-3 (Sgolay indicator). Polynomial functions 2<sup>nd</sup> orders were fitted to the derivative data of region-waveband, and under curve area, height and width of the function were calculated (detail described in Section 3.4.7 to 3.4.9). These waveband variables were used in the Secchi models to calculate the predicted SD for each lake (Table 4-30). The predicted SD was then correlated with the

real SD concentration measured from the sampled water of the same site (Table 4-31; Figure 4-16).

Table 4-30 Secchi depth ASD validation

Lake	Actual LNsd	Predicted LNsd		
		Area	Height/Width	Narrow Band
HESS0727	-0.598	0.203	0.283	1.663
BROO0727	0.000	0.475	0.534	1.010
ROGE0724	0.182	0.396	0.619	1.728
SAPP0725	0.336	0.902	0.855	2.457
MUSK0728	0.405	0.363	-0.067	1.302
HOUG0726	0.470	0.805	1.127	1.771
TAMA0605	0.531	0.865	0.623	1.169
MITC0725	0.642	0.574	0.589	1.543
JEHN0519	0.693	0.795	0.880	2.122
CLME0724	1.065	0.995	1.075	2.114
ARBU0726	1.163	1.368	1.183	2.429
HIGG0727	2.054	2.208	1.920	3.258

Table 4-31 Pearson correlation matrix of actual and predicted Secchi depth from ASD

Predicted SD	Area Method	Height/Width Method	Narrow Band Method
Actual SD	0.918	0.810	0.718

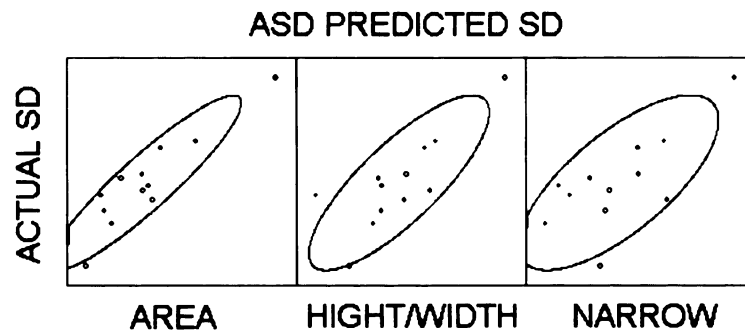


Figure 4-16 Correlation graphs between actual and predicted SD from ASD

Correlations between actual and predicted SD were very strong for all methods. The outlier point was Higgins Lake, which was the clearest lake in the data set (SD = 7.8 m; CHL = 1.13 mg/L). Comparing within the Sgolay models, region-waveband models are more accurate than the narrow-waveband model. The selected bands were able to differentiate and provide a very good indication of SD of various lakes in Michigan.

#### 4.4.2.2 Secchi Depth AISA Validation

AISA spectra were extracted from the 30 bands AISA imagery and processed according to Section 4.4.1.2. Sgolay SD models were applied to the AISA data set to predict SD for each lakes (Table 4-32). The predicted SD was then correlated with the actual reading SD from the same sample site (Table 4-33; Figure 4-17).

Table 4-32 Secchi depth AISA validation

Lake	Actual LNsd	Predicted LNsd		
		Area	Height/Width	Narrow Band
HESS0727	-0.598	3.459	-2.900	2.822
BROO0727	0.000	3.949	-1.588	3.720
ROGE0724	0.182	6.216	-1.769	2.489
SAPP0725	0.336	2.474	1.131	3.330
MUSK0728	0.405	-0.242	-0.433	1.132
HOUG0726	0.470	2.099	0.893	2.997
TAMA0605	0.588	2.246	0.323	2.303
MITC0725	0.642	1.942	-0.154	6.967
JEHN0519	0.916	1.991	1.352	5.997
CLME0724	1.065	2.423	1.410	4.213
ARBU0726	1.163	-0.990	2.236	5.810
HIGG0727	2.054	-10.069	2.238	5.843

Table 4-33 Pearson correlation matrix of actual and predicted Secchi depth from AISA

Predicted SD	Area Method	Height/Width Method	Narrow Band Method
Actual SD	-0.798	0.869	0.581

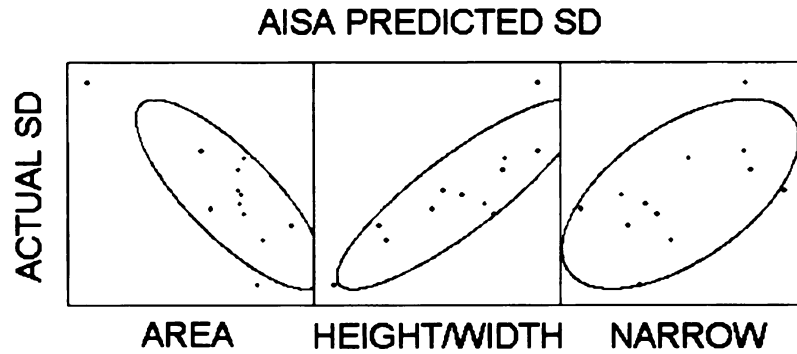


Figure 4-17 Correlation graphs between actual and predicted SD from AISA

Mitchell Lake and Muskegon Lake spectra were not reliable (explained in Section 4.4.1.2). These lakes were removed and the result shows an improvement on the narrow-waveband model (Table 4-34; Figure 4-18).

Table 4-34 Pearson correlation matrix of actual and predicted Secchi depth from AISA without Mitchell and Muskegon Lakes

Predicted SD	Area Method	Height/Width Method	Narrow Band Method
Actual SD	-0.820	0.872	0.735

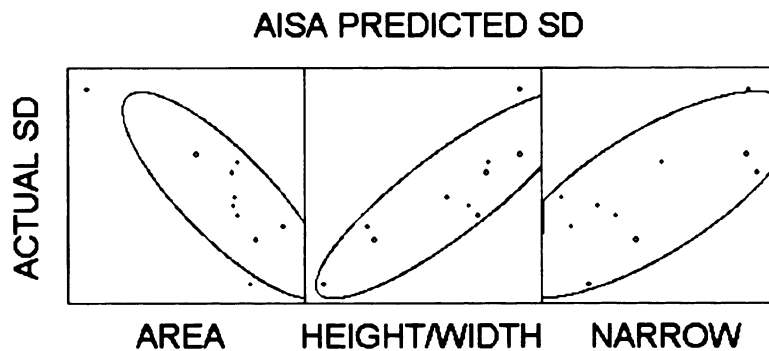


Figure 4-18 Correlation graphs between actual and predicted SD from AISA without Mitchell and Muskegon Lakes

#### 4.4.3 TSS Model Validation

The ASD and the AISA radiance spectra from 12 lakes were converted to volume reflectance and filtered with Savitsky Golay method. The filtered volume reflectance was then calculated for the 1<sup>st</sup> derivative. The derivative products were separated into narrow-wavebands and region-wavebands according to Tables 4-2 and 4-3 (Sgolay indicator). Polynomial functions 2<sup>nd</sup> orders were fitted to the derivative data of region-waveband, and under-curve area, height and width of the function were calculated (detail described in Section 3.4.7 to 3.4.9). These waveband variables were used in the TSS models to calculate the predicted TSS for each lake (Table 4-35).

##### 4.4.3.1 TSS ASD Validation

The predicted TSS values were correlated with the actual TSS concentration measured from the sampled water of the same site (Table 4-36; Figure 4-19).

Table 4-35 TSS ASD validation

Lake	Actual LNTss	Predicted LNTss		
		Area	Height/Width	Narrow Band
CLME0724	2.128	2.424	2.448	2.425
HIGG0727	2.197	2.313	2.348	2.338
MUSK0728	2.262	2.856	2.747	2.802
JEHN0519	2.303	2.479	2.494	2.515
ROGE0724	2.542	2.510	2.735	2.616
ARBU0726	2.580	2.410	2.375	2.498
SAPP0725	2.879	2.559	2.462	2.591
MITC0725	2.944	2.569	2.681	2.570
HESS0727	3.401	2.921	2.993	2.682
HOUG0726	3.440	2.488	2.512	2.511
TAMA0605	3.940	2.597	2.548	2.526
BROO0727	4.159	2.760	2.818	2.676

Table 4-36 Pearson correlation matrix of actual and predicted TSS from ASD

Predicted TSS	Area Method	Height/Width Method	Narrow Band Method
Actual TSS	0.453	0.442	0.294

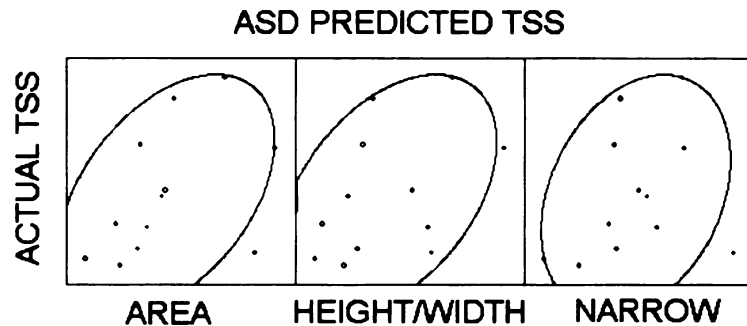


Figure 4-19 Correlation graphs between actual and predicted TSS biomass from ASD

TSS concentration for each lake was predicted using the TSS spectral indicator model developed in section 4.3.3 applied to spectral data from a handheld ASD spectroradiometer. The models tend to underpredict TSS values when concentration is high and slightly overpredict values when concentration is low. This may be because the data set used to develop the models was mostly from low TSS lakes. Therefore, the models tend to underpredict high TSS values resulting in relatively low correlations between actual and predicted TSS showed in the correlation graph point pattern. Comparing among all methods, the area model appears to have a stronger correlation between predicted and actual TSS.

#### 4.4.3.2 TSS AISA Validation

AISA spectra were extracted from the 30 bands AISA imagery and processed according to Section 4.4.1.2. Sgolay TSS models were applied to the AISA data set to predict TSS for each lakes (Table 4-37). The predicted TSS was then

correlated with the actual reading TSS from the same sample site (Table 4-38; Figure 4-20).

Table 4-37 TSS AISA validation

Lake	Actual LNTss	Predicted LNTss		
		Area	Height/Width	Narrow Band
CLME0724	2.128	2.847	3.168	2.377
HIGG0727	2.197	2.677	2.866	2.251
MUSK0728	2.262	3.812	3.923	2.417
ROGE0724	2.542	3.212	4.139	2.526
ARBU0726	2.580	2.628	2.787	2.411
TAMA0727	2.703	2.735	3.565	2.528
SAPP0725	2.879	2.509	3.192	2.424
MITC0725	2.944	2.599	3.796	2.526
JEHN0726	3.158	2.614	3.150	2.262
HESS0727	3.401	1.844	4.626	2.652
HOUG0726	3.440	2.673	3.330	2.433
BROO0727	4.159	2.237	4.207	2.655

Table 4-38 Pearson correlation matrix of actual and predicted TSS from AISA

Predicted TSS	Area Method	Height/Width Method	Narrow Band Method
Actual TSS	-0.640	0.456	0.580

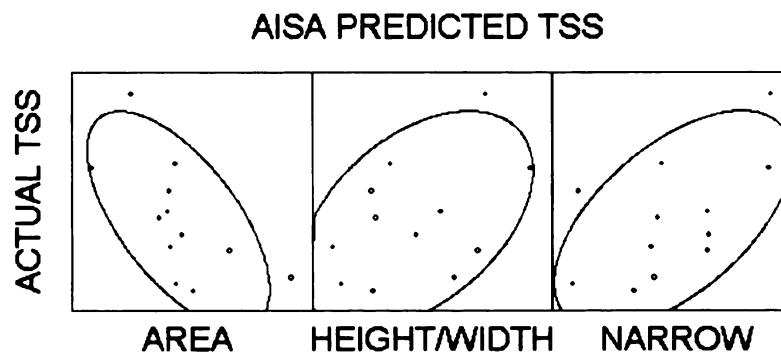
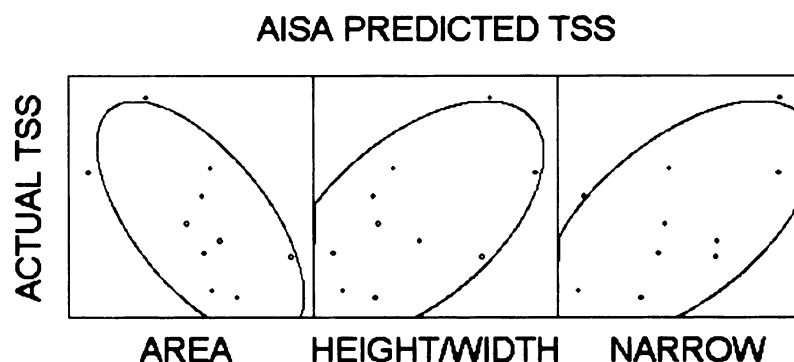


Figure 4-20 Correlation graphs between actual and predicted TSS from AISA

Two of the 12 AISA spectra were not reliable (discussed in Section 4.4.12). Therefore, they were removed from the validation. The new prediction improved only slightly (Table 4-39; Figure 4-21).

Table 4-39 Pearson correlation matrix of actual and predicted TSS from AISA without Mitchell and Muskegon Lakes

<b>Predicted TSS</b>	<b>Area Method</b>	<b>Height/Width Method</b>	<b>Narrow Band Method</b>
<b>Actual TSS</b>	-0.631	0.562	0.590



#### 4.4.4 NPOC Model Validation

Although Sgolay did not produce the best models in every case, it was selected as the method to validate because it produced better results for overall biophysical parameters.

##### 4.4.4.1 NPOC ASD Validation

The predicted NPOC data (Table 4-40) were correlated with the real NPOC concentration measured from the sampled water of the same site (Table 4-41; Figure 4-22).

Table 4-40 NPOC algae ASD validation

Lake	Actual LNnpoc	Predicted LNnpoc		
		Area	Height/Width	Narrow Band
ARBU0726	1.550	2.075	2.063	2.146
BROO0727	2.086	2.220	2.222	2.285
CLME0724	2.496	2.166	2.167	2.147
HESS0727	2.447	2.210	2.189	2.281
HIGG0727	1.227	2.128	2.105	1.953
HOU0726	2.259	2.229	2.223	2.236
JEHN0519	1.926	2.259	2.240	2.206
MITC0725	2.479	2.341	2.330	2.285
MUSK0728	2.257	2.516	2.520	2.276
ROGE0724	2.044	2.398	2.360	2.289
SAPP0725	2.123	2.248	2.218	2.128
TAMA0605	2.539	2.366	2.408	2.247

Table 4-41 Pearson correlation matrix of actual and predicted NPOC from ASD

Predicted NPOC	Area Method	Height/Width Method	Narrow Band Method
Actual NPOC	0.491	0.539	0.712

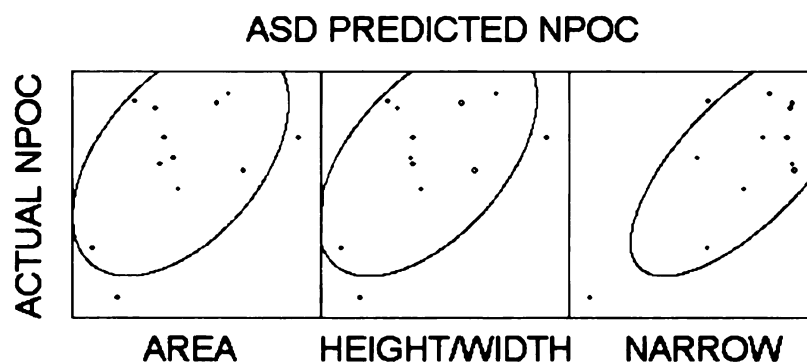


Figure 4-22 Correlation graphs between actual and predicted NPOC from ASD

The correlation graphs indicate no correlation between the actual and the predicted NPOC. Similar to TSS, NPOC data set mostly contain low NPOC lakes. A wide range of data was lacking in the model development process. Therefore, a model that captures specific optical features of NPOC was not successfully produced in this study.

#### 4.4.4.2 NPOC AISA Validation

The predicted NPOC concentration were calculated and correlated with the actual concentration values (Tables 4-42 and 4-43; Figure 4-23).

Table 4-42 NPOC AISA validation

Lake	Actual LNnpoc	Predicted LNnpoc		
		Area	Height/Width	Narrow Band
JEHN0726	1.227	1.256	2.637	2.043
MITC0725	1.550	1.379	2.510	2.136
SAPP0725	2.044	0.689	3.445	2.252
HOUG0726	2.086	0.905	3.116	2.266
ARBU0726	2.123	1.240	2.755	2.155
MUSK0728	2.257	0.866	3.959	2.263
CLME0724	2.259	1.030	2.871	2.214
BROO0727	2.447	1.074	3.044	2.276
HESS0727	2.479	0.624	3.345	2.230
ROGE0724	2.496	1.054	2.921	2.157

Table 4-43 Pearson correlation matrix of actual and predicted NPOC from AISA

Predicted NPOC	Area Method	Height/Width Method	Narrow Band Method
Actual NPOC	-0.569	0.499	0.718

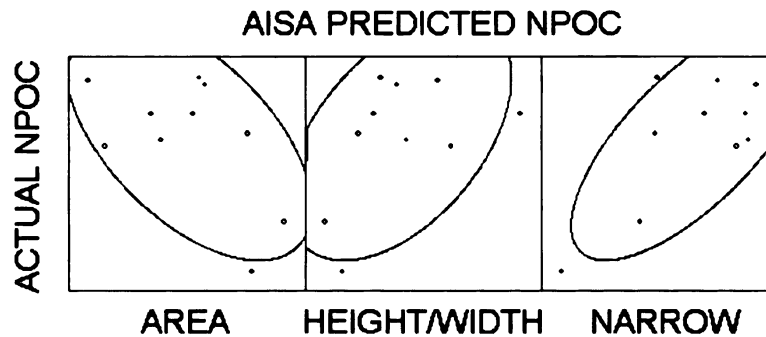


Figure 4-23 Correlation graphs between actual and predicted NPOC from AISA

The correlations between actual and predicted NPOC are very low. Considering correlation graph in Figure 4-23, there is no relationship between the predicted and actual NPOC for region-waveband models. However, narrow-waveband model appears to have a better correlation. This reflects the same explanation

with the TSS models that AISA configuration used in this study may not support region-waveband TSS models prediction. Therefore, no further test has been done on excluding Mitchell and Muskegon lake data.

#### 4.4.5 Algal Model Validation

The spectra of 12 lakes from ASD and AISA were used in the validation. The data set used to develop the models and the data set used for validation were compared (Table 4-44, Figure 4-24). Green algae was the only parameter that has approximately the same distribution between the modeling and validating data sets. Most of the validating data set for diatom and bluegreen algae had lower algal biomass.

Table 4-44 Statistical comparison of modeling and validating data set

Data set	Diatom		Green		Bluegreen	
	Model	Validate	Model	Validate	Model	Validate
<b>Min</b>	1259	30145	381352	868721	0	0
<b>Max</b>	47110080	9496427	27080095	24628622	19053542	11150160
<b>Mean</b>	1807403	957288	4363092	5196300	4960194	3057239
<b>Median</b>	96388	260910	2001618	3065090	3343379	1516637
<b>Std. Dev.</b>	7954953	2468981	6390964	6060236	5578742	3982201

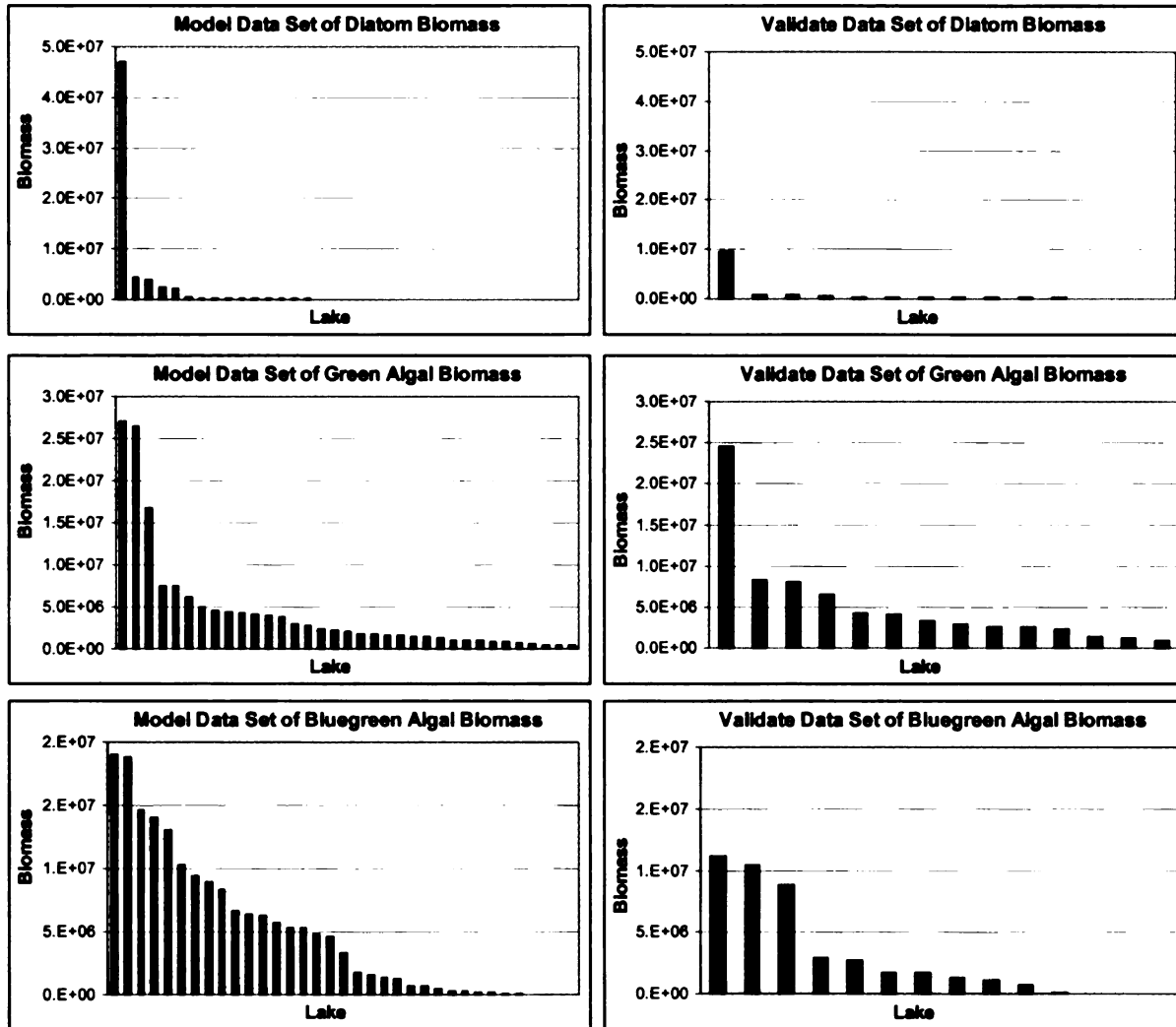


Figure 4-24 Distribution of modeling and validating data set

#### 4.4.5.1 Diatom ASD Validation

The ASD radiance spectra from 12 lakes were converted to volume reflectance and filtered with Savitsky Golay method. The filtered volume reflectance was then calculated for the 1<sup>st</sup> derivative. The derivative products were separated into narrow-wavebands and region-wavebands according to Tables 4-2 and 4-3 (Sgolay indicator). Polynomial functions 2<sup>nd</sup> orders were fitted to the derivative data of region-waveband, and under curve area, height and width of the function were calculated (detail described in section 3.4.7 to 3.4.9). These

waveband variables were used in the diatom biomass models to calculate the predicted diatom biomass for each lake (Table 4-45). The predicted diatom biomass was then correlated with the real diatom biomass concentration measured from the sampled water of the same site (Table 4-46; Figure 4-25).

Table 4-45 Diatom ASD validation

Lake	LNdiatom	Predicted LNdiatom		
		Area	Height/Width	Narrow Band
JEHN0519	7.539	9.174	10.222	11.787
MITC0725	10.314	9.439	9.852	11.622
SAPP0725	11.046	11.841	11.926	12.364
HOUG0726	11.934	11.263	11.592	12.922
ARBU0726	12.116	10.850	11.361	11.474
MUSK0728	12.161	11.994	11.821	11.974
CLME0724	12.554	12.265	12.415	11.142
BROO0727	12.582	11.632	11.968	12.050
HESS0727	12.639	12.134	11.943	12.667
ROGE0724	13.560	13.634	12.271	11.911
HIGG0727	13.579	12.616	11.960	12.201
TAMA0605	16.066	13.611	12.879	13.632

Table 4-46 Pearson correlation matrix of actual and predicted diatom from ASD

Predicted Diatom	Area Method	Height/Width Method	Narrow Band Method
Actual Diatom	0.887	0.841	0.498

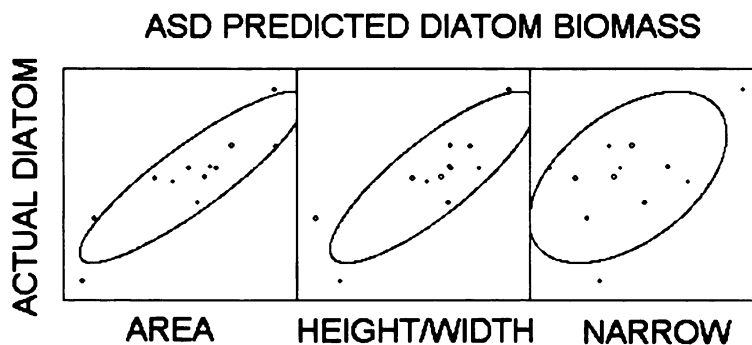


Figure 4-25 Correlation graphs between actual and predicted diatom biomass from ASD

Correlations between actual and predicted diatom were quite strong for both region waveband methods. Given a complexity in natural waters where many algal types coexist, the region waveband models could predict nearly 80 percent of diatom biomass ( $R^2 = 0.787$ ). The selected waveband regions are sensitive to changes in diatom biomass. Despite the fact that lakes that were used for validation have very low diatom biomass, and the data that used to create the models have very few diatom dominated lakes to begin with, wavebands used in the model were able to capture diatom optical characteristics.

#### 4.4.5.2 Diatom AISA Validation

AISA spectra were extracted from the 30 bands AISA imagery and processed according to Section 4.4.1.2. Sgolay SD models were applied to the AISA data set to predict diatom biomass for each lake (Table 4-47). The predicted diatom biomass was then correlated with the actual reading diatom biomass from the same sample site (Table 4-48; Figure 4-26).

Table 4-47 Diatom AISA validation

Lake	LNdiatom	Predicted LNdiatom		
		Area	Height/Width	Narrow Band
JEHN0726	7.539	-11.573	19.376	12.007
MITC0725	10.314	-11.819	18.185	11.994
SAPP0725	11.046	-2.418	16.887	13.249
HOUG0726	11.364	-5.579	19.955	11.564
ARBU0726	11.934	-3.237	18.499	10.936
MUSK0728	12.116	1.900	15.652	9.777
CLME0724	12.161	-11.614	21.813	11.396
BROO0727	12.554	0.088	16.598	8.934
HESS0727	12.582	-5.122	17.681	11.539
ROGE0724	13.560	0.285	26.576	11.177
HIGG0727	13.579	-13.855	19.632	12.519

Table 4-48 Pearson correlation matrix of actual and predicted diatom from AISA

<b>Predicted Diatom</b>	<b>Area Method</b>	<b>Height/Width Method</b>	<b>Narrow Band Method</b>
<b>Actual Diatom</b>	0.346	0.245	-0.280

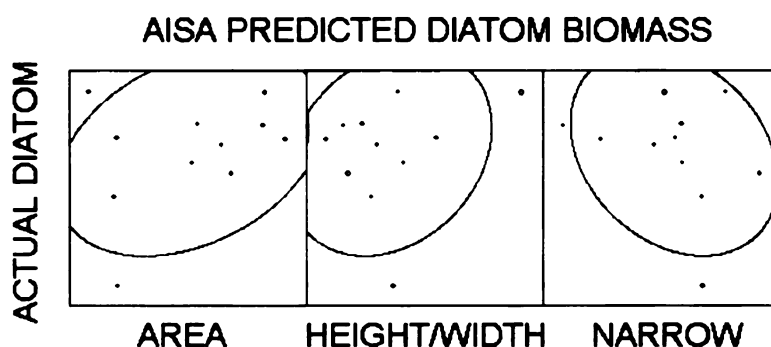


Figure 4-26 Correlation graphs between actual and predicted diatom from AISA

Two of the 12 AISA spectra were not reliable (discussed in Section 4.4.1.2). Therefore, they were removed from the validation. The result shows no improvement at all (Table 4-49; Figure 4-27). The reasons could be that the model is not sensitive to changes in diatom biomass, or the AISA spectral setting used in this study does not support the estimation of diatom biomass. Since ASD validation shows a very good result, the model should not be the reason that causes such a low predictability with the AISA data. AISA data set proved to produce high accuracy when applied with CHL (chlorophyll *a*) and SD (Secchi depth) models. However, the average bandwidth of 5 nm – 8 nm (mostly 8 nm for the selected bands), may not provide the detail features needed for biomass estimation of the algae. For example, band A (435 – 475 nm) has ASD input of 40 data point to the polynomial fitting curve, whereas, AISA only has 5 data point input into the model. In this case, AISA waveband actually ranges from 434.45 nm to 486.92 nm, which is not exactly same range as selected in

the models. The worst case is band D (670 nm – 690 nm), which only have 3 data point input from AISA with spectral range between 674.09 nm to 694.13 nm. Table 4-49 showed Pearson correlation matrix of actual and predicted diatom from AISA without Mitchell and Muskegon Lakes.

Table 4-49 Pearson correlation matrix of actual and predicted diatom from AISA without Mitchell and Muskegon Lakes

Predicted Diatom	Area Method	Height/Width Method	Narrow Band Method
Actual Diatom	0.315	-0.245	-0.283

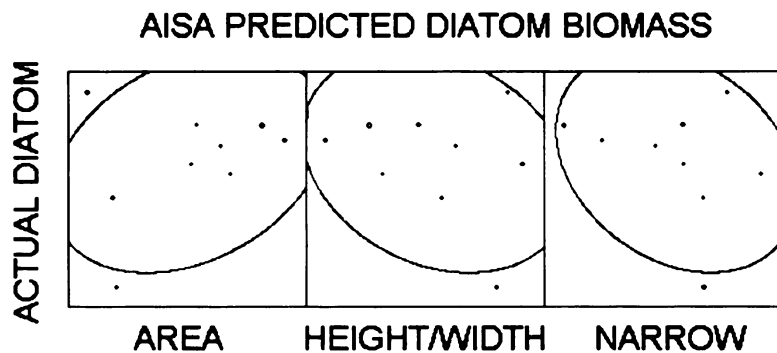


Figure 4-27 Correlation graphs between actual and predicted diatom from AISA without Mitchell and Muskegon Lakes

#### 4.4.5.3 Green Algae ASD Validation

The spectral indicator for green algae derived from Sgolay method consistently performed better than the other approaches. It was therefore selected as the best method and was used in the validation process. The predicted green algal biomass was calculated and correlated with the real green algal biomass measured from the sampled water of the same site (Tables 4-50 and 4-51; Figure 4-28).

Table 4-50 Green algae ASD validation

Lake	LNgreen	Predicted LNgreen		
		Area	Height/Width	Narrow Band
JEHN0519	13.039	14.149	14.384	19.987
MITC0725	13.675	14.512	14.824	17.338
SAPP0725	14.164	14.723	14.073	24.155
HOUG0726	14.662	14.345	14.308	18.697
ARBU0726	14.781	14.901	14.974	16.542
MUSK0728	14.993	15.467	15.545	14.168
CLME0724	15.215	14.335	14.448	16.954
BROO0727	15.251	14.565	14.944	17.821
HESS0727	15.254	14.346	14.789	19.185
ROGE0724	15.676	14.271	14.785	17.950
HIGG0727	15.887	16.358	15.780	14.922
TAMA0605	17.019	14.425	14.651	19.728

Table 4-51 Pearson correlation matrix of actual and predicted green algae from ASD

Predicted green	Area Method	Height/Width Method	Narrow Band Method
Actual green	0.249	0.360	-0.243

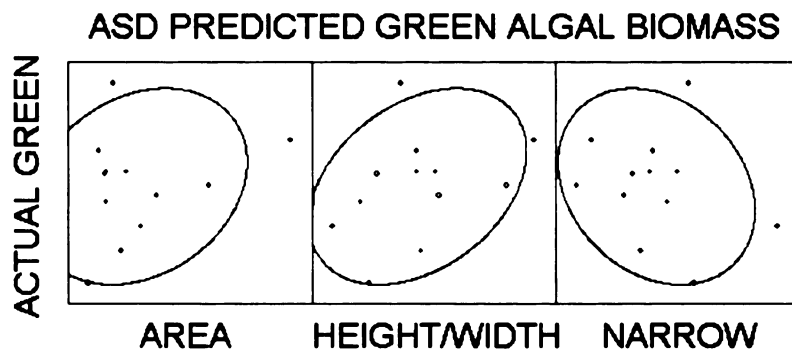


Figure 4-28 Correlation graphs between actual and predicted green algal biomass from ASD

There was no correlation between the actual and the predicted green algae. It could be because green algae do not have a unique or distinctive absorption/reflectance features other than the appearance of normal chlorophyll curve. The model that captures specific optical features that could detect green algae is not successfully produced in this study.

#### 4.4.5.4 Green Algae AISA Validation

The predicted green algal biomass were calculated and correlated with the actual green algal biomass (Tables 4-52 and 4-53; Figure 4-29).

Table 4-52 Green algae AISA validation

Lake	LN <sub>green</sub>	Predicted LN <sub>green</sub>		
		Area	Height/Width	Narrow-Band
JEHN0726	13.039	15.003	13.754	16.155
MITC0725	13.675	15.421	13.650	18.967
SAPP0725	14.044	15.757	13.894	12.954
HOUG0726	14.164	14.504	13.806	18.624
ARBU0726	14.662	15.336	13.682	15.429
MUSK0728	14.781	15.339	13.854	19.032
CLME0724	15.215	15.240	13.661	15.982
BROO0727	15.254	15.911	13.776	16.495
HESS0727	15.676	20.985	14.730	18.881
ROGE0724	15.887	16.937	13.664	10.815
HIGG0727	17.019	15.692	13.880	19.035

Table 4-53 Pearson correlation matrix of actual and predicted green algae from AISA

Predicted Green	Area Method	Height/Width Method	Narrow Band Method
Actual Green	0.405	0.273	0.017

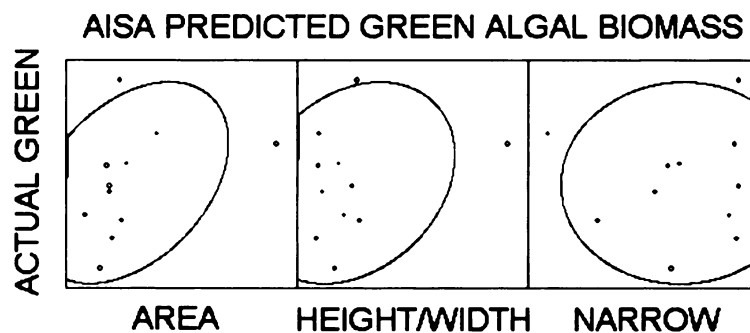


Figure 4-29 Correlation graphs between actual and predicted green algae from AISA

The correlations between actual and predicted green algae are very low.

Considering correlation graph in Figure 4-29, there is no relationship between the predicted and actual green algae. Therefore, no further test has been done on excluding Mitchell and Muskegon lake data.

#### 4.4.5.5 Bluegreen Algae ASD Validation

The spectral indicator for bluegreen algae derived from Sgolay method was used in the validation process. The predicted bluegreen algae was correlated with the real bluegreen algal biomass measured from the sampled water of the same site (Tables 4-54 and 4-55; Figure 4-30).

Table 4-54 Bluegreen algae ASD validation

Lake	LNbluegreen	Predicted LNbluegreen		
		Area	Height/Width	Narrow Band
JEHN0519	6.982	8.353	11.979	5.160
MITC0725	13.478	15.184	15.740	13.203
SAPP0725	13.501	14.828	14.910	10.995
HOU0726	13.940	16.128	16.173	13.681
ARBU0726	14.368	14.713	14.659	13.586
MUSK0728	14.379	12.830	11.462	10.587
CLME0724	14.899	13.211	14.373	13.176
BROO0727	15.664	14.988	14.997	11.384
HESS0727	15.992	16.150	15.292	11.387
ROGE0724	16.227	15.337	15.298	13.275

Table 4-55 Pearson correlation matrix of actual and predicted bluegreen algae from ASD

Predicted Bluegreen	Area Method	Height/Width Method	Narrow Band Method
Actual Bluegreen	0.849	0.536	0.811

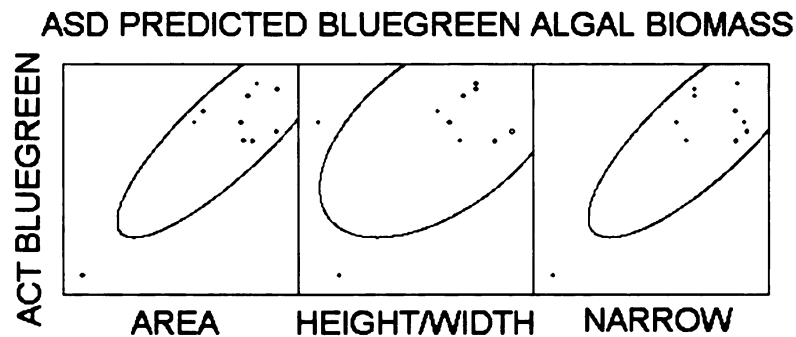


Figure 4-30 Correlation graphs between actual and predicted bluegreen algal biomass from ASD

Although the correlation coefficients are high, there was no strong correlation between the actual and the predicted green algae considering the correlation graph. It could be because the validate data set does not have high bluegreen biomass lakes that have the strong optical features mentioned in Section 4.4.5 (Figure 4-24).

#### 4.4.5.6 Bluegreen Algae AISA Validation

Statistical correlation was performed on the predicted bluegreen algal biomass were calculated and correlated with the actual biomass (Tables 4-56 and 4-57; Figure 4-31).

Table 4-56 Bluegreen algae AISA validation

Lake	LNbluegreen	Predicted LNbluegreen		
		Area	Height/Width	Narrow Band
JEHN0726	6.982	-104.087	-128.282	9.732
MITC0725	13.478	-11.129	-37.148	12.828
SAPP0725	13.501	-17.873	-45.334	10.719
HOUG0726	13.940	-6.085	-15.480	13.159
ARBU0726	14.075	-23.372	-51.623	12.200
MUSK0728	14.368	-29.146	-103.321	12.438
CLME0724	14.379	-1.465	-129.525	11.945
BROO0727	14.899	-23.879	-4.993	12.069
HESS0727	15.664	-22.247	-70.829	11.858
ROGE0724	15.992	-30.918	-121.843	12.744
HIGG0727	16.227	-26.086	-46.916	12.434

Table 4-57 Pearson correlation matrix of actual and predicted bluegreen algae from AISA

Predicted Bluegreen	Area Method	Height/Width Method	Narrow Band Method
Actual Bluegreen	0.793	0.308	0.746

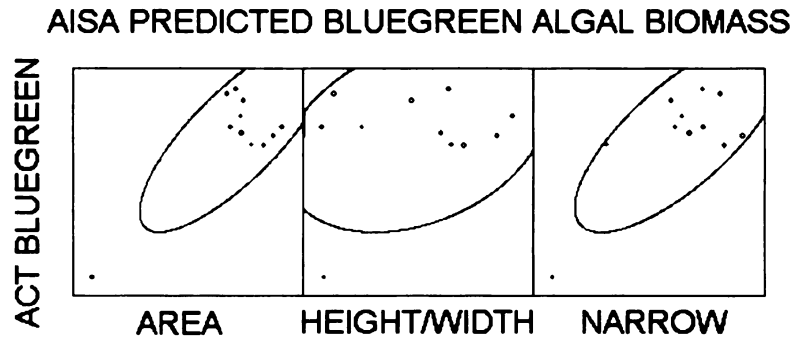


Figure 4-31 Correlation graphs between actual and predicted green algae from AISA

Although correlation coefficients are high, correlation graph also showed no relationship between AISA predicted and actual bluegreen algae. The Higgins lake data that were outliers was an exceptionally deep and clear lake. An experiment had been made to exclude Mitchell, Muskegon, and Higgins lakes to investigate if the model is able to predict bluegreen algal biomass at all since it was expected to predict a half of the actual data according to the model  $R^2$  (Tables 4-22 to 4-24). Correlation graph shows some degree of correlation in the region waveband methods, but the correlation appears to be negative suggesting that the model could not be used effectively with this AISA data (Table 4-58; Figure 4-32).

Table 4-58 Pearson correlation matrix of actual and predicted bluegreen algae from AISA without Mitchell, Muskegon, and Higgins Lakes

Predicted Bluegreen	Area Method	Height/Width Method	Narrow Band Method
Actual Bluegreen	-0.751	-0.516	0.164

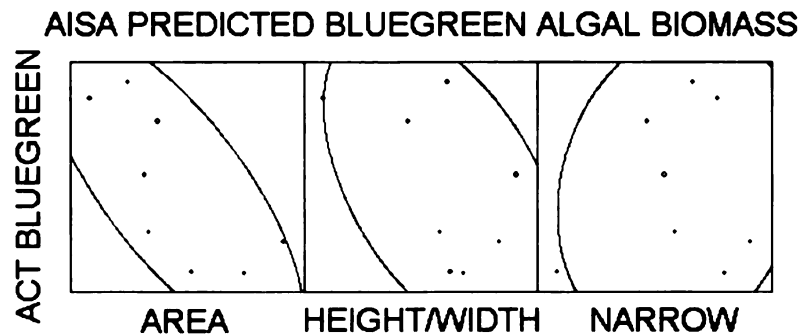


Figure 4-32 Correlation graphs between actual and predicted bluegreen algae from AISA without Mitchell, Muskegon, and Higgins Lakes

#### 4.5 Discussion on Spectral Indicators for Water Quality Assessment

Spectral indicator models developed from Savitsky Golay filter performed best among the four filters. Performances of the models developed from Savitsky Golay filter were summarized in this section. The dependant variables (spectral wavebands) were discussed in terms of their linkages to the water quality variables.

##### 4.5.1 Chlorophyll $\alpha$

The best CHL spectral indicator models and their accuracies were summarized in Table 4-59.

Table 4-59 Chlorophyll model performances

Index	Model	Model	Validation	Validation
		R <sup>2</sup>	ASD R <sup>2</sup>	AISA R <sup>2</sup>
Area	LN(CHL) = -1.687(A/G) + 1.509(D/G) - 0.331(F/E) + 1.132(G/D) + 3.234	<b>0.757</b>	0.612	0.393
Height/ Width	LN(CHL) = -1.930(A/G) - 5.181(B/D) + 5.891	0.699	<b>0.748</b>	0.469
Narrow	LN(CHL) = -38.605(A) + 42.536(E) - 5.108(E/H) - 1.549(G/A) + 9.801	0.754	0.561	<b>0.699</b>

The blue absorption band A (435 nm or 435 nm – 475 nm) and the ratio of it with the NIR peak band G (690 nm or 700 nm – 740 nm) were the key wavebands for chlorophyll assessment. Blue wavelengths not only contains the most information of water column as they penetrate deeper than other wavelengths, but they also represent an absorption region of CHL. NIR wavebands are no doubt the indicator of CHL. NIR wavelengths have been used in the inland vegetation indicators and blue wavelengths have been used in water quality indicators.

The ratio between maximum CHL absorption in red wavelengths and the NIR peak were selected repeatedly (region-waveband: D/G, F/E, G/D and narrow-waveband: E/H). The RED/NIR ratio has also been used extensively in vegetation studies. These wavebands are truly indicators of CHL.

#### 4.5.2 Secchi Depth

The best SD spectral indicator models and their accuracies were summarized in Table 4-60.

Table 4-60 Secchi depth model performances

<b>Index</b>	<b>Model</b>	<b>Model R<sup>2</sup></b>	<b>Validation ASD R<sup>2</sup></b>	<b>Validation AISA R<sup>2</sup></b>
Area	$\text{LN(SD)} = - 5.560(\text{A/B}) + 0.792(\text{A/G})$ $- 2.183(\text{B/F}) - 0.937(\text{E/C})$ $+ 3.955$	0.700	<b>0.843</b>	0.672
Height/ Width	$\text{LN(SD)} = - 47.187(\text{C}) - 1.742(\text{B/A})$ $- 0.597(\text{G/C}) + 4.559$	0.759	0.656	<b>0.760</b>
Narrow	$\text{LN(SD)} = -7.1088(\text{A}) + 1.1003(\text{D/A})$ $- 1.8842(\text{D/C}) - 1.0169(\text{G/C})$ $+ 2.871$	<b>0.768</b>	0.516	0.540

Shorter spectral wavelengths (blue waveband) between 435 nm – 475 nm (band A) explained clarity in water. Blue wavelength region approximately 400 nm – 500 nm has the least amount of absorption and scattering of incident light in the water column (Figure 2-6). These wavebands penetrate into the water column deeper than other wavelengths. Reflectance from them contains information of constituents in the water column. Therefore, they can be used to differentiate clear and turbid waters. Longer wavebands (> 520 nm) get absorbed by water very quickly; therefore, they could not detect and separate clear water from turbid water. The longer wavebands that appeared in the

models were mostly the indicators of chlorophyll. For examples, NIR peak for band G, maximum CHL absorption for band D and E. Since turbidity in the studied lakes was dominated by algal biomass, these selected bands could improve the predictability of the SD model.

When incident light penetrates into the water column, it interacts with inherent substances that are dissolved and suspended. Clarity measured by a Secchi disk can results from almost everything optical objects in the water, such as, algal biomass, inorganic suspended solid, and dissolved humic substances. After the incident light interacts with substances in water, it reflects back and gets measured by the remote sensor. The higher reflectance usually associates with the higher substances. Except for the case that water contains high concentration of dissolved organic carbon or other absorbing agents that low reflectance would indicate high concentration of constituent in water. Secchi depth (SD) is the measurement of visibility link to clarity of the water. It is almost a direct optical measurement. Low SD reading usually means turbid water. Turbid water has a lot of substances in the water for the incident light to interact with and reflect back. Therefore the spectral reflectance of this lake is expected to be high. Section 4.3.2 and Figure 4-11 showed that derivative product of the volume reflectance is higher in more turbid water (lower SD value) and lower in clearer water (higher SD value).

### 4.5.3 TSS and NPOC

The best TSS and NPOC spectral indicator models and their accuracies were summarized in Tables 4-61 and 4-62.

Table 4-61 TSS model performances

<b>Index</b>	<b>Model</b>	<b>Model R<sup>2</sup></b>	<b>Validation ASD R<sup>2</sup></b>	<b>Validation AISA R<sup>2</sup></b>
Area	$\text{LN(TSS)} = 0.420(D/A) + 1.088(E/D) + 0.295(G/E) + 0.405$	0.286	<b>0.205</b>	<b>0.398</b>
Height/ Width	$\text{LN(TSS)} = 0.213(G/C) + 2.273$	0.207	0.195	0.316
Narrow	$\text{LN(TSS)} = -1.224(F/H) + 3.876$	<b>0.326</b>	0.086	0.348

Table 4-62 NPOC model performances

<b>Index</b>	<b>Model</b>	<b>Model R<sup>2</sup></b>	<b>Validation ASD R<sup>2</sup></b>	<b>Validation AISA R<sup>2</sup></b>
Area	No Valid Model			
Height/ Width	$\text{LN(NPOC)} = 0.100(E/C) + 1.902$	<b>0.105</b>	<b>0.291</b>	<b>0.249</b>
Narrow	No Valid Model			

Majority of the lakes used in this study did not have high TSS or NPOC (Figure 4-1 and 4-3). Although the data were LN transformed to avoid the skewness problem (Figure 4-4), the accuracy of the TSS models were low and only height/width indicator produced a valid NPOC model. Although humic

substances (NPOC) produces distinctively low reflectance curve by significantly absorb incident light (Figure 4-12), one or two low reflectance signatures were not sufficient to produce a quantitative regression model.

#### 4.5.4 Algae

The best algal spectral indicator models and their accuracies were summarized in Tables 4-63 to 4-65.

Table 4-63 Diatom models performances

<b>Index</b>	<b>Model</b>	<b>Model R<sup>2</sup></b>	<b>Validation ASD R<sup>2</sup></b>	<b>Validation AISA R<sup>2</sup></b>
Area	$\text{LN}(\text{Diatom}) = 2.670(\text{A}/\text{D}) + 10.127(\text{D}/\text{C}) - 3.522(\text{G}/\text{C}) + 5.638$	0.208	<b>0.787</b>	<b>0.099</b>
Height/ Width	$\text{LN}(\text{Diatom}) = 0.752(\text{E}/\text{C}) - 1.729(\text{G}/\text{A}) + 11.663$	<b>0.216</b>	0.707	0.060
Narrow	$\text{LN}(\text{Diatom}) = 4.718(\text{A}/\text{D}) + 8.474$	0.206	0.248	0.080

Table 4-64 Green algae models performances

<b>Index</b>	<b>Model</b>	<b>Model R<sup>2</sup></b>	<b>Validation ASD R<sup>2</sup></b>	<b>Validation AISA R<sup>2</sup></b>
Area	$\text{LN}(\text{Green}) = 1.642(\text{A}/\text{D}) + 2.266(\text{E}/\text{A}) + 9.847$	0.285	0.062	<b>0.164</b>
Height/ Width	$\text{LN}(\text{Green}) = 0.375(\text{E}/\text{A}) + 13.343$	0.192	<b>0.130</b>	0.075
Narrow	$\text{LN}(\text{Green}) = -28.200(\text{A}) + 34.403(\text{D}) + 14.341(\text{A}/\text{B}) - 0.010$	<b>0.309</b>	0.059	0.000

Table 4-65 Bluegreen algae models performances

<b>Index</b>	<b>Model</b>	<b>Model R<sup>2</sup></b>	<b>Validation ASD R<sup>2</sup></b>	<b>Validation AISA R<sup>2</sup></b>
Area	$\text{LN(Bluegreen)} = - 3.123(A/G) + 1.977(C/A) - 66.849(D/B) - 7.727(D/E) + 28.569$	<b>0.580</b>	<b>0.721</b>	<b>0.564</b>
Height/ Width	$\text{LN(Bluegreen)} = 133.395(F) - 35.544(A/F) + 69.307(B/F) - 1.191(D/A) + 1.266$	0.353	0.287	0.266
Narrow	$\text{LN(Bluegreen)} = - 2.107(B/E) - 2.776(H/C) + 19.926$	0.320	0.658	0.027

Comparing all algae indicators, bluegreen model reported high R<sup>2</sup> but the correlation plot showed no correlation (Figure 4-30 to 4-32). In fact, only ASD diatom correlation graph showed a relatively strong correlation (Figure 4-25). None of the other algal validation demonstrated a relationship between the predicted and the actual algal biomass. AISA hyperspectral data in this study could not be effectively used with the algal indicators at all. The band width and location setting for the data used in this study may not be appropriate to the algal division assessment, although it worked better in the chlorophyll models.

There could be potential algal classification error associated with the algal biomass data, such as misclassification of Dinobryon (a Chrysophyte) to the green algae class. There was also some uncertainty associated in the

calculation of biovolume because no one reference source contained all of the standard biovolume for the algae found in studied samples. The standard biovolume for each species were determined from three different sources (Section 3.3.4) and some of them were different among the sources. In addition, not all of the species cell biovolumes could be found in the reference sources, and the exact number of cells within a unit was not recorded in the counting process. Therefore, the accuracy of biovolume determination was limited by insufficient data. Algal density was counted by unit (colonies), not by cell. Approximate number of cells per unit was determined before multiply the density with cell biovolume. The estimated biovolume of known species were used to determine a constant biovolume factor to represent each algal category. These factors were then multiplied with algal density for each lake. The final biovolume of algae in each lake represents a *relative* biomass of algae in each algal division. Figure 4-24 showed the range of algal biomass in the data sets. Diatoms dominated only one lake, green algae dominated a few lakes, and bluegreen algae (especially microcystis) appeared in many lakes and had an almost continuous range. This may explain why the bluegreen indicator models report higher  $R^2$  than other algal models. Bluegreen algae have absorption and reflectance features that are different from other algal type (discussed in Section 4.3.7), and wavebands where these features occur were selected by the regression model. Therefore, with larger and more complete data, there is a potential to assess bluegreen algae.

Comparing model accuracies of all variables, area region-waveband models performed better than narrow-waveband indicators. Region-waveband indicators take into account the wider range of wavelength that could be responsible to the predicting variables. The results showed the generalizability of the area region-waveband models that could capture changes in the signal of responding biophysical parameters in the water.

## **CHAPTER 5**

### **CONCLUSIONS AND FUTURE RESEARCH**

Hyperspectral remote sensing provides a valuable tool in water quality assessment. It has been successfully used to estimate spatial and temporal variation of water quality parameters primarily for marine waters, which has less optical complicating factors such as suspended solids and dissolved organic carbon than inland waters. Most of the previous hyperspectral studies on inland waters were performed over small spatial extents (e.g., one or a few lakes) or in controlled environments (e.g., laboratory spectral reading of several chlorophyll and suspended sediment conditions). This study was conducted in a natural environment of a large spatial extent (statewide scale) where several biophysical variables coexist. A total of 48 individual measurements of radiometric spectra, chlorophyll *a*, Secchi disc depth, suspended solid, non-purgable organic carbon, and phytoplankton species composition including diatom, green, and bluegreen algae, were collected during spring and summer of 2004. Hyperspectral sensors used in the study included a hand-held spectrometer (LabSpec® Pro, Range 350 nm – 2,500 nm, 1 nm interval with sampling interval 1.4 nm @ 350 nm – 1,050 nm and 2 nm @ 1,000 nm – 2,500 nm) and an Airborne Imaging Spectrometer for Applications (AISA, Range 434 nm – 900 nm, 3 nm – 8 nm bandwidth). The objectives of the study were (1) to identify optimal spectral bands that are most sensitive to water quality indicators in the various water bodies within Michigan; (2) to develop improved spectral water quality indicators; and (3) to compare the filter methods for noise

removal in hyperspectral remote sensing data. The purpose of the study was to develop generalizable algorithms that were spatially and temporally independent. Each of the objectives is discussed in the following sections.

### **5.1 Optimal Spectral Bands**

The most sensitive spectral bands that can be effectively used in inferring water quality information were identified in this study. Two sets of wavebands were located including narrow-wavebands and region-wavebands. The most sensitive narrow-wavebands (1 nm bandwidth) were at 435 nm, 455 nm, 470 nm, 565 nm, 670 nm, 675 nm, 690 nm, and 700 nm. Biophysical characteristics associated with these spectral bands were indicated in Table 4-3. The wavebands were identified using principle component analysis (PCA) and spectral derivative methods based on absorption and reflectance properties of the biophysical variables of interest. Region-wavebands were identified using a 1<sup>st</sup> derivative technique to detect spectral regions that were sensitive to changes in water quality variables. These spectral regions were 435 nm – 475 nm, 470 nm – 570 nm, 565 nm – 620 nm, 670 nm – 690 nm, 675 nm – 700 nm, 690 nm – 740 nm, and 700 nm – 740 nm. Table 4-2 explained biophysical characteristics associated with these wavebands. Different waveband regions were identified for different trophic waters.

Two spectral regions were detected for each of the near-infrared (NIR) and red regions to represent high and low trophic waters. Because the NIR peak shifted to the longer wavelengths when chlorophyll *a* increased, it was reasonable to

detect two spectral regions and compare which one was more sensitive to water quality parameters. The results clearly showed that the higher trophic waveband (waveband G) was selected in statistical process to use in the water quality indicator models more frequently for the NIR reflectance peak region, but the lower trophic waveband (waveband D) was used in the models more frequently for the red absorption region. For the NIR case, the selected waveband G had a narrower bandwidth (Figure 3-17), which automatically avoided an effect from the red absorption region (immediately next to it on the lower wavelength side). For the red spectral region case, waveband D covered the absorption feature better for most lakes.

Validation for each of the variables showed that 8-nm bandwidth AISA data provided similar accuracy as the 1-nm-bandwidth ASD data in the narrow-waveband models. However, when used in area and height/width region-waveband models, the 8-nm-bandwidth AISA produced lower accuracy than 1-nm-bandwidth ASD. The wide bandwidth of AISA particularly affected an implementation of water quality parameters in the region-waveband method, especially the height/width indicator method. It lowered the sensitivity of the spectral band regions when not enough data were available for the polynomial fitting process. For example, waveband D (670 nm – 690 nm) has 20 data values from the 1-nm-bandwidth ASD to input in the polynomial curve fitting, but only 3 data values from the 8-nm-bandwidth AISA. Results of this study suggest that the bandwidth for hyperspectral data to be effectively used in water quality assessment should be approximately 3 nm, or not more than 4

nm, and the waveband locations should be concentrated on wavelengths between 435 nm – 740 nm (with an exclusion of wavelength between 620 nm – 670 nm).

## **5.2 Spectral Indicators for Water Quality Assessment**

Quantitative relationships between water quality and remote sensing parameters with polynomial fitting were derived for seven water quality variables including Secchi depth (SD), Chlorophyll (CHL), Total Suspended Solid (TSS), Non-Purgable Organic Carbon (NPOC), diatom biomass, green algal biomass, and bluegreen algal biomass. Three spectral indicators – area, height/width, and narrow-wavebands – were developed and compared. Area-under-spectral-curve indicators were found to be the best indicators in this study in terms of goodness-of-fit reported by the regression models. Narrow-waveband indicators had the second best accuracy but the method is easier to use because these indicators used the filtered volume spectral reflectance from the lakes without processing through derivative calculation and polynomial fitting. Height/width indicators were not as sensitive to changes in biophysical variables as the other two indicators.

Among the seven spectral indicator models for water quality, Secchi depth, chlorophyll *a*, and bluegreen algal biomass models showed the most promising results in terms of using remote sensing to map water quality. High accuracies were reported in terms of goodness-of-fit when validated by hand-held and airborne spectrometer. The results showed goodness-of-fit ranked from the

Secchi depth ( $R^2$  0.76-0.84), chlorophyll *a* ( $R^2$  0.70-0.76), and bluegreen algae ( $R^2$  0.56-0.72) models. Spectral indicators for chlorophyll *a* used spectral regions from both low and high trophic types of water. They are therefore independent of trophic states. The models can be used to assess chlorophyll *a* condition in any waters regardless of trophic condition. The spectral indicators for TSS ( $R^2$  0.21-0.40), NPOC ( $R^2$  0.11-0.25), diatom ( $R^2$  0.10-0.79) and green algae ( $R^2$  0.13-0.31) did not produce accurate results due to limited availability of a wide range of these data. The data collection focused on a wide range of trophic state, which reflected in a continuous range of chlorophyll *a* and Secchi depth. Historical data for TSS, NPOC, and algal compositions in lakes were not available before the field data collection was conducted. Concentrations of these variables were low in most of the sampled lakes; therefore, the models were developed based on data that were bias toward the lower concentrations and tended to underestimate the actual values.

### **5.3 Effective Filters for Noise Removal**

A spectral filtering techniques need to be applied to hyperspectral data in order to remove noise generated from the atmosphere or within the sensor itself.

Three hyperspectral denoising filters – Savitsky Golay, wavelet Daubechies and wavelet Symlet – were compared for their ability to remove noise in the data while maintain sharp spectral absorption/reflectance features. Savitsky Golay proved to be the best method. It smoothed noise within the data while preserving sharp peaks and troughs because the filter calculated a local polynomial for every determined wavelength range (Figure 3-12). Symlet

wavelet was the second best method. It generated de-noised spectral signatures that seemed smooth but some of the high frequency noise still remained in the signature (Figure 3-13). The remaining noise showed in the 1<sup>st</sup> derivative product. Unlike Savitsky Golay, Symlet tended to flatten out the curves, which reduced the slope of the curve. As a result, derivatives from Symlet filter appeared flat and the wavelength range of absorption and reflectance features were more difficult to determine (Figure 3-15). Daubechies wavelet performed poorly in this study. It created a staircase artifact in the de-noised spectra, which generated a tremendous amount of zero values in the derivative product (Figure 3-12 and 3-15). The process required elimination of zero data, which reduce the spectral resolution of continuous 1-nm bandwidth to an inconsistent bandwidth depending on the location of zero values. When amounts of data were eliminated, polynomial fitting was based on fewer amounts of data than other filter methods.

#### **5.4 Major Findings**

The important contributions of this study include the development of an algorithm to answer remote sensing questions of which spectral wavebands are effective in inferring water quality information, and what filter method can be effective in removing noise and preserving important absorption and reflectance features. The study also answers the water quality monitoring question, “can remote sensing can be used effectively to assess water quality variables in natural ecosystem?” Quantitative relationships between remotely sensed spectra and three water quality indicators – Secchi depth, chlorophyll *a*

concentration, and bluegreen algal biomass – were developed with high accuracies in this study. Through this study, it was demonstrated that hyperspectral remote sensing could be used to infer water quality variables. Validation methods in the study showed that results from a hand-held hyperspectral instrument can be extended to airborne scale suggesting that hyperspectral remote sensing has a promising potential to be used to map water quality condition and facilitate improved water quality monitoring in large spatial extents at low cost.

The study also demonstrated that field measurements are unpredictably variable due to cloud condition, time of measurement, sun elevation angle, relative sun-target-sensor angle, and shadow casting from the boat. These potential sources of error could be avoided by taking multiple measurements at one site so that the spectra could be averaged and the effect of water surface glare minimized. Reference reflectance from the white reflectance panel must always be recorded immediately before and after the water reflectance measurements are taken in order to ensure the correction for inconsistent incident light. Water surface spectra should be taken as far from the boat as possible to avoid shadow effect. Measurements must be done consistently at the nadir angle regardless of waves on the water surface to keep the measurement of all lakes on the same standard. More spectra may be necessary if the water surface is rough.

Based on this study, a limited number of spectral bands were identified for water quality analysis. Based on the number of wavebands selected, it is suggested that hyperspectral data are not needed if multispectral data are designed to have narrow bandwidth position in the sensitive spectral wavelengths. The spectral wavebands identified in this study suggest the configuration of prototypes for the future satellite sensors, which provide useful spectral information of hundreds of water bodies at one time at reasonable cost.

### **5.5 Future Research**

(1) A new algal cell counting method needs to be employed to produce a better accurate *in situ* data. The algal samples should be counted to 300 units as did in this study but number of cells in a unit should also be recorded.

(2) Future research should include samples from more humic and high-suspended sediment lakes. The sampled lakes in this study were determined based on their trophic states because information on TSS or DOC of majority of lakes in Michigan was not obtainable. A more complete set of these data can improve the determination of spectral indicator models in the statistical process.

(3) Narrower and more frequent wavebands from an airborne hyperspectral sensor should be tested. Although the ASD proved useful according to the results and conclusion of this study and could save time and cost for water sampling and laboratory analysis, an airborne sensors such as AISA provides

additional spatial information such as mapping of water quality variables on a larger area. ASD measurements involve traveling to the lake, launching the boat, traveling to the sample sites, and then moving to the next lake. A maximum of seven lakes could be sampled in a working day by ASD method, but tens of lakes could be sampled by an airborne sensor in a shorter period of time.

(4) An analytical method similar to this study should be explored, deriving waveband regions and under-spectral-curve area directly from the spectral reflectance of the water instead of the derivative product of it. The derivative generally separated the reflectance curve in half. The method worked well in this study because it responded to changes in biophysical variables very well. However, by visual observation, the entire absorption/ reflectance curves from spectral reflectance seemed to respond with water quality as well. Therefore, they deserve further study.

**APPENDICES**

## APPENDIX A

### WATER QUALITY FIELD WORK PROTOCOL

1. Total 46 Michigan inland lakes, over 50 percent of which were in the Muskegon River Watershed, were selected based on their trophic states to have the widest range of trophic condition possible (Figure A-1; Table A-1). Trophic State Index (TSI) values were calculated from historical chlorophyll *a* (CHL) measurements from three sampling programs: (1) the Michigan Department of Environmental Quality's (MDEQ) Lake Water Quality Assessment (LWQA) Monitoring Program, (2) the Michigan Cooperative Lake Monitoring Program (CLMP), and (3) Professor R. Jan Stevenson's algal ecology lab, MSU Department of Zoology. These data were collected in spring and summer between May - August of 2001 to 2003.

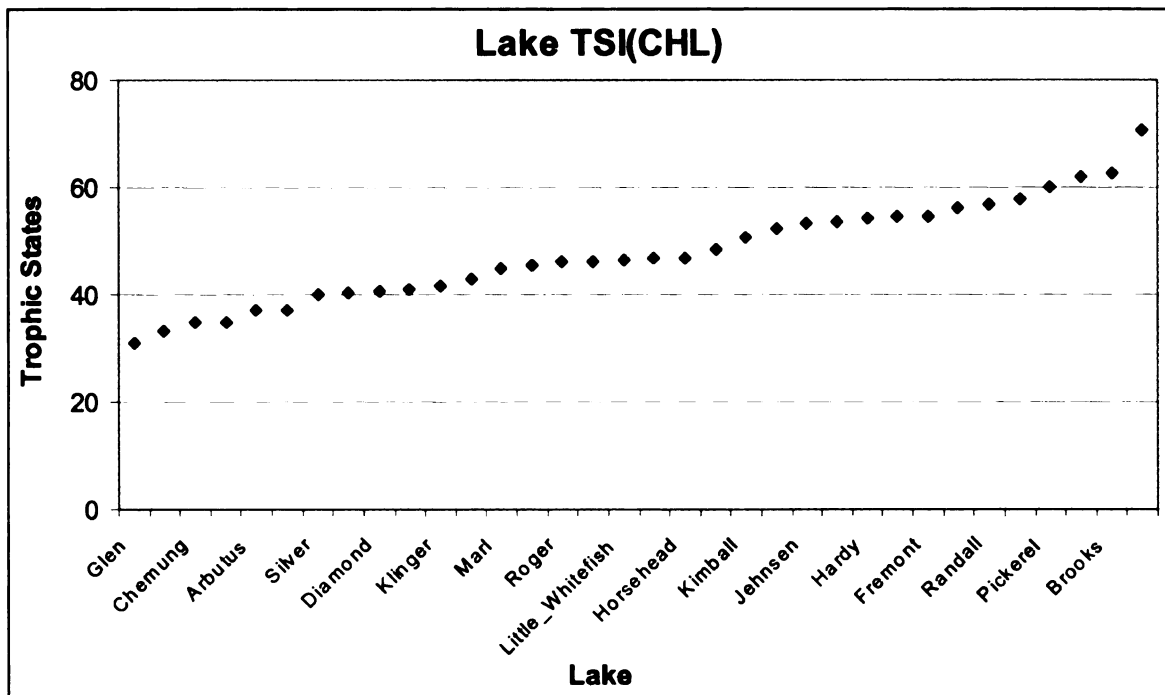


Figure A-1 Trophic conditions of the selected sample lakes

Table A-1 List of selected sample lakes

<b>Lake</b>	<b>TSI from CHL</b>	<b>Lake (continued)</b>	<b>TSI from CHL</b>
Glen (Big)	31.00	Muskegon	53.40
Higgins	33.28	Hardy Dam Pond	54.09
Chemung	35.00	Houghton	54.50
Sapphire	35.00	Fremont	54.60
Arbutus	37.00	Mitchell	55.98
Long Lake (Grand Traverse)	37.00	Randall	56.92
Silver	40.00	Croton dam pond	57.88
Clear (St. Joseph)	40.40	Pickerel	60.12
Diamond	40.50	Hess	62.00
Mecosta	40.98	Brooks	62.74
Klinger	41.50	Bear (Kalkaska)	70.61
Eagle	43.00	Belleville (Washtenaw)	unknown
Marl Lake	44.94	Cass (Oakland)	unknown
Big (Osceola)	45.50	Chipewa	unknown
Rogers Dam Pond	46.00	Cub	unknown
Tamarack	46.10	Ford (Washtenaw)	unknown
Little Whitefish	46.48	Hicks	unknown
Clear (Mecosta)	46.66	Kent (Oakland)	unknown
Horsehead Lake	46.77	Loon (Oakland)	unknown
Round (Mecosta)	48.50	Maceday (Oakland)	unknown
Kimball	50.50	Oakland (Oakland)	unknown
Pontiac (Oakland)	52.33	Orchard (Oakland)	unknown
Jehnsen	53.37	Paw Paw	unknown

2. Field work had been done in 13 weeks in two periods Apr 24 – Jun 12 and

Jul 17 – Aug 28 to collect:

2.1 GPS point coordinates

2.2 Spectral signatures using the ASD

2.3 Lake depth

2.4 Secchi-depth (SD)

2.5 Light extinction profile using LI-250 light meter

2.6 Dissolved Oxygen (DO)

2.7 Temperature

2.8 Chlorophyll *a* (Chl-*a*)

2.9 Total suspended solid (TSS)

2.10 Phytoplankton

2.11 Nutrients (TP and TN)

2.12 Dissolved organic carbon (DOC)

3. Procedure:

3.1 Launch the boat.

3.2 Turn on ASD and GPS.

3.3 Drive the boat to the deep basin of the lake. Lower the anchor. Record the GPS coordinate.

3.4 Measure the lake depth by lowering the Secchi disc to the bottom of the lake. Record the depth. Pull the Secchi disc up until it is visible. Record the Secchi-depth (SD).

3.5 Measure the light, DO, and Temperature. All the sensors are tied together with the lowering frame. Be sure to lower the lowering rope and not the sensor cables. Begin measurement from the surface of water (where water just covers the sensors). For lakes with shallower SD (< 4 m) record light, DO, and Temp every 0.5 m. For lakes with deeper SD (> 4 m) record every 1.0 m. Lower the sensors until the depth where light is lower 1 percent of the light at surface (at the beginning). Turn off the meters.

3.6 Water samples are collected for Chl-a, TSS, nutrients, algae, and color analysis. Samples for Chl-a, TSS, nutrients, and algae analysis will be taken using three methods: 1) Photic depth, 2) Secchi depth, and 3) Epilimnion depth. Samples for TN, TP, and DOC are taken using the photic depth method only.

- Photic depth can be calculated by multiplying the Secchi depth by 2.5. The depth is then divided by four to indicate the actual depth at which the water was collected each time. The mixture of the water from these four depths represents the column of the photic layer. After four liters of water is collected and drained into a bucket, it is transferred into one acid-washed 250ml-bottle for nutrients, two 30ml-glass vials for DOC, one 1,000ml-bottle for algae, one 1,000ml-bottle for Chl *a*, and one 1,000ml-bottle for TSS analysis.

- Secchi depth method collects water from the Secchi depth column.

The depth is divided into four depths. Approximately four liters of water are collected from four depths and mixed in a bucket. The sample is transferred into one acid-washed 250ml-bottle for nutrients, one 1,000ml-bottle for algae, and one 1,000ml-bottle for Chl-a and one 1,000ml-bottle for TSS analysis.

- The epilimnion layer does not appear in all lakes at the time of sampling. For lakes that have drastic changes in temperature profiles, one more set of samples will be collected for Chl-a, TSS, nutrients, and algae analysis. The epilimnion depth is divided by four to indicate the actual depths that samples are taken from.

- The chemical (M3) is added to the algae bottles to preserve algae cells. The rest of the samples are placed in a cooler. Samples for Chl-a and TSS are filtered *in situ* before covered with aluminum foil and kept in a freezer until analysis. Samples for DOC analysis are covered with aluminum foil on site and kept in a fridge until analysis. Samples for nutrients are kept in a freezer.

### 3.7 To take the spectral signatures

- Connect laptop with the ASD (after the ASD has warmed up for 15 minutes). Turn on the computer and navigate to FR B&W (an icon on the screen).

- Select 'Spectrum save' and change the path to the workspace folder to record spectral signatures. Change the starting number to 1. Change the view angle to match the angle on the sensor.

- Take out the white reflectance panel and hold the sensor above it. Be careful not to have any shadow on the panel. Click on 'OPT' and let the sensor calibrate. Once finished, continue to hold the sensor above the white reflectance panel and click on 'WR'. Perform the WR calibration. Save the white reflectance by pressing spacebar approximately 10 times.

- Hold the sensor approximately 1.5 meters above the water surface and save the water signature (approximately 10-15 signatures). Take another 10 signatures of white reflectance.

- Leave the laptop on if the distant to the next site is short. Move to the next site immediately or click on 'quit' and turn off the computer to save the laptop battery. Be sure to name the file differently when turning back on so it will not overwrite the existing signatures.

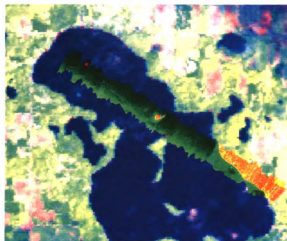
- To ensure enough samples in a bad weather situation, the ASD light source may be used if necessary when there is thick cloud cover.

- Move to two or three more sites in the lake to measure for the GPS coordinates, spectral signatures, and the Secchi depth. No water sample is taken at these sites. Turn off both laptop and ASD after finish the last site on the lake to save the batteries.

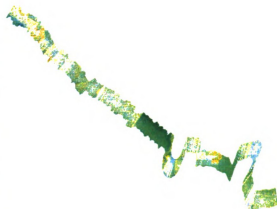
In summary, for each lake 3-4 sites are measured for spectral signature and SD, but only one deepest basin site is measured for Chl-a, TSS, algae, nutrients, and DOC. Depending on stratification of the lakes, two or three sets of Chl-a, TSS, nutrients, and algae samples are taken from each lake at the same site but at different depth.

**APPENDIX B**  
**AISA IMAGERY**

**AISA 20 bands imagery**



Long Lake (Grand Traverse)



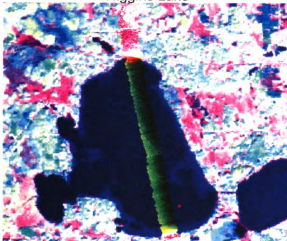
Silver Lake



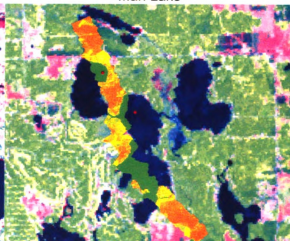
Higgins Lake



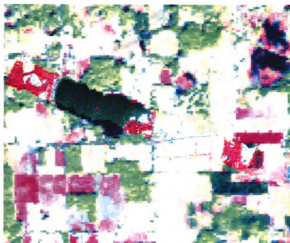
Marl Lake



Lake Mitchell



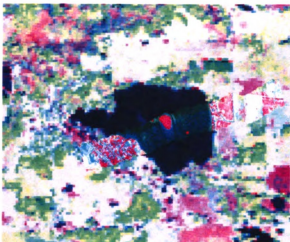
Mecosta and Round Lakes



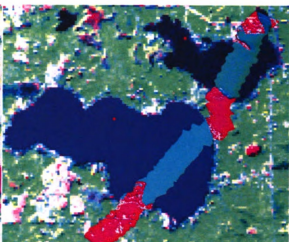
Clear Lake (Mecosta)



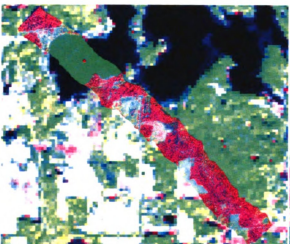
Roger Dam Pond



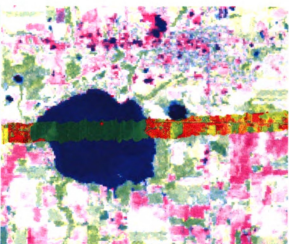
Tamarack Lake



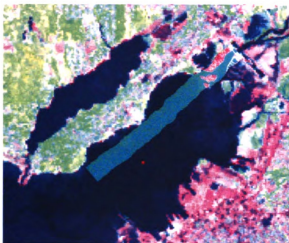
Brooks and Hess Lakes



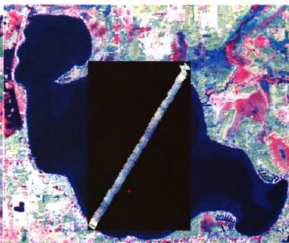
Kimball Lake



Fremont Lake



Muskegon Lake



Houghton Lake

**AISA 30 bands imagery**



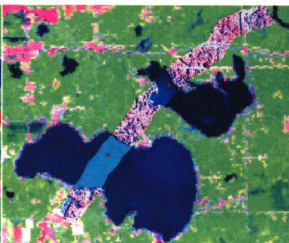
Muskegon Lake



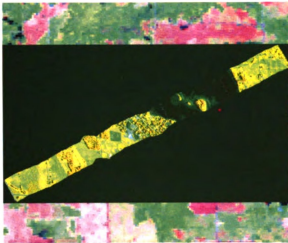
Fremont Lake



Kimball Lake



Brooks and Hess Lakes



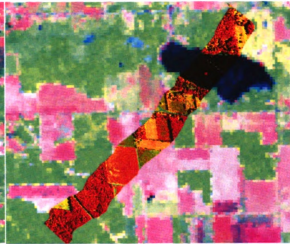
Tamarack Lake



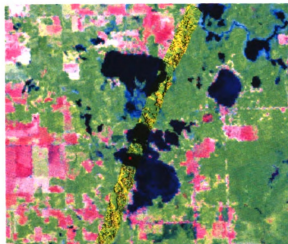
Hardy Dam Pond



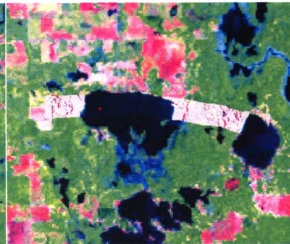
Roger Dam Pond



Clear Lake (Mecosta)



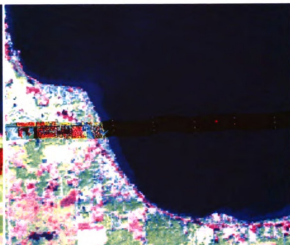
Horsehead Lake



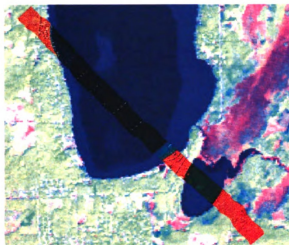
Jehnsen Lake



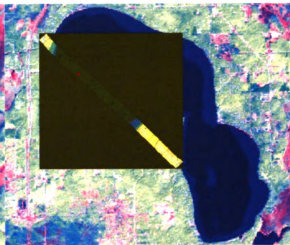
Sapphire Lake



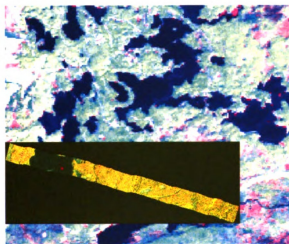
Houghton Lake



Marl Lake



Higgins Lake

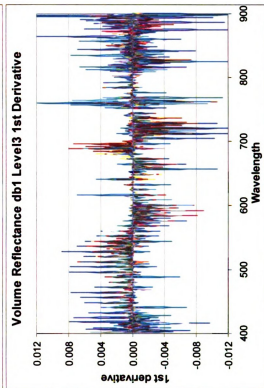
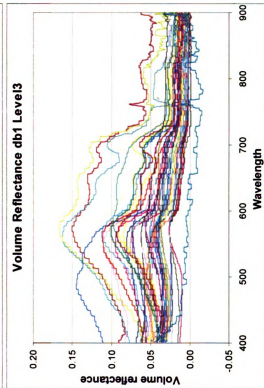
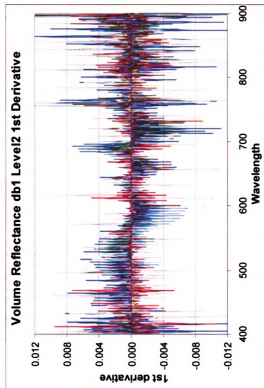
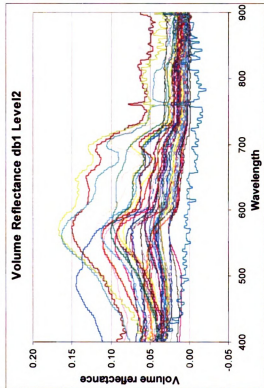


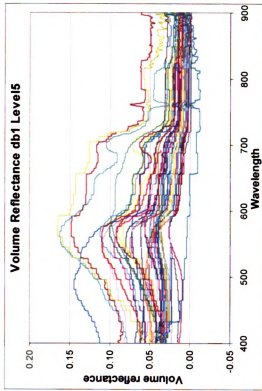
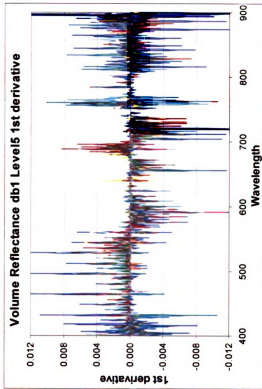
Arbutus Lake

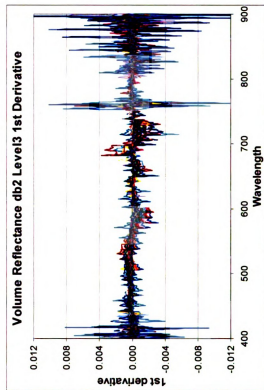
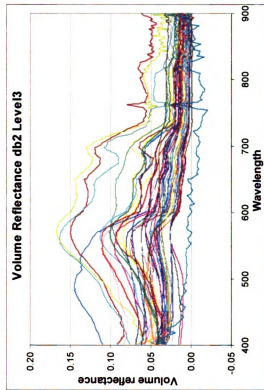
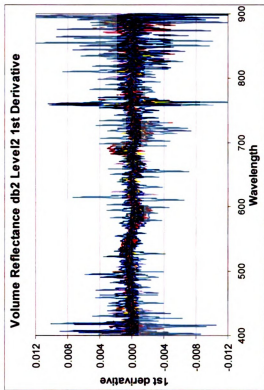
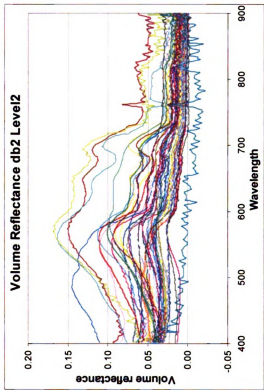


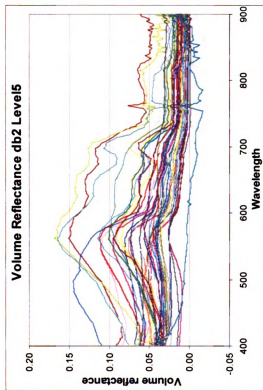
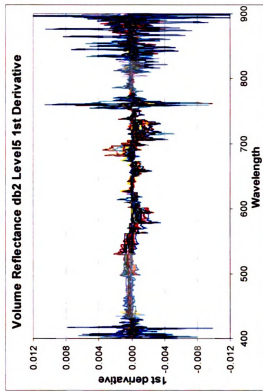
Long Lake (Grand Traverse)

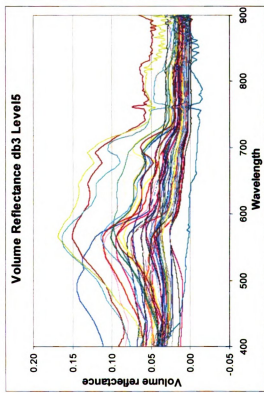
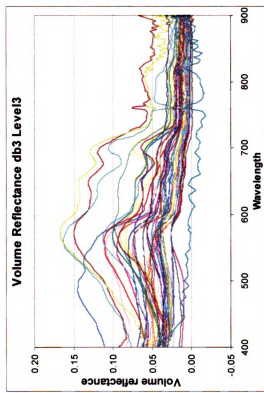
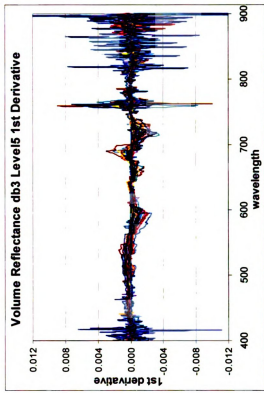
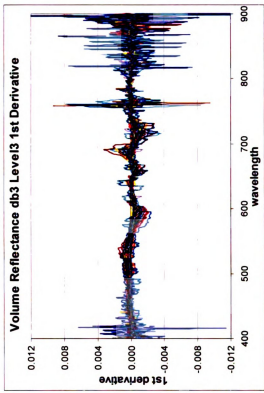
**APPENDIX C**  
**NOISE REMOVAL FILTERS COMPARISON**

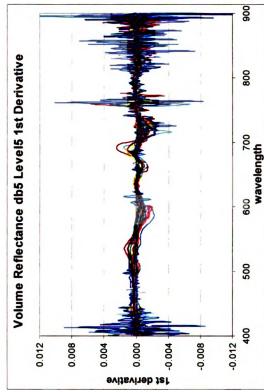
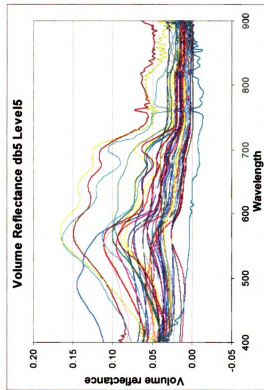
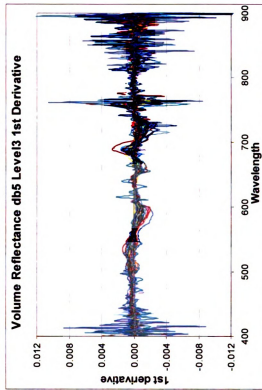
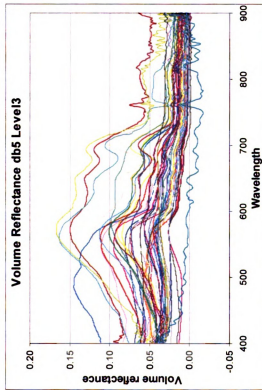












**APPENDIX D**  
**AREA UNDER THE SPECTRAL CURVE**

**Area under the curve used in area index sgolay filtered model data set**

<b>Band</b>	<b>A</b>	<b>B</b>	<b>C</b>	<b>D</b>	<b>E</b>	<b>F</b>	<b>G</b>
<b>Lake</b>	<b>435-475</b>	<b>470-570</b>	<b>565-620</b>	<b>670-690</b>	<b>675-700</b>	<b>690-740</b>	<b>700-740</b>
BEAR0819	0.0201	0.1189	0.0464	0.0189	0.0236	0.1153	0.0107
BELL0826	0.0169	0.1615	0.0386	0.0326	0.0401	0.1413	0.0408
BIG0820	0.0174	0.1378	0.0358	0.0178	0.0225	0.1205	0.0153
BROO0526	0.0132	0.1425	0.0305	0.0198	0.0275	0.1162	0.0135
CASS0810	0.0142	0.1347	0.0303	0.0176	0.0229	0.1190	0.0144
CHEM0826	0.0143	0.1333	0.0304	0.0186	0.0221	0.1201	0.0146
CHIP0820	0.0124	0.1403	0.0384	0.0183	0.0234	0.1208	0.0160
CLSJ0603	0.0188	0.1405	0.0452	0.0187	0.0243	0.1208	0.0164
CROT0605	0.0109	0.1245	0.0189	0.0195	0.0245	0.1217	0.0173
CUB0819	0.0200	0.1348	0.0470	0.0181	0.0221	0.1185	0.0130
DIAM0824	0.0246	0.1403	0.0740	0.0168	0.0214	0.1264	0.0206
EAGL0824	0.0157	0.1361	0.0390	0.0166	0.0208	0.1189	0.0137
FORD0826	0.0280	0.1910	0.0533	0.0384	0.0649	0.1531	0.0675
GLEN0819	0.0347	0.1004	0.0899	0.0154	0.0196	0.1226	0.0167
HESS0526	0.0363	0.1815	0.0582	0.0225	0.0402	0.1549	0.0586
HICK0820	0.0227	0.1734	0.0398	0.0293	0.0432	0.1509	0.0536
HIGG0608	0.0213	0.1159	0.0435	0.0173	0.0233	0.1145	0.0106
KENT0826	0.0150	0.1458	0.0332	0.0220	0.0259	0.1299	0.0245
KIMB0526	0.0272	0.1665	0.0195	0.0144	0.0171	0.1573	0.0491
KLIN0603	0.0203	0.1251	0.0476	0.0172	0.0228	0.1172	0.0126
LOON0810	0.0158	0.1375	0.0314	0.0182	0.0238	0.1176	0.0132
LOTU0807	0.0301	0.1569	0.0716	0.0147	0.0175	0.1313	0.0238
MACE0807	0.0278	0.1495	0.0654	0.0168	0.0212	0.1218	0.0162
MECO0608	0.0141	0.1295	0.0287	0.0179	0.0231	0.1205	0.0158
MECO0724	0.0224	0.1551	0.0385	0.0205	0.0216	0.1290	0.0210
AWRI0728	0.0140	0.1361	0.0254	0.0213	0.0284	0.1277	0.0248
OAKL0807	0.0160	0.1340	0.0298	0.0170	0.0219	0.1179	0.0131
ORCH0810	0.0280	0.1478	0.0685	0.0160	0.0191	0.1259	0.0189
PAWP0824	0.0244	0.1710	0.0594	0.0228	0.0296	0.1442	0.0403
PICK0526	0.0255	0.1729	0.0483	0.0261	0.0408	0.1471	0.0502
PONT0807	0.0274	0.1721	0.0458	0.0198	0.0252	0.1425	0.0371
RAND0603	0.0130	0.1294	0.0278	0.0198	0.0247	0.1188	0.0144
ROGE0519	0.0147	0.1344	0.0153	0.0193	0.0245	0.1285	0.0243
SILV0725	0.0264	0.1465	0.0582	0.0187	0.0230	0.1228	0.0174

**Area under the curve used in area index agolay filtered validation data set**

<b>Band</b>	<b>A</b>	<b>B</b>	<b>C</b>	<b>D</b>	<b>E</b>	<b>F</b>	<b>G</b>
<b>Lake</b>	<b>435-475</b>	<b>470-570</b>	<b>565-620</b>	<b>670-690</b>	<b>675-700</b>	<b>690-740</b>	<b>700-740</b>
ARBU0726	0.0193	0.1334	0.0545	0.0163	0.0217	0.1199	0.0150
BROO0727	0.0297	0.1754	0.0388	0.0217	0.0270	0.1697	0.0637
CLME0724	0.0167	0.1403	0.0381	0.0185	0.0223	0.1243	0.0185
HESS0727	0.0427	0.1982	0.0415	0.0207	0.0281	0.1846	0.0797
HIGG0727	0.0229	0.1095	0.0464	0.0174	0.0236	0.1127	0.0090
HOUG0726	0.0165	0.1432	0.0309	0.0176	0.0221	0.1254	0.0200
JEHN0519	0.0160	0.1413	0.0302	0.0189	0.0235	0.1231	0.0180
MITC0725	0.0164	0.1412	0.0244	0.0183	0.0231	0.1303	0.0251
MUSK0728	0.0121	0.1305	0.0231	0.0233	0.0302	0.1263	0.0237
ROGE0724	0.0187	0.1456	0.0224	0.0201	0.0239	0.1348	0.0291
SAPP0725	0.0152	0.1360	0.0332	0.0189	0.0251	0.1200	0.0161
TAMA0605	0.0118	0.1273	0.0242	0.0199	0.0242	0.1184	0.0133

**Area under the curve used in area index db1 filtered model data set**

<b>Band</b>	<b>A</b>	<b>B</b>	<b>C</b>	<b>D</b>	<b>F</b>	<b>G</b>
<b>Lake</b>	<b>435-485</b>	<b>485-575</b>	<b>550-630</b>	<b>675-700</b>	<b>690-745</b>	<b>700-745</b>
BEAR0819	0.1893	0.3664	0.4808	0.1100	0.4328	0.0978
BELLO826	0.1781	0.5562	0.4315	0.1552	0.4967	0.1710
BIG0820	0.1638	0.4882	0.4465	0.0892	0.4571	0.1097
BROO0526	0.1295	0.4497	0.3803	0.1180	0.4223	0.0894
CASS0810	0.1391	0.4551	0.3962	0.1056	0.4391	0.1018
CHEM0826	0.1322	0.4784	0.4374	0.0897	0.4602	0.1124
CHIP0820	0.1404	0.5042	0.4579	0.0903	0.4631	0.1219
CLSJ0603	0.1820	0.5054	0.4556	0.1030	0.4824	0.1367
CROT0605	0.1151	0.4034	0.3644	0.1067	0.4807	0.1404
CUB0819	0.1791	0.4693	0.5153	0.0937	0.4744	0.1175
DIAM0824	0.2078	0.4756	0.5168	0.0947	0.4714	0.1279
EAGL0824	0.1566	0.4786	0.4323	0.0924	0.4547	0.1149
FORD0826	0.2328	0.5876	0.4819	0.1885	0.5192	0.2120
GLEN0819	0.2436	0.2622	0.5618	0.0926	0.4766	0.1261
HESS0526	0.2350	0.5584	0.4794	0.1504	0.5019	0.1854
HICK0820	0.2133	0.6205	0.4299	0.1769	0.5304	0.2173
HIGG0608	0.2024	0.3394	0.4702	0.0899	0.4442	0.1023
KENT0826	0.1569	0.5148	0.4120	0.1110	0.4833	0.1306
KIMB0526	0.2041	0.5413	0.3436	0.0846	0.4951	0.1530
KLIN0603	0.1850	0.3899	0.4859	0.0905	0.4438	0.1097
LOON0810	0.1573	0.4954	0.4072	0.1022	0.4594	0.1171
LOTU0807	0.2245	0.5154	0.5119	0.0747	0.4828	0.1313
MACE0807	0.1904	0.4753	0.4469	0.0924	0.4451	0.1014
MECO0608	0.1370	0.4419	0.4037	0.1077	0.4737	0.1368
MECO0724	0.1970	0.6308	0.4667	0.1049	0.4998	0.1455
AWRI0728	0.1447	0.4895	0.4010	0.1242	0.4759	0.1400
OAKL0807	0.1606	0.4713	0.4266	0.0790	0.4795	0.1226
ORCH0810	0.2727	0.4788	0.5624	0.0860	0.4804	0.1217
PAWP0824	0.2064	0.5942	0.4947	0.1307	0.5355	0.1866
PICK0526	0.2194	0.5948	0.4734	0.1708	0.5244	0.2187
PONT0807	0.2397	0.5915	0.4345	0.1130	0.5210	0.1692
RAND0603	0.1335	0.4357	0.4143	0.1005	0.4853	0.1340
ROGE0519	0.1428	0.4442	0.3335	0.1123	0.4328	0.0981
SILV0725	0.2386	0.5051	0.5399	0.0989	0.4879	0.1319

**Area under the curve used in area index db1 filtered validation data set**

<b>Band</b>	<b>A</b>	<b>B</b>	<b>C</b>	<b>D</b>	<b>F</b>	<b>G</b>
<b>Wavelength</b>	<b>435-485</b>	<b>485-575</b>	<b>550-630</b>	<b>675-700</b>	<b>690-745</b>	<b>700-745</b>
ARBU0726	0.1674	0.4489	0.4517	0.0916	0.4496	0.1126
BROO0727	0.2673	0.7211	0.4611	0.1501	0.6208	0.2688
CLME0724	0.1566	0.5044	0.4420	0.1070	0.4673	0.1263
HESS0727	0.3171	0.8309	0.4566	0.1496	0.6180	0.2723
HIGG0727	0.1983	0.3219	0.4685	0.0995	0.4264	0.0920
HOUG0726	0.1496	0.5164	0.3987	0.1046	0.4661	0.1231
JEHN0519	0.1534	0.4568	0.3756	0.1122	0.4353	0.0997
MITC0725	0.1615	0.5078	0.3796	0.0951	0.4743	0.1324
MUSK0728	0.1234	0.4334	0.3888	0.1298	0.4523	0.1234
ROGE0724	0.1815	0.4970	0.3642	0.1151	0.4692	0.1282
SAPP0725	0.1499	0.4728	0.4066	0.1112	0.4512	0.1111
TAMA0605	0.1065	0.4322	0.4067	0.1035	0.4733	0.1163

**Area under the curve used in area index s8 filtered model data set**

<b>Band</b>	<b>A</b>	<b>B</b>	<b>C</b>	<b>D</b>	<b>E</b>	<b>F</b>	<b>G</b>
<b>Lake</b>	<b>435-475</b>	<b>470-570</b>	<b>565-620</b>	<b>670-690</b>	<b>675-700</b>	<b>690-740</b>	<b>700-740</b>
BEAR0819	0.0608	0.0801	0.0506	0.0697	0.0781	0.1429	0.0403
BELL0826	0.0572	0.1215	0.0380	0.0850	0.0916	0.1695	0.0712
BIG0820	0.0616	0.0994	0.0375	0.0664	0.0739	0.1480	0.0454
BROO0526	0.0613	0.1053	0.0322	0.0702	0.0778	0.1440	0.0440
CASS0810	0.0607	0.0970	0.0323	0.0672	0.0749	0.1467	0.0446
CHEM0826	0.0532	0.0964	0.0312	0.0682	0.0755	0.1485	0.0452
CHIP0820	0.0569	0.1021	0.0391	0.0669	0.0746	0.1486	0.0458
CLSJ0603	0.0584	0.1014	0.0471	0.0679	0.0756	0.1486	0.0463
CROT0605	0.0573	0.0880	0.0223	0.0700	0.0777	0.1493	0.0474
CUB0819	0.0593	0.0952	0.0493	0.0670	0.0747	0.1456	0.0419
DIAM0824	0.0611	0.1005	0.0763	0.0634	0.0701	0.1543	0.0508
EAGL0824	0.0556	0.0975	0.0386	0.0664	0.0747	0.1474	0.0438
FORD0826	0.0629	0.1476	0.0508	0.0985	0.1080	0.1803	0.1001
GLEN0819	0.0769	0.0592	0.0942	0.0631	0.0703	0.1503	0.0467
HESS0526	0.0755	0.1364	0.0563	0.0704	0.0767	0.1832	0.0917
HICK0820	0.0614	0.1322	0.0384	0.0805	0.0866	0.1790	0.0845
HIGG0608	0.0647	0.0767	0.0471	0.0681	0.0767	0.1423	0.0404
KENT0826	0.0589	0.1067	0.0344	0.0700	0.0762	0.1581	0.0547
KIMB0526	0.0737	0.1216	0.0214	0.0582	0.0628	0.1852	0.0795
KLIN0603	0.0647	0.0848	0.0506	0.0672	0.0751	0.1447	0.0429
LOON0810	0.0607	0.0989	0.0330	0.0681	0.0758	0.1455	0.0432
LOTU0807	0.0686	0.1119	0.0727	0.0598	0.0659	0.1596	0.0539
MACE0807	0.0684	0.1060	0.0673	0.0655	0.0730	0.1495	0.0462
MECO0608	0.0598	0.0923	0.0311	0.0673	0.0748	0.1482	0.0460
MECO0724	0.0654	0.1150	0.0405	0.0651	0.0709	0.1561	0.0497
AWRI0728	0.0576	0.0981	0.0278	0.0716	0.0788	0.1556	0.0553
OAKL0807	0.0584	0.0955	0.0317	0.0678	0.0756	0.1443	0.0422
ORCH0810	0.0656	0.1047	0.0702	0.0631	0.0691	0.1536	0.0483
PAWP0824	0.0582	0.1306	0.0578	0.0680	0.0731	0.1722	0.0702
PICK0526	0.0624	0.1308	0.0489	0.0780	0.0852	0.1745	0.0807
PONT0807	0.0664	0.1284	0.0466	0.0649	0.0699	0.1708	0.0675
RAND0603	0.0551	0.0916	0.0300	0.0704	0.0782	0.1469	0.0443
ROGE0519	0.0609	0.0962	0.0184	0.0705	0.0779	0.1563	0.0546
SILV0725	0.0628	0.1053	0.0604	0.0664	0.0736	0.1501	0.0467

**Area under the curve used in area index s8 filtered validation data set**

<b>Band</b>	<b>A</b>	<b>B</b>	<b>C</b>	<b>D</b>	<b>E</b>	<b>F</b>	<b>G</b>
<b>Lake</b>	<b>435-475</b>	<b>470-570</b>	<b>565-620</b>	<b>670-690</b>	<b>675-700</b>	<b>690-740</b>	<b>700-740</b>
ARBU0726	0.0606	0.0949	0.0568	0.0653	0.0728	0.1477	0.0452
BROO0727	0.0608	0.1307	0.0388	0.0635	0.0664	0.1967	0.0927
CLME0724	0.0573	0.1018	0.0401	0.0670	0.0742	0.1519	0.0485
HESS0727	0.0723	0.1501	0.0405	0.0630	0.0659	0.2134	0.1109
HIGG0727	0.0670	0.0710	0.0509	0.0689	0.0776	0.1404	0.0394
HOUG0726	0.0604	0.1049	0.0324	0.0652	0.0724	0.1531	0.0498
JEHN0519	0.0622	0.1025	0.0319	0.0681	0.0752	0.1509	0.0481
MITC0725	0.0619	0.1022	0.0263	0.0667	0.0734	0.1581	0.0554
MUSK0728	0.0575	0.0934	0.0262	0.0748	0.0823	0.1541	0.0542
ROGE0724	0.0627	0.1065	0.0243	0.0680	0.0741	0.1626	0.0590
SAPP0725	0.0594	0.0981	0.0351	0.0685	0.0760	0.1478	0.0462
TAMA0605	0.0536	0.0905	0.0266	0.0697	0.0771	0.1460	0.0431

**APPENDIX E**  
**MAXIMUM SPECTRAL CURVE HEIGHT**

Maximum height used in height/width index agolay filtered model data set

<b>Band</b>	<b>A</b>	<b>B</b>	<b>C</b>	<b>D</b>	<b>E</b>	<b>F</b>	<b>G</b>
<b>Lake</b>	<b>435-475</b>	<b>470-570</b>	<b>565-620</b>	<b>670-690</b>	<b>675-700</b>	<b>690-740</b>	<b>700-740</b>
BEAR0819	0.0005	0.0013	0.0011	0.0011	0.0012	0.0024	0.0004
BELLO826	0.0005	0.0019	0.0009	0.0018	0.0019	0.0034	0.0014
BIG0820	0.0004	0.0014	0.0009	0.0009	0.0011	0.0025	0.0005
BROO0526	0.0003	0.0015	0.0007	0.0011	0.0012	0.0025	0.0005
CASS0810	0.0004	0.0014	0.0007	0.0009	0.0010	0.0024	0.0004
CHEM0826	0.0004	0.0014	0.0007	0.0011	0.0011	0.0025	0.0005
CHIP0820	0.0004	0.0015	0.0010	0.0010	0.0012	0.0025	0.0005
CLSJ0603	0.0005	0.0015	0.0011	0.0010	0.0011	0.0025	0.0005
CROT0605	0.0004	0.0013	0.0004	0.0010	0.0012	0.0025	0.0005
CUB0819	0.0005	0.0015	0.0011	0.0010	0.0011	0.0025	0.0005
DIAM0824	0.0007	0.0017	0.0018	0.0009	0.0010	0.0026	0.0006
EAGL0824	0.0005	0.0014	0.0009	0.0011	0.0010	0.0025	0.0004
FORD0826	0.0008	0.0023	0.0012	0.0033	0.0032	0.0044	0.0026
GLEN0819	0.0009	0.0015	0.0023	0.0009	0.0009	0.0025	0.0005
HESS0526	0.0010	0.0022	0.0013	0.0020	0.0020	0.0042	0.0022
HICK0820	0.0006	0.0020	0.0009	0.0020	0.0021	0.0037	0.0017
HIGG0608	0.0006	0.0014	0.0010	0.0009	0.0010	0.0023	0.0003
KENT0826	0.0004	0.0016	0.0008	0.0012	0.0013	0.0027	0.0007
KIMB0526	0.0007	0.0017	0.0005	0.0008	0.0009	0.0035	0.0015
KLIN0603	0.0005	0.0014	0.0011	0.0009	0.0010	0.0024	0.0003
LOON0810	0.0004	0.0014	0.0007	0.0009	0.0011	0.0024	0.0005
LOTU0807	0.0008	0.0018	0.0019	0.0008	0.0009	0.0028	0.0008
MACE0807	0.0007	0.0017	0.0017	0.0009	0.0010	0.0025	0.0005
MECO0608	0.0004	0.0013	0.0006	0.0009	0.0010	0.0024	0.0004
MECO0724	0.0007	0.0016	0.0010	0.0011	0.0012	0.0028	0.0009
AWRI0728	0.0004	0.0014	0.0005	0.0012	0.0013	0.0028	0.0008
OAKL0807	0.0004	0.0014	0.0007	0.0010	0.0011	0.0024	0.0003
ORCH0810	0.0008	0.0017	0.0018	0.0009	0.0011	0.0026	0.0006
PAWP0824	0.0007	0.0020	0.0015	0.0014	0.0014	0.0033	0.0013
PICK0526	0.0007	0.0020	0.0011	0.0020	0.0020	0.0037	0.0017
PONT0807	0.0007	0.0019	0.0012	0.0011	0.0012	0.0032	0.0011
RAND0603	0.0004	0.0013	0.0006	0.0011	0.0012	0.0024	0.0004
ROGE0519	0.0004	0.0014	0.0003	0.0010	0.0011	0.0027	0.0007
SILV0725	0.0007	0.0017	0.0015	0.0010	0.0011	0.0025	0.0005

**Maximum height used in height/width index sgolay filtered validation data set**

<b>Band</b>	<b>A</b>	<b>B</b>	<b>C</b>	<b>D</b>	<b>E</b>	<b>F</b>	<b>G</b>
<b>Lake</b>	<b>435-475</b>	<b>470-570</b>	<b>565-620</b>	<b>670-690</b>	<b>675-700</b>	<b>690-740</b>	<b>700-740</b>
ARBU0726	0.0005	0.0015	0.0013	0.0008	0.0010	0.0025	0.0005
BROO0727	0.0008	0.0019	0.0010	0.0013	0.0014	0.0039	0.0018
CLME0724	0.0005	0.0015	0.0009	0.0010	0.0011	0.0025	0.0006
HESS0727	0.0012	0.0022	0.0011	0.0013	0.0014	0.0046	0.0027
HIGG0727	0.0006	0.0013	0.0011	0.0009	0.0010	0.0023	0.0003
HOUG0726	0.0005	0.0015	0.0007	0.0009	0.0011	0.0026	0.0006
JEHN0519	0.0004	0.0015	0.0007	0.0010	0.0011	0.0026	0.0006
MITC0725	0.0004	0.0015	0.0005	0.0010	0.0011	0.0028	0.0008
MUSK0728	0.0003	0.0014	0.0005	0.0012	0.0013	0.0028	0.0008
ROGE0724	0.0005	0.0015	0.0006	0.0011	0.0012	0.0029	0.0009
SAPP0725	0.0004	0.0014	0.0007	0.0010	0.0011	0.0025	0.0005
TAMA0605	0.0003	0.0013	0.0005	0.0010	0.0012	0.0025	0.0005

**Maximum height used in height/width index db1 filtered model data set**

<b>Band</b>	<b>A</b>	<b>B</b>	<b>C</b>	<b>D</b>	<b>F</b>	<b>G</b>
<b>Lake</b>	<b>435-485</b>	<b>485-575</b>	<b>550-630</b>	<b>675-700</b>	<b>690-745</b>	<b>700-745</b>
BEAR0819	0.0038	0.0048	0.0068	0.0067	0.0081	0.0032
BELL0826	0.0047	0.0071	0.0065	0.0069	0.0108	0.0050
BIG0820	0.0036	0.0059	0.0066	0.0063	0.0089	0.0029
BROO0526	0.0027	0.0052	0.0051	0.0050	0.0080	0.0023
CASS0810	0.0030	0.0053	0.0054	0.0046	0.0082	0.0025
CHEM0826	0.0032	0.0056	0.0066	0.0073	0.0090	0.0030
CHIP0820	0.0050	0.0065	0.0069	0.0053	0.0089	0.0034
CLSJ0603	0.0041	0.0069	0.0066	0.0069	0.0092	0.0035
CROT0605	0.0029	0.0047	0.0046	0.0078	0.0094	0.0040
CUB0819	0.0037	0.0061	0.0077	0.0095	0.0102	0.0032
DIAM0824	0.0045	0.0064	0.0073	0.0048	0.0088	0.0034
EAGL0824	0.0038	0.0060	0.0063	0.0118	0.0087	0.0031
FORD0826	0.0053	0.0076	0.0076	0.0089	0.0119	0.0065
GLEN0819	0.0050	0.0037	0.0078	0.0061	0.0093	0.0035
HESS0526	0.0049	0.0072	0.0071	0.0074	0.0108	0.0050
HICK0820	0.0050	0.0079	0.0070	0.0078	0.0113	0.0057
HIGG0608	0.0045	0.0044	0.0062	0.0044	0.0081	0.0025
KENT0826	0.0042	0.0060	0.0062	0.0055	0.0097	0.0036
KIMB0526	0.0042	0.0064	0.0052	0.0041	0.0095	0.0038
KLIN0603	0.0040	0.0051	0.0065	0.0048	0.0084	0.0029
LOON0810	0.0035	0.0060	0.0060	0.0064	0.0088	0.0031
LOTU0807	0.0051	0.0067	0.0076	0.0050	0.0094	0.0038
MACE0807	0.0040	0.0059	0.0064	0.0056	0.0087	0.0025
MECO0608	0.0029	0.0052	0.0055	0.0055	0.0090	0.0034
MECO0724	0.0050	0.0079	0.0084	0.0094	0.0107	0.0071
AWRI0728	0.0032	0.0060	0.0057	0.0057	0.0093	0.0035
OAKL0807	0.0035	0.0053	0.0061	0.0045	0.0101	0.0029
ORCH0810	0.0061	0.0069	0.0086	0.0089	0.0102	0.0029
PAWP0824	0.0045	0.0078	0.0083	0.0061	0.0105	0.0049
PICK0526	0.0045	0.0077	0.0077	0.0077	0.0116	0.0057
PONT0807	0.0061	0.0073	0.0068	0.0054	0.0100	0.0043
RAND0603	0.0032	0.0051	0.0058	0.0065	0.0093	0.0034
ROGE0519	0.0030	0.0050	0.0043	0.0052	0.0080	0.0022
SILV0725	0.0058	0.0067	0.0081	0.0091	0.0108	0.0051

**Maximum height used in height/width index db1 filtered validation data set**

<b>Band</b>	<b>A</b>	<b>B</b>	<b>C</b>	<b>D</b>	<b>F</b>	<b>G</b>
<b>Lake</b>	<b>435-485</b>	<b>485-575</b>	<b>550-630</b>	<b>675-700</b>	<b>690-745</b>	<b>700-745</b>
ARBU0726	0.0036	0.0055	0.0062	0.0040	0.0084	0.0026
BROO0727	0.0067	0.0101	0.0080	0.0075	0.0124	0.0067
CLME0724	0.0033	0.0061	0.0070	0.0078	0.0088	0.0032
HESS0727	0.0078	0.0113	0.0086	0.0071	0.0138	0.0082
HIGG0727	0.0043	0.0040	0.0064	0.0061	0.0081	0.0025
HOUG0726	0.0032	0.0062	0.0060	0.0073	0.0090	0.0032
JEHN0519	0.0032	0.0051	0.0051	0.0057	0.0081	0.0024
MITC0725	0.0041	0.0059	0.0056	0.0049	0.0091	0.0041
MUSK0728	0.0030	0.0052	0.0051	0.0056	0.0089	0.0032
ROGE0724	0.0042	0.0057	0.0053	0.0078	0.0089	0.0032
SAPP0725	0.0031	0.0057	0.0056	0.0055	0.0084	0.0027
TAMA0605	0.0029	0.0052	0.0057	0.0092	0.0101	0.0028

**Maximum height used in height/width index s8 filtered model data set**

<b>Band</b>	<b>A</b>	<b>B</b>	<b>C</b>	<b>D</b>	<b>E</b>	<b>F</b>	<b>G</b>
<b>Lake</b>	<b>435-475</b>	<b>470-570</b>	<b>565-620</b>	<b>670-690</b>	<b>675-700</b>	<b>690-740</b>	<b>700-740</b>
BEAR0819	0.0017	0.0011	0.0013	0.0019	0.0019	0.0031	0.0010
BELL0826	0.0016	0.0017	0.0009	0.0027	0.0026	0.0040	0.0022
BIG0820	0.0017	0.0013	0.0010	0.0018	0.0018	0.0031	0.0012
BROO0526	0.0016	0.0014	0.0008	0.0019	0.0019	0.0030	0.0013
CASS0810	0.0016	0.0012	0.0008	0.0018	0.0017	0.0030	0.0012
CHEM0826	0.0017	0.0012	0.0008	0.0018	0.0018	0.0031	0.0013
CHIP0820	0.0016	0.0014	0.0011	0.0018	0.0018	0.0031	0.0013
CLSJ0603	0.0016	0.0014	0.0012	0.0018	0.0018	0.0030	0.0012
CROT0605	0.0016	0.0011	0.0005	0.0018	0.0018	0.0030	0.0012
CUB0819	0.0018	0.0013	0.0013	0.0018	0.0018	0.0031	0.0011
DIAM0824	0.0018	0.0015	0.0021	0.0017	0.0017	0.0032	0.0014
EAGL0824	0.0015	0.0013	0.0011	0.0018	0.0019	0.0032	0.0011
FORD0826	0.0018	0.0023	0.0013	0.0038	0.0036	0.0052	0.0035
GLEN0819	0.0021	0.0009	0.0026	0.0017	0.0016	0.0031	0.0013
HESS0526	0.0021	0.0021	0.0014	0.0025	0.0025	0.0049	0.0030
HICK0820	0.0018	0.0019	0.0010	0.0027	0.0027	0.0044	0.0026
HIGG0608	0.0017	0.0010	0.0012	0.0018	0.0018	0.0030	0.0010
KENT0826	0.0017	0.0014	0.0009	0.0020	0.0020	0.0033	0.0015
KIMB0526	0.0019	0.0016	0.0006	0.0016	0.0016	0.0041	0.0023
KLIN0603	0.0017	0.0012	0.0013	0.0017	0.0017	0.0029	0.0011
LOON0810	0.0016	0.0013	0.0008	0.0018	0.0018	0.0030	0.0012
LOTU0807	0.0019	0.0016	0.0021	0.0016	0.0016	0.0033	0.0015
MACE0807	0.0019	0.0015	0.0019	0.0017	0.0017	0.0031	0.0012
MECO0608	0.0015	0.0012	0.0008	0.0018	0.0018	0.0030	0.0012
MECO0724	0.0019	0.0015	0.0011	0.0020	0.0019	0.0035	0.0016
AWRI0728	0.0015	0.0013	0.0006	0.0020	0.0020	0.0034	0.0015
OAKL0807	0.0015	0.0012	0.0008	0.0019	0.0019	0.0030	0.0011
ORCH0810	0.0018	0.0015	0.0019	0.0017	0.0017	0.0033	0.0013
PAWP0824	0.0017	0.0019	0.0016	0.0022	0.0022	0.0039	0.0021
PICK0526	0.0018	0.0019	0.0013	0.0025	0.0025	0.0043	0.0026
PONT0807	0.0018	0.0018	0.0013	0.0020	0.0019	0.0038	0.0019
RAND0603	0.0015	0.0012	0.0007	0.0019	0.0019	0.0030	0.0012
ROGE0519	0.0016	0.0012	0.0004	0.0019	0.0018	0.0033	0.0015
SILV0725	0.0022	0.0015	0.0017	0.0018	0.0018	0.0031	0.0013

**Maximum height used in height/width index s8 filtered validation data set**

<b>Band</b>	<b>A</b>	<b>B</b>	<b>C</b>	<b>D</b>	<b>E</b>	<b>F</b>	<b>G</b>
<b>Lake</b>	<b>435-475</b>	<b>470-570</b>	<b>565-620</b>	<b>670-690</b>	<b>675-700</b>	<b>690-740</b>	<b>700-740</b>
ARBU0726	0.0017	0.0013	0.0015	0.0017	0.0017	0.0030	0.0012
BROO0727	0.0017	0.0018	0.0011	0.0021	0.0021	0.0045	0.0027
CLME0724	0.0015	0.0013	0.0011	0.0018	0.0018	0.0031	0.0013
HESS0727	0.0023	0.0021	0.0012	0.0021	0.0021	0.0052	0.0035
HIGG0727	0.0017	0.0010	0.0013	0.0018	0.0018	0.0028	0.0010
HOUG0726	0.0021	0.0014	0.0008	0.0018	0.0017	0.0032	0.0014
JEHN0519	0.0016	0.0013	0.0008	0.0018	0.0018	0.0031	0.0013
MITC0725	0.0016	0.0013	0.0006	0.0018	0.0018	0.0033	0.0015
MUSK0728	0.0016	0.0012	0.0006	0.0021	0.0021	0.0033	0.0016
ROGE0724	0.0017	0.0014	0.0006	0.0019	0.0019	0.0035	0.0017
SAPP0725	0.0016	0.0013	0.0009	0.0018	0.0018	0.0031	0.0012
TAMA0605	0.0016	0.0012	0.0006	0.0019	0.0019	0.0031	0.0012

**APPENDIX F**  
**NARROW-WAVEBAND VOLUME REFLECTANCE**

**Volume reflectance used in narrow-band index sgolay filtered model data set**

<b>Band</b>	<b>A</b>	<b>B</b>	<b>C</b>	<b>D</b>	<b>E</b>	<b>F</b>	<b>G</b>	<b>H</b>
<b>Lake</b>	<b>435</b>	<b>455</b>	<b>470</b>	<b>565</b>	<b>670</b>	<b>675</b>	<b>690</b>	<b>700</b>
BEAR0819	0.0410	0.0438	0.0462	0.0419	0.0094	0.0099	0.0096	0.0076
BELL0826	0.0464	0.0476	0.0486	0.0845	0.0426	0.0442	0.0560	0.0586
BIG0820	0.0309	0.0325	0.0338	0.0457	0.0207	0.0206	0.0197	0.0172
BROO0526	0.0108	0.0102	0.0099	0.0262	0.0087	0.0080	0.0094	0.0095
CASS0810	0.0335	0.0330	0.0333	0.0420	0.0238	0.0235	0.0225	0.0205
CHEM0826	0.0358	0.0352	0.0357	0.0429	0.0249	0.0256	0.0247	0.0218
CHIP0820	0.0328	0.0315	0.0307	0.0449	0.0165	0.0162	0.0159	0.0137
CLSJ0603	0.0334	0.0353	0.0373	0.0530	0.0172	0.0170	0.0170	0.0153
CROT0605	0.0293	0.0267	0.0260	0.0246	0.0210	0.0211	0.0216	0.0198
CUB0819	0.0346	0.0372	0.0396	0.0503	0.0149	0.0152	0.0142	0.0113
DIAM0824	0.0794	0.0850	0.0889	0.1067	0.0357	0.0350	0.0336	0.0305
EAGL0824	0.0506	0.0500	0.0516	0.0623	0.0342	0.0346	0.0320	0.0295
FORD0826	0.0429	0.0499	0.0552	0.1213	0.0627	0.0603	0.0807	0.0987
GLEN0819	0.1216	0.1326	0.1401	0.1203	0.0363	0.0359	0.0329	0.0295
HESS0526	0.0859	0.0979	0.1060	0.1629	0.0954	0.0913	0.0979	0.1052
HICK0820	0.0355	0.0398	0.0431	0.0906	0.0577	0.0562	0.0673	0.0733
HIGG0608	0.0490	0.0520	0.0551	0.0474	0.0170	0.0168	0.0154	0.0141
KENT0826	0.0365	0.0364	0.0368	0.0565	0.0314	0.0318	0.0345	0.0318
KIMB0526	0.0445	0.0506	0.0556	0.0948	0.0839	0.0827	0.0794	0.0740
KLIN0603	0.0421	0.0447	0.0473	0.0486	0.0122	0.0119	0.0106	0.0086
LOON0810	0.0133	0.0135	0.0145	0.0261	0.0074	0.0073	0.0068	0.0052
LOTU0807	0.0642	0.0714	0.0780	0.1108	0.0418	0.0412	0.0377	0.0329
MACE0807	0.0364	0.0429	0.0482	0.0740	0.0173	0.0171	0.0152	0.0123
MECO0608	0.0584	0.0581	0.0583	0.0621	0.0447	0.0445	0.0437	0.0416
MECO0724	0.0318	0.0363	0.0388	0.0674	0.0373	0.0379	0.0390	0.0338
AWRI0728	0.0304	0.0300	0.0300	0.0402	0.0279	0.0275	0.0301	0.0300
OAKL0807	0.0265	0.0273	0.0278	0.0360	0.0199	0.0199	0.0180	0.0158
ORCH0810	0.0574	0.0633	0.0694	0.0935	0.0312	0.0308	0.0284	0.0241
PAWP0824	0.0576	0.0633	0.0671	0.1132	0.0525	0.0514	0.0560	0.0551
PICK0526	0.0346	0.0407	0.0448	0.0931	0.0506	0.0487	0.0571	0.0634
PONT0807	0.0431	0.0491	0.0545	0.1007	0.0596	0.0585	0.0603	0.0579
RAND0603	0.0242	0.0226	0.0228	0.0262	0.0112	0.0116	0.0121	0.0104
ROGE0519	0.0278	0.0276	0.0281	0.0361	0.0398	0.0400	0.0402	0.0386
SILV0725	0.0415	0.0473	0.0523	0.0746	0.0252	0.0251	0.0250	0.0222

**Volume reflectance used in narrow-band index sgolay filtered validation data set**

<b>Band</b>	<b>A</b>	<b>B</b>	<b>C</b>	<b>D</b>	<b>E</b>	<b>F</b>	<b>G</b>	<b>H</b>
<b>Lake</b>	<b>435</b>	<b>455</b>	<b>470</b>	<b>565</b>	<b>670</b>	<b>675</b>	<b>690</b>	<b>700</b>
ARBU0726	0.0653	0.0676	0.0698	0.0794	0.0328	0.0323	0.0302	0.0279
BROO0727	0.0863	0.0929	0.0999	0.1491	0.1156	0.1140	0.1181	0.1153
CLME0724	0.0315	0.0316	0.0335	0.0485	0.0196	0.0198	0.0193	0.0162
HESS0727	0.0694	0.0818	0.0947	0.1663	0.1263	0.1240	0.1278	0.1261
HIGG0727	0.0492	0.0534	0.0570	0.0436	0.0109	0.0107	0.0094	0.0082
HOUG0726	0.0316	0.0316	0.0337	0.0507	0.0300	0.0296	0.0287	0.0259
JEHN0519	0.0222	0.0227	0.0236	0.0386	0.0196	0.0197	0.0197	0.0173
MITC0725	0.0288	0.0295	0.0305	0.0455	0.0351	0.0348	0.0344	0.0320
MUSK0728	0.0372	0.0357	0.0352	0.0398	0.0285	0.0289	0.0328	0.0331
ROGE0724	0.0326	0.0349	0.0366	0.0552	0.0431	0.0433	0.0443	0.0415
SAPP0725	0.0256	0.0259	0.0264	0.0369	0.0145	0.0142	0.0144	0.0133
TAMA0605	0.0270	0.0252	0.0246	0.0257	0.0156	0.0158	0.0167	0.0140

**Volume reflectance used in narrow-band index db1 filtered model data set**

<b>Band</b>	<b>A</b>	<b>B</b>	<b>C</b>	<b>D</b>	<b>E</b>	<b>F</b>	<b>G</b>	<b>H</b>
<b>Lake</b>	<b>435</b>	<b>450</b>	<b>455</b>	<b>480</b>	<b>550</b>	<b>670</b>	<b>690</b>	<b>700</b>
BEAR0819	0.0409	0.0434	0.0437	0.0471	0.0458	0.0094	0.0092	0.0073
BELLO826	0.0461	0.0473	0.0473	0.0489	0.0813	0.0424	0.0569	0.0587
BIG0820	0.0312	0.0324	0.0324	0.0343	0.0445	0.0203	0.0191	0.0172
BROO0526	0.0108	0.0103	0.0103	0.0097	0.0235	0.0086	0.0098	0.0099
CASS0810	0.0335	0.0330	0.0330	0.0334	0.0404	0.0239	0.0222	0.0204
CHEM0826	0.0358	0.0353	0.0353	0.0351	0.0402	0.0253	0.0237	0.0219
CHIP0820	0.0323	0.0318	0.0318	0.0305	0.0429	0.0164	0.0157	0.0129
CLSJ0603	0.0331	0.0353	0.0353	0.0379	0.0526	0.0174	0.0168	0.0150
CROT0605	0.0286	0.0273	0.0273	0.0261	0.0245	0.0209	0.0212	0.0196
CUB0819	0.0345	0.0366	0.0366	0.0403	0.0508	0.0150	0.0136	0.0110
DIAM0824	0.0795	0.0841	0.0844	0.0899	0.1099	0.0361	0.0333	0.0309
EAGL0824	0.0504	0.0500	0.0500	0.0519	0.0613	0.0351	0.0304	0.0295
FORD0826	0.0428	0.0485	0.0494	0.0570	0.1157	0.0627	0.0801	0.1003
GLEN0819	0.1217	0.1308	0.1321	0.1427	0.1283	0.0369	0.0319	0.0298
HESS0526	0.0861	0.0958	0.0974	0.1089	0.1607	0.0948	0.0974	0.1057
HICK0820	0.0351	0.0391	0.0391	0.0441	0.0844	0.0586	0.0687	0.0737
HIGG0608	0.0493	0.0515	0.0515	0.0560	0.0508	0.0173	0.0155	0.0136
KENT0826	0.0362	0.0365	0.0365	0.0371	0.0537	0.0314	0.0344	0.0322
KIMB0526	0.0446	0.0494	0.0502	0.0583	0.0890	0.0841	0.0790	0.0747
KLIN0603	0.0424	0.0443	0.0444	0.0484	0.0514	0.0122	0.0103	0.0086
LOON0810	0.0133	0.0134	0.0134	0.0149	0.0246	0.0079	0.0066	0.0049
LOTU0807	0.0643	0.0702	0.0704	0.0809	0.1102	0.0422	0.0373	0.0332
MACE0807	0.0362	0.0414	0.0425	0.0503	0.0732	0.0175	0.0150	0.0123
MECO0608	0.0581	0.0580	0.0580	0.0582	0.0615	0.0449	0.0435	0.0420
MECO0724	0.0326	0.0374	0.0374	0.0404	0.0624	0.0363	0.0388	0.0334
AWRI0728	0.0298	0.0297	0.0297	0.0302	0.0391	0.0279	0.0305	0.0300
OAKL0807	0.0263	0.0274	0.0274	0.0282	0.0346	0.0202	0.0182	0.0156
ORCH0810	0.0575	0.0623	0.0623	0.0712	0.0946	0.0314	0.0279	0.0234
PAWP0824	0.0574	0.0625	0.0627	0.0680	0.1080	0.0528	0.0576	0.0549
PICK0526	0.0347	0.0400	0.0400	0.0462	0.0889	0.0519	0.0589	0.0639
PONT0807	0.0430	0.0484	0.0485	0.0568	0.0954	0.0599	0.0610	0.0583
RAND0603	0.0239	0.0225	0.0225	0.0227	0.0250	0.0110	0.0120	0.0099
ROGE0519	0.0278	0.0276	0.0276	0.0283	0.0344	0.0397	0.0402	0.0387
SILV0725	0.0425	0.0468	0.0468	0.0541	0.0761	0.0254	0.0244	0.0220

**Volume reflectance used in narrow-band index db1 filtered validation data set**

<b>Band</b>	<b>A</b>	<b>B</b>	<b>C</b>	<b>D</b>	<b>E</b>	<b>F</b>	<b>G</b>	<b>H</b>
<b>Lake</b>	<b>435</b>	<b>450</b>	<b>455</b>	<b>480</b>	<b>550</b>	<b>670</b>	<b>690</b>	<b>700</b>
ARBU0726	0.0651	0.0670	0.0671	0.0704	0.0805	0.0330	0.0298	0.0280
BROO0727	0.0869	0.0916	0.0916	0.1028	0.1435	0.1162	0.1190	0.1166
CLME0724	0.0313	0.0315	0.0315	0.0342	0.0463	0.0201	0.0188	0.0162
HESS0727	0.0720	0.0798	0.0798	0.0994	0.1579	0.1276	0.1290	0.1260
HIGG0727	0.0492	0.0529	0.0530	0.0581	0.0482	0.0110	0.0087	0.0084
HOUG0726	0.0315	0.0315	0.0315	0.0338	0.0475	0.0302	0.0283	0.0259
JEHN0519	0.0222	0.0226	0.0226	0.0240	0.0360	0.0196	0.0198	0.0175
MITC0725	0.0287	0.0295	0.0297	0.0309	0.0427	0.0353	0.0344	0.0317
MUSK0728	0.0372	0.0357	0.0357	0.0349	0.0400	0.0284	0.0330	0.0335
ROGE0724	0.0325	0.0346	0.0349	0.0371	0.0509	0.0433	0.0440	0.0420
SAPP0725	0.0255	0.0257	0.0257	0.0266	0.0360	0.0146	0.0145	0.0133
TAMA0605	0.0272	0.0250	0.0250	0.0245	0.0251	0.0153	0.0163	0.0138

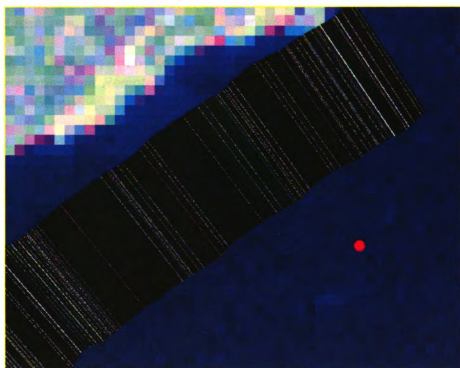
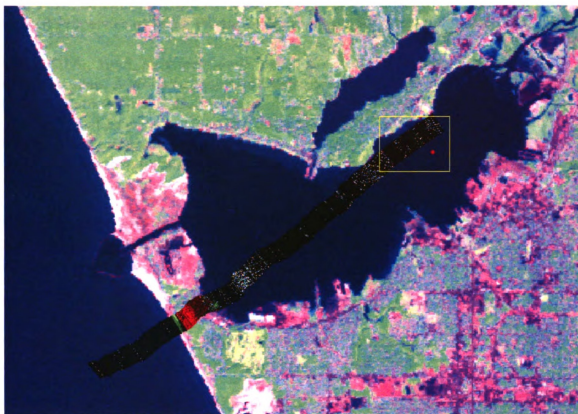
**Volume reflectance used in narrow-band index s8 filtered model data set**

<b>Band</b>	<b>A</b>	<b>B</b>	<b>C</b>	<b>D</b>	<b>E</b>	<b>F</b>	<b>G</b>	<b>H</b>
<b>Lake</b>	<b>435</b>	<b>450</b>	<b>490</b>	<b>560</b>	<b>660</b>	<b>690</b>	<b>698</b>	<b>700</b>
BEAR0819	0.0410	0.0428	0.0480	0.0436	0.0093	0.0099	0.0075	0.0071
BELL0826	0.0462	0.0470	0.0511	0.0844	0.0461	0.0567	0.0590	0.0588
BIG0820	0.0311	0.0321	0.0348	0.0454	0.0224	0.0198	0.0177	0.0171
BROO0526	0.0108	0.0103	0.0098	0.0257	0.0115	0.0096	0.0101	0.0098
CASS0810	0.0336	0.0329	0.0338	0.0417	0.0251	0.0227	0.0210	0.0205
CHEM0826	0.0360	0.0348	0.0353	0.0424	0.0252	0.0251	0.0222	0.0216
CHIP0820	0.0325	0.0319	0.0317	0.0441	0.0181	0.0162	0.0141	0.0133
CLSJ0603	0.0333	0.0345	0.0392	0.0532	0.0193	0.0175	0.0155	0.0152
CROT0605	0.0292	0.0274	0.0252	0.0246	0.0217	0.0218	0.0200	0.0198
CUB0819	0.0345	0.0373	0.0424	0.0509	0.0158	0.0149	0.0116	0.0110
DIAM0824	0.0791	0.0833	0.0917	0.1085	0.0389	0.0340	0.0313	0.0305
EAGL0824	0.0507	0.0488	0.0531	0.0620	0.0347	0.0329	0.0288	0.0290
FORD0826	0.0427	0.0478	0.0613	0.1212	0.0754	0.0799	0.0986	0.1010
GLEN0819	0.1213	0.1300	0.1450	0.1235	0.0381	0.0331	0.0301	0.0295
HESS0526	0.0856	0.0947	0.1135	0.1633	0.1079	0.0966	0.1068	0.1063
HICK0820	0.0355	0.0384	0.0471	0.0897	0.0661	0.0680	0.0744	0.0743
HIGG0608	0.0490	0.0509	0.0574	0.0489	0.0174	0.0159	0.0141	0.0138
KENT0826	0.0363	0.0365	0.0386	0.0559	0.0338	0.0352	0.0328	0.0319
KIMB0526	0.0445	0.0490	0.0632	0.0930	0.0875	0.0797	0.0755	0.0741
KLIN0603	0.0422	0.0439	0.0507	0.0497	0.0132	0.0106	0.0091	0.0087
LOON0810	0.0134	0.0130	0.0160	0.0254	0.0087	0.0073	0.0054	0.0049
LOTU0807	0.0640	0.0693	0.0858	0.1112	0.0445	0.0383	0.0336	0.0325
MACE0807	0.0362	0.0410	0.0547	0.0743	0.0185	0.0156	0.0127	0.0122
MECO0608	0.0583	0.0580	0.0583	0.0620	0.0463	0.0440	0.0421	0.0417
MECO0724	0.0326	0.0354	0.0419	0.0665	0.0405	0.0401	0.0346	0.0336
AWRI0728	0.0301	0.0301	0.0308	0.0399	0.0306	0.0303	0.0306	0.0303
OAKL0807	0.0263	0.0270	0.0293	0.0356	0.0198	0.0181	0.0164	0.0160
ORCH0810	0.0571	0.0611	0.0754	0.0942	0.0332	0.0294	0.0245	0.0239
PAWP0824	0.0574	0.0616	0.0701	0.1129	0.0593	0.0569	0.0566	0.0553
PICK0526	0.0345	0.0391	0.0497	0.0930	0.0585	0.0575	0.0639	0.0643
PONT0807	0.0430	0.0475	0.0609	0.0998	0.0651	0.0611	0.0594	0.0581
RAND0603	0.0244	0.0228	0.0233	0.0259	0.0115	0.0127	0.0106	0.0101
ROGE0519	0.0279	0.0276	0.0291	0.0356	0.0398	0.0403	0.0391	0.0386
SILV0725	0.0420	0.0454	0.0564	0.0749	0.0273	0.0253	0.0226	0.0218

**Volume reflectance used in narrow-band index s8 filtered validation data set**

<b>Band</b>	<b>A</b>	<b>B</b>	<b>C</b>	<b>D</b>	<b>E</b>	<b>F</b>	<b>G</b>	<b>H</b>
<b>Lake</b>	<b>435</b>	<b>450</b>	<b>490</b>	<b>560</b>	<b>660</b>	<b>690</b>	<b>698</b>	<b>700</b>
ARBU0726	0.0652	0.0668	0.0713	0.0803	0.0344	0.0304	0.0284	0.0279
BROO0727	0.0868	0.0910	0.1074	0.1480	0.1241	0.1191	0.1176	0.1157
CLME0724	0.0317	0.0310	0.0351	0.0479	0.0213	0.0197	0.0167	0.0163
HESS0727	0.0714	0.0776	0.1054	0.1644	0.1353	0.1284	0.1284	0.1265
HIGG0727	0.0490	0.0520	0.0586	0.0455	0.0112	0.0093	0.0083	0.0083
HOU0726	0.0319	0.0310	0.0347	0.0499	0.0324	0.0291	0.0263	0.0257
JEHN0519	0.0222	0.0224	0.0251	0.0380	0.0210	0.0200	0.0179	0.0173
MITC0725	0.0287	0.0294	0.0324	0.0447	0.0372	0.0347	0.0327	0.0320
MUSK0728	0.0371	0.0359	0.0348	0.0401	0.0306	0.0331	0.0335	0.0333
ROGE0724	0.0325	0.0343	0.0383	0.0540	0.0453	0.0449	0.0422	0.0415
SAPP0725	0.0254	0.0257	0.0271	0.0368	0.0166	0.0147	0.0137	0.0133
TAMA0605	0.0270	0.0251	0.0242	0.0253	0.0165	0.0173	0.0147	0.0142

**APPENDIX G**  
**PRACTICAL PROBLEM WITH AISA IMAGE**



## REFERENCES

- Ahn, Y. H., Bricaud, A., and A. Morel, 1992, Light Backscattering Efficiency and Related Properties of Some Phytoplankters, *Deep-Sea Research*, 39:1835-1855.
- Albert, D. A., 1995, Regional Landscape Ecosystems of Michigan, Minnesota, and Wisconsin: A Working Map and Classification, *General Technical Report NC-178*, St. Paul, MN: U.S. Department of Agriculture, Forest Service, North Central Forest Experiment Station, Jamestown, ND: Northern Prairie Wildlife Research Center Online,  
<http://www.npwrc.usgs.gov/resource/habitat/rlandscp/rlandscp.htm>  
(Version 03JUN1998).
- Anderson, D. M. and D. J. Garrison, editors, 1997, The Ecology and Oceanography of Harmful Algal Blooms, *Limnology and Oceanography*, 42:1009-1305.
- ASD Inc, 2006, Analytical Spectral Devices Inc., <http://www.asdi.com>.
- Asrar, G., 1989, *Theory and Applications of Optical Remote Sensing*, New York, Wiley Series in Remote Sensing, John Wiley & Sons, Inc.
- Becker, B. L., Lusch, D. P., and J. Qi, 2005, Identifying Optimal Spectral Bands from *In Situ* Measurements of Great Lakes Coastal Wetlands using Second-derivative Analysis, *Remote Sensing of Environment*, 97:238-248.
- Bukata, R. P., Jerome, J. H., Kondratyev, K. Y., and D. V. Pozdnyakov, 1995, *Optical Properties and Remote Sensing of Inland and Coastal Waters*, New York: CRC Press, 362 pp.
- Butler, W. L. and D. W. Hopkins, 1970, Higher Derivative Analysis of Complex Absorption Spectra, *Photochemistry and Photobiology*, 12:439-450.
- Buzzi, F., 2002, Phytoplankton Assemblages in Two Sub-basins of Lake Como, *Journal of Limnology*, 61(1):117-128.
- Capone, D. G., Zehr, J. P., Paerl, H. W., Bergman, B., and E. J. Carpenter, 1997, *Trichodesmium*, a Globally Significant Marine Cyanobacterium, *Science*, 276:1221-1229.

Carpenter, S. R., Caraco, N. F., Correll, D. L., Howarth, R. W., Sharrley, A. N., and V. H. Smith, 1998, Nonpoint Pollution of Surface Waters with Phosphorus and Nitrogen, *Ecological Applications*, 8(3):559-568.

Chappelle, E. W., Kim, M. S., and J. E. I. McMurtrey, 1992, Ratio Analysis of Reflectance Spectra (RARS): An Algorithm for the Remote Estimation of the Concentrations of Chlorophyll *a*, Chlorophyll *b*, and Carotenoids in Soybean Leaves, *Remote Sensing of Environment*, 39:239-247.

Clark, C. D., Ripley, H. T., Green, E. P., Edwards, A. J., and P. J. Mumby, 1997, Mapping and Measurement of Tropical Coastal Environments with Hyperspectral and High Spatial Resolution Data, *International Journal of Remote Sensing*, 18(2):237-242.

Clarke, G. K., Ewing, G. C., and C. J. Lorenzen, 1970, Spectra of Backscattered Light from the Sea Obtained from Aircraft as a Measure of Chlorophyll Concentration, *Science*, 167:1119-1121.

Cox, R. M., Forsythe, R. D., Vaughan, G. E., and L. L. Olmsted, 1998, Assessing Water Quality in the Catawba River Reservoirs using Landsat Thematic Mapper Satellite Data, *Lake and Reservoir Management*, 14:405-416.

Curran, P. J., Dungan, J. L., Macler, B. A., Plummer, S. E., and D. L. Peterson, 1992, Reflectance Spectroscopy of Fresh Shore Leaves for the Estimation of Chemical Concentration, *Remote Sensing of Environment*, 39:153-166.

Dall'Olmo, G., 2005, Advanced Algorithms for Remote Estimation of Water Quality, <http://calmaps.unl.edu/snrscoq/1>, PPT-file.

Dall'Olmo, G. and A. A. Gitelson, 2005, Effect of Bio-optical Parameter Variability on the Remote Estimation of Chlorophyll-*a* Concentration in Turbid Productive Waters: Experimental Results, *Applied Optics*, 44(3):412-422.

Davis, J. C., 1986, *Statistics and Data Analysis in Geology*, John Wiley & Sons, New York.

Dekker, A. G., 1993, Detection of Optical Water Quality Parameters for Eutrophic Waters by High Resolution Remote Sensing, *PhD Thesis*, Vrije Universiteit, Amsterdam.

Dekker, A. G. and S. W. M. Peters, 1993, A TM Study of Eutrophic Lakes in the Netherlands, *International Journal of Remote Sensing*, 14:799-821.

- Dekker, A. G., Malthus, T. J., Wijnen, M. W., and E. Seyhan, 1992, The Effect of Spectral Bandwidth and Positioning on the Spectral Signature Analysis of Inland Waters, *Remote Sensing of Environment*, 41:211-225.
- Dekker, A. G., Vos, R. J., and S. W. M. Peters, 2001, Comparison of Remote Sensing Data, Model Results and *In Situ* Data for Total Suspended Matter (TSM) in the Southern Frisian Lakes, *The Science of the Total Environment*, 268:197-214.
- Demetriades-Shah, T. H., Steven, M. D., and J. A. Clark, 1990, High Resolution Derivatives Spectra in Remote Sensing, *Remote Sensing of Environment*, 33:55-64.
- Doerffer, R., Fisher, J., Stossel, M., Brockmann, C., and H. Grassl, 1989, Analysis of Thematic Mapper Data for Studying the Suspended Matter Distribution in the Coastal Area of the German Bight (North Sea), *Remote Sensing of Environment*, 28:61-73.
- Dorr, J.A., Jr. and D. F. Eschman, 1984, Geology of Michigan, *University of Michigan Press*, Ann Arbor, MI: 470 pp.
- Doxaran, D., Froidefond, J.M., Lavender, S., and P. Castaing, 2002, Spectral Signature of Highly Turbid Waters: Application with SPOT data to Quantify Suspended Particulate Matter Concentrations, *Remote Sensing of Environment*, 81:149-161.
- Duda, R. O. and P. E. Hart, 1973, *Pattern Classification and Scene Analysis*, Wiley, New York.
- Eichenlaub, V.L., 1979, Weather and the Climate of The Great Lakes Region, *The University of Notre Dame Press*, Notre Dame, IN, 333 pp.
- Fell, A. F., and G. Smith, 1982, Higher Derivative Methods in Ultraviolet, Visible and Infrared Spectrophotometry, *The Analytical Proceedings*, 19:28-32.
- Fisher, S. G., 1994, Pattern, Process and Scale in Freshwater Ecosystems: Some Unifying Thoughts, In *Aquatic Ecology – Scale, Pattern and Process*, edited by P. S. Giller, A. G. Hildrew and D. G. Raffaelli (London: Blackwell Sciences Ltd), 575-592.
- Flink, P., Lindell, T., and C. Ostlund, 2001, Statistical Analysis of Hyperspectral Data from Two Swedish Lakes, *The Science of the Total Environment*, 268:155-169.

Fraser, R. S., 1998, Multispectral Remote Sensing of Turbidity Among Nebraska Sand Hills Lakes, *International Journal of Remote Sensing*, 19:3011-3016.

Gege, P., 2001, A Software Tool for Simulation and Analysis of Optical *In-situ* Spectra, *4th Berlin Workshop on Ocean Remote Sensing*, Berlin, Germany.

George, D. G. and T. J. Malthus, 2001, Using a Compact Airborne Spectrographic Imager to Monitor Phytoplankton Biomass in a Series of Lakes in North Wales, *The Science of the Total Environment*, 268:215-226.

Giardino, C., Pepe, M., Brivio, P. A., Ghezzi, P., and E. Zilioli, 2001, Detecting Chlorophyll, Secchi Disk Depth and Surface Temperature in a Sub-Alpine Lake using Landsat Imagery, *The Science of the Total Environment*, 268:19-29.

Gitelson, A. A., 1992, The Peak Near 700 nm on Radiance Spectra of Algae and Water: Relationships of its Magnitude and Position with Chlorophyll Concentration, *International Journal of Remote Sensing*, 13:3367-3373.

Gitelson, A., Garbuzov, G., Szilagyi, F., Mittenzwey, K. H., Karnieli, K., and A. Kaiser, 1993, Quantitative Remote Sensing Methods for Real-time Monitoring of Inland Waters Quality, *International Journal of Remote Sensing*, 14:1269-1295.

Goodin, D. G., L. Han, R. N. Fraser, D. C. Rundquist and W. A. Stebbins, 1993, Analysis of Suspended Solids in Water Using Remotely Sensed High Resolution Derivative Spectra, *Photogrammetric Engineering and Remote Sensing*, 59(4):505-510.

Gordon, H. R., 1987, Calibration Requirement and Methodology for Remote Sensors Viewing the Oceans in the Visible, *Remote Sensing of Environment*, 22:103-126.

Gordon, H. R., Brown, O. B., and M. M. Jacobs, 1975, Computed Relationships between the Inherent and Apparent Optical Properties of a Flat Homogenous Ocean, *Applied Optics*, 14:417-427.

Green, S., 1998, The Effect of Chlorophyll Concentration on Airborne Hyperspectral Reflectance, [www.ucd.ie/app-phys/stuart/MODEL.HTM](http://www.ucd.ie/app-phys/stuart/MODEL.HTM).

Hamilton, M. K., Davis, C. O., Rhea, W. J., Pilorz, S. H., and K. J. Cardel, 1993, Estimation Chlorophyll Content and Bathymetry of Lake Tahoe using AVIRIS Data, *Remote Sensing of Environment*, 44(2/3):217-230.

- Han, L., 1997, Spectral Reflectance with Varying Suspended Sediment Concentrations in Clear and Algae-Laden Waters, *Photogrammetric Engineering and Remote Sensing*, 63(6):701-705.
- Han, L. and D. C. Rundquist, 1997, Comparison of NIR/RED Ratio and First Derivative of Reflectance in Estimating Algal-Chlorophyll Concentration: A Case Study in a Turbid Reservoir, *Remote Sensing of Environment*, 62:253-261.
- Han, L. and D. C. Rundquist, 1998, The Impact of a Wind-roughened Water Surface on Remote Measurements of Turbidity, *International Journal of Remote Sensing*, 19(1):195-201.
- Han, L., Rundquist, D. C., Liu, L. L., Fraser, R. N., and J. F. Schalles, 1994, The Spectral Response of Algal Chlorophyll in Water with Varying Levels of Suspended Sediment, *International Journal of Remote Sensing*, 15:3707-3718.
- Harding, L. W., Itsweire, E. C., and W. E. Esalas, 1995, Algorithm Development for Recovering Chlorophyll Concentrations in the Chesapeake Bay using Aircraft Remote Sensing, 1989-91, *Photogrammetric Engineering and Remote Sensing*, 61(2):177-185.
- Harma, P., Vepsalainen, J., Hannonen, T., Pyhalahti, T., Kamari, J., Kallio, K., Eloheimo, K., and S. Koponen, 2001, Detection of Water Quality using Simulated Satellite Data and Semi-empirical Algorithms in Finland, *The Science of the Total Environment*, 268:107-121.
- Harrington, J. and R. L. Repic, 1995, Hyperspectral and Video Remote Sensing of Oklahoma Lakes, *Papers and Proceedings of Applied Geography Conferences*, 18:79-86.
- Heege, T. and J. Fischer, 2000, Sun Glitter Correction in Remote Sensing Imaging Spectrometry, *The XV Ocean Optics Conference, 16 – 20 October 2000* (Falls Church, VA: Office of Naval Research).
- Howarth, R., Anderson, D., Cloern, J., Elfring, C., Hopkinson, C. Lapointe, B., Malone, R., Marcus, N., McGlathery, K., Sharpley, A., and D. Walker, 2000, Nutrient Pollution of Coastal Rivers, Bays, and Seas, *Issues in Ecology*, Issue 7, [www.esa.org/science/Issues](http://www.esa.org/science/Issues).
- Huguenin, R. L. and J. L. Jones, 1986, Intelligent Information Extraction from Reflectance Spectra: Absorption Band Positions, *Journal of Geophysical Research*, 91:9585-9598.

IOCCG, 1998, Minimum Requirements for an Operational Ocean-colour Sensor for the Open Ocean, Reports of the International Ocean-Colour Coordinating Group, Number 1, Dartmouth, Canada.

Jensen, J. R., 1996, *Remote Sensing of the Environment: An Earth Resource Perspective*, Prentice Hall, Upper Saddle River, NJ.

Jensen, J. R., 2000. *Remote sensing of the environment: An Earth resource perspective*, Prentice Hall series in geographic information science, 544 pp.

Jupp, D. L. B., Kirk, J. T. O., and G. P. Harris, 1994, Detection, Identification and Mapping of Cyanobacteria – Using Remote Sensing to Measure the Optical Quality of Turbid Inland Waters, *Australian Journal of Marine and Freshwater Research*, 45:801-828.

Kallio, K., Koponen, S., and J. Pulliainen, 2003, Feasibility of Airborne Imaging Spectrometry for Lake Monitoring – A Case Study of Spatial Chlorophyll *a* Distribution in Two Meso-Eutrophic Lakes, *International Journal of Remote Sensing*, 24(19):3771-3790.

Kallio, K., Kutser, T., Hannonen, T., Koponen, S., Pulliainen, J., Vepsalainen, J., and T. Pyhalahti, 2001, Retrieval of Water Quality from Airborne Imaging Spectrometry of Various Lake Types in Different Seasons, *The Science of the Total Environment*, 268:59-77.

Kloiber, S. M., Brezonik, P. L., Olmanson, L. G., and M. E. Bauer, 2002, A Procedure for Regional Lake Water Clarity Assessment using Landsat Multispectral Data, *Remote Sensing of the Environment*, 82:38-47.

Koponen, S. Pulliainen, J., Servomaa, H., Zhang, Y., Hallikainen, M., Kallio, K., Vepsalainen, J., Pyhalahti, T., and T. Hannonen, 2001, Analysis on the Feasibility of Multi-source Remote Sensing Observations for Chl *a* Monitoring in Finnish Lakes, *The Science of the Total Environment*, 268:95-106.

Kotak, B. G., Kenefick, S. L., Fritz, D. L., Rousseaux, C. G., Prepas, E. E., and S. E. Hrudey, 1993, Occurrence and Toxicological Evaluation of Cyanobacterial Toxins in Alberta Lakes and Farm Dugouts, *Water Research*, 27:495-506.

Kotak, B. G., Prepas, E. E., and S. E. Hrudey, 1994, Blue Green Algal Toxins in Drinking Water Supplies: Research in Alberta, *Lake Line*, 14:37-40.

Kutser, T., Herlevi, A., Kallio, K., and K. Arst, 2001, A Hyperspectral Model for Interpretation of Passive Optical Remote Sensing Data from Turbid Lakes, *The Science of the Total Environment*, 268:47-58.

LabSphere, Inc., 2006,  
<http://www.globalspec.com/Supplier/Profile/Labsphere>.

Lathrop, R. G., 1992, Landsat Thematic Mapper Monitoring of Turbid Inland Water Quality, *Photogrammetric Engineering and Remote Sensing*, 46:286-280.

Lathrop, R. G. and T.M. Lillesand, 1989, Monitoring Water Quality and River Plume Transport in Green Bay, Lake Michigan with SPOT-1 imagery, *Photogrammetric Engineering and Remote Sensing*, 55(3):349-354.

Lillesand, T. M., 2002, Combining Satellite Remote Sensing and Volunteer Secchi Disk Measurement for Lake Transparency Monitoring, *Proceedings, National Monitoring Conference*.

Lillesand, T. M. and R. Q. Kiefer, 2000, *Remote Sensing and Image Interpretation*, 4<sup>th</sup> Edition, John Wiley and Sons, NY.

Lillesand, T. M., Johnson, W. L., Deuell, R. L., Lindstrom, O. M., and D. E. Meisner, 1983, Use of Landsat Data to Predict the Trophic State of Minnesota Lakes, *Photogrammetric Engineering and Remote Sensing*, 49(2):219-229.

Lodhi, M. S., D. C. Rundquist, L. Han and M. S. Juzila, 1997, The Potential for Remote Sensing of Loess Soils Suspended in Surface Waters, *Journal of the American Water Resources Association*, 33(1):111-127.

Malthus, T. J., Place, C. J., Bennet, S., and S. North, 1996, An Evaluation of the Airborne Thematic Mapper Sensor for Monitoring Inland Water Quality, *Proceeding of the 22<sup>nd</sup> Annual Conference of the Remote Sensing Society, September 1996*, University of Durham, 317-342.

Martin, M. E. and J. D. Aber, 1993, Measurements of Canopy Chemistry with 1992 AVIRIS Data at Blackhawk Island and Harvard Forest, in *The Forth Annual JPL Airborne Geoscience Workshop*, Washington D. C.

McComb, A. J. and J. A. Davis, 1993, Eutrophic Waters of Southwestern Australia, *Fertilizer Research*, 36:104-114.

Morel, A. and B. Gentili, 1993, Diffuse Reflectance of Oceanic Waters: II. Bidirectional Aspects, *Applied Optics* 32:6864-6879.

Nanu, L., 1993, Effect of Suspended Sediment Depth Distribution on Coastal Water Spectral Reflectance: Theoretical Simulation, *International Journal of Remote Sensing*, 14(2):225-239.

National Resources Inventory, 1987, Michigan Data, *USDA Soil Conservation Service*, East Lansing, Michigan.

NRC (National Research Council), 1993, *Managing Wastewater in Coastal Urban Areas*, National Academy Press, Washington, D. C., USA.

O'Reilly, J. E., Maritorena, S., Mitchell, B. G., Siegel, D. A., Carder, K. L., Garver, S. A., Kahru, M., and C. R. McClain, 1998, Ocean Color Chlorophyll Algorithms for SeaWiFS, *Journal of Geophysical Research*, 103:24937-24953.

Ostlund, C., Flink, P., Strombeck, N., Piersson, D., and T. Lindell, 2001, Mapping of the Water Quality of Lake Erken, Sweden, from Imaging Spectrometry and Landsat Thematic Mapper, *The Science of the Total Environment*, 268:139-154.

Ouillon, S., Forget, P., Froidefond, J.M., and J. J. Naudin, 1997, Estimating Suspended Matter Concentrations from SPOT Data and from Field Measurements in the Rhone River Plume, *Marine Technology Society Journal*, 31(2):15-20.

Palmstrom, N. S., Carlson, R. E., and G. D. Cooke, 1988, Potential Links between Eutrophication and Formation of Carcinogens in Drinking Water, *Lake and Reservoir Management*, 4:1-15.

Pattiaratchi, C., Lavery, P., Wyllie, A., and P. Hick, 1994, Estimates of Water Quality in Coastal Waters using Multi-date Landsat Thematic Mapper Data, *International Journal of Remote Sensing*, 15:1571-1584.

Penuelas, J., Gamon, J. A., Fredeen, A. L., Merino, J., and C. B. Field, 1994, Reflectance Indices Associated with Physiological Changes in Nitrogen- and Water-limited Sunflower Leaves, *Remote Sensing of Environment*, 48:135-146.

Pepe, M., Giardino, C., Borsani, G., Cardoso, A. C., Chiaudani, G., Premazzi, G., Rodari, E., and E. Zilioli, 2001, Relationship Between Apparent Optical Properties and Photosynthetic Pigments in the Sub-alpine Lake Iseo, *The Science of the Total Environment*, 268:31-45.

- Philpot, W. D., 1991, The Derivative Ratio Algorithm: Avoiding Atmospheric Effects in Remote Sensing, *IEEE Transactions on Geoscience and Remote Sensing*, 29(3):350-357.
- Postel, S. L., 1997, *Last Oasis. Second edition*, Island Press, Washington, D. C., USA.
- Postel, S. L. and S. R. Carpenter, 1997, *Freshwater Ecosystem Services*, G. C. Daily, editor. Nature's Services. Island Press, Washington, D. C., USA, pg 195-214.
- Postel, S. L., Daily, G. C., and P. R. Ehrlich, 1996, Human Appropriation of Renewable Fresh Water, *Science*, 271:785-788.
- Pulliainen, J., Kallio, K., Eloheimo, K., Koponen, S., Servomaa, H., Hannonen, T., Tauriainen, S., and M. Hallikainen, 2001, A Semi-Operative Approach to Lake Water Quality Retrieval from Remote Sensing Data, *The Science of the Total Environment*, 268:79-93.
- Rencz, A. N., 1999, *Remote Sensing for the Earth Sciences (Manual of Remote Sensing – Third Edition)*, John Wiley & Sons, Inc, 707 pp.
- Richards, J. A., 1993, *Remote Sensing Digital Image Analysis (2<sup>nd</sup> Edition)*, Springer Verlag, New York.
- Richards, J. A. and X Jia, 1999, *Remote Sensing Digital Image Analysis: An Introduction*, Springer, 363 pp.
- Ritchie, J. C. and C. M. Cooper, 1991, An Algorithm for Estimation Surface Suspended Sediment Concentrations with Landsat MSS Digital Data, *Water Resources Bulletin*, 27(3):373-379.
- Roelfsema, C., Dennison, B., Phinn, S., Dekker, A., and Brando, V., 2001, Remote Sensing of a Cyanobacterial Bloom (*Lyngbya majuscula*) in Moreton Bay, Australia, *IEEE*.
- Ruiz-Azuara, P., 1995, Multitemporal Analysis of "Simultaneous" Landsat Imagery (MSS and TM) for Monitoring Primary Production in a Small Tropical Coastal Lagoon, *Photogrammetric Engineering and Remote Sensing*, 61(2):187-198.
- Rummel, R. J., 1970, *Applied Factor Analysis*, Northwestern University Press, Evanston, IL.

Rundquist, D. C., Han, L., Schalles, J. F. and J. S. Peake, 1996, Remote Measurement of Algal Chlorophyll in Surface Waters: The Case for the First Derivative of Reflectance near 690 nm, *Photogrammetric Engineering and Remote Sensing*, 62(2):195-200.

Rundquist, D. C., Schalles, J. F. and J. S. Peake, 1995, The Response of Volume Reflectance to Manipulated Algal Concentrations Above Bright and Dark Bottoms at Various Depths in an Experimental Pool, *Geocarto International*, 10:5-14.

Sathyendranath, S. and T. Platt, 1989, Remote Sensing of Ocean Chlorophyll: Consequence of Nonuniform Pigment Profile, *Applied Optics*, 28:490-495.

Schmidt, K. S. and A. K. Skidmore, 2004, Smoothing Vegetation Spectra with Wavelets, *International Journal of Remote Sensing*, 25(6):1167-1184.

Schuette, B. and D. M. Skjaerlund, 1994, Michigan Farmland and Agriculture Development Task Force: Policy Recommendations and Options for the Future Growth of Michigan Agriculture: A Report to Governor John Dagler/ Michigan Farmland and Agriculture Development Task Force, *The Task Force, 1994*, Lansing, Michigan.

Seehausen, O., van Alphen, J. J. M., and F. Witte, 1997, Cichlid Fish Diversity Threatened by Eutrophication that Curbs Sexual Selection, *Science*, 277:1808-1811.

Shafique, N. A., Bradley, A. C., Fulk, F., and S. M. Cormier, 2001, The Selection of Narrow Wavebands for Optimizing Water Quality Monitoring on the Great Miami River, Ohio using Hyperspectral Remote Sensor Data, *Journal of Spatial Hydrology*, 1(1):1-22.

Slater, P. N., 1980, *Remote Sensing: Optics and Optical Systems*. Reading Mass: Addison-Wesley.

Smith, V. H., 1998, Cultural Eutrophication of Inland, Estuarine, and Coastal Waters. In M. L. Pace and P.M. Groffman, editors, *Successes, Limitations, and Frontiers in Ecosystem Science*, Springer-Verlag, New York, New York, USA.

Stevenson, R. J., Bothwell, M. L., and Lowe, R. L., 1996, *Algal Ecology: Freshwater Benthic Ecosystems*, Academic Press, San Diego, pg 718.

Subramaniam, A. and E. J. Carpenter, 1994, An Empirically Derived Protocol for the Detection of Blooms of the Marine Cyanobacterium *Trichodesmium* using CZCS Imagery, *International Journal of Remote Sensing*, 15:1559-1569.

Subramaniam, A., Carpenter, E. J., Karentz, D., and P. G. Falkowski, 1999, Optical Properties of the Marine Diazotrophic Cyanobacteria *Trichodesmium* spp. I. Absorption and Spectral Photosynthetic Characteristics, *Limnology and Oceanography*, 44:608-617.

Tassan, S., 1988, The Effect of Dissolved Yellow Substance on the Quantitative Retrieval of Chlorophyll and Total Suspended Sediment Concentrations from Remote Measurements of Water Colour, *International Journal of Remote Sensing*, 9(4):787-797.

The Academy of Natural Sciences, 2006, Biovolumes of Algal Taxa in Samples Collected by the USGS NAWQA program, <http://diatom.acnatsci.org/nawqa/2001biovol.asp>.

The Canadian Space Agency, 2003, Hyperspectral Remote Sensing: Applications for Marine, Coastal and Inland Waters, [www.space.gc.ca/asc/eng/satellites/hyper\\_marine.asp](http://www.space.gc.ca/asc/eng/satellites/hyper_marine.asp).

The MathWorks, Inc., 2006, Documentation for MathWorks Products, R2006a, [www.mathworks.com/access/helpdesk/help/helpdesk.html](http://www.mathworks.com/access/helpdesk/help/helpdesk.html).

Tsai, F. and Philpot, W., 1998, Derivative Analysis of Hyperspectral Data, *Remote Sensing of Environment*, 66:41-51.

U.S. EPA (U.S. Environmental Protection Agency), 1990, *National Water Quality Inventory*, 1988 Report to Congress, Office of Water (4503F), U.S. Government Printing Office, Washington, D. C., USA.

U.S. EPA (U.S. Environmental Protection Agency), 1996, *Environmental Indicators of water quality in the United States*. EPA 841-R-96-002. USEPA, Office of Water (4503F), U.S. Government Printing Office, Washington, D. C., USA.

Van Stokkom, H. T. C., Stokman, G. N. M., and J. W. Hovenier, 1993, Quantitative Use of Passive Optical Remote Sensing Over Coastal and Inland Water Bodies, *International Journal of Remote Sensing*, 14:541-563.

Veatch, J. O., 1941, Agricultural Land Classification and Land Types of Michigan, *Michigan State University, Agricultural Experiment Station, Special Bulletin*: no. 231 (First revision).

Veatch, J. O., 1953, Soil and Land of Michigan, *Memoir (Michigan State University, Agricultural Experiment Station)*, no. 7.

Verdin, J. P., 1985, Monitoring Water Quality Conditions in a Large Western Reservoir with Landsat Imagery, *Photogrammetric Engineering and Remote Sensing*, 51(3):343-353.

Vos, R. and M. Rijkeboer, 2000, Monitoring of Algal Blooms in Case 2 Waters with SesWIFS, *The XV Ocean Optics Conference, 16 – 20 October 2000* (Falls Church, VA: Office of Naval Research).

Wetzel, R. G., 1992, Clean Water: A Fading Resource, *Hydrobiologia*, 243/244:21-30.

Wetzel, R. G., 2001, *Limnology: Lake and River Ecosystems (3<sup>rd</sup> Edition)*, Academic Press, San Diego, 1006 pp.

Wrigley, R. C. and A. J. Horne, 1974, Remote Sensing and Lake Eutrophication, *Nature*, 250:217-215.

MICHIGAN STATE UNIVERSITY LIBRARIES



3 1293 02845 3607